Optical cryocooler design and demonstration for space applications

Rémi Vicente

Université Grenoble Alpes

THÈSE

Pour obtenir le grade de

DOCTEUR DE LA COMMUNAUTÉ UNIVERSITÉ GRENOBLE ALPES

Spécialité : **Physique appliquée**

Arrêté ministériel : 7 août 2006

Présentée par

Rémi Vicente

Thèse dirigée par **Dr. Gilles Nogues**
et co-encadrée par **Dr. Arnaud Gardelein**

préparée au sein **de l'Institut Néel, CNRS, Grenoble et Air Liquide Advanced Technologies, Sassenage**
dans **l'École Doctorale de Physique**

Optical Cryocooler Design and Demonstration for Space Applications

Thèse soutenue publiquement le **29 juin 2021**,
devant le jury composé de :

Pr. Benoit Boulanger
Professeur, Institut Néel - CNRS - Université Grenoble Alpes, Président

Pr. Ammar Sharaiha
Professeur, École Nationale d'Ingénieurs de Brest, Rapporteur

Pr. Alberto Di Lieto
Professeur associé, Université de Pise - MEGA Materials, Rapporteur

Dr. Michel Brune
Directeur de recherche, Laboratoire Kastler Brossel - CNRS, Examinateur

Dr. Jacques Berthon
Ingénieur, Chef du service optique spatiale, CNES, Examinateur

M. Thierry Tirolien
Ingénieur, Autorité thermique et cryogénie spatiale, ESA, Invité

Abstract

Optical refrigeration in solids or laser cooling in solids is a breakthrough technology, reaching cryogenic temperatures (below 120 K –150 K) by the illumination of rare-earths ions doped crystals with an infrared laser at the adapted wavelength. The excitation of such a crystal near the gap wavelengths between fundamental and excited ionic states allows to predominantly stimulate the Anti-Stokes emission process, phenomenon by which the crystal re-emits more light than it has absorbed, hence cooling it down. Cryocoolers based on this revolutionary principle have the potential to ease or render possible a number of instrumental applications where vibrations and the bulkiness of traditional mechanical cryocoolers (ex. : Stirling/Pulse-Tube, Joule-Thomson, Turbo-Brayton) are stumbling blocks. The historical major targeted application is the cooling of detectors onboard Earth observation satellites, especially in the most sensitive instruments where vibrations are detrimental for performances, or onboard small satellites such as Microsatellites or even Nanosatellites, disposing of limited payloads and strong associated constraints. This thesis inserts in the frame of a French collaboration between Air Liquide Advanced Technologies (Sassenage), European leader of space cryogenics and Institut Néel, CNRS (Grenoble). The first goal of my thesis was to demonstrate the operation of a Laser Cryocooler prototype aimed at space applications for the first time in Europe. In three years, we successfully designed, developed and operated a Laser Cooler laboratory prototype capable of reaching cryogenics temperatures, thus advancing this technology to TRL 3 maturity. The 7.5% Ytterbium doped $YLiF_4$ cooling crystal lent by the University of Pisa for our experiment is capable of cooling down to temperatures close to 130 K (-153 ℃) with 10 W of absorbed laser power in about 30 minutes. In our system, the laser is supplied to the cooling crystal through an optical fiber in order to already take into account some of the constraints in a satellite application, making it a world premiere. The second goal of my thesis was to study the feasibility and suitability of Laser Cryocoolers for future Earth observation satellites. Based on the power architecture of small low earth orbit infrared observation satellites, we compared the balance of a solution with a Laser Cryocooler versus a Pulse-Tube based solution in terms of size, weight and power at the level of the whole satellite. We show that a Laser Cryocooler is a compact system which allows for internal volume and mass savings in the payload part, on top of its other advantages. Laser Cryocoolers are miniaturized, vibrationless and features reduced thermal losses due to the optical and contact-free nature of the technology. This work hence opens the way to a new family of optical cryocoolers for future space applications.

Résumé

Le refroidissement optique dans les solides ou refroidissement laser dans les solides est une technologie de rupture, atteignant des températures cryogéniques (inférieures à 120 K –150 K) par l'éclairement de cristaux dopés aux ions de terre-rares avec un laser infrarouge à la longueur d'onde adaptée. L'excitation d'un tel cristal aux longueurs d'ondes proches du gap entre états fondamentaux et états excités ioniques permet de stimuler préférentiellement le processus d'émission Anti-Stokes, phénomène par lequel le cristal réémet plus de puissance lumineuse que ce qu'il a absorbé, provoquant ainsi son refroidissement. Les cryo-refroidisseurs basés sur ce principe révolutionnaire ont le potentiel de faciliter ou rendre possible nombre d'applications ou les vibrations et l'encombrement des cryo-refroidisseurs mécaniques traditionnels (ex. : Stirling/Pulse-Tube, Joule-Thomson, Turbo-Brayton) sont des points bloquants. L'application majeure historiquement visée est le refroidissement des détecteurs à bord des satellites d'observation de la terre, particulièrement dans les instruments les plus sensibles pour lesquels les vibrations sont préjudiciables aux performances, ou encore à bord de petits satellites du type Microsatellite ou même Nanosatellite, disposant d'une partie charge utile réduite et de fortes contraintes associées. Cette thèse s'inscrit au sein d'une collaboration française entre Air Liquide Advanced Technologies (Sassenage), leader Européen de la cryogénie spatiale et l'Institut Néel, CNRS (Grenoble). Le premier but de ma thèse a été de démontrer le fonctionnement d'un prototype de Cryo-refroidisseur Laser en vue d'applications spatiales pour la première fois en Europe. En trois ans, nous avons conçu, développé et fait marcher un prototype de refroidisseur Laser capable d'atteindre des températures cryogéniques, avançant ainsi la maturité de cette technologie au niveau TRL 3. Le cristal refroidisseur de $YLiF_4$ dopé à 7.5% d'Ytterbium prêté par l'Université de Pise pour notre expérience est capable de refroidir à des températures proches de 130 K (-153 ℃) avec 1 0 W de puissance laser absorbée en environ 30 minutes. Dans notre système, le laser est acheminé vers le crystal refroidisseur à travers une fibre optique dans le but de déjà prendre en compte certaines contraintes d'une application satellite, pour la première fois au monde. Le second but de ma thèse a été d'étudier la faisabilité et la pertinence d'un Cryo-refroidisseur Laser pour les futurs satellites d'observation de la Terre. Basés sur l'architecture électrique des petits satellites d'observation infrarouge, nous avons comparé le bilan d'une solution Cryo-refroidisseur Laser versus solution Pulse-Tube en termes de volume, poids et puissance au niveau du satellite complet. Nous montrons que le Cryo-refoidisseur Laser est un système compact qui permet des économies de volume interne et de masse dans la partie charge utile, en plus de ses autres avantages. Les Cryo-refroidisseurs Laser sont miniaturisés, sans vibrations et présentent des pertes thermiques réduites de part la nature optique et sans contact de la technologie. Ce travail ouvre donc la voie vers une nouvelle famille de cryo-refroidisseurs optiques pour les futures applications spatiales.

Acknowledgements

So this is it ! Three years have passed in the blink of an eye and, as it is the tradition, it is now time for me to thank all the people who crossed my path along this journey.

I'll start with my Mom and my Dad, without whom I would never have had the chance to arrive there. They gave me a good education, a free mind and an insatiable curiosity for sciences, especially physics and technology. I remember the good times in Toulouse when I was a child and we went to visit the "Cité de l'Espace" museum together. I was always amazed by the infinity of space and the ingenious machines conceived by mankind to reach it. I never thought I would take a (modest) part in this story one day too.

I strongly believe in the power of teamwork, that having good relationships, being capable of dealing with everyone and building a cohesive team is a key for achieving big things at work and in life. This is especially relevant in our careers, where crucial interests are at stake and mistakes can get very costly. Hence, this project would be nothing without the people who contributed to its realization, by providing their ideas or their help.

I want to thank, of course, Gilles Nogues and Arnaud Gardelein, my supervisors. Thank you for putting your trust in me, for your time, your patience and dedication. You've always been of good advice and I've learned much thanks to you. It's a pleasure and a chance to be working with you.

I want to thank the colleagues at Institut Néel, the NPSC team and my fellow PhD students friends. Special thanks to those three who contributed actively on our project: David Jegouso who crash-coursed me on Zemax before I could fly on my own, and for being there when in dire times with lasers (especially with a certain Titanium:Sapphire laser, damn !); Laurent Del Rey, our mechanical engineer with his invaluable experience, who taught me a few things related to mechanical design and machining; Jérôme Debray, our master polisher, who shared a bit of his art with me and helped us with the crystals.

I want to thank also the colleagues at Air Liquide Advanced Technologies, who watched me come and go from their place to the lab all along these three years. Special thanks to Jean-Michel Niot for his knowledge in space cryogenics and for following our project since its very start.

I want to thank all the people at Pisa for always being really nice, supportive and welcoming people each time I came to visit you, and for our fruitful collaboration: Prof. Mauro Tonelli, Prof. Alberto Di Lieto, Gianni Cittadino, Eugenio Damiano, Francesco Caminati, Ilaria Grassini (sorry for the re-polishing work by the way !).

I want to thank the jury members who did me the honour of attending my defense: Prof. Benoit Boulanger from Néel, Prof. Ammar Sharaiha from ENIB, Michel Brune from LKB, Jacques Berthon from CNES, and especially Thierry Tirolien from ESA for seeing the potential of our technology and interacting with our consortium.

I want to thank my Bros and my friends for always being there for me when I come back to Toulouse, even if I was not so much there for them lately after this busy period and a pandemic. I promise we'll catch up !

At last, I want to have a thought for my previous teachers and supervisors who extended a hand to me, counseled me in times of my life where I needed it and were sources of inspiration during my studies, thus shaping my interests and my choices in life: Adam Walters, William Nicolazzi, Pierre Cafarelli, Philippe Peille and Hervé Geoffray.

Thank you everyone !

From the birth of Space Age and space cryogenics, October 4th 1957, to the day of my birth, October 4th 1992, exactly 35 years have passed on Earth. And from then to now, almost 30 years have passed again.

Yet, mankind still has so much to learn and to explore !

I dedicate this work to the people who, like me, keep gazing at the sky, dreaming of new worlds and pushing the limits of knowledge and technology always further. May this work mark the beginning of a new adventure.

Rémi

Contents

Introduction **1**

1 Cryogenics for space applications **6**

1.1 History of cryogenics and space cryogenics 7

1.1.1 Cryogenics 7

1.1.2 Space cryogenics 9

1.2 Refrigeration in space: state-of-the-art 11

1.2.1 Applications 11

1.2.2 Cryocoolers overview 13

1.3 Upcoming missions involving space cryogenics 29

1.3.1 Cryogenics for large satellites 29

1.3.2 Cryogenics for medium satellites 33

1.3.3 Cryogenics for small satellites 34

1.4 Conclusion: space cryogenics and Laser Cooling 37

References 38

2 Laser cooling in solids: fundamentals and prospects **44**

2.1 History of optical refrigeration 45

2.2 Rare-earths doped solids 47

2.3 Theory of Anti-Stokes cooling in rare-earths doped crystals 56

2.3.1 The ideal cooling model 56

2.3.2 The four levels model 58

2.4 Anti-Stokes cooling in Yb:YLF 64

2.4.1 YLF matrix properties 64

2.4.2 Electronic properties of Yb:YLF . . . 68
2.4.3 Optical properties . . . 71
2.4.4 Cooling efficiency . . . 83
References . . . 86

3 Laser cooling in solids for space applications 92
3.1 SWaP analysis at satellite level . . . 93
3.1.1 Base hypotheses . . . 93
3.1.2 Laser cooler preliminary architecture . . . 97
3.1.3 Budget for a Laser Cooler . . . 100
3.1.4 Miniature Pulse Tube Cooler architecture . . . 105
3.1.5 Budget for a Miniature Pulse Tube Cooler . . . 106
3.1.6 Discussion . . . 109
3.2 Laser cooling onboard CubeSats with co-doped crystals . . . 111
3.3 Towards a prototype taking space constraints into account . . . 116
3.3.1 Space constraints and exigences . . . 116
3.4 Crystal growths requirements to reach nominal performances . . . 118
3.5 Conclusion: towards an engineering model . . . 121
References . . . 121

4 Laser Cryocooler design and development 128
4.1 Optical design . . . 129
4.1.1 Pumping schemes . . . 129
4.1.2 Suitable crystal geometries . . . 132
4.1.3 High power fiber coupling design . . . 134
4.1.4 Optical cavity design . . . 137
4.2 Prototype development . . . 161
4.2.1 Coupling bench . . . 161
4.2.2 Cooling bench . . . 162
4.3 Cooling crystals validation . . . 173
4.3.1 Samples . . . 174

4.3.2 Orientation, cutting and polishing . . . 175
4.3.3 Surface and volumes defects inspection . . . 177
4.3.4 Absorption spectroscopy . . . 182
4.3.5 Fluorescence spectroscopy . . . 188
4.3.6 Cooling efficiency measurements . . . 191
References . . . 195

5 Demonstrating Europe's first Laser Cryocooler prototype 200
5.1 Thermometers in the experiment . . . 201
5.1.1 Crystal temperature . . . 201
5.1.2 Clamshell temperature . . . 207
5.2 Prototype overview and operation . . . 210
5.3 Cooling demonstration at cryogenics temperatures . . . 214
5.3.1 First series of results: cooling down to 160 K . . . 214
5.3.2 Improved support and measurements: cooling down below 130 K . . . 215
5.3.3 Thermal model and cooling power . . . 218
5.3.4 Analysis of a run with decreasing pump power . . . 223
5.4 Conclusion: operation of a Laser Cryocooler . . . 227
References . . . 228

A Yb:YLF properties 236
A.1 General properties . . . 236
A.2 Specific heat capacity . . . 237

Conclusion 234
Publications . . . 234
Presentations . . . 234

B HR 4000 spectrometer calibration 240
B.1 Spectral response calibration . . . 240
B.2 Wavelength calibration . . . 241

List of Figures

1.1 Georges Claude's invention for separating the constituents of liquefied air and Kamerlingh Onnes's apparatus for the first liquefaction of helium. 8

1.2 Sputnik 1 and the Apollo Service Module. 9

1.3 Mariner probes 6/7 and the Infrared Astronomical Satellite. 10

1.4 Ariane 5 during its first commercial flight, and the ISO satellite. 12

1.5 Schematic of best performing sensors and readout electronics technologies available over the light's spectrum. 12

1.6 Inventory of all the cooling technologies adaptable to space and their typical temperature of operation with the addition of laser cooling. 14

1.7 Cosmic microwave background observed by the Planck satellite. 15

1.8 Space radiator thermal dissipation for different surfaces and temperatures. . 16

1.9 Examples of passive cooling with Sentinel 5-P and Planck. 17

1.10 Peltier cooler principle and example of a commercial 5 stages Peltier. 17

1.11 Cooling cycle in a Stirling cooler. 19

1.12 Examples of space qualified Stirling cryocoolers. 19

1.13 Schematic of a Pulse Tube cooler. 20

1.14 Large Pulse Tube Cooler for Meteosat Third Generation. 21

1.15 Schematic of a Reverse Turbo Brayton cycle. 22

1.16 MELFI Turbo-Brayton cooler which operates onboard the ISS for organic samples conservation. 22

1.17 Schematic of an open cycle J-T cooler. 23

1.18 Examples of JT cryocoolers. 23

1.19 Principle of a sorption cooler. 24

1.20 CEA SBT Sorption cooler designed for the Herschel mission. 24

1.21 Dilution cooler schematic and example from Cryoconcept. 26
1.22 Planck cryogenic architecture. 26
1.23 Schematic and operation principle of an ADR. 27
1.24 Examples of space qualified ADRs. 27
1.25 Pictures of the first two prototypes of Laser Cryocoolers existing in the world. 28
1.26 Artist view of the ATHENA telescope. 30
1.27 Cryogenic chain of Athena X-IFU instrument. 30
1.28 CAD view of the different cryocoolers assembled together in Athena's cryo-chain. 31
1.29 Artist view of the JWST telescope. 32
1.30 Sun shield of the JWST, as long as a tennis court. 33
1.31 MTG and MetOp-SG upcoming earth observation missions. 33
1.32 Overview of the Microcarb instrument. 35
1.33 Schematic of the CubeSats form factors up to 12U with the corresponding scale. 36
1.34 Number of nanosatellites launched through the years since 1998 and predicted launches as of january 2020. 37

2.1 Schematic of the Anti-Stokes cooling principle. 45
2.2 Minimal temperature achieved with laser cooling in solids over the years. . . 47
2.3 Rare-earth elements highlighted in the periodic table of elements. 48
2.4 Illustrations of rare-earths applications in several high-technologies domains. 49
2.5 Radial probability densities of 4f, 5s, 5p and 6s orbitals. 49
2.6 Electronic structure of rare-earths doped solids. 53
2.7 Schematic of the observed energy levels of Ytterbium doped $YLiF_4$ crystals. 53
2.8 Approximated position of 4f energy levels in rare-earths doped solids, a.k.a. Dieke's diagram. 54
2.9 Ideal cooling efficiency of the Anti-Stokes process as a function of laser pump wavelength between ambient and cryogenics temperatures. 57
2.10 Energy diagram of the four levels model of Anti-Stokes cooling. 58
2.11 Lowest values allowed for the product of external quantum efficiency and absorption efficiency to get net cooling with the Anti-Stokes fluorescence process. 64

2.12 Schematic of the YLF atomic lattice. 65

2.13 Phase diagram of the LiF-YF_3 mixture 66

2.14 Czochralski growth and melt temperature control as performed at the University of Pisa. 67

2.15 Bridgman growth schematic. 67

2.16 Micro pulling-down growth schematic. 68

2.17 Observed energy levels in Yb:YLF. 69

2.18 Cooperative mechanism in co-doped Tm,Yb:YLF and observed improvement in cooling efficiency. 70

2.19 Radiative lifetime in Yb:YLF. 71

2.20 Temperature dependence of the fluorescence lifetime in Yb:YLF. 72

2.21 Schematic of the Varian Cary 5000 spectro-photometer used at the University of Pisa for measuring room temperature absorption of Yb:YLF. 73

2.22 Absorption coefficient of 10%Yb:YLF at room temperature in E$\|$c and E$\perp$c directions. 74

2.23 Absorption cross-section of 10%Yb:YLF as a function of temperature, obtained by McCumber reciprocity method. 75

2.24 Absorption coefficient of 10%Yb:YLF as a function of temperature, obtained by McCumber reciprocity method. Zoom in the range around 1020 nm. . . . 76

2.25 Absorption coefficient of 10%Yb:YLF as a function of temperature, obtained by McCumber reciprocity method. Zoom in the range around 1020 nm in semi-log scale. 76

2.26 Absorption coefficient of 10%Yb:YLF as a function of temperature, obtained by spectro-photometry below 990 nm and replaced with reciprocity calculated values above 990 nm. 77

2.27 Typical experimental setup for measuring fluorescence spectra as a function of temperature. 77

2.28 Polarized $E \parallel c$ fluorescence intensity of 10% Yb:YLF as a function of temperature. 78

2.29 Polarized $E \perp c$ fluorescence intensity of 10% Yb:YLF as a function of temperature. 79

2.30 Room temperature emission cross sections of 10%Yb:YLF calculated from fluorescence spectra. 80

2.31 Polarized $E \parallel c$ emission cross-section of 10%Yb:YLF as a function of temperature. . . . 80

2.32 Polarized $E \perp c$ emission cross-section for 10% Yb:YLF as a function of temperature. . . . 81

2.33 Mean fluorescence wavelength as a function of temperature. . . . 82

2.34 Theoretical cooling efficiency as a function of temperature and pump wavelength for a crystal with $\eta_{ext} = 0.996$ and $a_b = 2e-5$ cm^{-1}. . . . 84

2.35 Theoretical cooling efficiency as a function of temperature and wavelength, plotted as a 2D color plot for a crystal with $\eta_{ext} = 0.996$ and $a_b = 2e-5$ cm^{-1}. 84

2.36 Schematic of the pump-probe setup used for precise determination of background absorption and external quantum efficiency at cryogenics temperatures. 86

2.37 Theoretical cooling efficiency as a function of temperature and wavelength, plotted as a 2D color plot considering the background absorption decay at low temperatures. . . . 87

3.1 Schematic of the considered heat sources at the focal plane level. . . . 94

3.2 Schematized functional architecture of a Laser Cryocooler and its subsystems, the Cryogenic Laser Optical Exchanger (CLOE) and the Laser Electronics Assembly (LEA). . . . 98

3.3 Left: Preliminary CAD concept of a Laser Cryocooler mounted at the back of a cryostat. Right: Side cut showing the main elements contained in a Laser Cryocooler. . . . 99

3.4 LC sub-systems redundancy hypothesis considered in this study. . . . 100

3.5 Concept of a focal plane architecture with redundant Miniature Pulse Tube Coolers. . . . 107

3.6 Satellite comparison between Pulse-Tube architecture and Laser Cooler architecture. . . . 110

3.7 Thermal losses estimation as a function of the crystal's temperature for 10 W absorbed power. . . . 114

3.10 Histogram of independent Yb:YLF Czochralski growths as a function of background absorption. . . . 119

3.11 Probability of getting a crystal with $a_b < x$. . . . 120

3.12 Average number of growths required to get a crystal with $a_b < x$. . . . 120

4.1 Schematic of an intra-cavity laser cooler. 130
4.2 Schematic of a radiation balanced laser. 131
4.3 Extra-cavity Laser Cooler at the University of New Mexico. 132
4.4 View of the cooling crystal in the American Laser Cooler. 132
4.5 Examples of optical maze shaped crystals. 133
4.7 Coupling bench schematic showing the different elements. 135
4.8 Required coupling focal length at 1020 nm as a function of the optical fiber core diameter, plotted for several couples of fiber core/numerical aperture found on Nufern's catalog. 137
4.9 Fabry-Perot resonant cavity and impedance matching condition. 138
4.10 Common types of multi-pass cells. 138
4.11 Percent of absorbed pump power as a function of round-trips number in 10%Yb:YLF, plotted for several temperatures. Losses in the mirrors are neglected. 139
4.12 Schematic of an ideal square round-trips pattern with N_s spots with beam diameter d in a section of side s around the input mirror. Here, N = 24. . . . 140
4.13 Input hole radius as a function of the number of round-trips, plotted for crystal sections 2 mm, 3 mm and 4 mm. 140
4.14 Input transmission and lower bound tolerances. 141
4.15 Absorption as a function of the hole radius, plotted for cryogenic temperatures. 142
4.16 Example of a Lissajous figure calculation plotted for N up to 50 round-trips for input angles of 1°in both x and y directions. 145
4.17 Maximal number of round-trips as a function of effective cavity length between 0 and 100 mm. 146
4.18 Gaussian beam divergence and linear approximation. 147
4.19 Lissajous figure calculation taking into account the Gaussian beam divergence for input angles of 1°in both x and y directions, plotte d for the first 50 round-trips. 147
4.20 Maximal number of round-trips as a function of effective cavity length between 0 and 100 mm, taking into account the Gaussian beam divergence. . 148
4.21 Lissajoux figure size as a function of input tilt angles. 149
4.22 Average number of round-trips as a function of input tilt angles, calculated for effective cavity lengths 20/30/40 mm. 149

4.23 YLF ordinary refractive index no and extraordinary refractive index ne at 300 K. 152

4.24 Zemax CAD view of the optical cavity with the crystal at its center. 152

4.25 Maximal and average errors committed by the linear approximation compared to the real Gaussian beam divergence, for waist radius between 50 μm and 250 μm. 153

4.26 Power repartition at the multi-pass cavity level for a crystal at a temperature of 150 K. 154

4.27 Simulated absorbed power as a function of tilt angles of the second mirror, for an input power of 50 W. 154

4.28 Power repartition as a function of tilt angles of the second mirror for an input power of 50 W. 155

4.29 Fresnel losses and absorbed power as a function of cavity length for different mirrors curvature radius. for an input power of 50 W. 155

4.30 Fiber collimator optimization during the design process in Zemax. 156

4.31 Variation of the waist position as a function of the variation of the fiber to lens distance, relatively from the optimal fiber position $\delta z = 0$. 157

4.32 Variation of the waist radius as a function of the variation of the fiber to lens distance, relatively from the optimal fiber position $\delta z = 0$. 157

4.33 Lissajous figure inside a section of 3x3 mm in the final design with an angle on the input beam and a tilt on the second mirror. 158

4.34 Schematic of the cavity viewed from the top, indicating the distances in the final design. 159

4.35 Zemax simulation of the cavity viewed from the top. 159

4.36 Schematic of the cavity viewed from the side, indicating the distances in the final design. 160

4.37 Zemax simulation of the cavity viewed from the side. 160

4.38 Photograph of the coupling bench open showing all the optical elements. . . 161

4.39 Photograph of the coupling bench closed. 162

4.40 Schematic of the fluid and electrical connections in the cooling bench. . . . 163

4.41 Reflectance and thermal emissivity of Almeco's TiNOX solar absorber coating. 164

4.42 Photographs of the clamshell with fibers used in the first version to hold the crystal. 165

4.43 Photographs at different steps of the clamshell base, clamshell hat and collimator mount after fabrication and during assembly. 166

4.44 Photography of the cooling bench mounted in the vacuum enclosure, showing all the interfaces. 167

4.45 Image of a prepared PM optical fiber at the beginning of the stripped section observed with an electronic microscope (secondary electrons image). 168

4.46 Tip of a stripped and cleaved PM optical fiber observed with an electronic microscope. 168

4.47 Tip of a stripped and cleaved PM optical fiber observed with an electronic microscope, zoom on the fiber's core. 169

4.48 Laser beam at the fiber collimator's output observed with a Vis-NIR camera with increasing exposure times. 169

4.49 Photograph of the glued collimator and the pieces used to hold the collimator during the alignment step. 170

4.50 Cylindrical mirrors center observed with an electronic microscope and optical microscope. 170

4.51 Trench in the first supplied cylindrical mirror made with Focused Ion Beam (FIB). 171

4.52 FIB lithography of the first mirror observed with the electronic microscope. . 172

4.53 Center of the first supplied cylindrical mirror after lithography and laquer cap removal, observed with an optical microscope in white light (right) and in dark field (left). 172

4.54 Images of the Lissajous figure observed through the cavity second mirror with the dummy fused silica crystal. 173

4.55 From left to right: Photography of cooling crystals number 1, 2 and 3 used during this thesis. 175

4.56 Co-doped crystal collection 190 before and during Brewster cutting. 176

4.57 Laue X-ray back scattering principle and Orient Express software. 176

4.58 First crystal (collection 190) on the goniometer head and during polishing. . 177

4.59 Electronics microscope images of the crystal surface state after polishing before cleaning. 179

4.60 Electronics microscope images of the crystal surface state after polishing and cleaning. 180

4.61 Optical microscope observation of crystal 3, 7.5%Yb:YLF taken in clean room environment just after receiving the crystal. 181

4.62 Photographs of the red laser scattering analysis in two places along the length of the second crystal. 182

4.63 Photograph of the crystal scattering when illuminated with a blue laser. . . . 183

4.64 Transmission obtained with Lambda 900 spectro-photometer on sample 1. . 184

4.65 Measured absorption for sample 1 taken obtained with the Lambda 900 spectro-photometer. 184

4.66 Measured transmission for 10%Yb-0.01%Tm:YLF (coll. 190) with the Bruker 70v FTIR. 186

4.67 Measured absorption coefficient for 10%Yb-0.01%Tm:YLF (coll. 190) with the Bruker 70v FTIR. 187

4.68 Measured absorption coefficient for 10%Yb-0.01%Tm:YLF (coll. 190) with the Bruker 70v FTIR, zoom in the low signal features around 685 nm and 785 nm, attributable to Thulium co-doping. 187

4.69 Thulium doped YLF absorption bands in both polarizations. 188

4.70 Photographs of the crystal mounted in the He cryostat for temperature dependent fluorescence spectroscopy. 189

4.71 Photograph of the crystal's image after the 2f-2f relay, as seen by the Vis-NIR camera. 190

4.72 Measured E$\|$c fluorescence as a function of temperature. 190

4.73 Measured E$\perp$c fluorescence as a function of temperature. 191

4.74 Comparison between 10%Yb:YLF absorption obtained with reciprocity (left) and reference absorption from the University of Pisa obtained by direct measurement (right). The peak at 960 nm is completely flattened at low temperatures due to fluorescence re-absorption with the reciprocity method. 191

4.75 Setup used at the University of Pisa for the measurement of cooling efficiency at room temperature. 193

4.76 Temperature of 10%Yb:YLF as a function of time, pumped at 1020 nm in vacuum. 193

4.77 Measured cooling efficiency for the 10% Yb:YLF crystal. 194

4.78 Measured cooling efficiency for the 7.5% Yb:YLF crystal. 194

4.79 Theoretical cooling efficiency as a function of temperature and wavelength for the 7.5% Yb:YLF crystal. 195

5.1 7.5 % Yb:YLF crystal lent by the University of Pisa/MEGA Materials, pumped with 2 W of laser power at 1020 nm. 201

5.2 FLIR Lepton 3.5 camera and VOx micro-bolometers typical spectral response. 202

5.3 Photography of the thermal camera mounted above the crystal and thermal infrared scene viewed by the thermal camera. 203

5.4 Schematic of the external thermal camera calibration. 204

5.5 Thermal camera images during calibration at ambient temperature and around 250 K. 204

5.6 Apparent temperature as a function of the real temperature for a slab of YLF and a piece of Acktar Spectral Black. 205

5.7 Thermal camera calibration for the conversion between apparent and true YLF temperature. 206

5.8 PT100 RTD and resistance as a function of temperature. 208

5.9 4-wires PT100 RTD measurement principle. 208

5.10 PT100 positions in the experiment and temperature acquisition unit Agilent 34970A. 209

5.11 PT100 RTDs temperatures as a function of time after opening the water flow. 209

5.12 Schematic of the optical setup in the cooling experiment. 210

5.13 Photography of the Laser Cryocooler prototype showing the cold head in the vacuum enclosure. 211

5.14 Photography of the cooling crystal at the center of the astigmatic multi-pass cavity. 212

5.15 Close-up photograph of the cooling crystal at the center of the multi-pass cavity laying on the silica aerogel pads. 212

5.16 Photography of the experiment with the vacuum enclosure closed. 213

5.17 Crystal cooling down viewed by the thermal camera. 213

5.18 7.5% Yb:YLF crystal temperature as a function of time monitored with the calibrated thermal camera and with the DLT method at cryogenics temperatures. 214

5.19 Lissajous figure observed after 1 hour of cooling. 215

5.20 YLF crystal, black-body and camera temperature monitored as a function of time by the thermal camera before correction. 216

5.21 7.5% Yb:YLF crystal temperature as a function of time, as seen by the thermal camera after calibration. The dashed red line indicates the temperature of 160 K below which the camera is uncalibrated. 216

5.22 Differential Luminescence Thermometry for the best cooling run. 217

5.23 7.5%Yb:YLF crystal temperature as a function of time. 217

5.24 Fitted thermal model during the crystal's warm-up. 219

5.25 Thermal losses estimated from the fitted model. 219

5.26 Raw YLF temperature obtained with DLT and smoothed data used for the thermal model during cool-down. 220

5.27 Estimated thermal losses during cool-down. 220

5.28 Estimated cooling power as a function of time. 221

5.29 Comparison between achieved cooling efficiency and theoretical estimated cooling efficiency. 221

5.30 Revised cooling efficiency as a function of temperature and pump wavelength fitting the measured cooling efficiency. 222

5.31 YLF crystal, black-body and camera temperature monitored as a function of time by the thermal camera before correction for the run with decreasing pump power steps. 223

5.32 7.5%Yb:YLF crystal temperature as a function of time, as seen by the thermal camera after calibration for the run with decreasing pump power steps. The dashed red line indicates the temperature of 160 K below which the camera is uncalibrated. 224

5.33 Differential Luminescence Thermometry in the run with decreasing pump power steps. 224

5.34 7.5%Yb:YLF crystal temperature as a function of time for the run with decreasing pump power steps. 225

5.35 Raw YLF temperature obtained with DLT and smoothed data used for the thermal model during cool-down for the run with decreasing pump power steps. 226

5.36 Estimated thermal losses during cool-down for the run with decreasing pump powers. 226

5.37 Estimated cooling power as a function of time for the run with decreasing pump powers. 227

A.1 Doped Yb:YLF specific heat capacity as calculated with the Debye model. . 237

B.1 DH-2000-CAL calibration lamp reference spectra and measured signal with the HR4000 spectrometer. 240

B.2 HR4000 spectrometer response. 241

B.3 Photograph of the spectrometer's multi-mode fiber positioned in front of the Neon pencil lamp. 242

B.4 Neon lamp emission spectrum. 242

B.5 Krypton lamp emission spectrum. 242

B.6 Xenon lamp emission spectrum. 243

B.7 Spectrometer wavelength error for a set of well identified rare gases peaks with known wavelength. 243

List of Tables

1.1 Inventory of best performing sensors and readout electronics technologies available over the light's spectrum. 13

1.2 A short list of infrared emissivities for various materials. 15

2.1 Number of Stark sub-levels for trivalent rare-earth ions with an odd number of electrons as a function of the matrix local symmetry. 52

2.2 Number of Stark sub-levels for trivalent rare-earth ions with an even number of electrons as a function of the matrix local symmetry. 52

3.1 Parameters for the considered sun-synchronous orbit observation mission. . 93

3.2 Estimated values of the different heat sources terms at the focal plane level. 94

3.3 Solar array estimated efficiency and specifications, at beginning-of-life (BOL) and en-of-life (EOL). 96

3.4 Saft VES16 cells specifications. 96

3.5 CLOE size, volume and weight specifications. 98

3.6 LEA size, volume and weight specifications. 100

3.7 Volume and weight of a LC system. 101

3.8 LEA electronics estimated efficiency. 102

3.9 Cooling and optical requirements for a LC architecture. 103

3.10 Electrical power requirements for a LC architecture. 103

3.11 Solar array sizing for a LC architecture. 103

3.12 Batteries sizing for a LC architecture. 104

3.13 Thermal control sizing for a LC architecture. 104

3.14 Satellite SWaP summary for a LC architecture. 105

3.15 CMA mechanical specifications. 106

3.16 CDE mechanical specifications. 106
3.17 Estimated volume and weight of a MPTC architecture. 107
3.18 Estimated Pulse Tube efficiency, losses, and required cooling power. 108
3.19 Power requirements for a MPTC architecture. 108
3.20 Solar array sizing for a MPTC architecture. 108
3.21 Batteries sizing for a MPTC architecture. 109
3.22 Thermal control sizing for a MPTC architecture. 109
3.23 Satellite SWaP summary for a MPTC architecture. 110
3.24 SWaP analysis summary. 110

4.1 Specifications and required tests for the validation of cooling crystals. 174
4.2 Summary of the cooling crystals samples used during this thesis. 175

A.1 Yb:YLF general physical, thermal and optical properties. 236

Introduction

I conducted this PhD at Air Liquide Advanced Technologies (Sassenage, France) and Institut Néel, CNRS, Université Grenoble Alpes (Grenoble, France) from 2018 to 2021. During these 3 years, I had the amazing chance to develop and demonstrate for the first time in Europe a new type of cryocooler intended for space applications: the Laser Cryocooler.

Laser cooling in solids or optical refrigeration in solids is the branch of physics which studies the possibility of cooling condensed matter by taking advantage of the fundamental emission and absorption properties of materials. The Anti-Stokes effect, by which a material re-emits in average more light than it has absorbed is at the basis of the cooling principle.

The relatively recent demonstration of this effect in the 90's makes it an emerging research subject, less than three decades old. In the last decade, the engineering of cooling materials allowed exceptional results with rare-earths doped fluoride crystals reaching near liquid nitrogen temperatures. Current record of solid-state cooling is set at 87 K with Yb:YLF crystals. This has led to a gain of interest in the field, motivated by the potential exciting new applications allowed by compact and vibration-free coolers, much like the popular thermoelectric coolers but able to access cryogenics temperatures.

Research and development is intrinsically linked to space exploration: each launch being costly, satellites and instruments are produced each time in very small quantities, sometimes with technologies still at the state of laboratory prototypes at the beginning of a mission. Lessons need to be taken after each launch in order to maximize the success of future missions. Air Liquide's space research branch, Air Liquide Advanced Technologies is the European leader in space cryogenics and notably supplies Pulse-Tube cryocoolers for infrared observation satellites. With the increasing performances and requirements of space instruments, especially in terms of mechanical vibrations, Air Liquide is preparing the future by developing the Laser Cooling technology.

In that context, Air Liquide teams-up with a historical partner in the Grenoble scene: Institut Néel - CNRS, with whom they had already demonstrated the dilution refrigerator for the Planck ESA mission. The "European Laser Cooling Consortium" also gathers the main actors of the Laser Cooling scene in Europe: the University of Pisa and their startup MEGA Materials (Italy), world leaders in the growth of state-of-the-art cooling crystals; and

the company Lumium (Netherlands), interested with the development of new Laser Cooler designs.

The goal of my thesis is to provide a clear introduction to this emerging research and engineering subject at system level. I will expose the related concepts of laser cooling in solids and the results obtained during my work. Another goal is to demonstrate that Laser Cooling is a technology of the future, which has the potential to bring a small revolution in the ease-of-use for a number of systems and scientific instruments where vibrations are detrimental. Targeted space applications include high ground resolution imagers, spectrometers or interferometers, but also the smallest classes of satellites such as Microsatellites or even Nanosatellites, where the bulkiness of traditional solutions is an issue. This manuscript is arranged in 5 parts.

In chapter one, as an introduction to my work, I present a state-of-the-art of space cryogenics and the panel of cooling technologies implemented on-board satellites, in order to put this work into the wider context of space cryogenics. This chapter concludes on the future space missions requiring the use of cryogenics, the challenges and trends in future space cryogenics.

In chapter two, I present the principles of optical refrigeration in solids: its history and theory, which kind of materials are suitable. It concludes on the general applications of Anti-Stokes cooling.

In chapter three, I present the comparative size, weight and power analysis of a laser cooler architecture onboard an infrared observation satellite which was published in 2020 at the occasion of the 28^{th} Space Cryogenics Workshop. In this study, we show that a laser cooler allows for mass and payload volume reduction compared to a solution based on mechanical cryocoolers, on top its other advantages.

In chapter four, I present the design of the first European laser cryocooler prototype. This chapter covers first the optical design aspects, and then the mechanical design and mounting of the cooling bench.

In chapter five, I present the results acquired during this thesis. The first part shows the results concerning cooling crystals: spectroscopy, surface and volume defects characterization, cooling efficiency. In the second part, I present the thermometers used in the experiment to measure the cooling crystal's temperature and I show the results of our cooling down runs. It concludes on the cooling power estimation with a thermal model of the cooling head.

The conclusion of my thesis draws a picture of the work accomplished during these last 3 years and the work left to do in order to use this technology in space for observation satellites.

Chapter 1

Cryogenics for space applications

This chapter presents the context and state of the art of space cryogenics. The goal is to answer the question "What is cryogenics and why is it useful in space ?". In the first section, I take a quick look at the concepts which led to the birth of cryogenics and I give a quick history of space cryogenics in order to understand the goals of these discipline. In the second section, the different applications of space cryogenics are listed and I specifically show the importance of cryogenics for the performance of sensors as well as the different kinds of detectors which need cryogenics in space. Then, a state of the art of cryogenics technologies available in space is given. Each cooling technology is reviewed and I describe its principles, with its advantages and weaknesses in order to put the laser cooling technology into the wider context of cryogenics onboard satellites. In the third section, I give a quick outlook of the future trends and marking missions involving cryogenics in the next decade.

Ce chapitre présente le contexte et l'état de l'art en cryogénie spatiale. Le but est de répondre à la question "Qu'est-ce que la cryogénie et pourquoi est-elle utile dans l'espace ?". Dans la première section, je reviens rapidement sur les principes à l'origine de la cryogénie et je donne un rapide historique de la cryogénie spatiale dans le but de comprendre les objectifs de cette discipline. Dans la seconde section, les différentes applications de la cryogénie spatiale sont listées et je montre spécifiquement l'importance de la cryogénie pour la performance des capteurs ainsi que les différents types de détecteurs qui ont besoin de cryogénie dans l'espace. L'état de l'art en cryogénie spatiale est ensuite dressé. Chaque technologie de refroidissement est passée en revue et son principe décrit, avec ses avantages et ses inconvénients, dans le but de place la technologie de refroidissement laser dans le contexte plus général de la cryogénie dans les satellites. Dans la troisième section, je donne un rapide aperçu des futures tendances et des missions marquantes implicant la cryogénie spatiale dans la prochaine décénnie.

1.1 History of cryogenics and space cryogenics

1.1.1 Cryogenics

Cryogenics refers to a corpus of disciplines and techniques with the aim of cooling matter down to low temperatures. Etymologically, the word "cryogenics" is derived from the association of the ancient greek words "krýos", "cold/chilly" and "génos", "produced by/descending from". But, to be complete in our definition, we must specify exactly what are low temperatures.

And to begin with, what is temperature ? A 21^{st} century physicist could answer: "*Easy ! Temperature is a measure of one of the various forms of energy observed in nature. It is related to the agitation of atoms. When an object is hot, it possesses a lot of thermal energy and when it is cold, it possesses a small amount of thermal energy."* But it was not always that clear and theses ideas emerged relatively recently compared to other fundamental physical concepts such as optics or gravitation.

Until the 19^{th} century, temperature was defined and measured relatively to phenomenons observable around room temperature. For example, Fahrenheit's scale (1724) was constructed using two references temperatures: a low temperature corresponding to the freezing temperature of salty water, and a high temperature corresponding to the human body's temperature. Celsius's scale (1742) was constructed with the freezing temperature of water defined at 0℃ and its boiling temperature defined at 100℃.

It wasn't until 1848 that Sir William Thomson, Lord Kelvin, established a scale where the temperature is defined relatively to a physical quantity: the thermal energy contained inside substances. He derived that the lowest temperature achievable by any body, zero Kelvins, is equal to -273.15°C. The absolute zero was discovered, marking the beginning of a world-wide competition to reach the lowest temperature experimentally. In the meantime, Ludwig Boltzmann, founding father of statistical physics and supporter of the atomistic theory devised that the average kinetic energy of the molecules contained in a gas is proportional to its temperature with a factor k:

$$< E >= N \times k \times T \tag{1.1}$$

Up to a constant N depending on the gas studied. k was later named k_B in honor of Boltzmann's work, the fundamental constant of physics relating energy to temperature.

Following the fundamental work of Sadi Carnot on thermal machines in 1824 [1], it was well known that by transferring heat into the gas contained in a piston by heating one end while the other end is cold, one was able to transform the heat energy into mechanical work,

i.e. to make a motor. But the reverse process is also possible: by transferring mechanical work into a gas using cycles of compressions and expansions, one is able to convert mechanical energy into a temperature difference between a cold and hot side, following the principle of the Joule expansion.

Soon, the first machines converting mechanical work into cold were created and the gases contained in the air, one after another, were successively liquefied, separated and produced in industrial quantities all around the world, as the efficiency of these "liquefiers" increased (Figure 1.1). ***Cryogenics was born.*** We can now complete the definitions of cryogenics by the notion of "how cold is it ?". A commonly accepted definition of cryogenic temperatures are temperature below 150 K –120 K. In the US, NIST defines (arbitrarily) cryogenics temperatures as temperatures below 123 K.

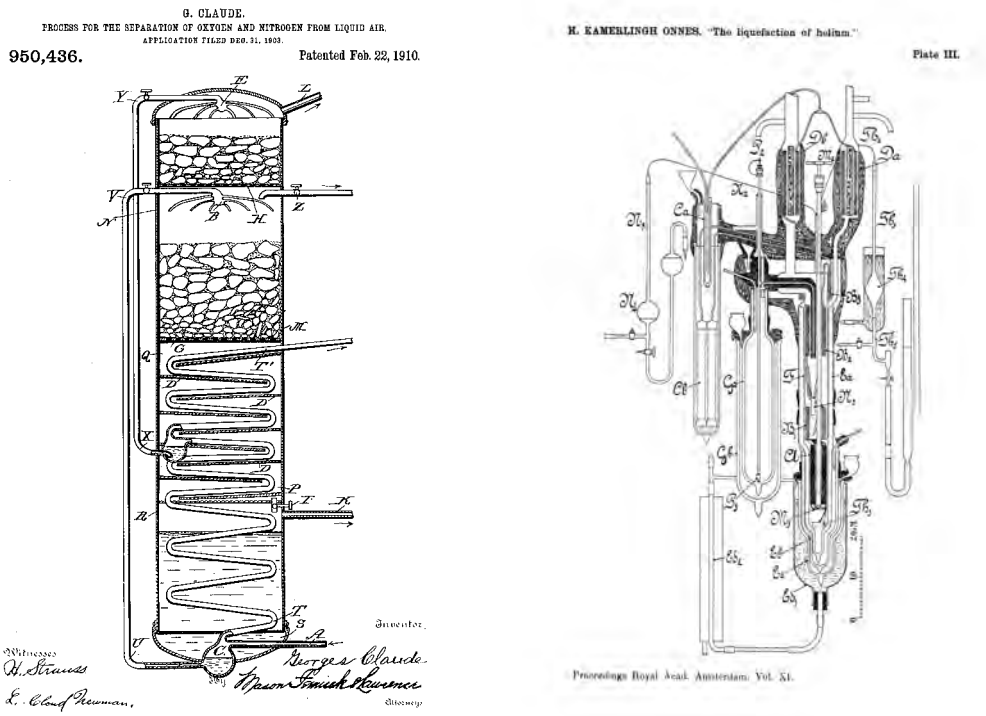

Figure 1.1: *Left: Drawing of Georges Claude's 1903 invention for separating the constituents of liquefied air [2]. The air (gaseous) supplied from tube A is pumped up through a heat exchanger tube in contact with liquid air. Upon rising in the column, oxygen becomes liquid first and falls into flask C, while nitrogen becomes liquid at lower temperature, collected higher in flask X. Right: Drawing of Kamerlingh Onnes's apparatus for the liquefaction of helium. At the bottom of the experiment, surrounded by a flask of liquid hydrogen, a flask of liquid air and a flask of alcohol, helium is cooled by a Joule-Thomson expansion through valve M_J. After 14 hours of cooling the system, the first liquid helium drop was observed in 1908 [3].*

As of today, "L'Air Liquide, Société Anonyme pour l'Exploitation des Procédés Georges Claude", now become Air Liquide, world leader of gases, continues to carry-on the vision of these pioneers, who for the first time liquefied the air components and put them inside bottles [2].

More than ever, cryogenics plays an important role in our lives behind the curtains. In every lab in the world, dewars containing liquid nitrogen and liquid helium are used daily. They are invaluable and essential tools for scientists: by enabling easy access to low temperatures, they have rendered possible the study of fundamental interactions within matter, leading to incalculable technical progress in the fields of physics and biology. In every hospital in the world, gases are used for medical applications and liquid nitrogen is used in MRI's superconductor coils.

But more than just on the ground, for the past 50 years, cryogenics has become a vital domain in space. Each month, space launchers take-off, propelled thanks to the reaction between liquid hydrogen and liquid oxygen. At each second above our heads flies dozens of satellites containing cryocoolers, allowing them to operate their detectors at low temperatures in order to get the best performances.

1.1.2 Space cryogenics

Space cryogenics, as the name suggests, is the combination of two research fields: astronautics and cryogenics. Its aim is to develop cooling systems for spacecrafts (launchers, satellites or rovers) in order to fulfill different tasks or needs related to low temperature physics.

Space cryogenics began in the 1960's around the same time as space conquest. In 1957, the launch of the first artificial satellite Sputnik 1 onboard a liquid oxygen propelled rocket marked as well the first use of cryogenics in a spacecraft.

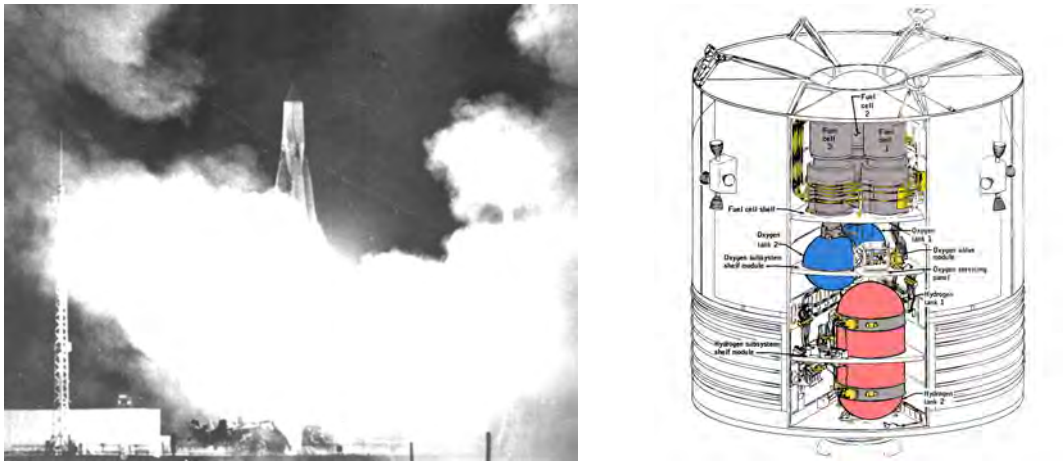

Figure 1.2: *Left: Photography of the launch of Sputnik 1, first human artificial satellite on October 4$^{\text{th}}$, 1957. Source: ESA/Roscosmos. Right: Schematic of the Apollo Service Module, sector 4, showing the oxygen and hydrogen tanks. Source: NASA History Division.*

In 1968, the first dewars flying into space were embarked onboard the Apollo missions, inside the Apollo Service Module. They contained liquid hydrogen for fuel cells and liquid

oxygen for breathing. The next year in 1969, the first cryocoolers were launched into space on-board the Martian probes Mariner 6 and 7. The Joule-Thomson coolers were designed to operate a spectrometer at the temperature of 22 K, performing a spectral survey of Mars's atmosphere in the mid-infrared. These surveys allowed to confirm that the atmosphere of Mars is composed mostly of CO_2, and even to find traces of water.

In 1983, the IRAS satellite became the first observation satellite to be cooled with liquid helium at 4 K, embarking a dewar filled with 480 litres. The IRAS mission allowed to perform for the first time a full sky survey with unprecedented sensitivity in the mid and far infrared.

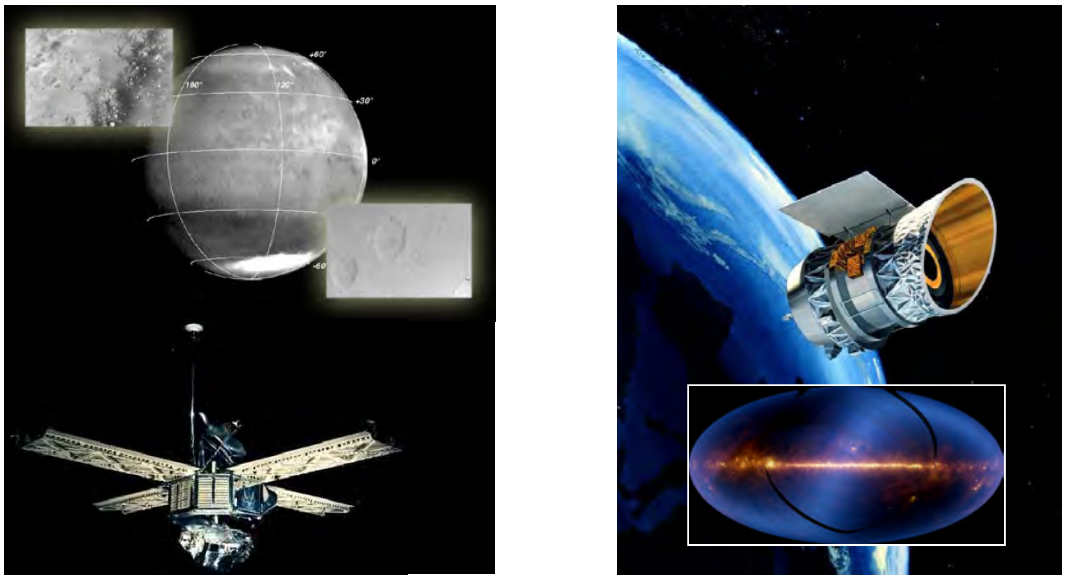

Figure 1.3: *Left:Picture of Mariner 6/7 along with some of its photos of Mars. Right: Infrared Astronomical Satellite (IRAS) launched in 1983. The inset shows the infrared all-sky survey it took during its 6 month of operation. Source: NASA/ JPL-Caltech.*

In the 1980's and 1990's, worldwide research in space cryogenics focused on developing new mechanical cryocoolers solutions with extended longevity and increased efficiency. In such systems, vibrations became quickly a concern which led to the development of mechanical cryocoolers with reduced exported vibration levels, first with the Oxford Stirling cooler and then with the development of Pulse Tube coolers.

A more exhaustive history of cryogenics for space applications can be found in the paper [4] from R.G. Ross, Jr. who took a part in these developments at NASA, commemorating the 50^{th} anniversary of space cryogenics. We can cite as well the paper [5] from ESA-ESTEC presenting a good summary of past 2000's activities in space cryogenics from the European side.

1.2 Refrigeration in space: state-of-the-art

1.2.1 Applications

As stated before, space cryogenics can be used for various task. For example, these tasks can be:

- Cryogenics for space transportation vehicles (launchers, rockets). The use of liquefacted gases (H2, O2) is required for primary propulsion of rockets. Chemical reaction between oxygen and hydrogen provides the powerful thrust needed to exit the atmosphere in a compact volume.
- Cryogenics for imaging systems. The cooling of image sensors onboard observation satellites enables to reach lower thermal noises. As noise is reduced, more details and features appears on a single image and the instrument becomes more sensitive. Infrared optics needs to be cooled in the same way in order to avoid the sensor from seeing its own temperature (a phenomenon known as narcissus).
- Cryogenics related to the environment. For example, Martian rovers require the use of heat pipes which withstand cryogenic temperatures in order to provide a stable temperature to its subsystems, when the temperature on the Martian surface can vary between -150 °C and +20 °C. On Titan, largest moon of Saturn, the exploration of liquid ethane/methane mares with a submarine would require to deal with cryogenics temperatures around 93 K.
- Cryogenics for samples conservation. An example is the MELFI refrigerator onboard the ISS, which provides a temperature -80 °C for the conservation of organic samples.

In practice, most space cryocoolers, especially those operating at low and very low temperatures are designed to address the thematic of imaging systems. Until the 2000's, sensors for space observation and ground astronomy were roughly divided into two categories. In the first category we find photo-detectors based on semi-conductors or photo-multipliers. They covers the range from UV and Far infrared in direct photo-current response, and extend in the x-ray and gamma by the addition of scintillators. In the second category, we find instruments which uses millimetric or radio wave antennas.

A third type of devices is emerging: sensors and amplifiers based on superconductors, which have been actively investigated for the past 20 years. Superconductive thermal detectors such as Transition Edge Sensors (TES) calorimeters or Kinetic Inductance Detectors (KID) bolometers offers sensitivities several times higher than their photo-detector counterparts and lower noise, as well as new spectral-imaging and photon counting possibilities. Figure 1.5 summarizes the different sensors technologies used onboard satellites.

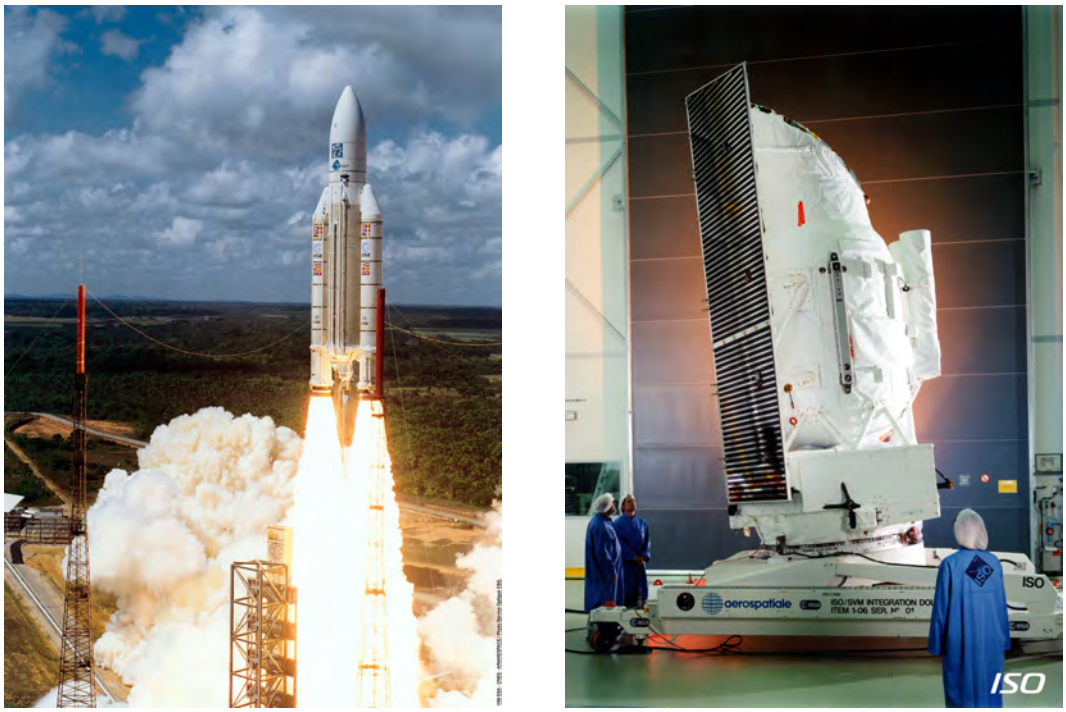

Figure 1.4: *Left: Ariane 5 first commercial flight in december 1999 with the satellite XMM-Newton on its board. The launcher's core propeller, "Étage Principal Cryogénique" (EPC) uses two tanks filled with respectively 26 tons of liquid hydrogen and 135 tons of liquid oxygen maintained at cryogenic temperatures during filling and supplied to the Vulcan engine during liftoff. Right: ISO, first ESA mission to embark a liquid He^4 dewar. Source: ESA.*

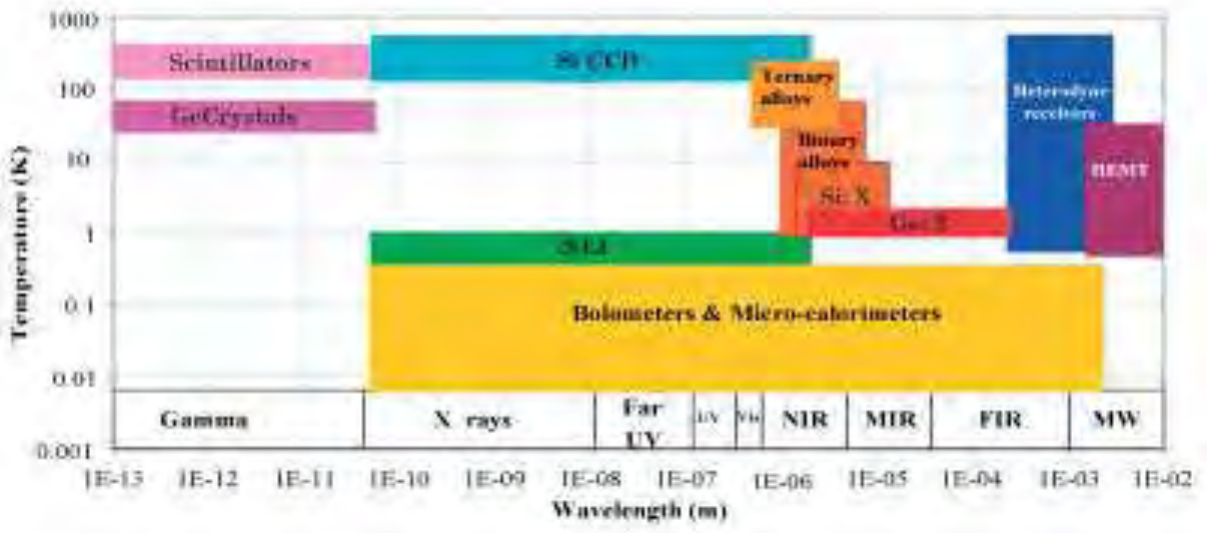

Figure 1.5: *Schematic of best performing sensors and readout electronics technologies available over the light's spectrum, adapted from [5].*

Sensors	Temperature	Spectral range/Comments
TES	$<$ 100 mK	Any (limited by source count and readout chain noise) In practice, used in X-ray/gamma and MW astronomy
KID	$<$ 100 mK	UV & visible up to SWIR/MWIR, MW
Ge	$<$ 100 K	Gamma
HgCdTe (LWIR)	20 K - 50 K	Long wave infrared (8 - 15 μm)
HgCdTe (MWIR)	50 K - 100 K	Mid wave infrared (3 - 8 μm)
HgCdTe (SWIR)	100 K - 200 K	Short wave infrared (1.5 - 3 μm)
Si CCD/CMOS	200 K - 300 K	UV, visible, near infrared ($<$ 1 μm)
Readout electronics	Temperature	Comments
HEMT	$<$ 4 K	Low noise amplifier, used in radio-telescopes
SQUID	$<$ 4 K	Low noise amplifier, used in frequency multiplexing
SIS	$<$ 4 K	Heterodyne detection mixer used in radio-telescopes

Table 1.1: *Inventory of best performing sensors and readout electronics technologies available over the light's spectrum.*

For all these instruments, low temperatures are critical. Indeed, thermal agitation of electrons in conductors presenting a certain resistance R creates a white noise known as Johnson noise, which RMS amplitude is given following the law:

$$v = \sqrt{4k_B T \Delta f} \tag{1.2}$$

With Δf the spectral band-pass over which it is measured. Dissipation of Johnson noise inside resistive electrical elements yields an associated noise power defined as:

$$P_{Noise} = \frac{v^2}{R} = 4k_B T \Delta f \tag{1.3}$$

In detectors, noise is more than just raw Johnson noise and its true form as a function of temperature depends on the whole readout chain elements. Noise is rather expressed in terms of the final observable quantity: dark current intensity in counts per pixels or electrons per second and per pixel.

We see the interest of cooling: for photo-detectors and classical amplifiers, its ensures a low thermal noise, hence a high level of accuracy in the details of an image. For superconductors devices, it allows to reach the superconducting phase featuring the absence of electrical resistance.

1.2.2 Cryocoolers overview

Nowadays, every scientific space telescope uses a combination of several cryocoolers to reach temperatures below 1 K, and most of the medium to large size earth observation satellites embark at least one instrument which requires cryogenic temperatures between 10 K and 150 K. Space cryogenics have become essential and a number of technologies

exist to reach cold temperatures, as shown in Figure 1.6. They can be split into several categories.

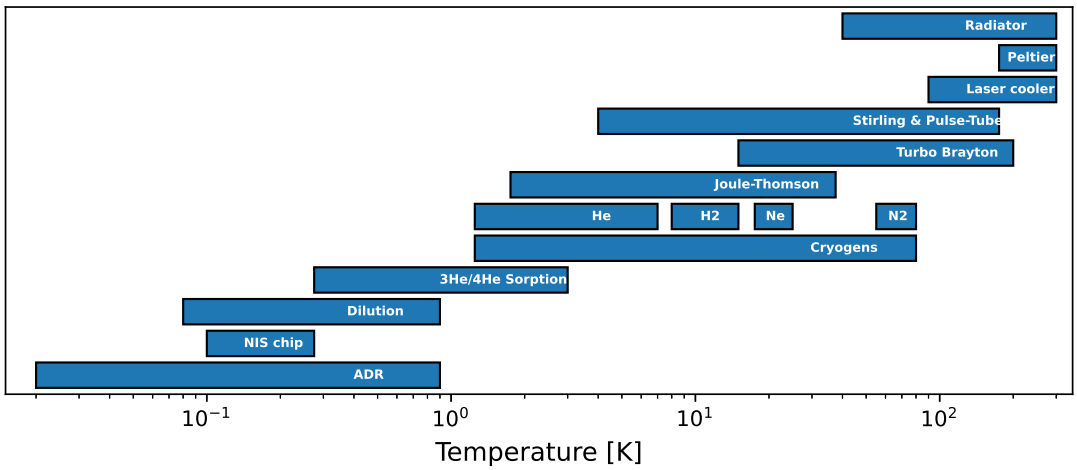

Figure 1.6: *Inventory of all the cooling technologies adaptable to space and their typical temperature of operation, adapted from [6] with the addition of laser cooling.*

Some of those technologies can cool down from ambient to cryogenic temperatures: radiators, laser, mechanical cryocoolers, liquid cryogens.

Historically, liquid cryogens Dewars are one of the first cryocoolers which began to fly into space. For cooling purposes, liquid helium was always used as it possess the lowest boiling temperature, 4 K. However they have finite lifetimes, typically a few years where the others systems can last for a longer period. For example, the Infrared Space Observatory (ISO) shown in Figure 1.4, first ESA mission to embark a dewar filled with 2268 litres of liquid helium was designed for a lifetime of only 18 months. Nowadays, sending a Dewar full of liquid helium is considered as a no longer viable solution: with the improvement of solar arrays efficiency, it has become simpler and lighter to use active cryocoolers, which can have lifetimes of more than 5 years.

Cryocoolers that can reach temperatures below 4 K and as low a as few mili-Kelvins exist: sorption, dilution, adiabatic demagnetization refrigerators. They require either liquid helium or mechanical cryocooler as first stages. Dilution and sorption make use of liquid helium in their cooling principle, hence they need special considerations and verifications in order to be used in zero-gravity.

Finally, mechanical cryocoolers (Stirling/Pulse-Tube, Turbo-Brayton, Joule-Thomson) are based on compressors which export vibrations, even in minimal levels to their surroundings, while the others technologies are vibration-free.

Each one of those coolers can be used a specific application depending on the mission's drive: parameters such as the goal observation spectral band, the available size/weight/power budget, the satellite's orbit. The specifics of these cryocoolers will be detailed in the next sections.

Passive coolers

Passive cooling designates the use of a radiating surface (or radiator) expelling heat towards deep space. Indeed, deep space behaves as a black-body at a temperature of about 2.73 K, with excellent thermal isotropy (Figure 1.7).

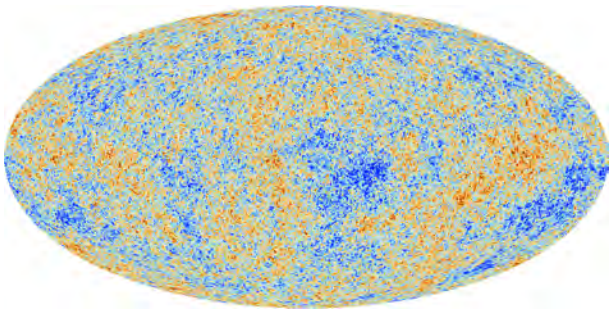

Figure 1.7: *Cosmic microwave background observed by the Planck satellite. Source: ESA. The cosmic background is the radiation from the primordial universe (big-bang) which is seen red-shifted in the far infrared/millimeter range due to the universe expansion. Its spectrum corresponds to a black-body at a temperature of 2.7260 K with fluctuations of only ± 0.0013 K.*

A space-radiator is the one of the most simple cooler. Its principle relies on Stefan-Boltzmann's law. The heat flux emitted by a radiator towards deep space is given by the equation:

$$P = A_r \varepsilon \sigma (T_r^4 - T_s^4) \tag{1.4}$$

With A_r the radiator's surface, ε the surface's infrared emissivity, T_r and T_s the radiator and outer space temperature respectively.

In practice, all objects are grey bodies, meaning that they emit only a fraction of a black-body's power due to their reflectivity. Their emissivity is lower than 1. Table Table 1.2 shows examples of common materials and their emissivities.

Material	Emissivity
Black Scotch Tape	0.97
Concrete	0.9
Paper	0.86
Anodized aluminium	0.77
Sapphire	0.76
Polished gold/silver/copper	0.02 - 0.05

Table 1.2: *A short list of infrared emissivities for various materials.*

Radiators are often used in large astrophysics missions as primary stages in support to active cryocoolers. For earth observation missions where temperatures in the range 100 K -300 K are required, there is a trade-off between reliability and power consumption of an active cryocooler on one side, and size/weight required for a radiator on the other side.

When the mission can accommodate to have its radiators always facing deep space and avoiding pointing towards the sun or the earth, (at the expense of a baffle sometimes) then passive cooling is a cost efficient and robust solution. For missions where the satellite has high mobility and its aiming can change a lot to observe multiple regions, active cryocoolers are preferred.

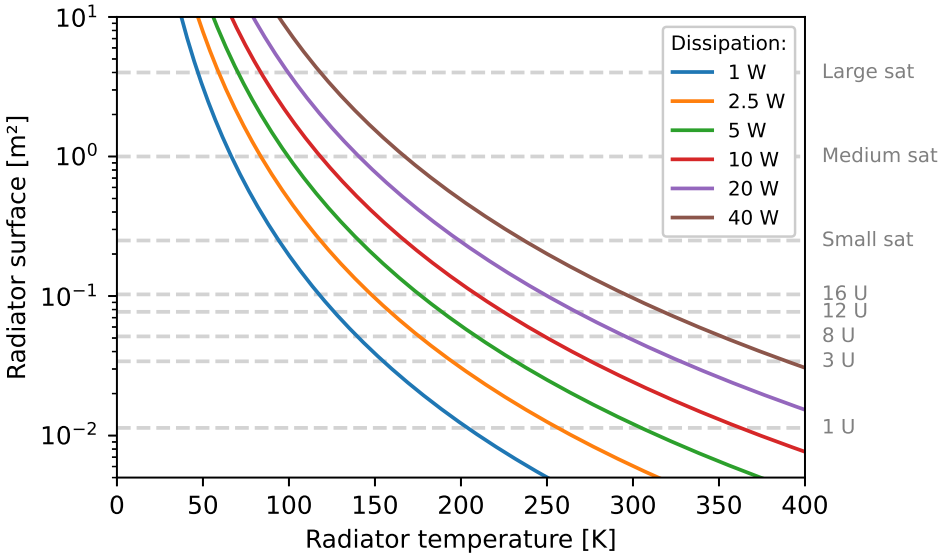

Figure 1.8: *Radiator surface as a function of temperature plotted using Eq. (1.4) for cooling powers between 1 W and 40 W. Typical side surfaces of satellites from CubeSats standards to large satellites are indicated. Dissipation values can be halved depending on view factors with the Earth or reflecting surfaces like solar panels.*

Figure 1.8 shows the radiator surface required as a function of its temperature for several cooling powers, assuming an emissivity of 0.9 and a radiator facing deep space with no other light sources. We see that at temperatures above 200 K, relatively small radiator patches can ensure thermal regulation of a few Watts to a dozen of Watts. Below 100 K, reaching a few Watts to a dozen of Watts of cooling requires significantly larger radiators which in turn needs a lot of structures to be supported and baffled. In that range, it is more favorable tu use a radiator above cryogenics temperature which provides cold interfaces to active cryocoolers.

Passive coolers are present in satellites in various forms. Usually in the form of simple panels oriented towards space, they can be of more complicated design: for example by integrating several stages of radiating surfaces facing each-others in order to reject thermal radiation (V-grooves). The main drawback is the orbit and aiming constraint which limits the satellite "mobility". For that reason, the largest radiators can only be accommodated far from Earth, on space telescopes located at the Lagrange points.

Sentinel 5-P is an example of middle class satellite using a radiator to cool down the Tropomi instrument down to 140 K [7]. Planck, shown in Figure 1.9 is an example of large class satellite using passive cooling as first cold stage at about 60 K [8].

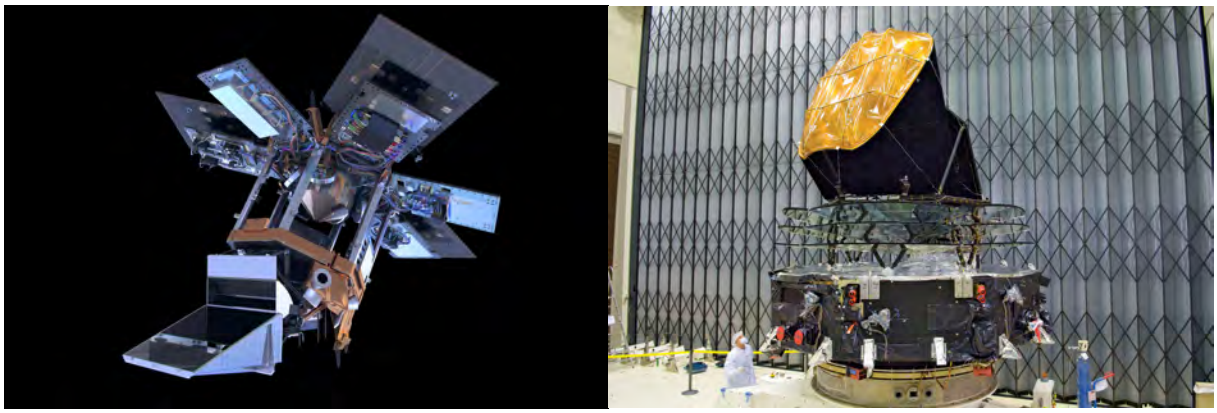

Figure 1.9: *Left: Artist view of the Sentinel 5-P satellite with its passive cooler on the Tropomi instrument. Right: Photography of the Planck satellite before its final integration.*

Thermo-electric / Peltier coolers

Thermo-electric coolers (TEC) or Peltier coolers are based on the junction of n type, metal and p types semiconductors. Upon sending a current in the junction, electrons start circulation between the junctions. Electrons crossing from n to p materials lose energy, leading to heating in that junction. At the opposite, electrons gain energy when crossing from p to n, leading to cooling in these junctions (Figure 1.10).

Advantages of Peltier coolers are their cheap price and simplicity of operation. Peltier modules are generally made of Bi_2Te_3 semiconductor alloys which have been the preferred materials for the past 60 years [9]. Despite some improvement reached in the labs [10], Peltier coolers have displayed in practice stagnating efficiencies in commercial models for the past two decades.

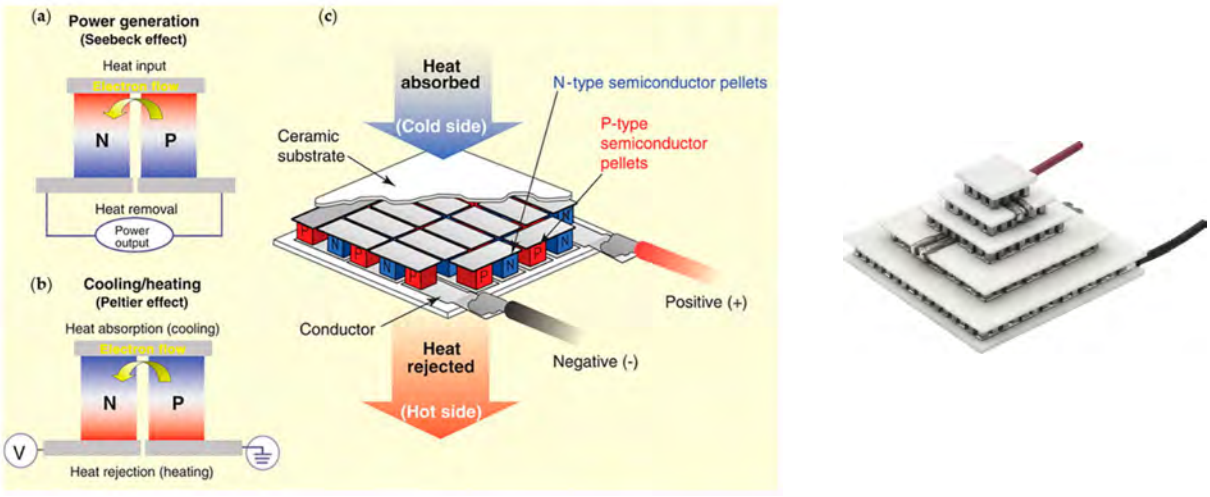

Figure 1.10: *Left: Peltier cooler principle, from reference [11]. Right:Example of a 5 stages Peltier cooler from Laird Thermal Systems, model MS5-257-10-15-11-W8. Manufacturer specification features a minimal achievable temperature of 171 K with 23 W input power for a hot side maintained at 27℃.*

The main drawback of Peltier coolers is that their efficiency collapses when aiming for a

ΔT superior to 60 K, requiring several stages of cascaded Peltier in order reach lower temperatures. Lowest temperature difference achievable with commercial multi-stages Peltier is around ΔT = 120 K with electrical power of approximately 30 W, thus limiting practical applications of Peltier coolers to temperatures above 200 K.

Another drawback of Peltier coolers when aiming for low temperatures is the need to maintain the hot side temperature as low as possible. Indeed, due to conduction between the cold and hot side, any temperature increase of the hot side will lead to a proportional increase on the cold side. In a satellite, it would require the use of a radiator and active thermal regulation in order to get stable hot and cold sides temperatures.

Stirling coolers

Stirling coolers are based on the thermodynamic cycle of the same name. Invented in 1816 by Robert Stirling, engines following this principle features a warm and a cold side with a piston oscillating in between. Several types of Stirling engines exists, with more or less complex designs where there can be one or two pistons, free or attached to a flywheel.

The operation cycle of a Stirling cooler is presented in Figure 1.11. The cycle starts when the pistons are in configuration (a): the left piston compresses the gas contained in the chamber.

(b): pressures rises accordingly while temperature remains constant (isothermal compression).

(c): the gas volume is moved through the regenerator where it loses part of its heat (isochoric cooling).

(d): the cold piston expands and the pressure in the chamber lowers (isothermal expansion).

(a): the whole gas volume is sent to the hot side through the refrigerator (isochoric heating) where it acquires again an ambient temperature.

Stirling coolers were developed and launched in space applications for focal planes cooling since the 70's [4]. Since then, R&D emphasis was put on the improvement of lifetime and reliability, with the integration of magnetic bearings and flexure springs in latest designs, as shown in Figure 1.12.

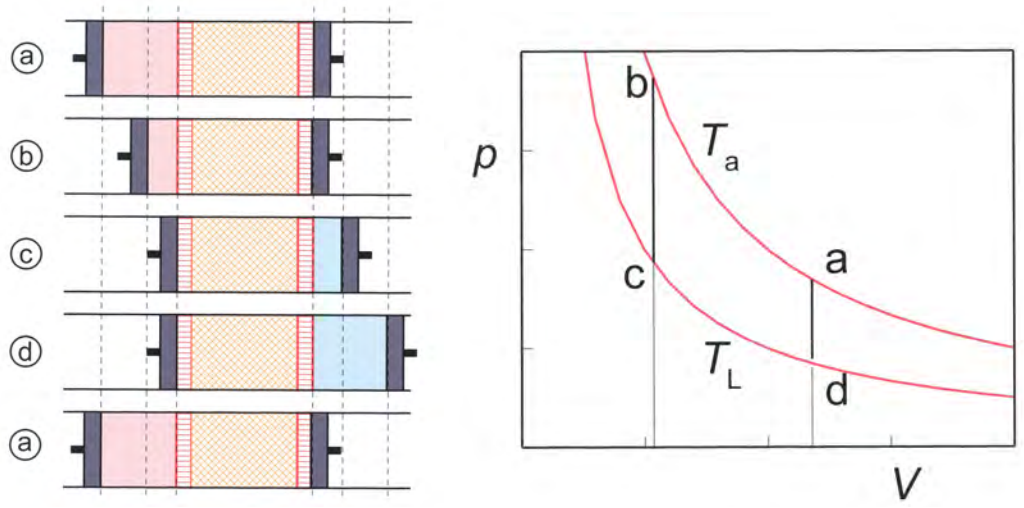

Figure 1.11: *Cooling cycle in a Stirling cooler. Left: Schematic of the four states in the cooling cycle. Right: Cycle on the PV diagram. Figures from reference [12].*

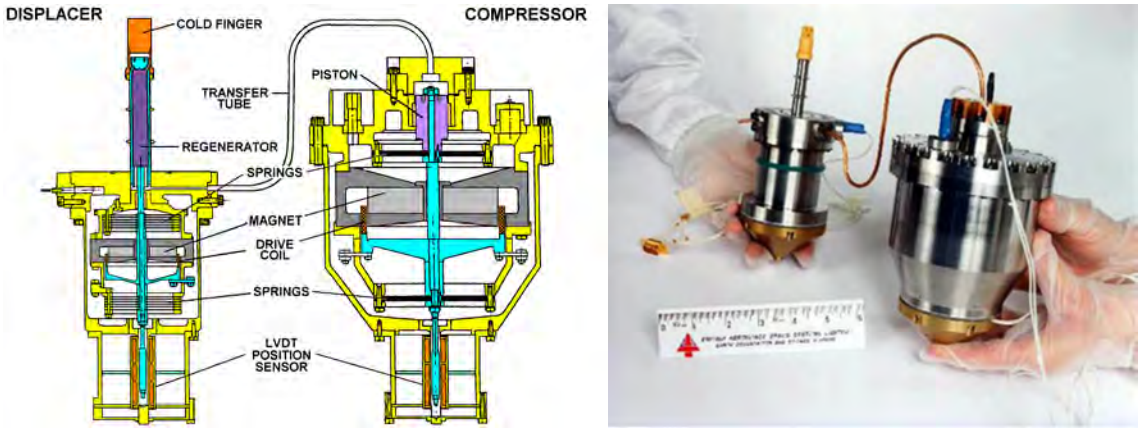

Figure 1.12: *Examples of space qualified Stirling cryocoolers in the 90's. Right: Oxford Stirling cryocooler schematic from reference [4]. Left: 50K/80K Stirling cryocooler manufactured by Astrium (UK) (formerly MMS) with 1.75 W cooling power at 80 K for 50 W electrical input. Source: ESA.*

Pulse-Tube coolers

Invented in the 60's by Gifford and Longsworth, Pulse-tube coolers are a variant based on Stirling's cycle where the piston is remotely located from the cold head, thus lowering the exported vibrations levels. The name Pulse-tube is misleading since there are no pulses in the operation. Typical pulse-tube designs are schematized in Figure 1.13. The cooling cycle in a pulse-tube cooler is the following:

- Piston compression. The gas contained in the regenerator flows into the tube. The gas located at the end of the tube has a high pressure, while the gas near the opening of the tube has a pressure tending to zero. The end of the tube heats-up, while the opening cools-down.

- Piston dilatation. The gas contained in the tube is adiabatically dilated and hence

cools down. The cold gas flows back into the regenerator where it absorbs heat from the regenerator. The regenerator cools down a bit.

- Piston compression. A new cycle begins, the gas contained in the system is compressed and its temperature instantly increases. The volume contained in the regenerator is sent back to the tube.

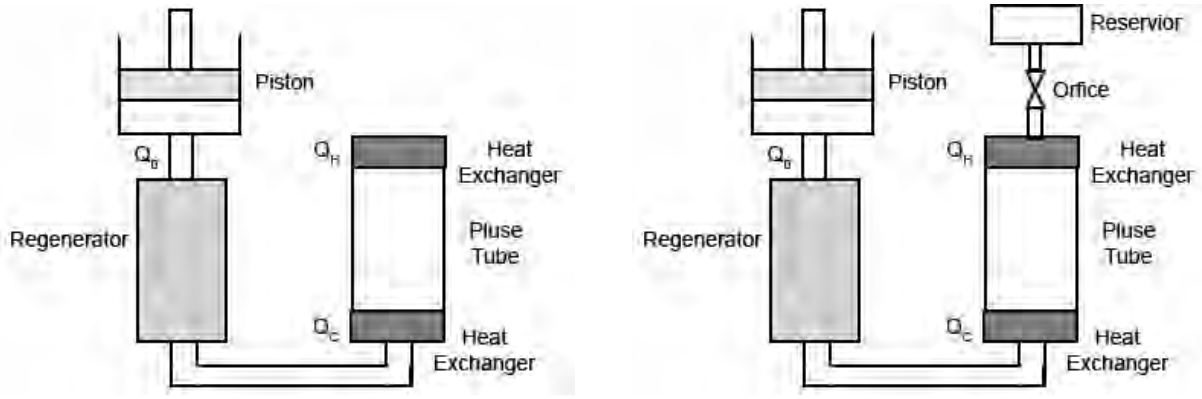

Figure 1.13: *Schematic of a Pulse Tube cooler from [13]. Left: first historical design. Right: improved design by the addition of a needle valve and a buffer volume (inertance).*

Heat exchangers (heatpipes, radiators) are connected to the hot side to keep it thermalized. The cold side is connected to the part to cool down through a cold finger, a mechanical link with high thermal conductivity (generally copper) and radiatively insulated from the hot surroundings with a gold coating.

However there was a problem in the initial design. In the compression phase, the gas is heating at the end of the tube. It then travels back to the regenerator when the piston relaxes back. The hot gas traveling back to the regenerator heats up the cold part when it leaves the tube.

In the 80's, the design was improved by Mikulin [14] and then Radebaugh [15], by adding a needle valve and a reservoir at the warm end of the tube, making a buffer volume. The addition of that buffer or "inertance" introduces a phase delay in the gas flow. The warm gas stays around the warm end, while the cold gas stays around the cold end. Even further improvements were achieved with the addition of a second orifice connected between the regenerator and the warm end. Reaching the optimal efficiency in modern pulse tubes is a matter of adaptating the phase of the gas flows.

The development of pulse-tubes cryocoolers for space applications started in the 90's in the US, as an alternative to Stirling coolers with reduced vibrations. They started to be popular in the 2000's and became until then the standard machines for cooling with low vibrations in the range 150 K - 4 K onboard satellites. We can cite the Large Pulse Tube Cryocooler, shown in Figure 1.14 which is developed by Air Liquide Advanced Technologies under CEA licence, jointly with Thales Cryogenics which manufactures the compressor. The LPTC is

Figure 1.14: *Large Pulse Tube Cooler (LPTC) for Meteosat Third Generation (MTG). The technology was developed by Air Liquide Advanced Technologies, CEA and Thales Cryogenics. Source: ESA.*

specified for a cooling power of 2 W - 8 W in the range 50 K - 80 K. It was selected for several incoming European missions such as MTG and METOP.

Reverse Turbo Brayton coolers

Reverse Turbo Brayton coolers are based on the cycle of the same name, where a turbine with high rotation speed (typically 100,000 RPMs) compresses a gas, which is then expanded thus cooling the load. The cold gas returns in closed loop to the compressor, passing through heat exchangers connected to the hot gas flow, as shown in Figure 1.15.

Due to the presence of a turbo-compressor, Turbo-Brayton cryocoolers features vibrations at high mechanical frequencies, typically above 1000 Hz. Some authors falsely advertise this particularity as "vibration-free" mechanical cryocoolers [16]. Vibrations might or might not be a problem depending on the system's mechanical resonances, but even if vibrations are above a certain frequency, non-linear behaviors can still create vibrations below that value.

A Turbo-Brayton cooler was used onboard the Hubble telescope for the NICMOS instrument. Nowadays, they are also used since the 2000's onboard the ISS. The MELFI system, "Minus Eighty degree centigrade Laboratory Freezer for the ISS" designed by Air Liquide Advanced Technologies provides a cooling power of 93 W of cooling power at 178 K with an excellent efficiency of 9% [17]. Initially specified with a lifetime of 10 years, the first models have been running now for 15 years without maintenance.

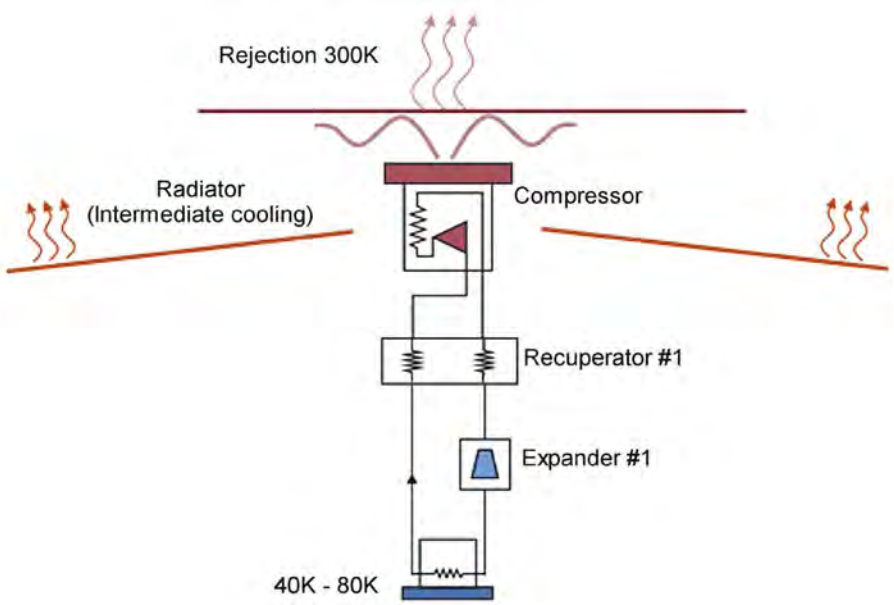

Figure 1.15: *Schematic of a Reverse Turbo Brayton cycle, from reference [16].*

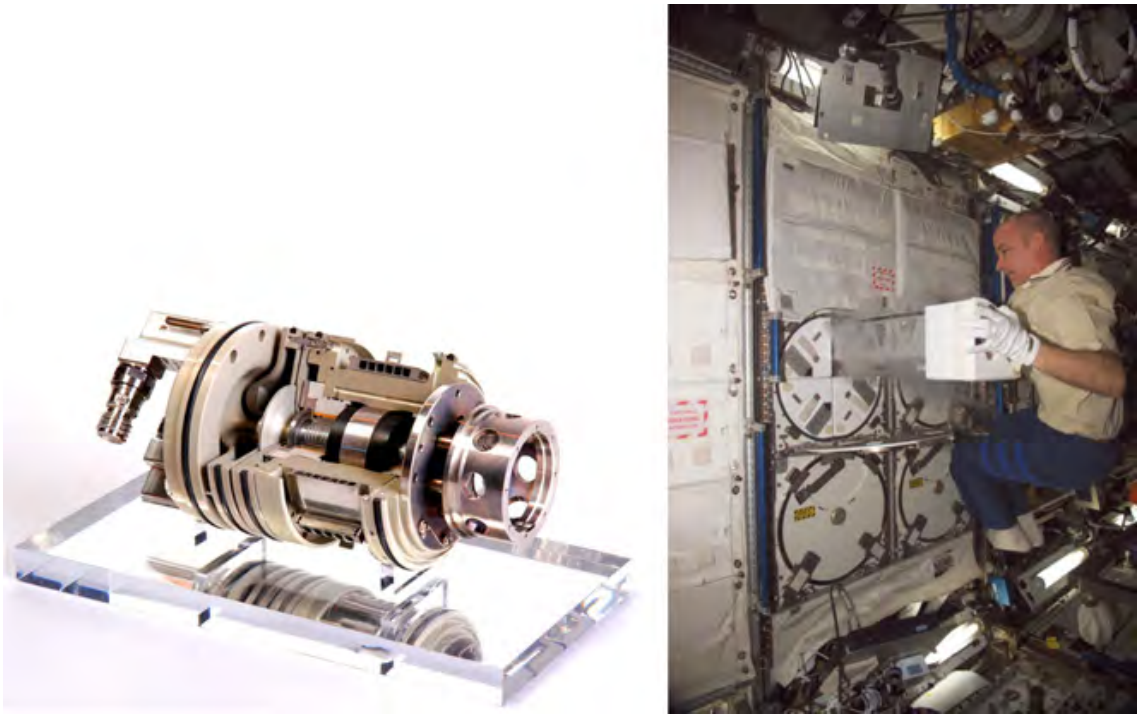

Figure 1.16: *MELFI Turbo-Brayton cooler which operates onboard the ISS, manufactured by Air Liquide Advanced Technologies, provides a cold storage for scientific experiments and organic samples [18].*

Joule-Thomson coolers

A Joule-Thomson cooler is a type of mechanical cooler which relies on the Joule-Thomson expansion. It uses a compressor to send the gas through a throttle valve. After the valve, the gas is at a lower pressure and cools down following the Joule-Thomson expansion. The cold gas is then re-used, usually passing through a heat exchanger around the compression

chamber in order to pre-cool the hot gas. A schematic of J-T coolers principle is shown in Figure 1.17.

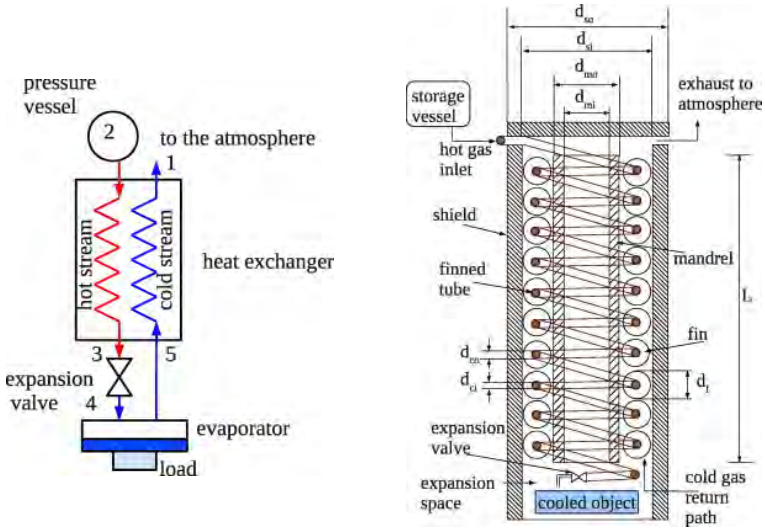

Figure 1.17: *Left: Schematic of an open cycle J-T cooler. Right: Practical design of a JT micro-cooler with a heat exchanger around the hot gas flow. Figures from reference [19].*

Joule-Thomson were used in the first mechanical cryocoolers. Closed loop Joule-Thomson cryocoolers are based on a recuperative cycle, not reversible. Hence they have lower efficiency than Stirling/Pulse-tube cryocoolers.

Joule-Thomson coolers are also used when the application requires fast cooling down times, on the order of a few seconds from 300 K to 100 K. J-T micro-coolers are often used for tactical applications such as heat tracking systems in missiles (Figure 1.18).

Figure 1.18: *Left: J-T cryocooler cooling down a temperature of 2 K. Source: RAL. Right: J-T micro-coolers manufactured by Air Liquide Advanced Technologies [20].*

Sorption coolers

Sorption (or adsorption) coolers work by successive condensation and evaporation of a volume of helium in a closed container. The cooling cycle of sorption coolers is schematized in Figure 1.19. The cooling cycle starts by lowering the frame temperature to 4 K. Helium

is trapped in the porous media or pump. The pump heat switch is disconnected and the pump heated with a resistive heater up to 40 K. Helium outgasses until it reaches saturating vapor pressure and then condensates in the tube at the contact of the cold condenser. Liquid helium fills the evaporator (Figure 1.19: left). Cooling is then initiated by turning off the heater, connecting the pump heat switch and disconnecting the evaporator switch (Figure 1.19: right). The helium pressure lowers and it evaporates, thus cooling the evaporator part down to minimal temperatures around 200 mK.

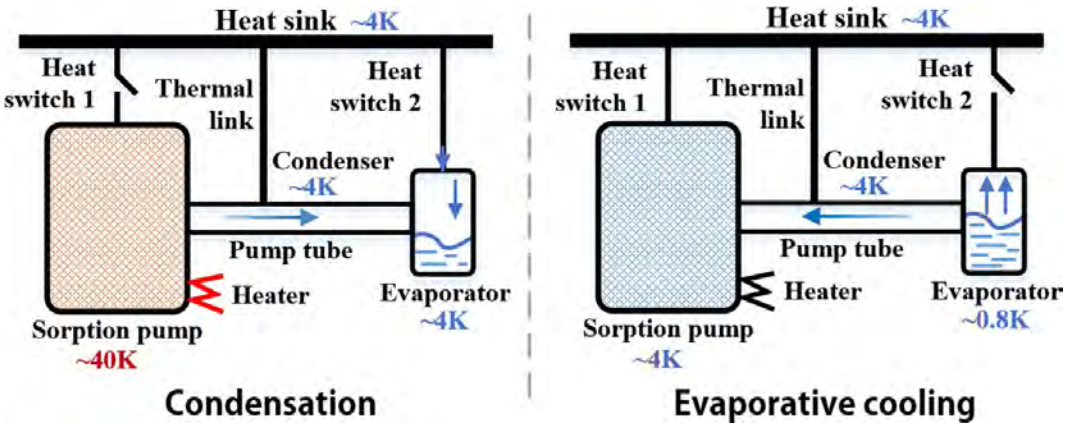

Figure 1.19: *Principle of a sorption cooler, from reference [21].*

In practice, sorption coolers are vibration free and reliable, although they need a primary cooling stage at 4 K. They can operate for several days with cooling powers around 100μW, with a recycling time of a couple hours [22]. A drawback is that they need to take zero-gravity into account, as their principle relies on helium evaporation and liquefaction. Figure 1.20 shows an example of sorption cooler developed at CEA-SBT for space applications.

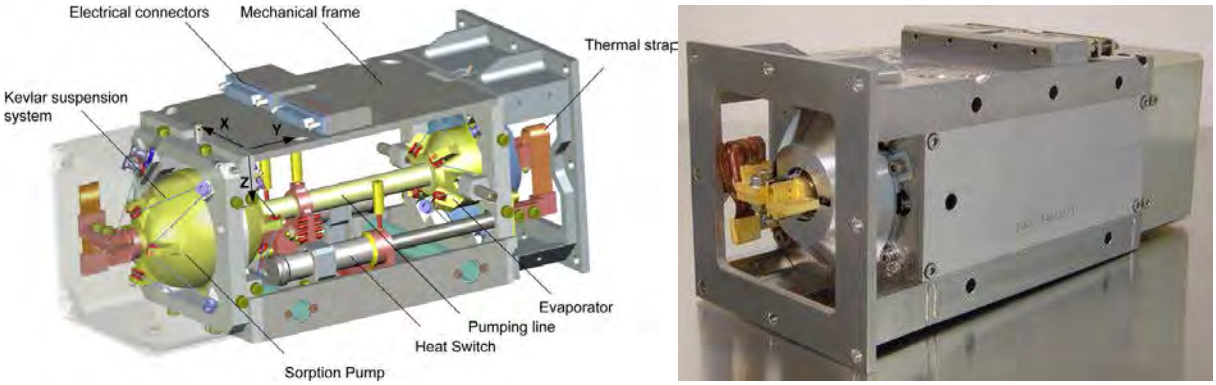

Figure 1.20: *CEA SBT Sorption cooler designed for the Herschel mission. Right: detailed CAD view. Left: Engineering model. Figures from references [23].*

Dilution refrigerators

Dilution refrigerators are based on the dilution of liquid pure He^3 into a mixture containing approximately 6% liquid He^3 and 94% liquid He^4. A mixture of He^3 and He^4 possess on its phase diagram a tri-critical point at 0.86 K and a forbidden phase below this temperature. When cooled below this temperature, the He^3/He^4 mixture can only exist in the superfluid state at some concentrations. When tending to the absolute zero, the mixture can only contain at maximum 6% He^3, meaning that the excess quantity of pure He^3 which has not diluted into the mixture will form a pure phase above the mixed phase.

Based on these observations, if the concentration of He^3 in the mixed phase is now decreased, some of the He^3 atoms in the pure phase will cross the phase boundary and dilute into the mixed phase. Upon crossing the phase barrier, the liquid He^3 that was in the normal state undergoes a phase transition and becomes superfluid, pumping a fraction of heat from its environment in the process, hence cooling in the process.

Dilution refrigerators are constituted from a mixing chamber, where a continuous flow of liquid He^3 is supplied and diluted inside the mixed phase. The He^3 is then extracted out of the dilute phase using a 1-K pot (or 1-K still) where the He^3 evaporates before He^4 and is pumped back into the system. The cold finger is connected to the mixing chamber. Figure 1.21 features a schematic (left) of a traditional dilution cooler and a picture (right) of an actual dilution cooler with the mixing chamber and cold finger located at the bottom.

Dilution refrigerators can attain temperatures below 300 mK, with no theoretical limit to the minimal temperature achievable. Though, below 2 mK, the viscosity of He^3 increases to the point where the pipes sections must be decreased and their length increased, which end-up in bulkier cryostats.

Dilution refrigerators are nowadays popular machines to reach very low temperatures in lab experiments or applications that use superconductors. We can cite the James Clerk Maxwell Telescope which uses a dilution refrigerator incorporated in the SCUBA-2 instrument platform, containing a detector with Transition Edge Sensors cooled at around 75 mK [25].

However, they are considered unpractical for operation onboard satellites. Indeed, dilution refrigerators require rather complex plumbing which end up taking a lot of space in a satellite. Moreover, its principle relies on the pumping of the lighter He^3 which floats on top of the heavier He^4 mixed phase. The dilution refrigerator needs a more complex system in order to work in zero-gravity.

Tackling these challenges, Air Liquide Advanced Technologies and Institut Néel CNRS developed in 2006 the first space compatible dilution refrigerator, which embarked on the Planck satellite from ESA [26]. It successfully maintained a temperature of 100 mK for more

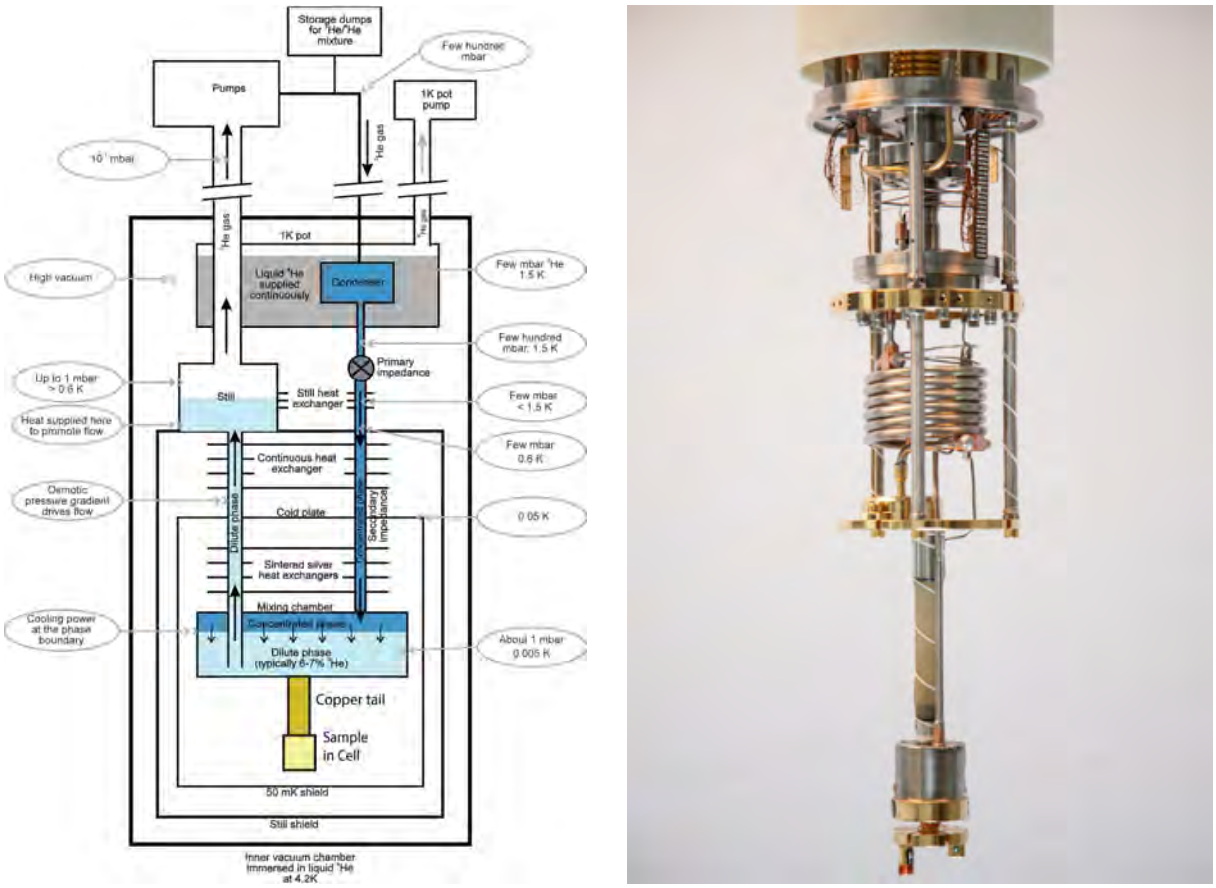

Figure 1.21: *Right: Schematic of a classical wet dilution refrigerator, from [24]. Left: Wet dilution refrigerator from Cryoconcept, subsidiary company of Air Liquide.*

than 2 years and observed the diffuse cosmological background with 0.1 mK resolution (Figure 1.7). For simplicity reasons the system was designed as an open loop dilution, meaning that it doesn't include the distillation system to recycle the helium isotopes back into the cryocooler.

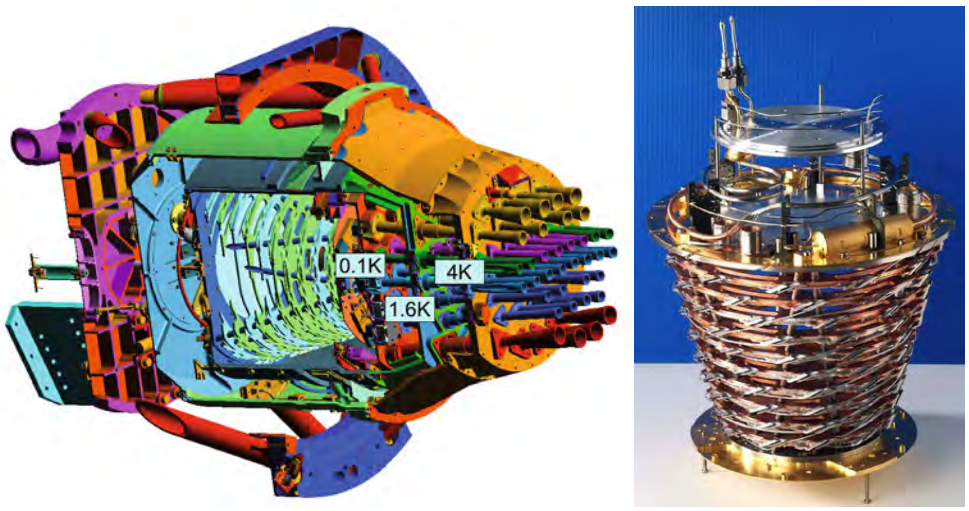

Figure 1.22: *Planck cryogenic architecture. Left: HFI instrument thermal design, from [27]. Right: Planck's dilution cryocooler, source: ESA.*

Adiabatic Demagnetization Refrigerators

Adiabatic demagnetization refrigerators, abbreviated ADR are based on the magneto-caloric effect in paramagnetic materials. A paramagnetic, under the effect of an external field will acquire a magnetization, the magnetic dipoles of its atoms or molecules aligning in the same direction of the external field. Upon switching on a strong magnet around the paramagnetic substance, its magnetic dipoles will be forced to align with the field lines, heating in the process (Figure 1.23: "Recycling"). By closing the heat switch connected to a cold heat sink, the ADR temperature is kept constant. The cooling process is begins after switching off the physical contact with the heat sink and turning off the magnet (Figure 1.23: "Operating").

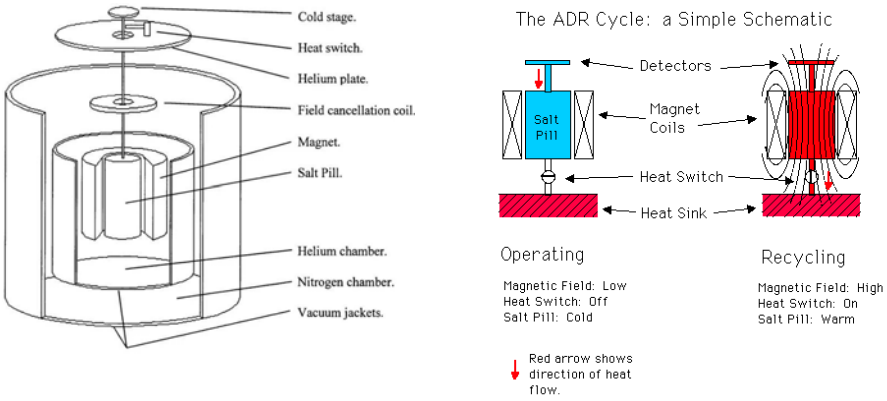

Figure 1.23: *Left: Schematic of a single-stage ADR from reference [28]. Right: Operation principle of an ADR from reference [29].*

ADR refrigerators are now preferred over dilution refrigerators to go below 300 mK onboard satellites, as they are simpler and more electrically efficient as well. They were used in the missions Astro-E2 and Astro-H, which unfortunately suffered both from early platform failures. Even though, the ADRs operated nominally over those short periods of time.

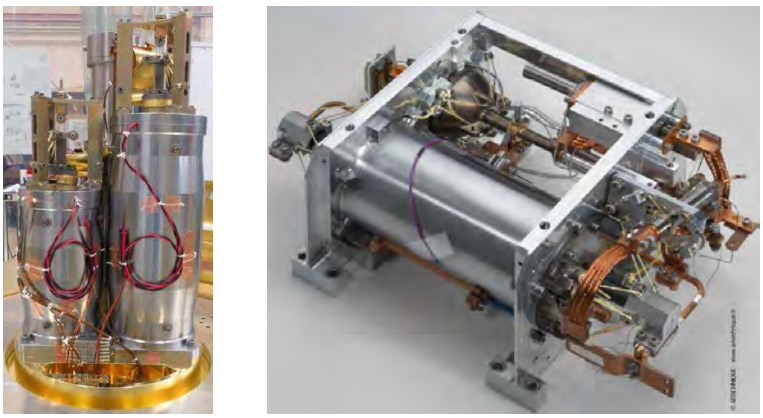

Figure 1.24: *Left: Astro-H 50 mK ADR made by NASA Goddard Space Flight Center [30]. Right: Hybrid dilution-ADR cooler developed by CEA-SBT for the Athena mission.*

Laser Cooling in solids

Solid state Laser Cooling (or optical cooling) is an innovative cooling method based on the stimulation of Anti-Stokes fluorescence inside materials possessing absorption bands such as rare-earth doped crystals or semi-conductors. When excited at the proper wavelength with a laser, the cooling media absorbs and re-emmit more optical power than initially supplied, extracting heat out of the materials.

As of today, it is the one and only all-solid-state cooler capable of reaching cryogenics temperatures, thus outperforming Peltier coolers under 200 K. In a Laser Cryocooler, the power is supplied to the cold head by a laser beam, featuring a miniaturized from factor. The method is free of any moving part or mechanism hence highly reliable and vibration-free. Moreover, the contact-less nature of the cooling process allows reduced thermal losses.

Thanks to these advantages, Laser Cooling has the potential to bring a small revolution in the domain of space cryogenics by enabling a new generation of miniaturized and vibration-free cryocoolers.

Only two Laser Cryocooler prototypes exists right now in the world, as shown in Figure 1.25. The first one was researched by the University of New Mexico and Los Alamos National Lab since 2010 [31]. In 2018, the first instrument cooled with a Laser Cryocooler was demonstrated [32] with the cooling of a FTIR at a temperature of 135 K.

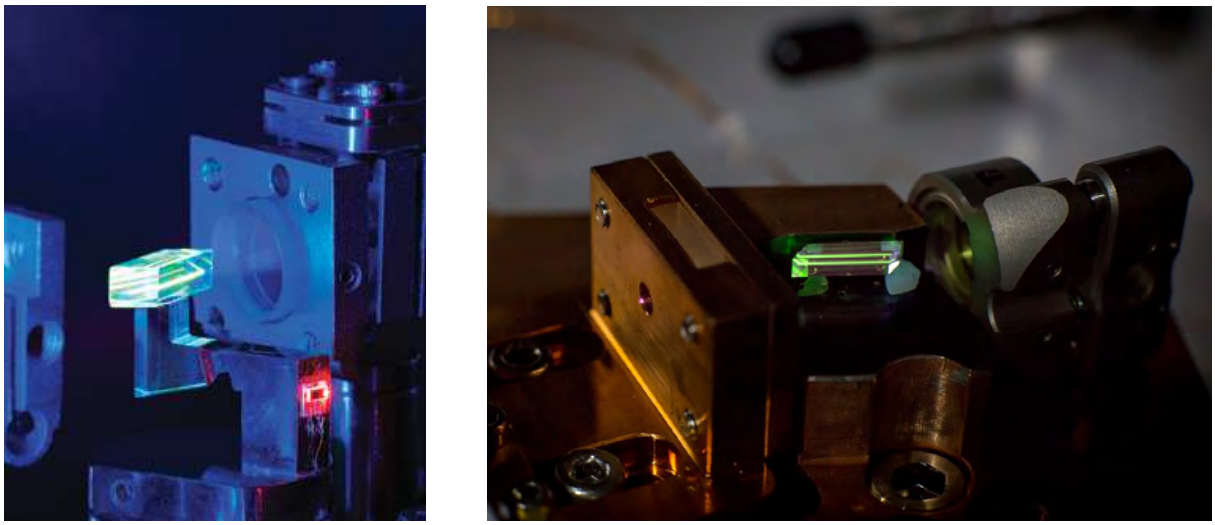

Figure 1.25: *Pictures of the prototypes of Laser Cryocoolers existing in the world. Left: The Laser Cryocooler at the University of New Mexico [33]. Right: The Laser Cryocooler at Institut Néel (this work).*

Since 2018, our group has been researching and developing a Laser Cryocooler prototype at Institut Néel for space applications. As detailed in this thesis, the successful cryocooler operation allowed to cool down a crystal at cryogenics temperatures, thus reaching TRL 3 level for this technology in Europe, an important step towards future space applications.

1.3 Upcoming missions involving space cryogenics

The goal of this section is to give a small overview of several problems faced nowadays in space cryogenics through the prism of some missions expected to launch within the next decade. With some selected examples, we will see the applications of space cryogenics and why it's important to keep researching in that field, discovering new cooling methods and improving the ones existing.

1.3.1 Cryogenics for large satellites

As seen in the previous sections, most of the large satellites are science driven telescopes, launched with the purpose of answering some of the fundamental questions asked in physics and astrophysics. Naturally, from their large size, those satellites generally can accommodate complex cryogenic chains with several cryocoolers stages. It is interesting to take a look at cryogenics onboard the two biggest flagship missions of this decade: ATHENA and the JWST.

Athena

Acronym of "Advanced Telescope for High Energy Astrophysics", Athena is the second Large class space telescope mission selected for the ESA Cosmic Vision program (Figure 1.26). The telescope will observe the X-ray spectra coming from the hottest regions in the universe, such as black holes, neutron stars and supernovaes. Its goal is to study the link between black holes formation and the shape of the largest objects observable in the universe such as galaxies clusters or superclusters [34].

Due to the X-ray spectral range, Athena requires a 14 meters long focal length with a "lens" made of silicon bricks, deviating and focusing X-rays arriving at grazing incidence. Its main instrument, the X-ray Integral Field Unit or X-IFU will use a detector matrix of 3840 Transition Edge Sensors cooled at a temperature of 50 mK. Increasingly popular on ground based telescopes, it will be the first time that this technology is employed onboard a space telescope. To operate these detectors, the satellite will require an unprecedented cryogenic chain, composed of 5 intermediary stages between 300 K and 2 K with shields in Russian dolls arrangement, as shown in Figure 1.27.

The chain will embark most of the low temperature cryocoolers types cited earlier in this chapter:

Figure 1.26: *Artist view of the ATHENA telescope. Source: Athena X-ray Observatory.*

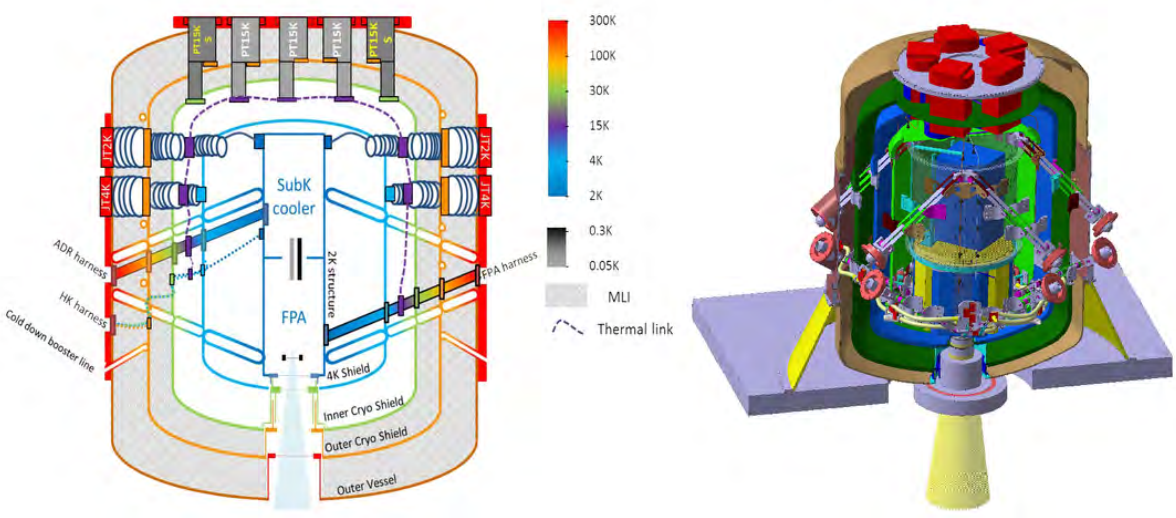

Figure 1.27: *Cryogenic chain of ATHENA X-IFU instrument, featuring 5 intermediary stages of shields from ambient to 2 K, until reaching the temperature of 50 mK at the Focal Plane Array level. Figure from reference [34].*

- At ambient rejection temperature, five dual stage Pulse-tube coolers PT-15K from Air Liquide Advanced Technologies: two for precooling at 30 K and three for the 15 K stage.
- At rejection temperature 80 K: two JT-2K from Jaxa, precooled at 30 K by the PT-15K, and two other JT-4K precooled by Stirling coolers.
- At last, an hybrid sorption/ADR developed by CEA-SBT, with an input temperature of 2 K, a stage at 300 mK and the final stage at 50 mK.

A preliminary CAD view of the cryo-chain assembly is shown in Figure 1.28. From the number of sub-systems involved, it is obvious in this project that thermal design, cryocoolers

efficiency and reliability are critical points.

To conclude, Athena is perhaps the most ambitious and cryogenics demanding satellite of the 2020-2030 decade, and through it we see the key, enabling role of cryogenics for the newest observation satellites and the complexity to reach those low temperatures with "dry" solutions that don't necessitate a liquid helium Dewar.

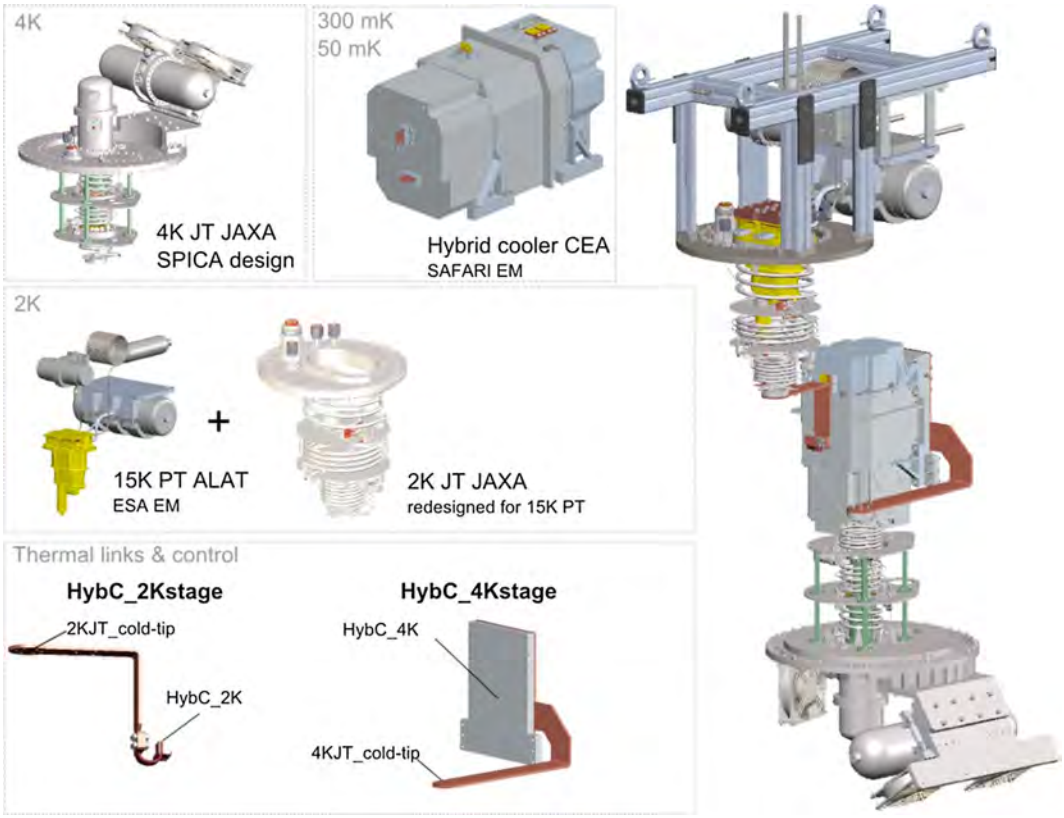

Figure 1.28: *CAD view of the different cryocoolers assembled together in Athena's cryo-chain, from reference [35].*

James Webb Space Telescope

The James Webb Space Telescope, abbreviated JWST is NASA's next large telescope, as shown in Figure 1.29. Its goal is to observe the infrared light coming from the furthest, faintest sources in the universe, coming from stars and galaxies moments after their formation between 1 million and 1 billion years after the Big Bang.

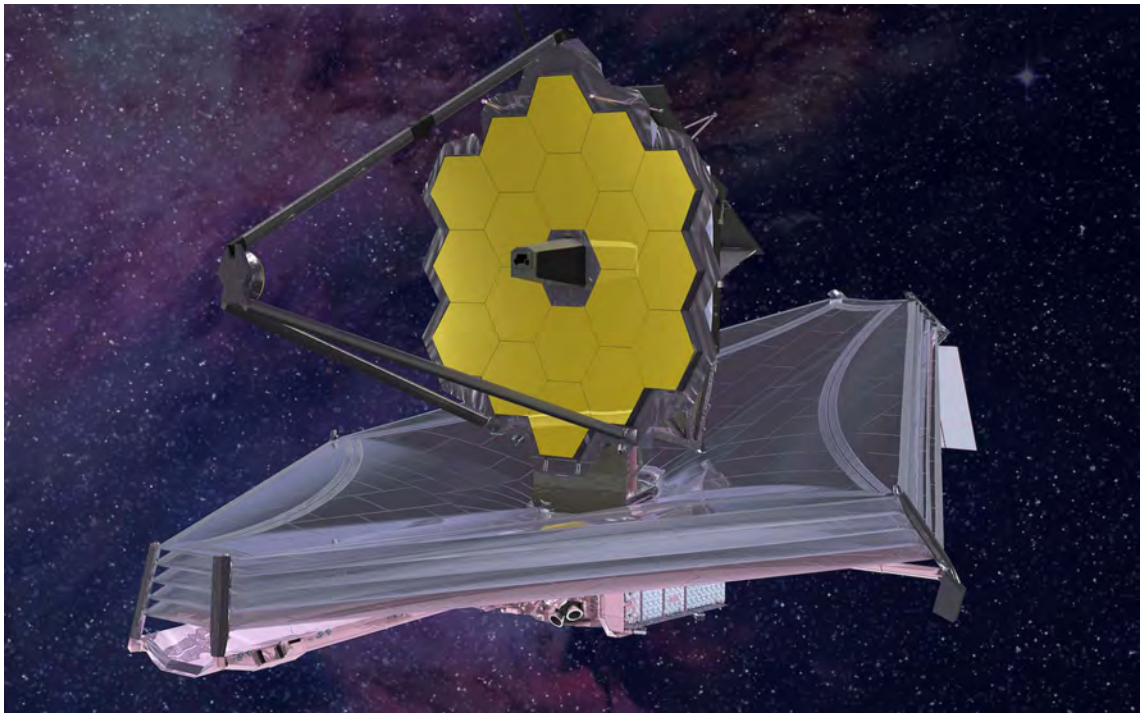

Figure 1.29: *Artist view of the JWST telescope. Source: NASA.*

The JWST will embark several infrared observation instruments, a deployed telescope with unprecedented area made of gold coated Beryllium mirrors, and a large sunshield (as large as a tennis court) with V-grooves design acting as passive cooler for the payload instruments.

The first aluminium coated kapton layer, facing the sun, have 0.05 mm thickness while the four others have 0.025 mm thickness, fours times thinner than a paper sheet. The coldest layer will reach a temperature of 36 K. In total, the JWST will use 13 HgCdTe detectors (10 in NIRCam, 2 in NIRSpec, 1 in FGS/NIRISS) maintained at that temperature, and 3 Si:As detectors in the MIRI instrument, requiring alone one Pulse-Tube for pre-cooling at 18 K and one JT cooler at 7 K.

The needs here are very different than ATHENA. Particularly, in the case of the JWST, the instruments do not require very low temperatures but there is a large number of infrared detectors. We see another philosophy which combines a high amount of passive cooling/thermal control and fewer active cryocoolers in order to meet the mission requirements.

Figure 1.30: *Sun shield of the JWST being tested at Northrop Grumman Corporation's Space Park facility. Its size is that of a tennis court: approximately 20 meters long per 15 meters large. Source: NASA.*

1.3.2 Cryogenics for medium satellites

MTG and MetOp-SG

The Meteosat Third Generation (MTG) and Meteorological Operational satellite - Second Generation (MetOp-SG) are Europe's new meteorological satellites planned for service between 2020 and 2040, as shown in Figure 1.31.

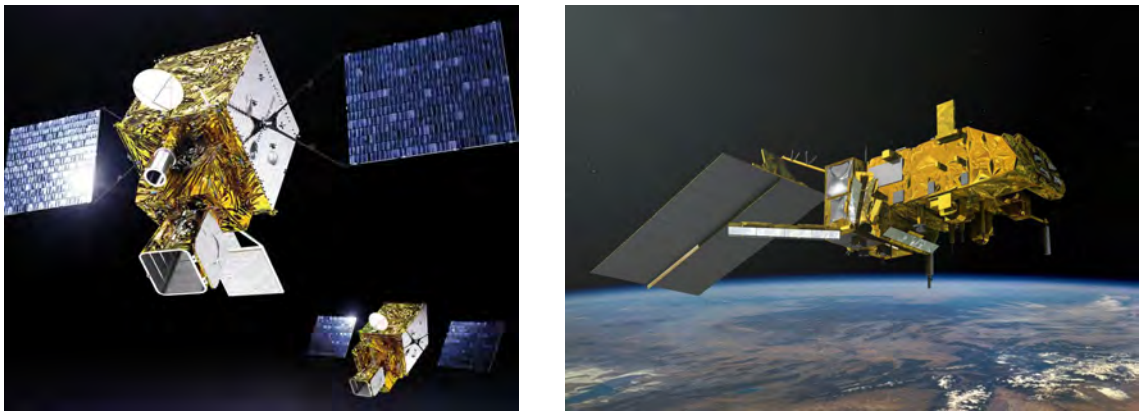

Figure 1.31: *Left: Artist view of MTG-I and MTG-S. Source: Thales Alenia Space. Right: Artist view of MetOp-SG. Source: Airbus Defense and Space.*

The MTG program is specified to provide continuous atmospheric observation over Europe, Middle-East, Africa and part of South-America in order to improve future weather forecasts. To meet the requirements, the new satellites will be launched in geostationary orbit and will have 3-axes stabilized platforms.

A total of 6 satellites will be launched, in two versions: MTG-Imager (4 satellites) and MTG-Sounder (2 satellites). The imager MTG-I will take hyperspectral images of a full hemisphere every 2.5 minutes in 16 spectral bands between 400 nm and 13 µm, with at least 2 km spatial resolution. It will also monitor lightnings. The sounder MTG-S based on a Fourier Transform Interferometer will take full infrared spectra between 4.6-6.25 μm and 8.3-14.3 μm with 4 km spatial resolution in the full hemisphere every hour.

The MetOp-SG program is the European contribution to global meteorological coverage, sequel of the MetOp satellites. It consists in a series of 3 satellites that will be launched between 2023 and 2038 in polar orbit. The IASI-NG sounder (Interféromètre Atmosphérique de Sondage dans l'Infrarouge - New Generation) is a Fourier Transform Interferometer coupled to an infrared imager. Based on an iteration over the first generation IASI, it will feature a two-fold improvement in spectral resolution and signal-to-noise ratio [36]. In the same way as IRS, its goal is to retrieve the air water levels by analyzing the Earth's infrared transmission through the atmosphere. A particularity is that these instruments are able to give a measure of the atmosphere's composition layer by layer.

To reach the specified performances, each one of these 9 satellites will embark Pulse-Tube LPTC cryocoolers from Air Liquide Advanced Technologies (Figure 1.14) which can cool at a temperature of 50 K. We understand that in the context of earth observation satellites with each time increased requirements and complexity, constraint on cryogenics and thermal engineering increases as well as tolerances becomes tighter. For example, in interferometric systems, even the faintest vibrations generated by mechanical cryocoolers can become an issue. We see also and again that cryogenics, through the cooling of these space instruments for applications such as weather forecasts plays an unexpected role in our daily lives.

1.3.3 Cryogenics for small satellites

Small satellites can be widely different by their goals and instruments. Some don't require cryogenics at all because they don't need particularly low noise instruments. Those who does require cryogenics such as small infrared earth-observation satellites generally don't need temperatures below 70 K, and their detectors are generally smaller than those used in larger satellites, resulting in reduced thermal dissipation and hence cooling power required.

Microcarb

Microcarb is the example of a typical small infrared observation mission. The satellite is based on a Myriade platform developed by CNES. Its goal is to monitor in low earth orbit the worldwide carbon-dioxide emissions starting from 2021. Its only instrument is a spectrometer based on an "echelle" diffraction grating. It will measure the atmosphere transmission spectra in three near infrared bands: O_2 from 0.76 μm to 1.27 μm, and CO_2 around 1.6 μm and 2 μm.

The infrared detector, a Lynred NGP-SWIR features a large HgCdTe matrix 1024x1024 with low noise figure and thermal dissipation on the order of 150 mW. From the cryogenics point of view, it is interesting to see that for a specified focal plane temperature of 150 K, the choice was made in favor of a passive radiator inside a baffle instead of active cooling with Pulse-Tubes. This choice was probably motivated by similar bulkiness between both solutions, in defavor of Pulse-Tubes due to microvibrations and lesser reliability.

A view of Microcarb is shown Figure 1.32, along with the payload architecture. We can notice that the baffle and instrument cryostat occupies almost half of the payload volume.

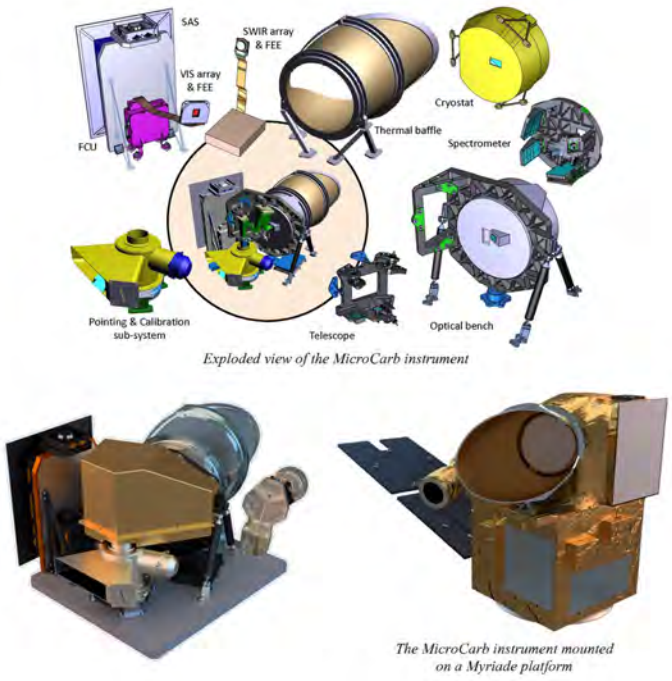

Figure 1.32: *Overview of the Microcarb instrument, from reference [37].*

In chapter 3, we review the feasibility of a Microcarb like mission, comparing an architecture with redundant Laser Cryocoolers with redundant Pulse Tubes Coolers. We show that, where the Pulse-Tube architecture is bulkier at payload level, a Laser Cryocooler architecture allows for excellent volume savings in the payload, as well as overall mass savings at the price of a larger electrical consumption.

Nanosatellites/CubeSats

Nanosatellites are satellites with weight typically less than a dozen of kilograms. From these nanosatellites, CubeSats are a unique example of a standard that emerged in the space industry. CubeSats are composed of multiples of a base unit "1U" which measures 10 cm x 10 cm x 10 cm, as shown in Figure 1.33.

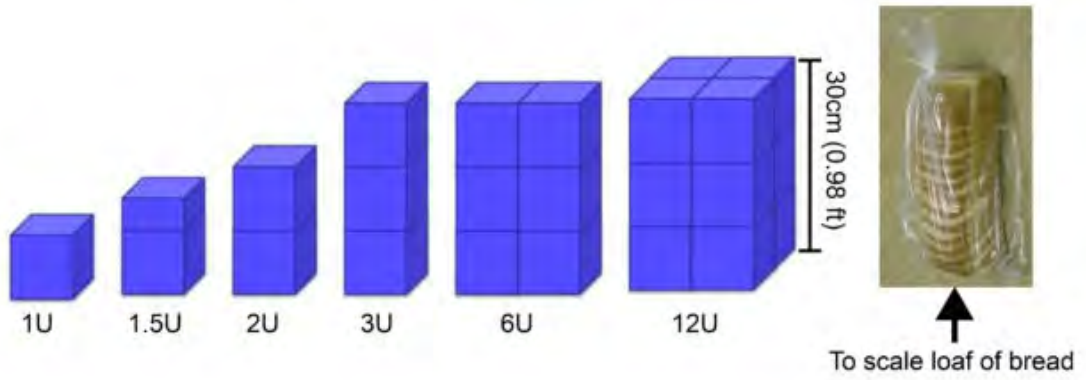

Figure 1.33: *Schematic of the CubeSats form factors up to 12U with the corresponding scale, from reference [38].*

In the "New-Space" paradigm, Cubesats allows quick design, quick testing and lower-cost access to space for actors which could not afford it otherwise such as universities. Due to their reduced dimensions, many CubeSats can be launched at once, or they can be launched in "piggy-backing" along with larger class satellites. As shown in Figure 1.34, the number of nanosatellites launched each year has been largely increasing since the 2000's. Nowadays, between 150 and 300 nansatellites are launched every year. Predictions foresees an exponential growth of the number of launch, sign of the popularity of this solution.

Nanosatellites and Cubesats can require thermal control but they traditionally don't embark cryogenics instruments, due to the reduced allowed payload volume. The perspective of improving Laser Cooling to a point where the power consumption becomes CubeSats compatible is exciting with regards to the new markets and applications opportunities. Bringing cryogenics solutions to this smallest class of satellites could mean a revolution in the applications, opening the door to space for miniature cryo-cooled instruments.

Still in chapter 3, we show that it is already realistic to consider Laser Cooling for CubeSats. With the improvement of this technology under reasonable hypotheses, power consumption could be reduced enough to fit 12 U CubeSats within less than a decade.

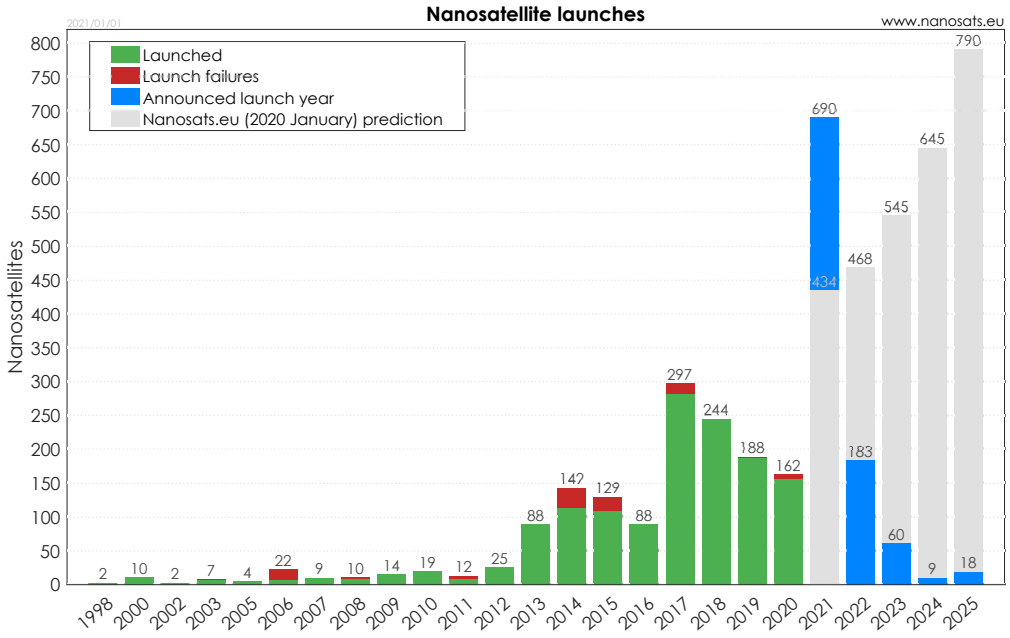

Figure 1.34: *Number of nanosatellites launched through the years since 1998 and predicted launches as of january 2020, from reference [39]. The trend shows the increasing popularity of this solution, as an easy access to space for new actors such as universities.*

1.4 Conclusion: space cryogenics and Laser Cooling

Cryogenics is the science of cooling down to low temperatures below 120 - 150 K. The discipline has largely evolved since its first steps in the beginning of the 20^{th} century, and it has now become fundamental for spacecrafts propulsion and space instruments.

In these instruments, sensor technologies are divided between photo-detectors (gamma to 100 μm), thermal detectors (X-ray to 1 mm) and radio antennas (above 100 μm). Photo-detectors, in order to reach low dark current and hence low noise figures requires cooling down to cryogenic temperatures.

In the 4 K - 150 K range, many different cryocooler technologies are available. Mechanical cryocoolers can reach low temperatures while staying relatively efficient. On the other side they feature moving parts which are subject to wearing, and generate vibrations, detrimental for the most sensitive instruments. Passive cooling can be a cost effective and simple solution above 100 K, at the condition of large enough radiators and special accommodations such as a baffle depending on the orbit. Below 100 K, "V-grooves" multi-stage radiators exist, which in practice were only implemented in large space telescopes so far due to size and orbit constraints.

Thermal detectors, in their most sensitive and latest types are made out of supercon-

ducting materials. These materials need temperatures below 1 K to operate, sometimes as low as 50 mK. Reaching those very low temperatures is a challenge which impacts strongly the design of space telescopes, requiring the combination of several types of cryocoolers to meet the temperature and cooling power requirements. Other superconducting devices such as SQUIDs amplifiers and SIS mixers for radio-telescopes requires at least temperatures of 4 K.

Currently, three technologies are able to match sub-Kelvin temperatures. Dilution refrigerators, based on the mixing of He^3 and He^4. They come at the cost of increased complexity and volume in the pipes design in order to work in zero-gravity; Sorption coolers, based on evaporation cycles of helium in a closed container; Adiabatic Demagnetization Refrigerators or ADR, based on the energy loss when switching a paramagnetic material from its magnetic to disordered state.

Faced with increasingly complex space instruments requiring each time higher performances and tighter tolerances, cryogenics has a bright (and busy !) future and a large part to play in tomorrow's space success.

But another challenge addressed to space cryogenics is that of miniaturization. Today, with the CubeSats "boom" and the New-Space paradigm emergence, a vast playground of applications onboard the smallest satellites is yet to be explored, which represents exciting opportunities for Laser Cooling in the future.

Laser Cryocoolers are, at the time of writing this thesis, the only type of active coolers capable of reaching cryogenic temperatures from ambient in a vibration-free method. This innovative and vibration free cooling method can be miniaturized and present many other advantages compared to mechanical cryocoolers such as reduced thermal losses and no EMC. To conclude, this technology possess a huge potential for enabling new applications onboard small satellites which relies on cryogenics and this new paradigm could even bring a small revolution in the domain within the next decade.

References

[1] S. Carnot, "Réflexions sur la puissance motrice du feu et sur les machines propres à développer cette puissance," 1824 (cit. on p. 7).

[2] G. Claude, "Process for the separation of oxygen and nitrogen from liquid air," *US Patent US950436A*, 1903. [Online]. Available: https://patents.google.com/patent/US950436A/en (cit. on p. 8).

[3] K. H. Onnes, "The Liquefaction of Helium," *Royal Netherlands Academy of Arts and Sciences*, 1909 (cit. on p. 8).

[4] R. G. Ross, “Aerospace Coolers: a 50-Year Quest for Long-life Cryogenic Cooling in Space,” *Cryogenic Engineering: Fifty Years of Progress*, 2006.
DOI: 10.1007/0-387-46896-X_11 (cit. on pp. 10, 18, 19).

[5] M. Linder, N. Rando, A. Peacock, and B. Collaudin, “Cryogenics in Space - A review of the missions and technologies,” *ESA Bulletin*, 2001. [Online]. Available: http://www.esa.int/esapub/bulletin/bullet107/bul107_12.pdf (cit. on pp. 10, 12).

[6] N. Rando, “Cryogenics in Space,” *Observing Photons in Space, ISSI Scientific Reports Series, ESA/ISSI*, 2010.
DOI: 10.1007/978-1-4614-7804-1_37 (cit. on p. 14).

[7] P. Zevenbergen and R. Van Brakel, “Thermal Testing of the Sentinel 5 Precursor TROPOMI earth observation instrument,” *46th International Conference on Environmental Systems*, 2016 (cit. on p. 16).

[8] The Planck Collaboration, “Planck early results. II. The thermal performance of Planck,” *Astronomy and Astrophysics*, 2011.
DOI: 10.1051/0004-6361/201116486 (cit. on p. 16).

[9] J. Mao, G. Chen, and Z. Ren, “Thermoelectric cooling materials,” *Nature Materials*, 2020.
DOI: 10.1038/s41563-020-00852-w (cit. on p. 17).

[10] B. Poudel, Q. Hao, Y. Ma, Y. Lan, A. Minnich, B. Yu, X. Yan, D. Wang, A. Muto, D. Vashaee, X. Chen, J. Liu, M. S. Dresselhaus, G. Chen, and Z. Ren, “High-Thermoelectric Performance of Nanostructured Bismuth Antimony Telluride Bulk Alloys,” *Science*, 2008.
DOI: 10.1126/science.1156446 (cit. on p. 17).

[11] L. E. Bell, “Cooling, Heating, Generating Power, and Recovering Waste Heat with Thermoelectric Systems,” *Science*, 2008.
DOI: 10.1126/science.1158899 (cit. on p. 17).

[12] A. de Waele, *Basic Operation of Cryocoolers and Related Thermal Machines*. 2011.
DOI: 10.1007/s10909-011-0373-x (cit. on p. 19).

[13] J. Bert, “Pulse Tube Cryocoolers: A Cryogen-Free Path to 2K,” *Coursework for Physics 210, Stanford University*, 2007. [Online]. Available: http://large.stanford.edu/courses/2007/ph210/bert2/ (cit. on p. 20).

[14] E. I. Mikulin, A. A. Tarasov, and M. P. Shkrebyonock, “Low-Temperature Expansion Pulse Tubes,” 1984.
DOI: 10.1007/978-1-4613-9865-3_72 (cit. on p. 20).

[15] R. Radebaugh, J. Zimmerman, D. R. Smith, and B. Louie, “A Comparison of Three Types of Pulse Tube Refrigerators: New Methods for Reaching 60K,” 1986. DOI: 10.1007/978-1-4613-2213-9_88 (cit. on p. 20).

[16] J. Tanchon, J. Lacapere, A. Molyneaux, M. Harris, S. Hill, S. M. Abu-Sharkh, and T. Tirolien, *A Turbo-Brayton Cryocooler for Future European Observation Satellite Generation*. 2016 (cit. on pp. 21, 22).

[17] T. Trollier, J. Tanchon, J. Buquet, A. Ravex, and P. Crespi, “Air Liquide space cryocooler systems,” *Cryogenics*, 2008. DOI: 10.1016/j.cryogenics.2008.03.010 (cit. on p. 21).

[18] A. Petrivelli, “The ESA Laboratory Support Equipment for the ISS,” *ESA bulletin*, 2002 (cit. on p. 22).

[19] R. M. Damle and M. D. Atrey, “Transient simulation of a miniature Joule–Thomson (J–T) cryocooler with and without the distributed J–T effect,” *Cryogenics*, 2015. DOI: 10.1016/j.cryogenics.2014.10.003 (cit. on p. 23).

[20] Air Liquide Advanced Technologies, “Joule-Thomson miniature coolers,” [Online]. Available: https://advancedtech.airliquide.com/joule-thomson-miniature-coolers (cit. on p. 23).

[21] X. Xi, J. Wang, L. Chen, Y. Zhou, and J. Wang, “Progress and Challenges of Sub-Kelvin Sorption Cooler and Its Prospects for Space Application,” *Journal of Low Temperature Physics*, 2020. DOI: 10.1007/s10909-020-02442-1 (cit. on p. 24).

[22] L. Duband, I. Charles, J.-M. Duval, E. Ercolani, P. Gully, N. Luchier, T. Prouve, and P. Thibault, “Space Cryogenics at CEA-SBT,” *Proc. of SPIE*, 2017. DOI: 10.1117/12.2308267 (cit. on p. 24).

[23] L. Duband, “Space cryocooler developments,” *Physics Procedia*, 2015. DOI: 10.1016/j.phpro.2015.06.003 (cit. on p. 24).

[24] K. A. Schreiber, “Low Temperature Measurement Techniques,” *Springer Theses*, 2019. DOI: 10.1007/978-3-030-26322-5_3 (cit. on p. 26).

[25] D. Bintley, J. T. Kuroda, E. G. Starman, S. Craig, and W. S. Holland, “Performance of the SCUBA-2 dry dilution refrigerator: 4 years of operation at the JCMT,” *Proc. of SPIE*, 2012. DOI: 10.1117/12.926540 (cit. on p. 25).

[26] S. Triqueneaux, L. Sentis, P. Camus, A. Benoit, and G. Guyot, “Design and performance of the dilution cooler system for the Planck mission,” *Cryogenics*, 2006. DOI: 10.1016/j.cryogenics.2005.12.004 (cit. on p. 25).

[27] The Planck Collaboration, “Planck pre-launch status: The HFI instrument, from specification to actual performance,” *Astronomy and Astrophysics*, 2010.
DOI: 10.1051/0004-6361/200912975 (cit. on p. 26).

[28] P. A. Bromiley, “Development of an Adiabatic Demagnetisation Refrigerator for use in Space,” *PhD Thesis*, 1999 (cit. on p. 27).

[29] M. O. Kimball and E. A. Silk, “GSFC Adiabatic Demagnetization Refrigerator,” 2014. [Online]. Available: https://cryo.gsfc.nasa.gov/ADR/ADR.html (cit. on p. 27).

[30] P. J. Shirron et al., “Design and on-orbit operation of theadiabatic demagnetizationrefrigerator on the Hitomi Soft X-raySpectrometer instrument,” *Proc. of SPIE*, 2016.
DOI: 10.1117/12.2231301 (cit. on p. 27).

[31] S. D. Melgaard, *Cryogenic optical refrigeration: Laser cooling of solids below 123 K*. 2013. [Online]. Available: https://digitalrepository.unm.edu/ose_etds/24/ (cit. on p. 28).

[32] M. P. Hehlen, J. Meng, A. R. Albrecht, E. R. Lee, A. Gragossian, S. P. Love, C. E. Hamilton, R. I. Epstein, and M. Sheik-Bahae, “First demonstration of an all-solid-state optical cryocooler,” *Light: Science & Applications*, 2018.
DOI: 10.1038/s41377-018-0028-7 (cit. on p. 28).

[33] J. Wallace, “Optical Cooling: All-optical cryogenic cooling of sensors eliminates vibration,” *LaserFocusWorld*, 2018. [Online]. Available: https://digital.laserfocusworld.com/laserfocusworld/201807 (cit. on p. 28).

[34] The Athena Collaboration, “The ATHENA X-ray Integral Field Unit (X-IFU),” *Proc. of SPIE*, 2018.
DOI: 10.1117/12.2312409 (cit. on pp. 29, 30).

[35] T. Prouve, “ATHENA X-IFU 300 K-50 mK cryochain demonstrator cryostat,” *Cryogenics*, 2018.
DOI: 10.1016/j.cryogenics.2017.11.009 (cit. on p. 31).

[36] F. Bernard, B. Calvel, F. Pasternak, R. Davancens, C. Buil, E. Baldit, C. Luitot, and A. Penquer, “Overview of IASI-NG the new generation of infrared atmospheric sounder,” *Proc. of SPIE*, 2014.
DOI: 10.1117/12.2304101 (cit. on p. 34).

[37] F. Pasternak, P. Bernard, L. Georges, and V. Pascal, “The microcarb instrument,” *Proc. of SPIE*, 2016.
DOI: 10.1117/12.2296225 (cit. on p. 35).

[38] Boston University, “Cubesats,” 2017. [Online]. Available: https://sites.bu.edu/cupid/2017/07/16/cubesats/ (cit. on p. 36).

[39] E. Julu, “Nanosats Database,” 2021. [Online]. Available: https://www.nanosats.eu/ (cit. on p. 37).

Chapter 2

Laser cooling in solids: fundamentals and prospects

The aim of this chapter is to present the details and principles associated to laser cooling in solids, as well as its applications. I start with a history of laser cooling in solids, from its theoretical formulation nearly one century ago, until the spectacular progress observed during the last decade. I then develop the electronic properties of rare-earths doped materials before exposing the principles of Anti-Stokes cooling in these materials. The particular case of our material, the Yb:YLF cooling crystal is detailed with its physical properties and its cooling efficiency. Finally, I present some of the future prospects regarding laser cooling in solids: the new generations of cooling materials as well as the spin-off applications of the Laser Cryocooler.

Le but de ce chapitre est de présenter en détails les principes associés au refroidissement laser dans les solides, ainsi que ses applications. Je commence par détailler l'histoire du refroidissement laser dans les solides, de ses premières formulations théoriques il y a presque un siècle, jusqu'au progrès spectaculaires observés durant la dernière décennie. Je développe ensuite les propriétés électroniques des matériaux dopés terres-rares avant d'exposer les principes du refroidissement Anti-Stokes dans ces matériaux. Le cas particulier de notre matériau, le cristal refroidisseur Yb:YLF est détaillé avec ses propriétés physiques et son efficacité de refroidissement. Enfin, je présente quelques-unes des futures perspectives concernant le refroidissement laser dans les solides: les nouvelles générations de matériaux refroidisseurs ainsi que les applications spin-off du Cryo-refroidisseur Laser.

2.1 History of optical refrigeration

To understand the birth of optical refrigeration, one has to plunge into the history of light and spectroscopy. In 1852, the British physicist Stokes published the treaty "On the change of refrangibility of light" where he describes that ultraviolet light crossing certain materials such as fluorine is responsible of visible blue light emission [1]. The concept of fluorescence was born.

Elaborating on Planck's work on black-body radiation [2], in 1905 Einstein in his paper "On a heuristic viewpoint concerning the production and transformation of light" advanced as an explanation to the photo-electric effect that light is made out of photon particles, and that they exchange energy with matter in discrete packets, their energy being related to the wavelength of light [3].

Following these discoveries, it was postulated as the "Stokes law" that the light being transmitted through a piece of matter would only exit with lower frequencies (longer wavelengths) and could only lose energy. In 1928, Raman discovered that this law is violated: in his experiment, part of the light would exit with higher frequencies (shorter wavelengths) [4]. Later, the light exiting with lower energy would be called "Stokes emission" and that with higher energy would be called "Anti-Stokes" emission. In 1929, Pringsheim postulated that the Anti-Stokes light would generate cold inside the material, as energy conservation suggests [5], as shown in Figure 2.1.

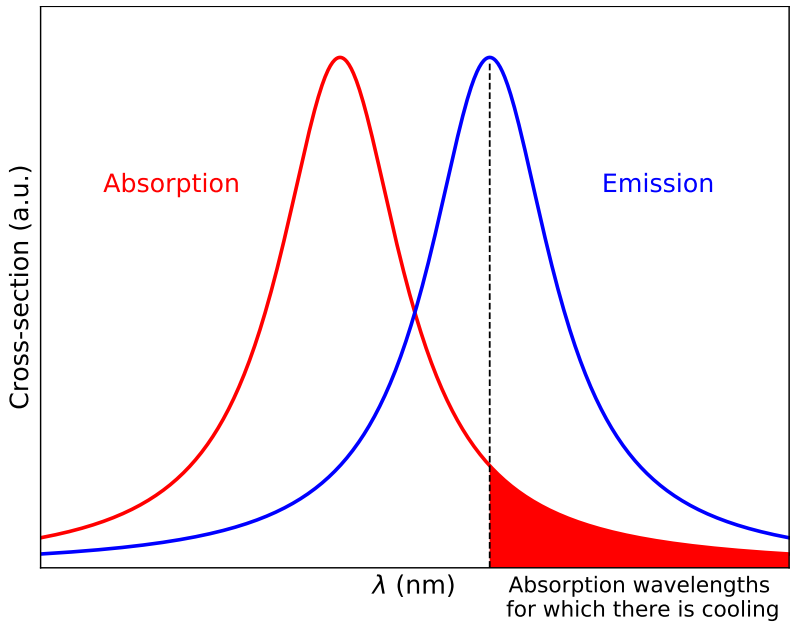

Figure 2.1: *Schematic of the Anti-Stokes cooling principle. The absorption spectrum of the material is shown in red and its emission spectrum shown in blue with a certain shift. For excitation wavelengths superior to the mean emission wavelength, in average more energy is emitted than the material has absorbed, thus cooling the material.*

However, some physicist thought that this process was not allowed, fearing that it might

break the second law of thermodynamics stating that a system cannot lose entropy and only gain it through its physical changes. In 1946, Landau calculated that photo-luminescent cooling was allowed: as the radiation exiting out of the material is emitted isotropically and randomly, there is no decrease of the system's entropy [6].

In 1950, Alfred Kastler described the phenomenon known as population inversion. He postulated that light could be used to generate a Stokes emission generating heat "effet luminocalorifique", but an Anti-Stokes emission as well generating cold "effet luminofrigorifique" [7].

Surprisingly enough, laser cooling in solids has been formulated earlier than its counterpart in single atoms which appeared in the 70's. Spectacular results in cold atoms led to several Nobel prizes in those domains (1966, 1997, 2001, 2012) and laser cooling in gases became known to a wider audience than its counterpart in solids.

For a long time, the proof of optical cooling in solids remained elusive. In 1968, a team led by Kushida and Geusic at Bell Laboratories tried to perform a cooling experiment on 1% Nd:YAG [8]. They got close to net cooling and observed relative cooling compared to undoped YAG, but the sample still heated up a bit and they concluded that their crystal contained too many impurities. Finally, in 1995, a team led by Richard Epstein from the University of New Mexico (UNM) and supported by the Los Alamos National Lab (LANL) and the United States Naval Academy (USNA) demonstrated net cooling in an Yb:ZBLANP glass, yielding the indisputable proof that a solid can be cooled using Anti-Stokes fluorescence [9]. The same year, Edwards from LANL started designing the first optical cryocooler [10] and proposed the first project for aerospace applications [11]. The paper from Mungan and Gosnell [12] re-traces a detailed history of these pioneering events before the 2000's.

Nearly ten years after the initial solid state cooling discovery, two studies by Mills from Ball Aerospace were made in order to assess the performance of laser cryocoolers. Analyzing these studies from an historical point of view and considering that the first optical cryocoolers began to be implemented at the time the author is writing this thesis, we can say that even if some space agencies and space industrial companies had become aware of this technology, the initial project was probably too ahead on its time and the cooling efficiency too low at the beginning to be practically implemented.

Progressively, new tools and methods to improve the cooling process were investigated in the 2000's. The potential of cooling semiconductors instead of rare-earth doped solids has been patented [13] and studied [14] since 2002 by Mansoor Sheik-Bahae from University of New Mexico . However, experiments in III-V semiconductors with near-unity external quantum efficiency yielded no net cooling [15], either due to still unknown mechanisms hindering the cooling process or too high background absorption from residual defects or impurities.

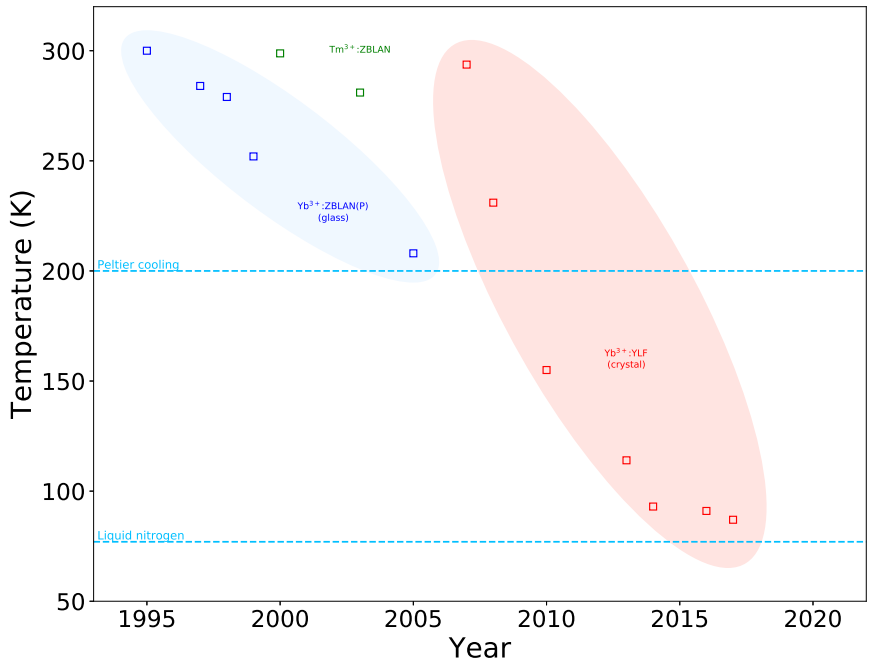

Figure 2.2: *Minimal temperature achieved with laser cooling in solids over the years, from the discovery of laser cooling in solids in the 90's to nowadays.*

In the 2010's, a spectacular gap was closed with Yb:YLF crystals made at the University of Pisa by the team of Mauro Tonelli. At the beginning of this decade, laser cooling in solids reached cryogenic temperatures. At the end of the decade we are now at 87 K, only ten degrees above the symbolic liquid nitrogen boiling point.

2.2 Rare-earths doped solids

Rare-earths are a group of 17 metallic elements with similar properties, formed of lanthanides (or lanthanoids, Z = 57 to Z = 71) with the addition of two other metals, Scandium (Z = 21) and Yttrium (Z = 39), as shown in Figure 2.3.

Rare-earth elements are found on Earth with abundances ranging from 0.5 ppm (Thulium) to 60 ppm (Cerium), at the exception of Promethium which possess only radioactive isotopes and is observed only in infinitesimal traces as a result of the fission of heavier elements. In their natural forms, rare-earth elements ores have similar metallic appearances. They are used in a variety of technical applications, such as strong permanent magnets, phosphors for LED lighting, solid state lasers and superconductors, as illustrated in Figure 2.4.

Due to these technical applications, the demand and production of rare-earth elements have been growing up exponentially since the 70's. Nowadays, between 150,000 and 175,000 tons of rare-earth oxydes are extracted each year from deposits. More than 80%

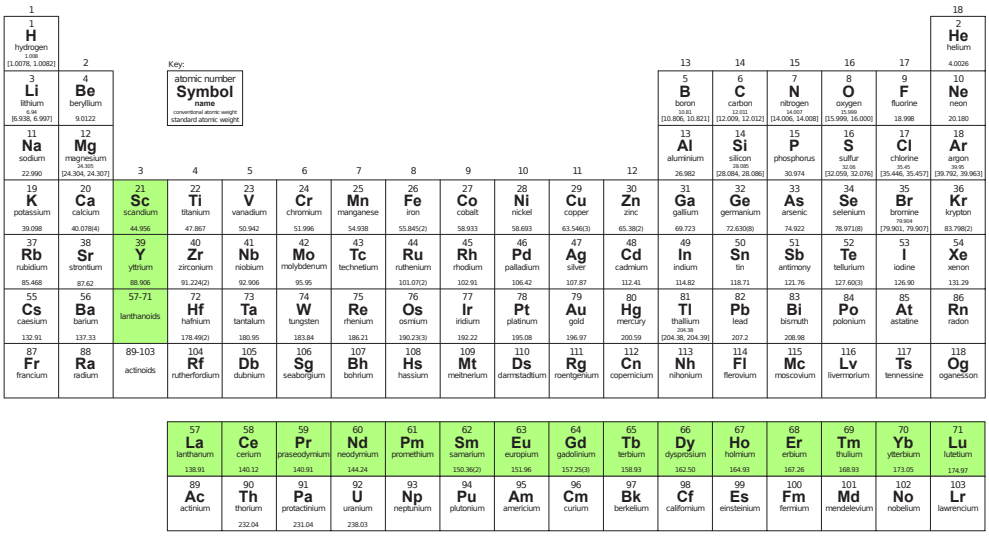

Figure 2.3: *Rare-earth elements highlighted in the periodic table of elements, adapted from [16].*

of that production is supplied by China, while 15% is located in Australia and 5% in the rest of the world. Approximately 25% of that production is used in the petroleum chemical industry as catalyst (Cerium, Lanthanum) and 25% in magnets (Neodymium), the rest for other applications.

For photonics applications, rare-earths are used as dopants inside transparent crystal matrix. Those synthesis materials are usually grown inside furnaces with process such as Czochralski or Bridgeman. Very little raw rare-earth base powder is required, as they are used for dopants in small quantities usually below a few percent of the material composition. The addition of rare-earth inside a crystal or a glass allows the material to absorb and emit light at certain fixed and known wavelengths. Provided a resonant optical cavity and a pump laser, those particular emission wavelength can be used to make solid state lasers with usually good efficiency, higher than those of gas-based lasers. Rare-earths doped materials possess remarkable electronic properties which make them particularly suitable for those applications as detailed in the following sections.

The electonic structure of rare-earths in solid matrix

In practice, rare-earths are never found in their neutral valence state. They tend to lose 3 electrons in order to acquire a $[Xe]4f^n$ structure. At the exception of some elements, most rare-earth elements are hence trivalent. Due to the higher radius of the 5s, 5p and 6s closed shells, 4f valence electrons are electrostatically shielded from outside perturbations, as shown in Figure 2.5. They are weakly reactive, they don't participate in chemical bonds with other atoms, and they are weakly affected by surrounding crystal fields when embedded in solid matrix.

As stated before, rare-earths can replace some other elements with similar radius in a

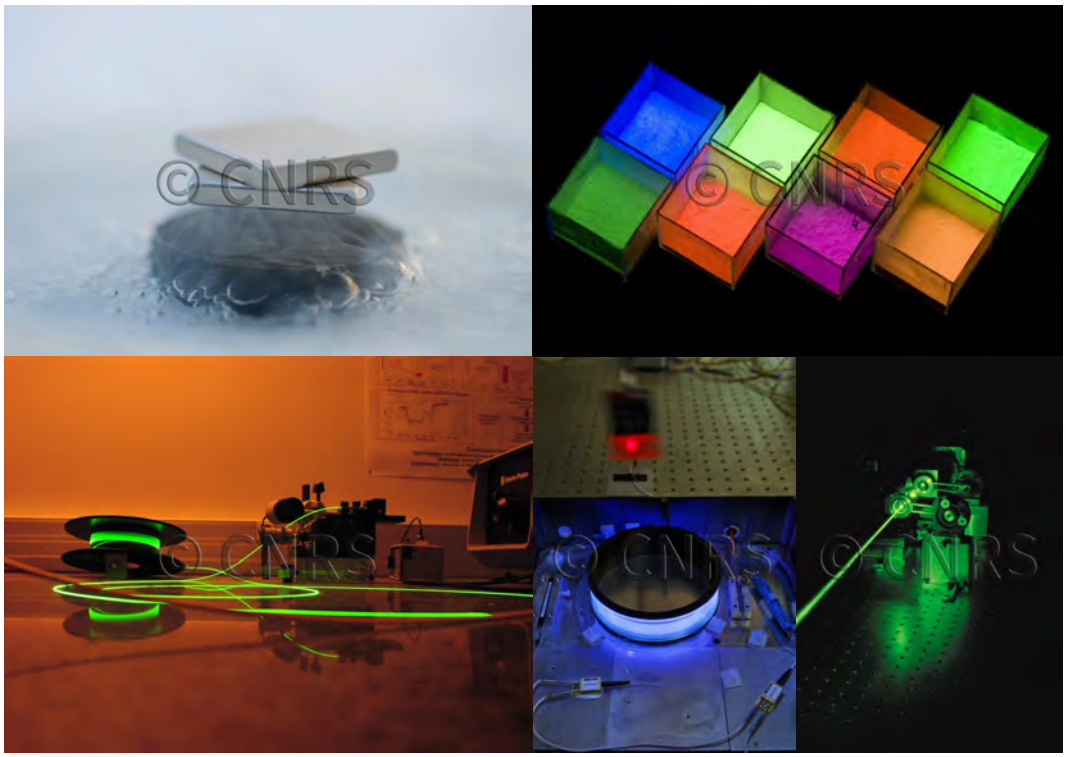

Figure 2.4: *Illustrations of rare-earths applications in several high-technologies domains. From up-right to down-left: Neodymium alloy magnets in levitation above an Yttrium-Barium-Copper-Oxide (YBCO) high temperature superconductor cooled with liquid nitrogen; Rare-earth based luminophores powders under UV excitation; Erbium doped fiber amplifier; Ytterbium doped fiber laser emitting in the near infrared; Green laser based on a Neodymium doped Gadolinium crystal matrix (Nd:GdCOB). Images: CNRS Photothèque.*

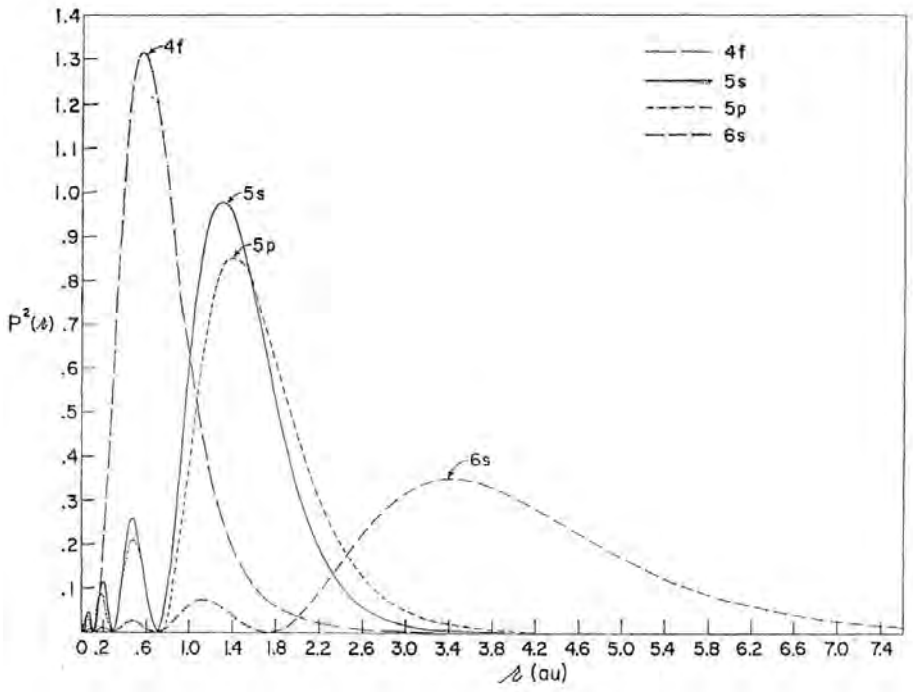

Figure 2.5: *Radial probability densities of 4f, 5s, 5p and 6s electrons in Gd^{+} calculated by Hartree-Fock method, from reference [17]. The 4f electrons are "shielded" from external electromagnetic perturbations by the electrons occupying the outer shells.*

crystal to form a doping. When a rare-earth ion is embedded into a matrix, it behaves almost as a free ion. Finding the energy levels of 4f electrons in that configuration can be done using perturbation theory. The Hamiltonian of a free ion can be written as:

$$\hat{H}_{Free-ion} = \hat{H}_0 + \hat{H}_{Coulomb} + \hat{H}_{Spin-orbit} \tag{2.1}$$

And the Hamiltonian of a rare-earth ion inside a matrix is a perturbation of the free ion :

$$\hat{H}_{Matrix-ion} = \hat{H}_{Free-ion} + \hat{H}_{Crystal-field} \tag{2.2}$$

Where each of the terms in Eq. (2.1) and Eq. (2.2) are described in the following sections.

Central field approximation

The zeroth order term in the perturbation theory designates the mechanical energy of the electrons within the 4f orbital without additional disturbances. We have:

$$\hat{H}_0 = \sum_{i=1}^{N} \left(\frac{p_i^2}{2m_e} + V(r_i) \right) \tag{2.3}$$

In principle, the potential energy of an electron around the nucleus interacting with N other electrons should be written as the sum of the electron-nucleus potential and the sum of each electron-electron interaction (Coulomb repulsion). Due to the N-interacting electrons, the Schrödinger's equation becomes a N-body problem which has generally no analytical solution for $N > 3$. In a first approximation at the zeroth order perturbation theory, the potential seen by a 4f electron moving around the nucleus can be approximated as a central field with spherical symmetry with an effective charge Z^* accounting for the other electrons (the nucleus field is considered as screened by the electrons in the first electronic shells). Under the "central field approximation", and replacing the kinetic energy by its operator, the unperturbed Hamiltonian can be written as:

$$\hat{H}_0 = -\left(\frac{\hbar^2}{2m_e} \right) \sum_{i=1}^{N} \nabla_i^2 - \sum_{i=1}^{N} \frac{Z^* e}{4\pi\epsilon_0 r_i} \tag{2.4}$$

With Z^* the effective charge of the screened nucleus through the electronic cloud, e the electron charge, r_i the electron position relatively to the nucleus and ϵ_0 the vacuum permittivity.

Coulomb interaction

The electron-electron repulsion or Coulomb term can be solved in the first order of perturbation theory. We have:

$$\hat{H}_{Coulomb} = \sum_{i<j}^{N} \frac{e^2}{4\pi\epsilon_0 r_{ij}} \tag{2.5}$$

Introducing this term in the Schrödinger equation lifts the degeneracy between electrons in the same shell. The angular momentum operator $\hat{l}_i$ does not commute with the Hamiltonian. Hence, l and m_l are no longer adequate quantum numbers to count the energy states. However, the squared total angular momentum operator $\hat{L}^2$ and the total squared spin operator $\hat{S}^2$ commutes with the new Hamiltonian, which means that the total angular momentum and the total spin momentum are numbers which adequately describe the number of different electronic states. In rare-earths, the Coulomb energy separation is on the order of $\sim 10^4$ cm^{-1} (~ 1 eV).

Spin-orbit interaction

The spin-orbit term designates the interaction between two electrons due to the magnetic dipolar interaction of their spin. An analogous description of this interaction can be seen as two magnets attracting or repulsing each-others depending on their distance and the orientation of their poles. We have:

$$\hat{H}_{Spin-orbit} = \sum_{i=1}^{N} \zeta_i l_i.s_i \tag{2.6}$$

Where ζ is the spin-orbit interaction constant, l the angular momentum and s the magnetic spin momentum of the considered electron. Under the spin orbit coupling, there is no longer degeneracy of the spin component, and the "good" quantum numbers which describes the number of states are n, L/m_L, S/m_S, J/m_J. An energy state is then labelled in the Russel-Saunders spectroscopic notation $^{2(S+1)}L_J$. In rare-earths, the spin-orbit energy separation is on the order of $\sim 10^3$ cm^{-1} (~ 0.1 eV).

Crystal field interaction

The number of sub-levels due to crystal field interaction depends on the value of J and the symmetry of the surrounding matrix. If J is half integer, which means that n is odd, Kramer's degeneracy theorem states that each Stark level is at least two fold degenerate, hence there are a maximum of $(2J+1)/2$ sub-levels. The total number of Stark sub-levels

for odd electrons rare-earth ions is given in Table 2.1.

n odd: Ce^{3+}, Nd^{3+}, Sm^{3+}, Gd^{3+}, Dy^{3+}, Er^{3+}, Yb^{3+}		J value:								
		$\frac{1}{2}$	$\frac{3}{2}$	$\frac{5}{2}$	$\frac{7}{2}$	$\frac{9}{2}$	$\frac{11}{2}$	$\frac{13}{2}$	$\frac{15}{2}$	$\frac{17}{2}$
Local symmetry:	Schönflies designation:	Number of Stark sub-levels:								
Cubic	O_h, T_d, O, T_h, T	1	1	2	3	3	4	5	5	6
Other symmetries		1	2	3	4	5	6	7	8	9
Amorphous		1	2	3	4	5	6	7	8	9

Table 2.1: *Number of Stark sub-levels for trivalent rare-earth ions with an odd number of electrons as a function of the matrix local symmetry.*

If J is integer, which means that n is even, the number of sub-levels depends on the host symmetry, more precisely on the number of irreducible representations of the crystal symmetry group. For low symmetry or amorphous hosts, Stark sub-levels degeneracy is entirely lifted. In that case the number of sub-levels is maximal and equal to $2J + 1$. The total number of Stark sub-levels for even electrons rare-earth ions is given in Table 2.2.

n even: Pr^{3+}, Pm^{3+}, Eu^{3+}, Tb^{3+}, Ho^{3+}, Tm^{3+}, Yb^{2+}		J value:								
		0	1	2	3	4	5	6	7	8
Local symmetry:	Schönflies designation:	Number of Stark sub-levels:								
Cubic	O_h, T_d, O, T_h, T	1	1	2	3	4	4	6	6	7
Hexagonal	$D_{6h}, D_{3h}, C_{6v}, D_6, C_{6h}, C_{3h}, C_6$	1	2	3	5	6	7	9	10	11
Trigonal	$D_{3d}, C_{3v}, D_3, C_{3i}, C_3$	1	2	3	5	6	7	9	10	11
Tetragonal	$D_{4h}, D_{2d}, C_{4v}, D_4, C_{4h}, S_4, C_4$	1	2	4	5	7	8	10	11	13
Orthorhombic	D_{2h}, C_{2v}, D_2	1	3	5	7	9	11	13	15	17
Monoclinic	C_{2h}, C_s, C_2	1	3	5	7	9	11	13	15	17
Triclinic	C_i, C_1	1	3	5	7	9	11	13	15	17
Amorphous		1	3	5	7	9	11	13	15	17

Table 2.2: *Number of Stark sub-levels for trivalent rare-earth ions with an even number of electrons as a function of the matrix local symmetry.*

In rare-earths the crystal field energy separation is on the order of $\sim 10^2$ cm^{-1} (~ 0.01 eV), at the difference of transition metal doped crystals (such as Ti:sapphire) or transition metal complexes were it is much higher, on the order of $\sim 10^4$ cm^{-1}. One of the most remarkable property of rare-earths doped solids is that due to the weak crystal field energy splitting, the energy levels don't differ much, whatever the crystal matrix is considered. That weak interaction with the surrounding atoms translates as well to a small homogeneous broadening and sharp emission lines.

Total electronic structure

Combining the perturbations from the central field, Coulomb interaction, spin-orbit interaction and crystal field, one gets the Hamiltonian for a rare-earth ion embedded into a solid matrix describing the energy of an electron in the 4f shell. Diagonalization of the

Hamiltonian allows to find the energy levels, solutions of the time-independent Schrödinger equation:

$$\hat{H}_{Matrix-ion}\psi(\vec{r},\vec{\theta},\vec{\phi}) = E\psi(\vec{r},\vec{\theta},\vec{\phi}) \tag{2.7}$$

Where ψ is a wave-function describing the probability density of finding an electron at position $(\vec{r},\vec{\theta},\vec{\phi})$ in spherical coordinates.

The total electronic structure of 4f states in rare-earth doped solids is schematized in Figure 2.6 with the energy order of each interaction.

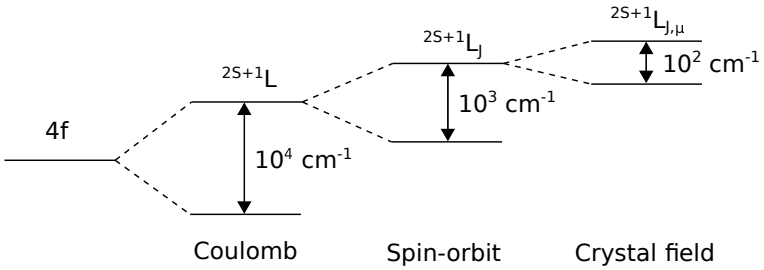

Figure 2.6: *Electronic structure of rare-earths doped solids.*

The 4f structure of every rare-earth ions was studied following this approach for the first time by Dieke and Crosswhite in 1963 [18]. The comparison between theoretical levels and observed energy levels allows to fit the parameters describing the coupling terms and the crystal field strength, for each rare-earth ion and each matrix. The approximate position of observed 4f energy levels in trivalent rare-earths doped solids is shown in Figure 2.8. Our system of interest, Yb:YLF, features one of the simplest structure, as shown in Figure 2.17.

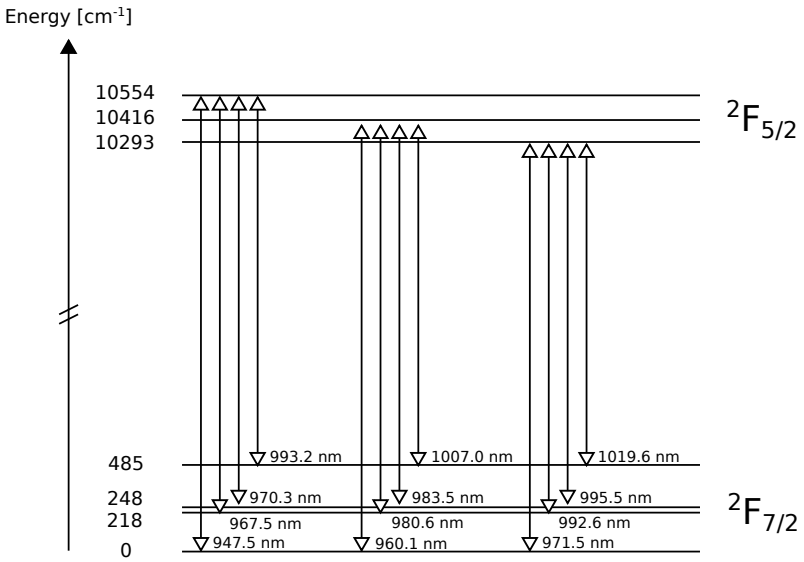

Figure 2.7: *Schematic of the observed energy levels of Ytterbium doped $YLiF_4$ crystals (Yb:YLF). It is one of the simplest systems with only two Stark manifolds, containing 4 levels in the ground manifold $^2F_{7/2}$ and 3 levels in the excited manifold $^2F_{5/2}$.*

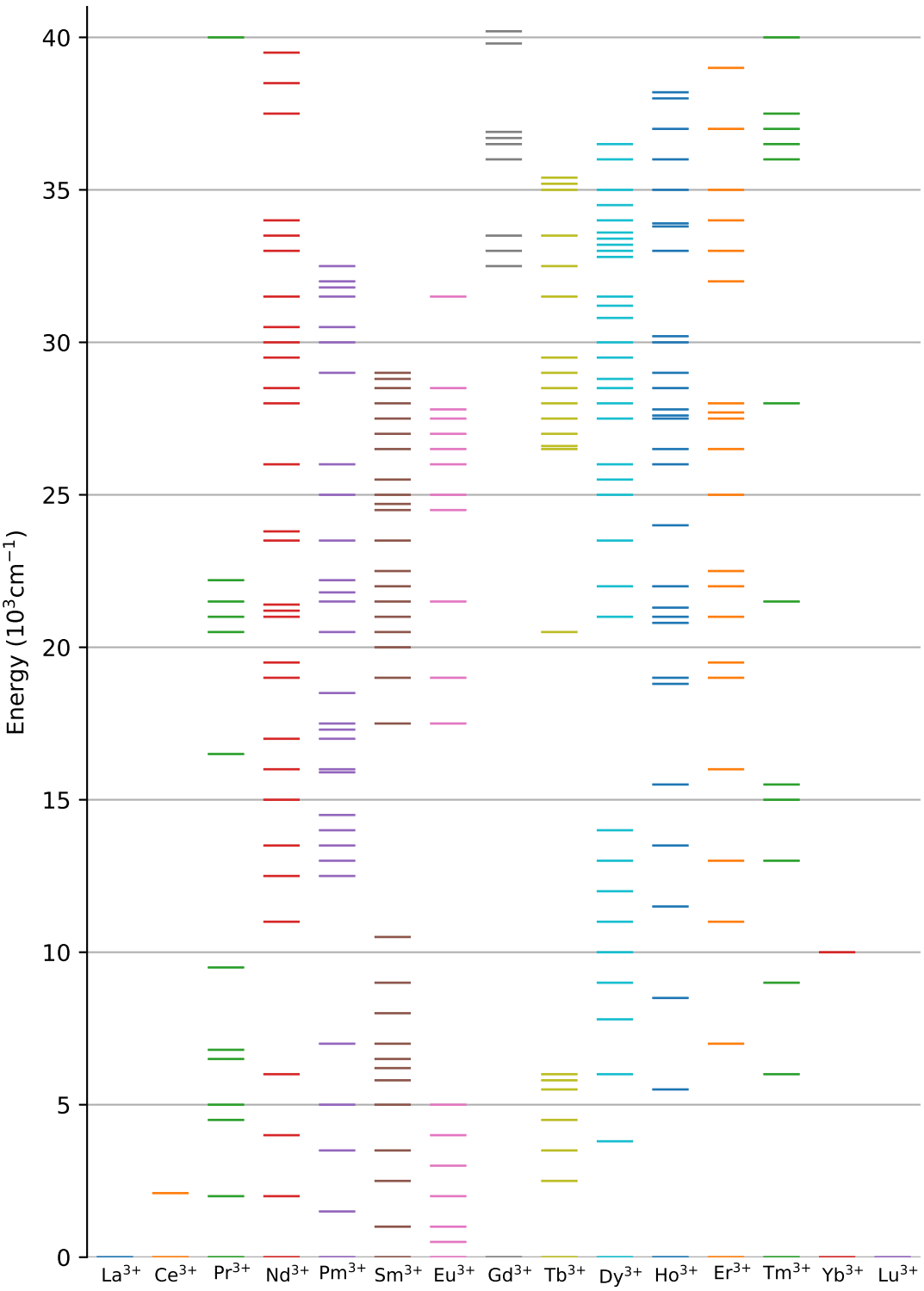

Figure 2.8: *Approximated position of 4f energy levels in rare-earths doped solids, adapted from Dieke's diagram [18]. Remarkably, due to the weak interaction of the crystal field on 4f orbitals, these levels are always around the same positions whatever the crystal matrix studied.*

Absorption and emission spectra

Due to the shielding of 4f electronic states, there is little interaction between these states and the surrounding matrix electric field. Hence, rare-earths ions in matrix behaves almost as free-ion and they feature spectral lines broadening dominated by homogeneous broadening resulting from interaction with phonons (vibrations of the atomic lattice), an effect which decreases with temperature. Absorption and emission spectra of rare-earths doped solids possess sharp lines even at high temperature compared to semi-conductors or transition metal doped solids.

Absorption cross-sections of rare-earths doped crystals are easily accessible by scanning the transmission of a sample over the range of wavelengths corresponding to an absorption band. This is achieved typically inside a spectro-photometer which uses a monochromator for that purpose. Another option is to measure the transmission of a tunable laser beam. However, both options might be costly in the infrared, where monochromators, detectors and laser sources are not as common as in the UV-visible range.

In some cases it is hence convenient to predict the absorption and emission features of rare-earths doped materials. Absorption and emission properties can be calculated using a formalism know as Judd-Ofelt theory. According to this theory, the oscillator strength associated to the intensity of 4f-4f electric dipole transitions can be expressed as:

$$f_{ED} = \frac{8\pi^2 m_e}{3h}\frac{v}{(2J+1)}\frac{\chi_{ED}}{n}\sum_{\lambda=2,4,6}\Omega_\lambda| < l^N, S, L, J|U^\lambda|l^N, S', L', J' > |^2 \tag{2.8}$$

And the oscillator strength associated to magnetic dipole transitions can be expressed as:

$$f_{MD} = \frac{h\nu}{6m_e c^2}\frac{n}{2J+1}| < l^N, S, L, J|L + gS|l^N, S', L', J' > |^2 \tag{2.9}$$

Where the parameters Ω are fitted from the experiment using real absorption or emission cross sections. Judd-Ofelt theory allows then to simulate the full absorption and emission spectra, providing generally good agreement with observed spectra. A more exhaustive detail of rare-earth electronic properties and Judd-Ofelt theory can be found in reference [19]. The software RELIC (Rare Earth Level and Intensity Calculations) from the Los Alamos National Lab allows to compute the Judd-Ofelt parameters from absorption/emission data [20].

2.3 Theory of Anti-Stokes cooling in rare-earths doped crystals

Cooling in rare-earths doped materials is achieved by stimulating Anti-Stokes emission preferably over the Stokes emission, which generates heat in the material. For this purpose, it is necessary to excite the material near the gap energy between ground and excited states, such that the energy which is re-emitted is superior to that which was absorbed. In this section, we establish an approximate and widely adopted formula for the cooling efficiency under the four-levels model as a function of the Anti-Stokes shift, the material absorption, the parasitic absorption and the external quantum efficiency. We show that cooling can only be achieved in excellent quality crystals.

2.3.1 The ideal cooling model

In an ideal Anti-Stokes cooling cycle, photons with energy $h\nu$ are first absorbed by the rare-earths ions, populating the excited state electronic manifold. They thermalize quickly by the absorption of phonons with a time constant on the order of $\tau_{phonon} = 10^{-12}$ s. Then, the electrons decay radiatively back to the ground energy state with the emission of a photon with mean fluorescence energy $h\nu_f$ with a much longer time constant $\tau_{fluo} = 10^{-3}$ s characteristic of fluorescence in rare-earths doped crystals.

If we consider this simple process, the cooling power is equal to the difference between absorbed and emitted power:

$$P_{cool} = h\nu_f - h\nu \tag{2.10}$$

And the cooling efficiency is simply the ratio of the cooling power over the absorbed power:

$$\eta_c = \frac{P_{cool}}{P_{abs}} = \frac{h\nu - h\nu_f}{h\nu} = \frac{\lambda_f - \lambda}{\lambda_f} \tag{2.11}$$

With the mean fluorescence frequency ν_f defined as:

$$\nu_f = \frac{\int \nu\phi(\nu)d\nu}{\int \phi(\nu)d\nu} \tag{2.12}$$

Here $\phi(\nu)$ is the emitted spectral flux expressed in terms of photons per units of frequency, which as some authors point out should not be confused with $S(\nu)$ the emitted

spectral flux in terms of power per units of frequency. The measurable quantity being $S(\lambda)$, we have the relationship:

$$S(\lambda) = \frac{hc}{\lambda}\phi(\lambda) = \frac{hc}{\lambda}\phi(\nu)\frac{d\nu}{d\lambda} \tag{2.13}$$

Knowing that $\frac{d\nu}{d\lambda} = \frac{c}{\lambda^2}$, we have:

$$S(\lambda) = \frac{hc^2}{\lambda^3}\phi(\nu) \tag{2.14}$$

The definition of the mean fluorescence frequency can be transformed to express the mean fluorescence wavelength instead. We have:

$$E_f = h\nu_f = \frac{\int \nu\phi(\nu)d\nu}{\int \phi(\nu)d\nu} = \frac{\int \frac{hc}{\lambda}\frac{\lambda}{hc}S(\lambda)\frac{d\lambda}{d\nu}d\nu}{\int \frac{\lambda}{hc}S(\lambda)\frac{d\lambda}{d\nu}d\nu} = hc\frac{\int S(\lambda)d\lambda}{\int \lambda S(\lambda)d\lambda} = \frac{hc}{\lambda_f} \tag{2.15}$$

And hence the mean fluorescence wavelength is equal to:

$$\lambda_f = \frac{\int \lambda S(\lambda)d\lambda}{\int S(\lambda)d\lambda} \tag{2.16}$$

According to the equation of cooling efficiency, in the ideal model, there would be no limit on the achievable cooling efficiency which would tend to infinity as the laser pump wavelength tends to long wavelengths, as shown in Figure 2.9.

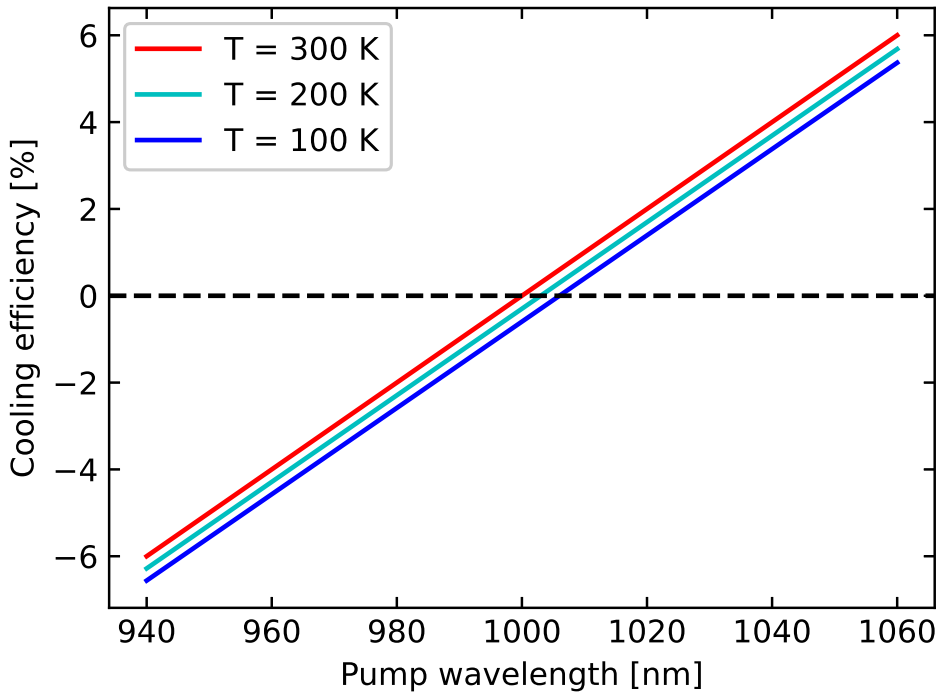

Figure 2.9: *Ideal cooling efficiency of the Anti-Stokes process as a function of laser pump wavelength, plotted for 10% Yb:YLF assuming mean fluorescence wavelength of 1000 nm at 300K, 1003 nm at 200 K, and 1006 nm at 100 K.*

The decrease of cooling efficiency due solely to Anti-Stokes red-shift with decreasing temperature can be observed as well: for Ytterbium, at a given pump wavelength there is a reduction of only 0.7 % between ideal cooling efficiency at ambient temperature and ideal cooling efficiency at 100 K.

However, this very simple model does not take into account two parameters which limit in practice the Anti-Stokes cooling efficiency:

- The background absorption associated to impurities in the material which absorbs the fluorescence photons and convert them to heat.
- The external quantum efficiency, which is defined as the probability that an absorbed photon is re-emitted and escapes out of the material. EQE accounts for two effects: non-radiative decays inside the material due to phonons, and fluorescence trapping of the photons within the material due to re-absorption processes and internal reflections at the crystal's interfaces.

2.3.2 The four levels model

To refine the study of Anti-Stokes cooling, we define the four levels model schematized in Figure 2.10 as a simplification from the exact structure of Yb:YLF presented before.

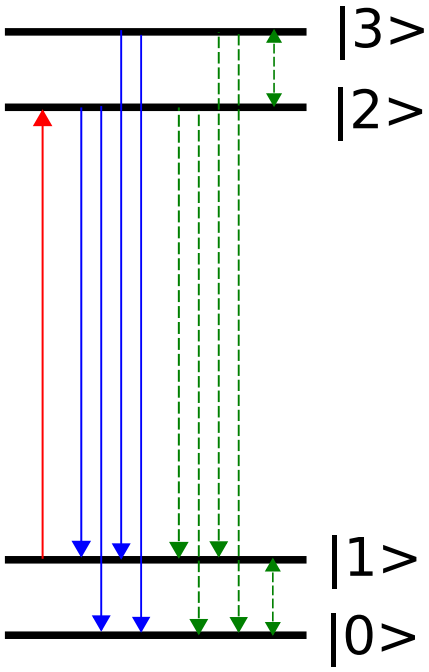

Figure 2.10: *Energy diagram of the four levels model of Anti-Stokes cooling.*

In this model, there are two states $|0>$ and $|1>$ corresponding to the ground manifold of a rare-earth ion, and two states $|2>$ and $|3>$ corresponding to the excited manifold.

We consider a laser pump excitation at the gap energy which induces stimulated emission of level $|2>$ to level $|1>$. Spontaneous emission occurs between each excited state to each ground state, as well as non-radiative decay. We consider that there is a non-radiative probability to go from state 0 to 1 and state 2 to 3 due to thermal energy following Boltzmann's distribution, and a non radiative decay rate from 1 to 0 and 3 to 2 with the creation of phonons.

Radiative transitions between same Stark manifolds (e.g. from 1 to 0 and from 3 to 2) are not considered, as they are forbidden by Laporte's rule based on parity of the orbitals. In practice those transitions are allowed only under external magnetic field which is not the case here.

Based on Einstein's rate equations for transitions between energy levels, we have:

$$\begin{aligned}\frac{dN_0}{dt} &= W_{20r}N_2 + W_{20nr}N_2 + W_{30r}N_3 \\ &+W_{30nr}N_3 + w_1N_1 - w_1N_0\rho_g(T)\end{aligned} \tag{2.17}$$

$$\begin{aligned}\frac{dN_1}{dt} &= -B_{12}N_1\rho_l + B_{21}N_2\rho_l + W_{21r}N_2 + W_{21nr}N_2 + W_{31r}N_3 \\ &+W_{31nr}N_3 - w_1N_1 + w_1N_0\rho_g(T)\end{aligned} \tag{2.18}$$

$$\begin{aligned}\frac{dN_2}{dt} &= B_{12}N_1\rho_l - B_{21}N_2\rho_l - W_{21r}N_2 - W_{21nr}N_2 - W_{20r}N_2 \\ &-W_{20nr}N_2 - W_{23nr}N_2 + w_2N_3 - w_2N_2\rho_u(T)\end{aligned} \tag{2.19}$$

$$\begin{aligned}\frac{dN_3}{dt} &= -W_{31r}N_3 - W_{31nr}N_3 - W_{30r}N_3 \\ &-W_{30nr}N_3 - w_2N_3 + w_2N_2\rho_u(T)\end{aligned} \tag{2.20}$$

And the conservation of total population:

$$N_{tot} = N_0 + N_1 + N_2 + N_3 \tag{2.21}$$

$$\frac{dN_{tot}}{dt} = 0 \tag{2.22}$$

Where we have the following parameters:

- N_i the electronic population in state i and $\frac{dN_i}{dt}$ the corresponding variation of that state's population as a function of time.
- B_{ij} the coefficient of absorption and B_{ji} the coefficient of stimulated emission.
- W_{ijr} the coefficient of spontaneous emission from state i to state j (also known as A_{ij} Einstein coefficients).
- W_{ijnr} the coefficient of non-radiative decay from state i to state j.
- w_i the electron phonon interaction coefficient for state i.
- ρ_l the pump light (laser) energy density and $\rho(T)$ the energy density corresponding to thermalization following Boltzmann distribution.

According to Boltzmann's statistics, the distribution of electrons in ground and upper levels evolves according to the equations:

$$\rho_g(T) = \frac{g_1}{g_0} e^{-\delta E_g / k_B T} \tag{2.23}$$

$$\rho_u(T) = \frac{g_3}{g_2} e^{-\delta E_u / k_B T} \tag{2.24}$$

The rate equations can be simplified and expressed as a function of directly measurable terms. For a system where level i possess a degeneracy g_i and level j a degeneracy g_j, we have the following relationship between B_{ij} and B_{ji}:

$$g_i B_{ij} = g_j B_{ji} \tag{2.25}$$

The Einstein coefficients B_{ij} are linked to the absorption cross section σ_{ij} by the relationship:

$$\sigma_{ij} = B_{ij} \frac{h\nu}{c} \tag{2.26}$$

The pump laser energy density can be expressed as a function of the local intensity by the relationship:

$$\rho_l = \frac{I}{c} \tag{2.27}$$

By performing those simplifications, approximating all the radiative decay terms W_{ijr} equal to the same value W_r and all the non-radiative decay terms W_{ijnr} equal to the same value W_{nr}, the rate equations can be re-written in the same fashion as reference [21]:

$$\frac{dN_0}{dt} = \frac{R}{2}(N_2 + N_3) + w_1(N_1 - \frac{g_1}{g_0}N_0 e^{-\delta E_g/k_B T}) \tag{2.28}$$

$$\frac{dN_1}{dt} = -\sigma_{12}(N_1 - \frac{g_1}{g2}N_2)\frac{I}{h\nu} + \frac{R}{2}(N_2 + N_3) - w_1(N_1 - \frac{g_1}{g_0}N_0 e^{-\delta E_g/k_B T}) \tag{2.29}$$

$$\frac{dN_2}{dt} = \sigma_{12}(N_1 - \frac{g_1}{g2}N_2)\frac{I}{h\nu} - RN_2 + w_2(N_3 - \frac{g_3}{g_2}N_2 e^{-\delta E_u/k_B T}) \tag{2.30}$$

$$\frac{dN_3}{dt} = -RN_3 - w_2(N_3 - \frac{g_3}{g_2}N_2 e^{-\delta E_u/k_B T}) \tag{2.31}$$

$$N_{tot} = N_0 + N_1 + N_2 + N_3 \tag{2.32}$$

Where $R = 2W_r + 2W_{nr}$. The power deposited in the system P_{net} is expressed as the difference between absorbed and radiated contributions:

$$P_{net} = \sigma_{12}N_1 I - \frac{g_1 N_2}{g_2 N_1}I - W_r[N_2(E_{21} + E_{20}) + N_3(E_{31} + E_{30})] + a_b I \tag{2.33}$$

Now let us look for solution in when the system has reached thermal equilibrium. In steady state conditions, the N_i derivatives equal to zero:

$$\frac{dN_0}{dt} = \frac{dN_1}{dt} = \frac{dN_2}{dt} = \frac{dN_3}{dt} = 0 \tag{2.34}$$

By solving the populations equations, we can re-write the deposited power as :

$$P_{net} = a_b I + a_r I[1 - \frac{h\nu_f}{h\nu}(\frac{\eta_e W_r}{\eta_e W_r + W_{nr}})] \tag{2.35}$$

Where we define here the external quantum efficiency, ratio of the photons exiting the system over those who are trapped inside, either due to total internal-reflection or re-absorption:

$$\boxed{\eta_{ext} = \frac{\eta_e W_r}{\eta_e W_r + W_{nr}}} \tag{2.36}$$

In this model, the mean fluorescence energy is defined as:

$$h\nu_f = h\nu + \frac{\delta E_g}{2} + \frac{\delta E_u}{1 + (1 + R/w_2)e^{\delta E_u / k_B T}} \tag{2.37}$$

The resonant absorption is expressed:

$$a_r = \frac{\sigma_{12} N_t}{(1 + e^{\delta E_g / k_B T})} \tag{2.38}$$

Assuming an incident laser power absorbed :

$$P_{abs} = P_0 \frac{a_r}{a_r + a_b}(1 - e^{-a_{tot} L}) + P_0 \frac{a_b}{a_r + a_b}(1 - e^{-a_{tot} L}) \tag{2.39}$$

Equation 2.26 can be expressed as :

$$P_{net} = P_0(1 - e^{-a_{tot} L})(a_r - a_r \eta_{ext} \frac{\lambda}{\lambda_f})/(a_r + a_b) \tag{2.40}$$

The absorbed power supplied to the system contributes to cooling with efficiency η_{cool} and we have the equation:

$$P_{net} = P_{abs} \eta_{cool} \tag{2.41}$$

Identifying for η_{cool} yields the expression:

$$\eta_{cool} = (a_r - a_r \eta_{ext} \frac{\lambda}{\lambda_f})/(a_r + a_b) = 1 - \eta_{ext} \frac{\lambda}{\lambda_f} \frac{a_r}{a_r + a_b} \tag{2.42}$$

We can define the absorption efficiency η_{abs} as:

$$\boxed{\eta_{abs} = \frac{a_r}{a_r + a_b}} \tag{2.43}$$

And the cooling efficiency η_{cool} in the 4-levels model can be finally expressed as:

$$\boxed{\eta_{cool} = \eta_{ext}\eta_{abs}\frac{\lambda}{\lambda_f} - 1} \tag{2.44}$$

Where η_{cool} is defined positive for cooling and negative for heating.

Although we neglected the fine structure of our manifolds and effects linked to saturation intensity, the cooling efficiency in the 4-levels model allows to reproduce the most important features of Anti-Stokes cooling. Following Eq. (2.44), we can derive the condition for cooling to happen. Assuming that the extracted energy is on the order of k_BT each time the cooling cycle happens, the Anti-Stokes shift term becomes:

$$\frac{\lambda}{\lambda_f} = \frac{E_f}{E} = \frac{E + k_BT}{E} = 1 + \frac{k_BT}{h\nu} \tag{2.45}$$

And cooling efficiency becomes:

$$\eta_{cool} = \eta_{ext}\eta_{abs}(1 + \frac{k_BT}{h\nu}) - 1 \tag{2.46}$$

By definition, cooling efficiency should be positive to get cooling, and we have the inequality:

$$\eta_{ext}\eta_{abs}(1 + \frac{k_BT}{h\nu}) > 1 \tag{2.47}$$

Equivalent to:

$$\eta_{ext}\eta_{abs} > \frac{1}{(1 + \frac{k_BT}{h\nu})} \tag{2.48}$$

Assuming a cooling cycle such as Yb:YLF, with a gap around 1020 nm, we can calculate the minimal value of the product $\eta_{ext}\eta_{abs}$ for which there is cooling, as shown in Figure 2.11. At room temperature, it should be no less than 98%, while at cryogenics temperatures, it should exceed 99%.

These results highlight the need for exquisite materials with low impurities and high external quantum efficiency in order to reach the best cooling performances. In practice, typical external quantum efficiencies range from 98.5 % to 99.5 % in Yb:YLF, with a total number of impurities around 10 ppm, leading to background absorption values on the order of 10^{-4} cm^{-1}.

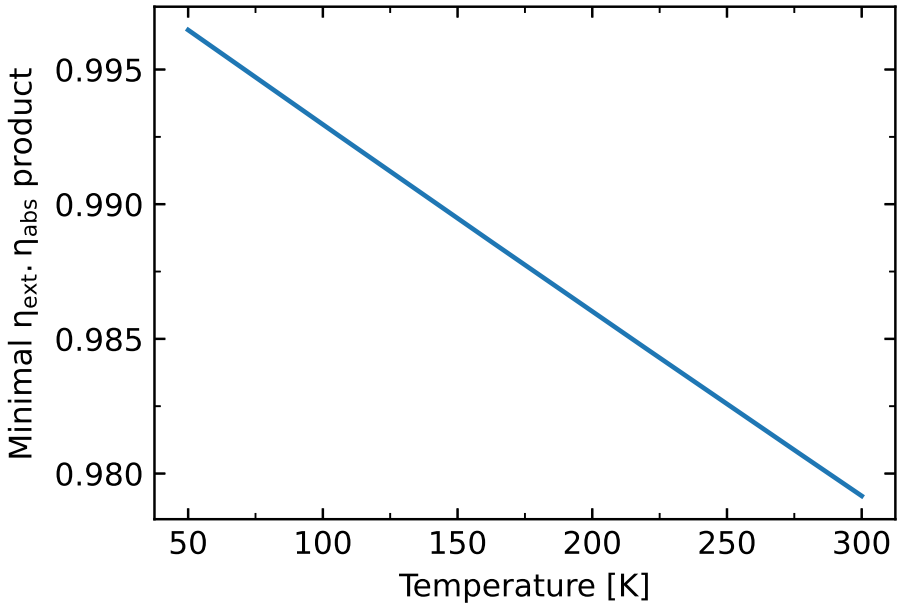

Figure 2.11: *Lowest values allowed for the product $\eta_{ext}.\eta_{abs}$ in order to get net cooling with the Anti-Stokes fluorescence process. Calculation assumes an Yb^{3+} doped system with energy gap at 1020 nm.*

2.4 Anti-Stokes cooling in Yb:YLF

2.4.1 YLF matrix properties

$YLiF_4$, abbreviated YLF is a common crystal used for laser applications as gain media. It is currently the record setting crystal type for laser cooling in solids. Its general properties are given in table Table A.1. Compared to other crystals, YLF possess relatively high thermal conductivity with low thermal expansion coefficients which produces reduced thermal lens effect when used in laser cavities. It is also non-hygroscopic as opposed to other optical refrigeration materials such as ZBLAN glasses [22], which allows for high durability.

Crystal structure

The YLF crystal unit cell is shown in Figure 2.12. It belongs to the tetragonal body centered group. In tetragonal arrangement, the lattice has two sides of equal length along $\vec{a}$ directions and one side with a different length along $\vec{c}$ direction. Reported values in YLF are $a = 0.5197$ nm and $c = 1.0735$ nm [23].From a symmetry point of view, the crystal belongs to the scheelite type with crystallographic $I4_{1/a}$ space group.

A tetragonal structure means that the crystal is uniaxial: light traveling in the $\vec{a}$ directions will interact with different electric dipoles than light traveling in $\vec{c}$ direction. The crystal is hence birefringent, with ordinary optical index n_o for light traveling in direction parallel to $\vec{c}$ and extraordinary index n_e for light in the direction $\vec{a}$.

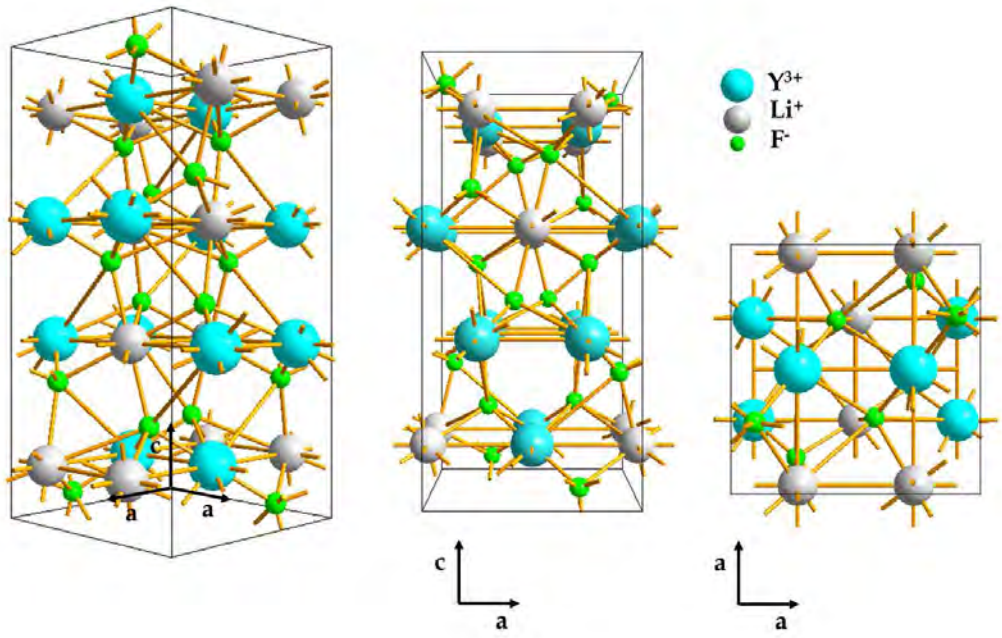

Figure 2.12: *Schematic of the YLF atomic lattice, from reference [24]. Dielectric $\vec{a}$ and $\vec{c}$ axes are indicated.*

Crystal growth

Like all laser crystals, YLF is a synthesis material manufactured by crystal growth in special furnaces. YLiF4 can be obtained by melting a mixture of LiF and YF3 powders. However, one must take some precautions in the process with the proportions of base powders. Figure 2.13 shows the phase diagram of the LiF - YF3 mixture as a function of the mixture temperature and YF3 concentration. The base growth concept goes as follows: LiF and YF3 are melted in a crucible until reaching an homogeneous liquid phase. The temperature is then lowered until reaching the solid LiYF4 formation temperature, shown as the red boundary in the diagram. The particularity is that YF3 concentration cannot be allowed to be in stoichiometric proportions with LiF. YF3 concentration should stay within the range [20 % - 48 %] at all times during the growth. Below 20 % one would crystallize solid LiF, while above 48 % we would crystallize YF3. LiF will hence be in excess at all times during the growth. The more YF3 is consumed to form LiYF4, the more its proportion compared to LiF will decrease. The growth will hence follow the solid red line until reaching the 20% lower YF3 concentration where LiF is formed.

We see that in order to obtain good quality, defect free crystals, precise temperature control of the melt should be ensured as the melting temperature will also decrease during the growth. Good homogeneity of the melt should also be ensured to avoid local formation of solid LiF or YF3 grains. In practice, YLF crystals are traditionally prepared following three different methods.

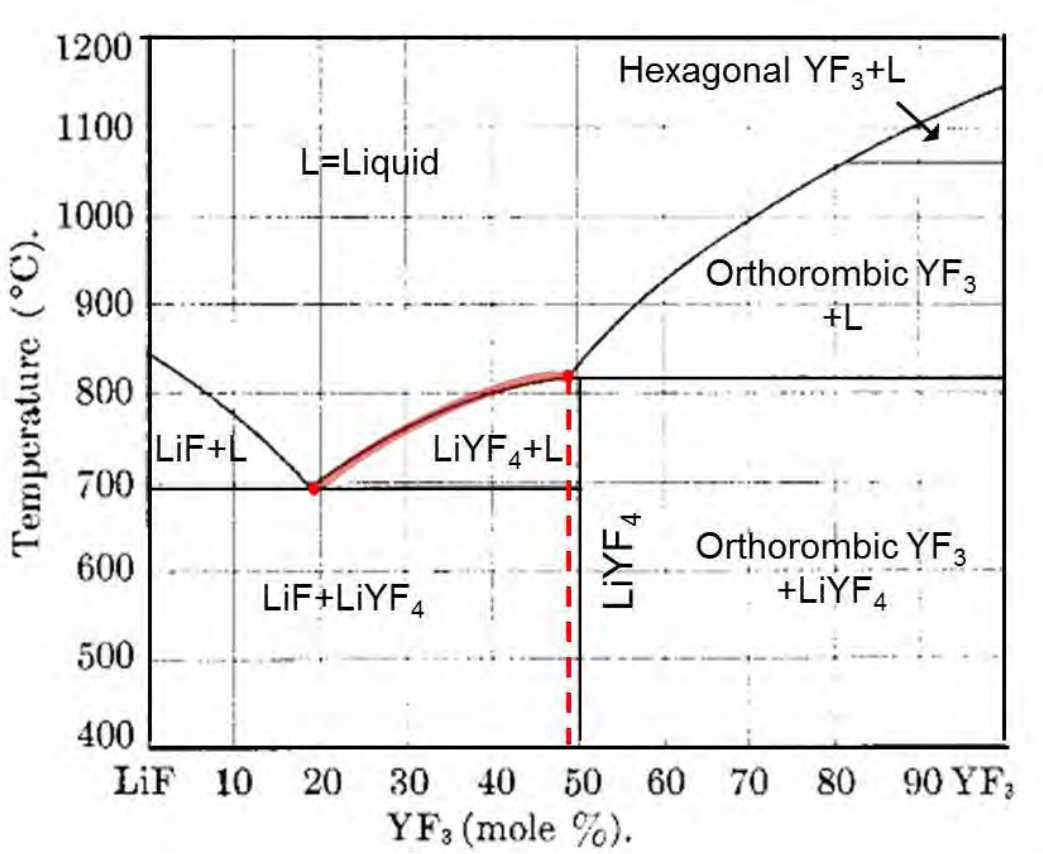

Figure 2.13: *Phase diagram of the LiF-YF_3 mixture, from reference [24]. The dashed red line indicates the maximal YF_3 concentration allowable in the mixture in order to obtain pure $LiYF_4$.*

The Czochralski method features the melting of YLF base constituents, either resistively or by electromagnetic induction inside a static crucible (Figure 2.14). At the University of Pisa, Czochralski growth is of the resistive type, with a platinum crucible is located inside a furnace, at the center of a large resistive heater. To avoid dust contaminants and oxidation, the setup is kept under inert Argon and CF_4 atmosphere mixed in equal quantities. During the growth, a high voltage generator is used to power the coil.

To initiate crystallization along the desired crystalline axis, an oriented mono-crystalline YLF seed is approached and dipped at the surface of the melt. It is then pulled-up very slowly, at speeds on the order of 1 mm/h, while being also rotated at speeds around 10 rpm to ensure homogeneity of the melt.

The crystallization speed and hence the boule diameter depends on the melt's temperature. Precise temperature control is achieved by monitoring the meniscus angle between the melt and the growing crystal using a laser and a photodiode. Setting up a PID loop on the photodiode signal allows to regulate the melt temperature with +/- 0.1 °C precision and control the boule diameter with variations of only +/- 0.25 mm. More detailed informations about the particularities of YLF Czochralski growth can be found in references [24] and [25] from University of Pisa.

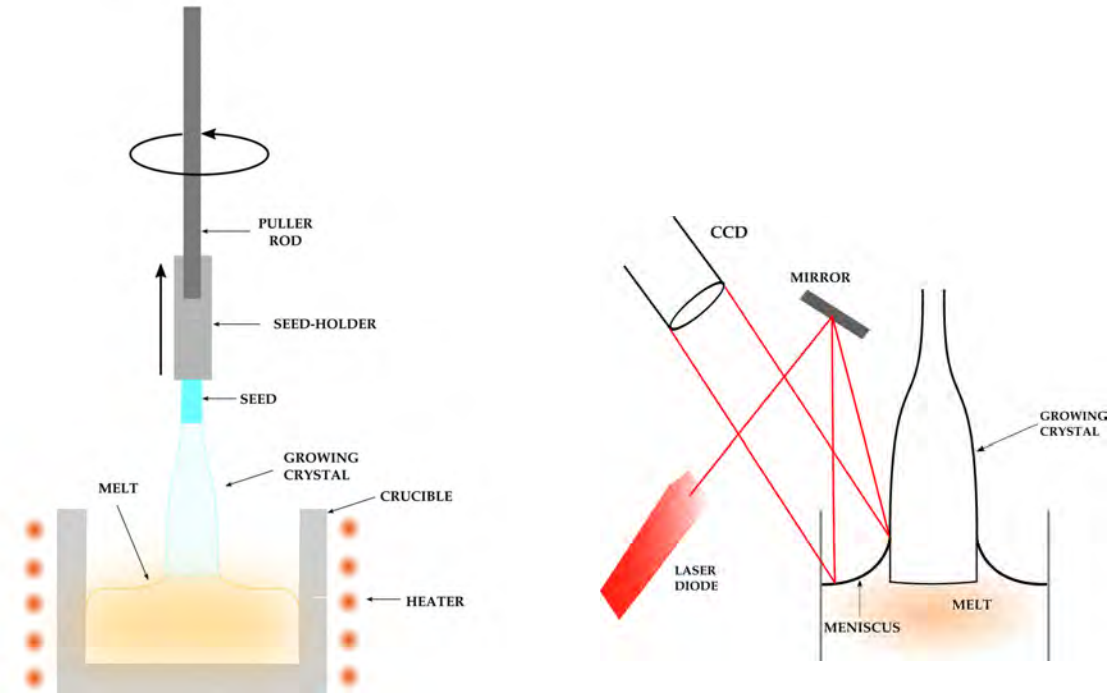

Figure 2.14: *Czochralski growth as performed at the University of Pisa, from reference [24]. Left: Schematic of the growth apparatus. Left: Schematic of the temperature/diameter control method.*

The Bridgman method features also the melting of YLF either by resistance or induction heating, but this time inside and ampoule suspended by a wire and descended in the furnace through the coil (Figure 2.15).

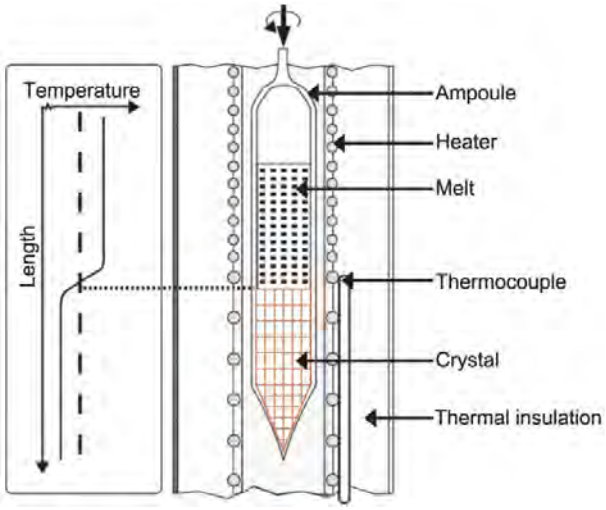

Figure 2.15: *Bridgman growth schematic, from reference [26].*

As stated in reference [27], this method would be suitable for significantly faster growths cycles. The base quantity of raw powders can be typically a few grams to 10 g, allowing for purification methods to be performed. Furthermore, one growth can be performed in only one week instead of two to three weeks with classical Czochralski. The method showed however poor quality, grainy growth in YLF and good results in LuLiF (LLF), attributed to

the incongruent melting behavior of YLF where LLF is congruent and can be grown from stoichiometric quantities.

The micro pulling-down method is used for growing crystal fibers and rods. A crucible with a neck and a hole at its bottom is inductively heated inside a coil. The melt escapes at the bottom of the crucible and crystallize when cooling down (Figure 2.16).

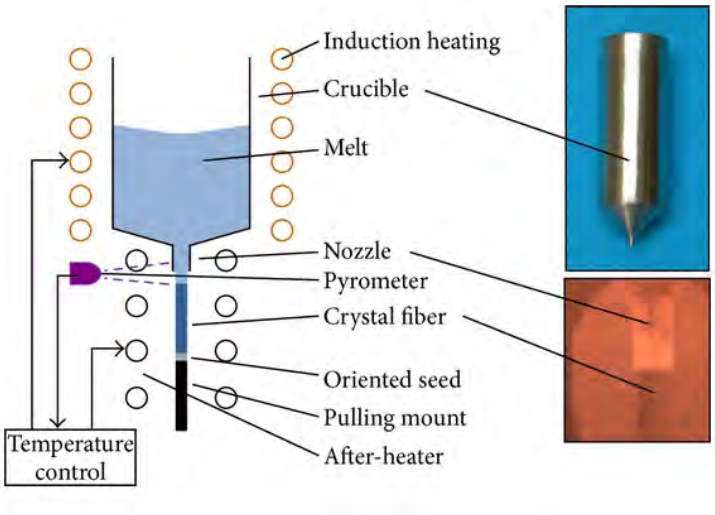

Figure 2.16: *Micro pulling-down growth schematic, from reference [28].*

2.4.2 Electronic properties of Yb:YLF

Energy levels

As stated before, by taking a look at Dieke's diagram (Figure 2.8) we can see that Yb^{3+}, together with Ce^{3+} features the simplest energy structure among rare-earths doped solids as they possess only two Stark manifolds.

The electronic structure of Yb:YLF can be found by applying the atomic structure quantum theory. The value of the principal quantum number n in Yb^{3+} being $n = 4$ and $l = 3$ for the f shell, the total orbital angular momentum L has value 3, the total spin momentum S has value 1/2, hence the total angular momentum in the spin-orbit coupling J takes values J = [l - s ... l+s] = [5/2 ; 7/2]. In the Russell-Saunders notation, we have two manifolds $2F_{5/2}$ and $2F_{7/2}$. According to the Table 2.1 which details the number of Stark multiplets for odd n, in tetragonal YLF symmetry then Yb^{3+} possess 4 levels in the $2F_{7/2}$ ground state and 3 levels in the $2F_{5/2}$ excited state.

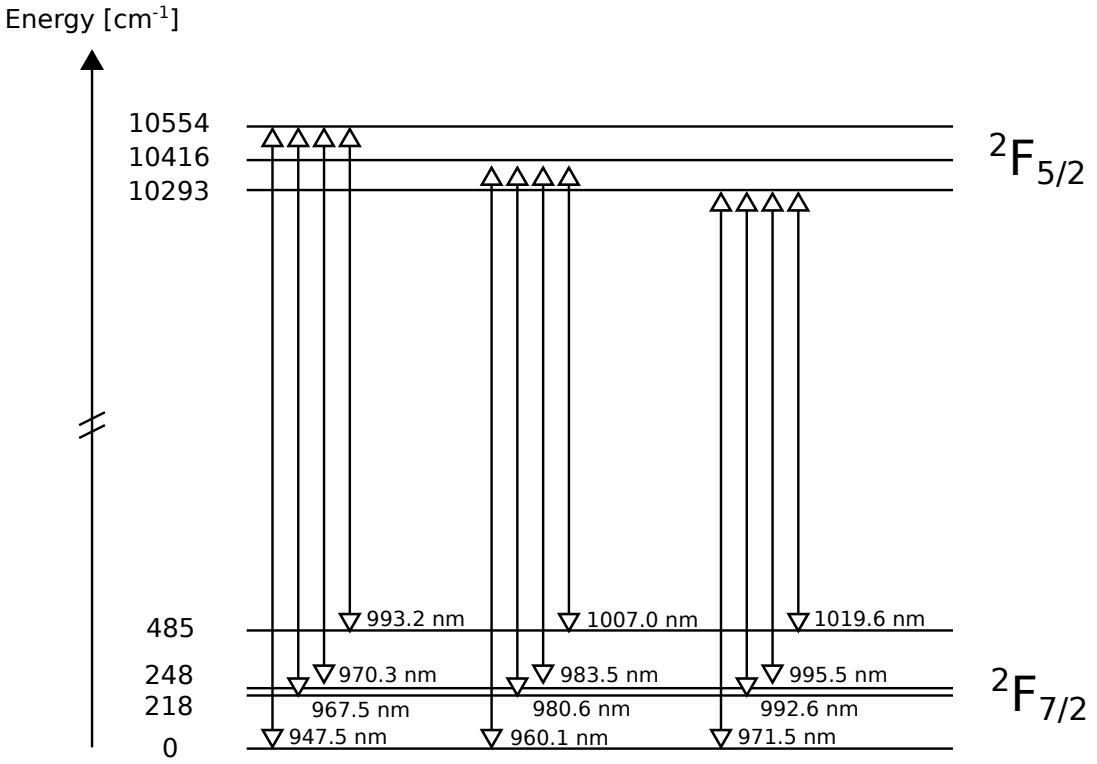

Figure 2.17: *Schematic of the observed energy levels of Ytterbium doped YLiF4 crystals (Yb:YLF). It is one of the simplest systems with only two Stark manifolds, containing 4 levels in the ground manifold $^2F_{7/2}$ and 3 levels in the excited manifold $^2F_{5/2}$.*

Fluorescence lifetime

A particularity of rare-earths is that they have long fluorescence lifetimes, in the order of a few milliseconds. Radiative and non-radiative decay probabilities are related to the lifetime of photons in the excited manifold by the relationship:

$$\tau = \frac{1}{\sum W_r + W_{nr}} \tag{2.49}$$

Where W_r are the radiative probabilities and W_{nr} the non-radiative probabilities . Several mechanisms can affect the excited states lifetimes.

Radiative decay: Radiative decay corresponds to spontaneous emission, Einstein's A coefficient. The probability of radiative decay between two levels depends on the frequency separation, degeneracy and transition type (electric of magnetic dipole) between an initial state ψ_i and final state ψ_f, following the formula:

$$A_{if} = \frac{64\pi^4\nu_{ij}^3}{3hc^3 g_i} | < \psi_j | \hat{P} | \psi_i > |^2 \tag{2.50}$$

Non-radiative decay: Non-radiative decay depends on the electron-phonon interaction. If the gap energy between ground and excited state is small, there is a probability that an excited electron returns to the ground state with the emission of several phonons, heating in the process. The number of phonons emitted in the process is on the order of:

$$p = \Delta E / \hbar \omega_{max} \tag{2.51}$$

With ω_{max} the maximum phonon cut-off energy. Under the model of Riseberg and Moos [29] describing the electron-phonon interaction for trivalent rare-earths ions in glassy matrix, it was demonstrated that the multi-phonon decay rate W decreases exponentially with the gap energy ΔE:

$$W = Ce^{-\alpha \Delta E} \tag{2.52}$$

Where *"C and α are constant which are characteristic of the particular crystal"* [29]. It is commonly admitted now that non-radiative decay are negligible when $\Delta E > 8\hbar\omega_{max}$. In YLF, the cut-off phonon energy is around 350 cm^{-1}, one of the smaller phonon energy among crystal matrix, and well below the energy gap in Yb:YLF on the order of 10000 cm^{-1}.

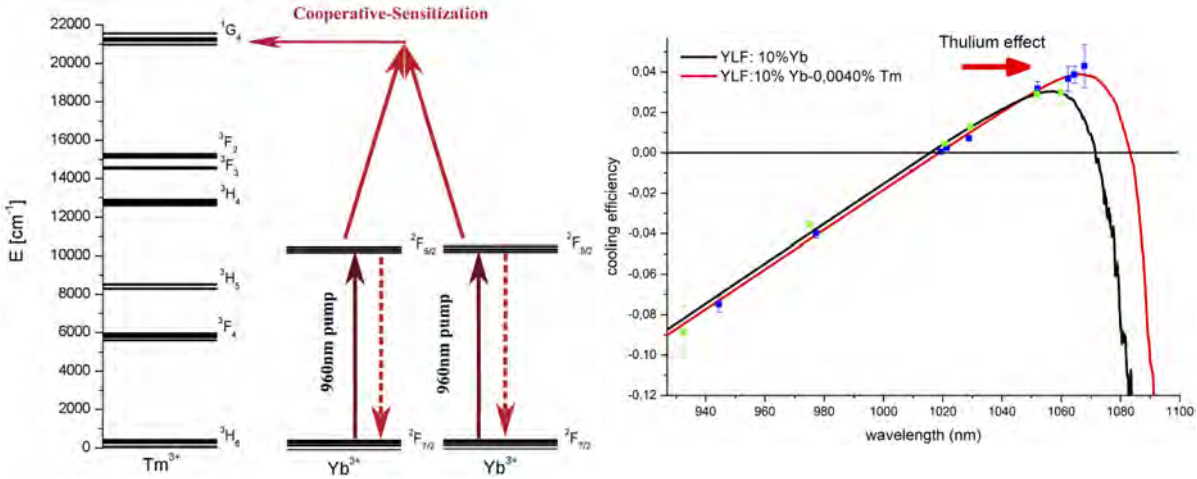

Figure 2.18: *Cooperative-sensitization energy transfer in co-doped Tm,Yb:YLF (left), and observed improvement in cooling efficiency of co-doped 0.004%Tm,10%Yb:YLF compared to 10%Yb:YLF grown from the same raw materials. Figures adapted from reference [30].*

Cooperative mechanisms: These mechanisms involve the combined de-excitation of two rare-earths ions. They are of importance because they add new relaxation channels which can contribute to radiative or non-radiative decays, thus improving or reducing the cooling efficiency process. For example, latest results showed an improvement in cooling efficiency of Yb:YLF when co-doping with Thulium, attributed to the cooperative de-

excitation of two Yb^{3+} ions to excite one Tm^{3+} ion, as shown in Figure 2.18.

Measurements of fluorescence lifetime in Yb:YLF: In the case of single doped Yb:YLF, the radiative lifetime can be measured by exciting the crystal and measuring the delay between the laser emission and the fluorescence emission. For heavily doped samples, the lifetime is affected by fluorescence re-absorption, leading to over-estimated fluorescence lifetimes.

The "pinhole method" allows to measure the intrinsic fluorescence lifetime by performing the lifetime measurement through pinhole masks of known apertures. The extrapolation of these measurements for an infinitely small pinhole allows to recover the intrinsic fluorescence lifetime, as shown in Figure 2.19 measured for 5%Yb:YLF by reference [24].The measured for τ is between 2.1 ms and 2.2 ms, consistent with literature [31].

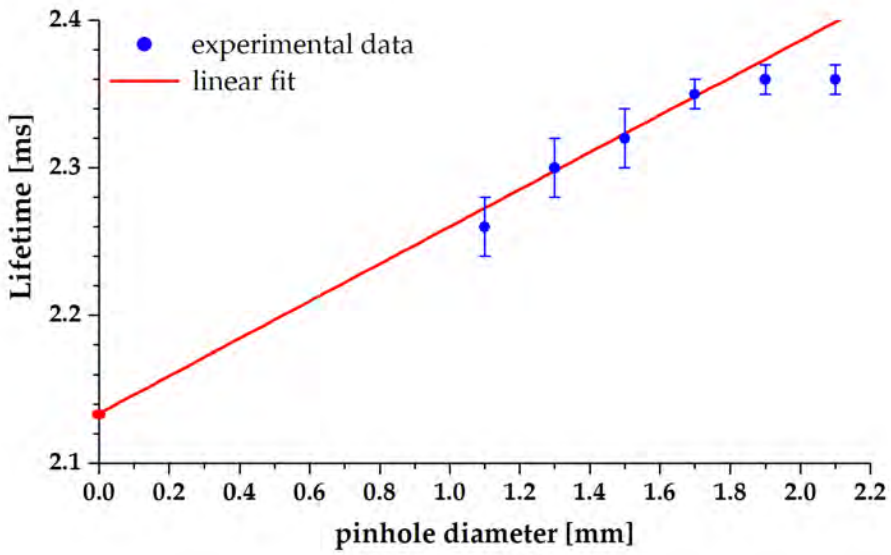

Figure 2.19: *Radiative lifetime in Yb:YLF, measured by the pinhole method in reference [24].*

Additional investigations from reference [32] have highlighted the fact that fluorescence lifetime is a quantity that depends on temperature, due to the electronic population of the excited Stark levels being dependent on temperature following Maxwell-Boltzmann distribution. Fluorescence lifetime as a function of temperature in 5%Yb:YLF is shown in Figure 2.20.

2.4.3 Optical properties

Yb^{3+} emission and absorption bands are located in the near infrared between 950 nm and 1020 nm. Compared to other rare-earths ions, this is an advantage as it is easy to find laser diodes, laser sources and relatively cheap Silicon detectors in the near-infrared for

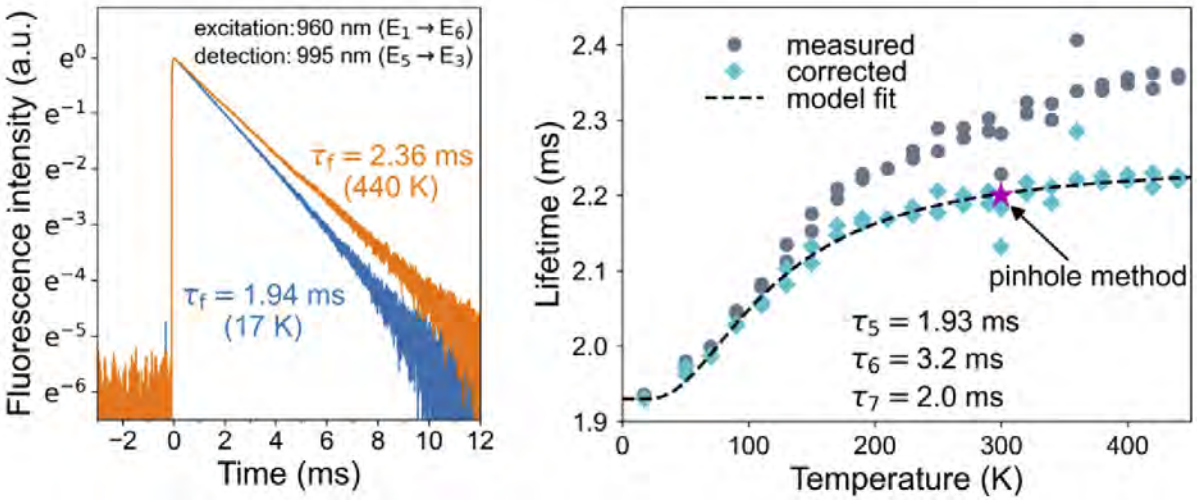

Figure 2.20: *Temperature dependence of the fluorescence lifetime in 5%Yb:YLF, adapted from reference [32]. Left: 5%Yb:YLF measured fluorescence intensity decay as a function of time, for a crystal at 440 K and at 17 K. Right: 5%Yb:YLF fluorescence lifetime as a function of temperature, corrected for re-absorption.* τ_5*,* τ_6 *and* τ_7 *denotes the individual lifetimes of the excited Stark levels* E_5*,* E_6 *and* E_7*.*

the characterization of Yb:YLF optical properties. From the uniaxial symmetry of YLF, Yb^{3+} possess different absorption/emission spectra depending if light is absorbed/seen along direction E$\|$c or direction E$\perp$c, as will be detailed in the following sections.

Absorption properties

Absorption is a measure of transitions to higher energy excited states in matter. There are three related quantities which describes the absorption of a sample: the transmission, which describes the percentage of light which passes through a the sample; the absorption coefficient (in cm^{-1}) which describes the characteristic length over which the absorption happens, and the absorption cross-section (in cm^{-2}) which describes the probability of one photon to be absorbed.

Traditionally, the preferred method to measure the absorption of a sample is by using a spectro-photometer, as shown in Figure 2.21. This type of instrument features a lamp source, providing light over a wide range of wavelengths. A monochromator filters out selectively only one wavelength and send it through two paths. The sample is positioned in one of the paths while the other path is used as reference. The light coming from both paths is then sent on a detector. The signal from the reference path is then subtracted from the sample path to give the sample transmission as a function of wavelength.

The absorption coefficient $\alpha(\lambda, T)$ is related to the transmission $T_{\%}$ of a sample knowing its length l following the Beer-Lambert law:

$$T_{\%} = 100 \times e^{-\alpha(\lambda,T)l} \tag{2.53}$$

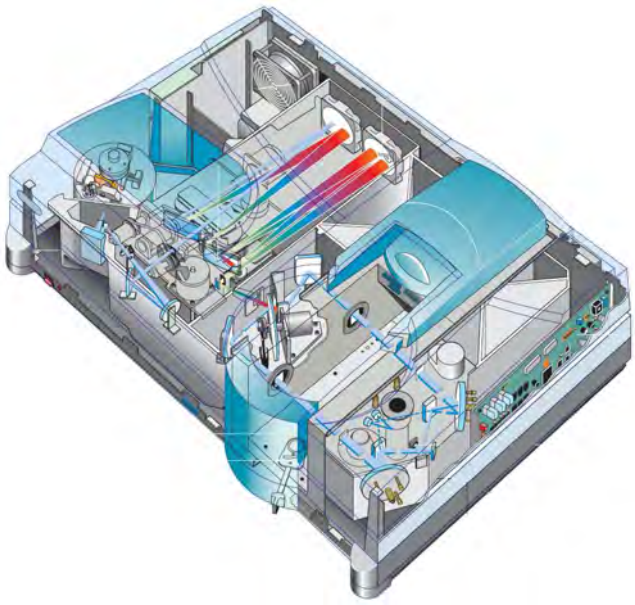

Figure 2.21: *Schematic of the Varian Cary 5000 spectro-photometer used at the University of Pisa for measuring room temperature absorption of Yb:YLF.*

Inversely, by measuring the transmission of a sample, one can calculate its absorption coefficient:

$$\alpha(\lambda, T) = -\frac{ln(T_{\%}/100)}{l} \tag{2.54}$$

Yb:YLF absorption coefficients at room temperature: The absorption coefficient of 10%Yb:YLF was measured in reference [24] and [25] by means of absorption spectrophotometry at ambient temperature, as shown in Figure 2.22.

Yb:YLF absorption cross-sections at room temperature: Absorption cross-sections can be found simple by dividing absorption coefficient data by the concentration of Ytterbium ions:

$$\sigma_{abs} = \frac{\alpha}{p_{\%}.N_{ions}} \tag{2.55}$$

With $p_{\%}$ the Yb^{3+} doping percentage and $N_{ions} = 1.4 \times 10^{20} ions/cm^3$ the density of Yb^{3+} ions in a 1% doped sample.

We see from Figure 2.22 an important feature of Yb:YLF. Light in $E \parallel c$ polarization is absorbed about twice as much the $E \perp c$ polarization at 1020 nm. It means that in order to achieve maximal absorbed power and cooling efficiency, one has to pump Yb:YLF samples with $E \parallel c$ polarized light.

The reciprocity method: At low temperatures, Yb:YLF absorption spectra could very well be measured with the same method by a spectro-photometer integrating a regulated cryo-

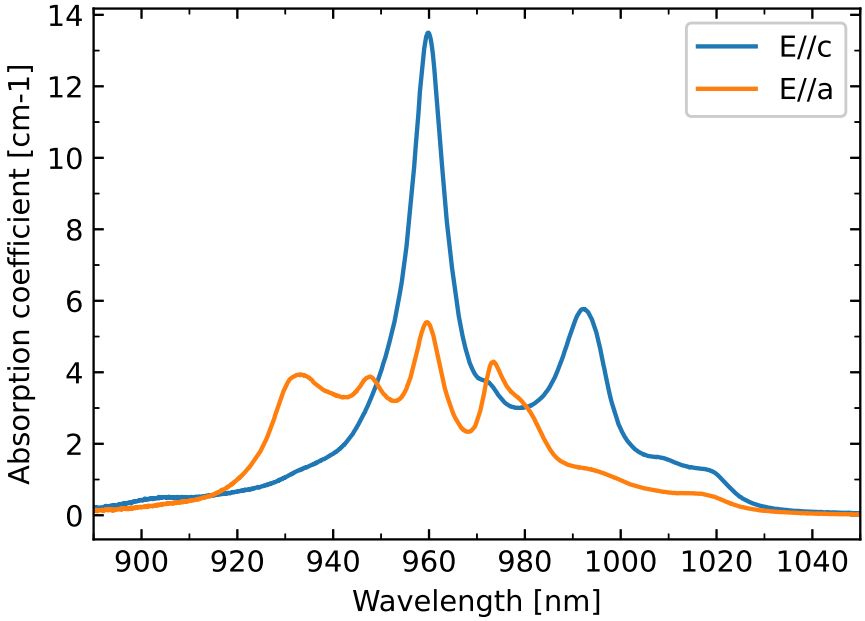

Figure 2.22: *Absorption coefficient of 10%Yb:YLF at room temperature in E||c and E⊥c directions, from reference [24].*

stat. However, absorption above 1000 nm quickly collapses due to the thermal depletion of the upper Stark levels in the ground manifold $^2F_{7/2}$, thus reducing the precision of the absorption measurement in the range of interest for laser cooling, around 1020 nm. A method exists to overcome this issue, taking advantage of the correlation between absorption and emission properties. The relationship known as McCumber relation or reciprocity method allows calculating the absorption cross-sections from emission, or inversely emission from absorption. We have:

$$\sigma_e(\lambda, T) = \frac{Z_l}{Z_u}\sigma_a(\lambda, T)exp\left(\frac{E_{zpl} - \frac{hc}{\lambda}}{k_B T}\right) \tag{2.56}$$

And inversely:

$$\sigma_a(\lambda, T) = \frac{Z_u}{Z_l}\sigma_e(\lambda, T)exp\left(-\frac{E_{zpl} - \frac{hc}{\lambda}}{k_B T}\right) \tag{2.57}$$

With Z_l and Z_u the partition functions of the lower and upper electronic manifolds, E_{zpl} the "zero phonon line".

The zero phonon line or ZPL is defined as the exact wavelength separation between the lowest ground state level and the lowest excited state level. Its meaning is that it is the only electronic transition whose absorption or emission does not relies on phonon/thermalization.

For that reason, at low temperatures (below 10 K), it is the only peak which is observable on both the absorption and emission spectra. The value of 971.6 nm or $E_{zpl} = 10293$ cm^{-1} was reported in literature [33][24].

Yb:YLF absorption at low temperatures: It follows that absorption can be retrieved using the reciprocity method based on emission spectra, as shown in Figure 2.23.

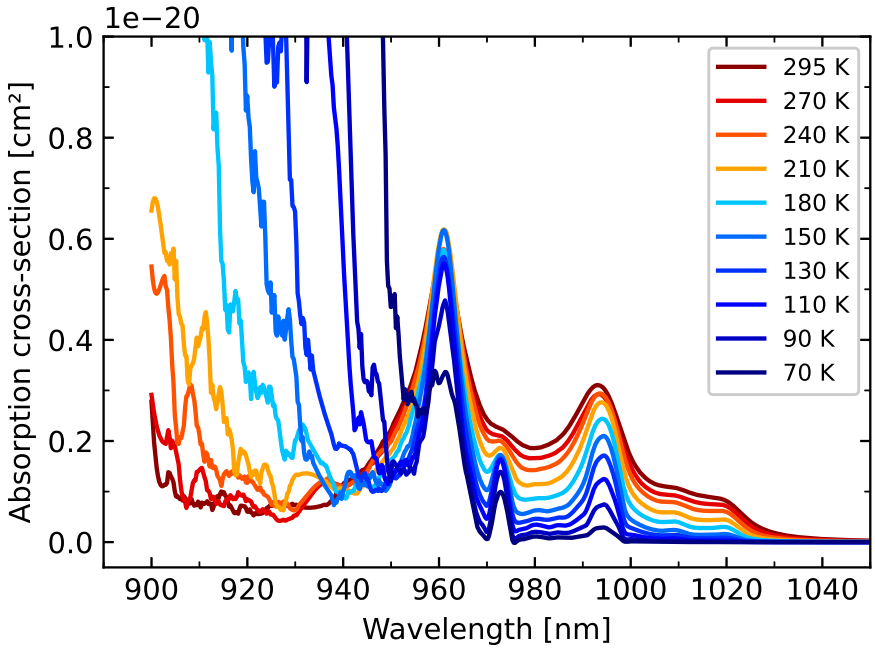

Figure 2.23: *Absorption cross-section of 10%Yb:YLF as a function of temperature, obtained by McCumber reciprocity method.*

We have three comments on the reciprocity method. First, we see that the shape below 960 nm is distorded due to the term $exp\left(-\frac{E_{zpl}-\frac{hc}{\lambda}}{k_B T}\right)$ in the reciprocity formula. The method should hence be used for retrieving absorption bellow at wavelengths above the ZPL wavelength 971.5 nm rather than below.

Secondly, we see that compared to spectro-photometer measurements at room temperature, the maximum peak value for $E \parallel c$ absorption cross-section is only on the order of 6e-21 cm^2 instead of almost 1e-20 cm^2. It means that the associated fluorescence measurements are plagued with fluorescence re-absorption, an issue in heavily doped samples.

As a last point, we see that the absorption cross-sections above 1000 nm are well predicted and with very little noise, which is the point of using the reciprocity method. A zoom on that range is shown in Figure 2.24 and plotted semi-log scale in Figure 2.25.

It is worth noticing from Figure 2.25 that at 1020 nm, Yb:YLF absorption loses one order of magnitude between room temperature and 150 K, another order of magnitude at 90 K and again an order of magnitude from 90 to 70 K. The implications of this decaying absorption for the design of optical cryocoolers are discussed in Chapter 4.

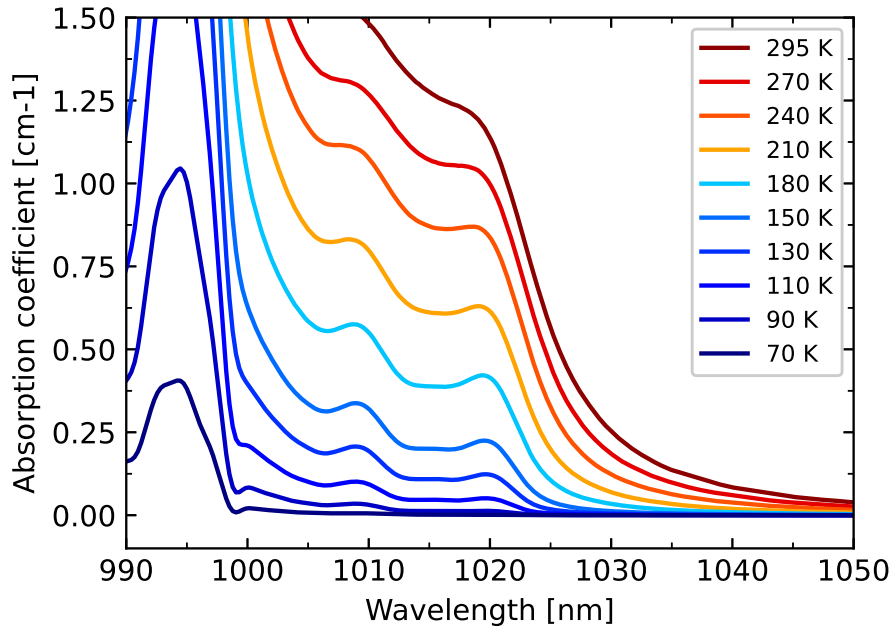

Figure 2.24: *Absorption coefficient of 10%Yb:YLF as a function of temperature, obtained by McCumber reciprocity method. Zoom in the range around 1020 nm.*

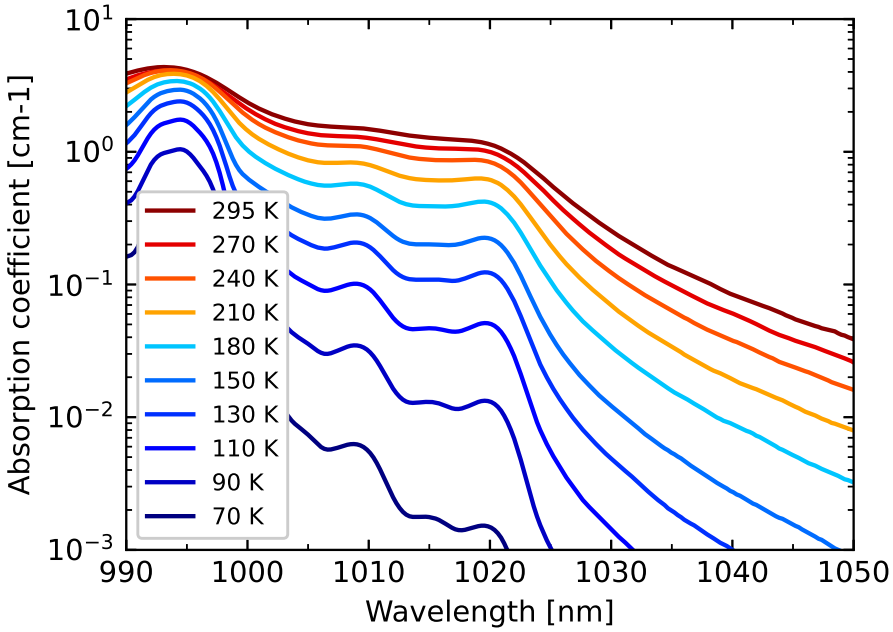

Figure 2.25: *Absorption coefficient of 10%Yb:YLF as a function of temperature, obtained by McCumber reciprocity method. Zoom in the range around 1020 nm in semi-log scale.*

Full absorption curves in 10%Yb:YLF were measured by references [24] and [25] by spectro-photometry and replacing the values in the long wavelengths tail by the values obtained by reciprocity, as shown in Figure 2.26.

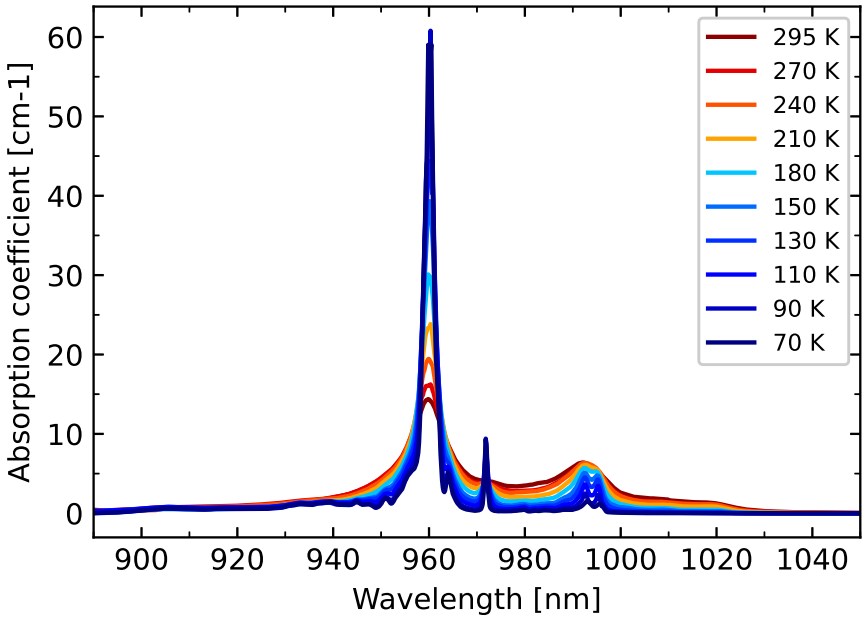

Figure 2.26: *Absorption coefficient of 10%Yb:YLF as a function of temperature, obtained by spectrophotometry below 990 nm and replaced with reciprocity calculated values above 990 nm, from reference [25].*

Emission properties

Yb:YLF fluorescence intensity: At low doping levels, it is straightforward to obtain the Yb:YLF fluorescence emission spectra. By pumping the sample with a laser at any wavelength in the absorption band, the crystal will emit fluorescence light which can be observed through a polarizer and analyzed using a spectrometer (Figure 2.27).

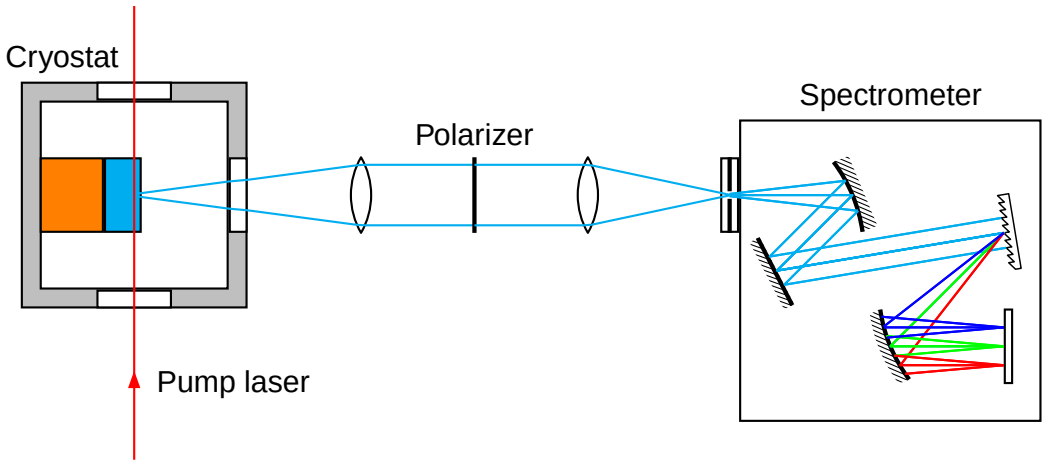

Figure 2.27: *Typical experimental setup for measuring fluorescence spectra as a function of temperature. The crystal sample is located inside a temperature controlled cryostat and excited with a pump laser on its very edge in order to minimize fluorescence re-absorption. Fluorescence light is then collected and analyzed using a spectrometer. A polarizer allows to select either E//c or E//a polarization.*

However, at high doping levels, special care should be taken in these measurements as the fluorescence intensity signal is plagued by two problems.

The first one is the re-absorption phenomenon. In heavily doped samples (over 1% Yb), fluorescence light is trapped inside the sample, the photons being absorbed and emitted several times before escaping the medium. This effect leads to underestimated intensities values corresponding to most absorbing wavelengths and overestimated values corresponding to low absorbing wavelengths.

The second problem is thermalization of the sample. When lit by some pump laser at known wavelength λ, the sample will either locally heat-up or cool-down, depending on the cooling efficiency $\eta_c(\lambda, T)$. The sample has to be well thermalized in cryostat experiments in order to achieve the precision on temperature dependency, for example by putting the crystal in a clamp with indium foil to ensure good thermal contact [25], or by soldering the sample on the cryostat plate with indium [31]. The measurement should also be quick to ensure that the sample's temperature does not vary too much due to pump absorption.

10%Yb:YLF fluorescence spectra were measured by references [24] and [25] in both polarizations, as shown in Figure 2.28 and Figure 2.29.

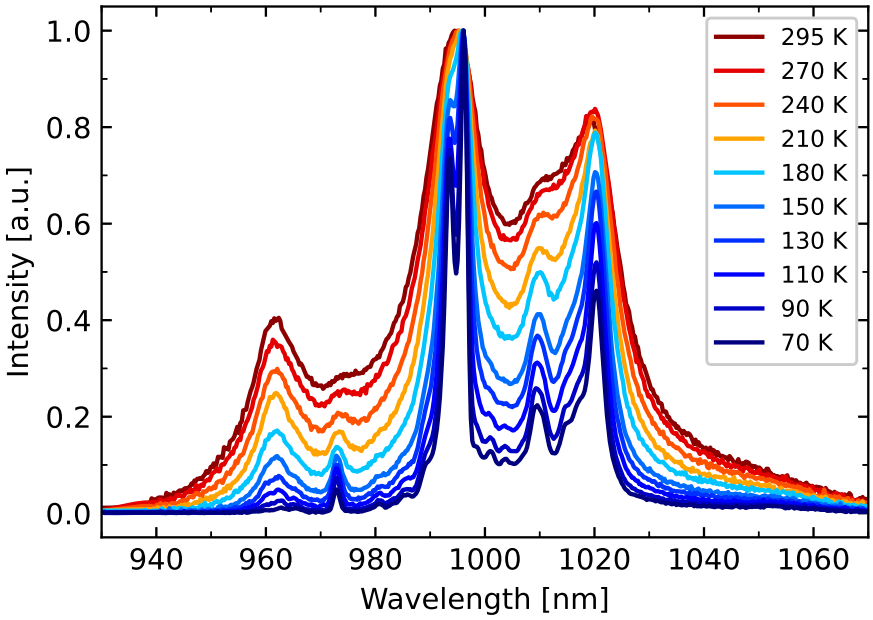

Figure 2.28: *Polarized $E \parallel c$ fluorescence intensity of 10% Yb:YLF as a function of temperature, measured by reference [25]. Spectra were normalized with respect to their maximal intensity.*

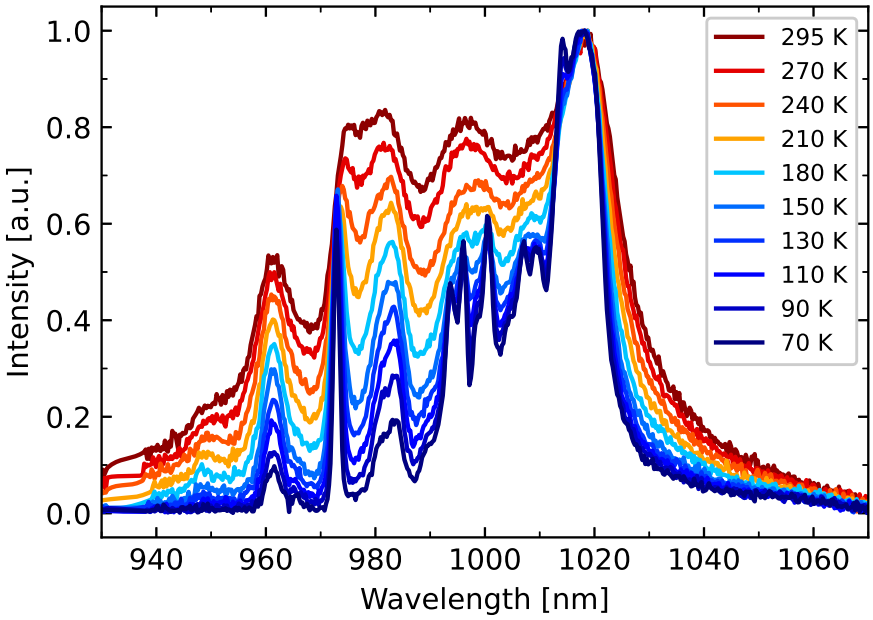

Figure 2.29: *Polarized $E \perp c$ fluorescence intensity of 10% Yb:YLF as a function of temperature, measured by reference [25]. Spectra were normalized with respect to their maximal intensity.*

Yb:YLF emission cross-sections: Knowing the radiative lifetime of the the excited manifold, the emission cross-sections in both polarizations can be calculated from the fluorescence intensities from the "modified" Füchtbauer-Ladenburg formula (also refereed as $\beta - \tau$ method):

$$\sigma_{e,E\|c} = \frac{\lambda^5}{8\pi c n^2 \tau_r} \frac{I_{E\|c}}{\int \left(\frac{1}{3} I_{E\|c} + \frac{2}{3} I_{E\perp c}\right) \lambda d\lambda} \tag{2.58}$$

And:

$$\sigma_{e,E\perp c} = \frac{\lambda^5}{8\pi c n^2 \tau_r} \frac{I_{E\perp c}}{\int \left(\frac{1}{3} I_{E\|c} + \frac{2}{3} I_{E\perp c}\right) \lambda d\lambda} \tag{2.59}$$

Figure 2.30 shows the room temperature emission cross section for 10% Yb:YLF as calculated from the fluorescence spectra. Fluorescence spectroscopy using a temperature controlled cryostat allows to retrieve the emission cross section as a function of temperature by the same method, as shown in Figure 2.31 and Figure 2.32.

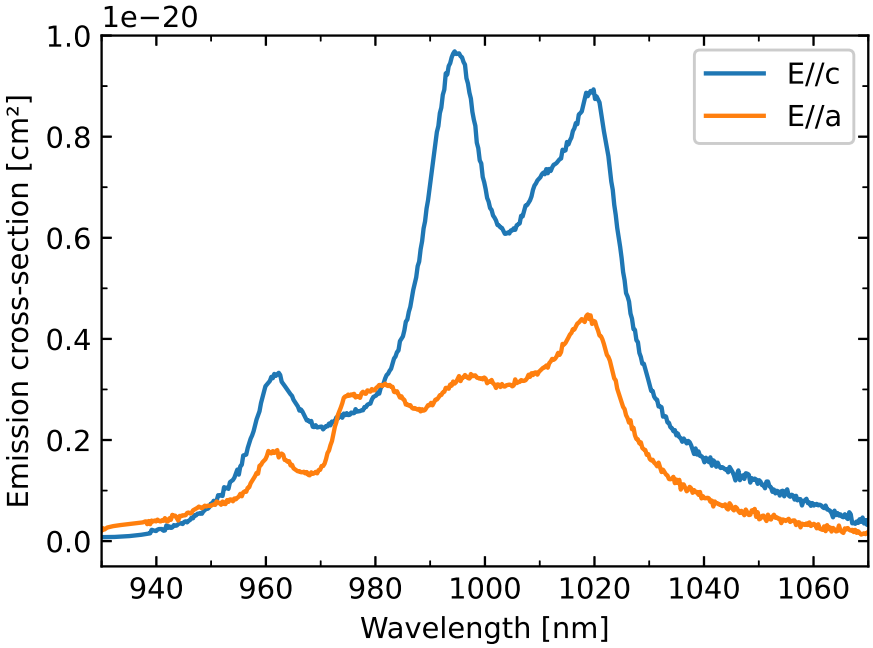

Figure 2.30: *Room temperature emission cross sections of 10%Yb:YLF calculated from fluorescence spectra measured by reference [25].*

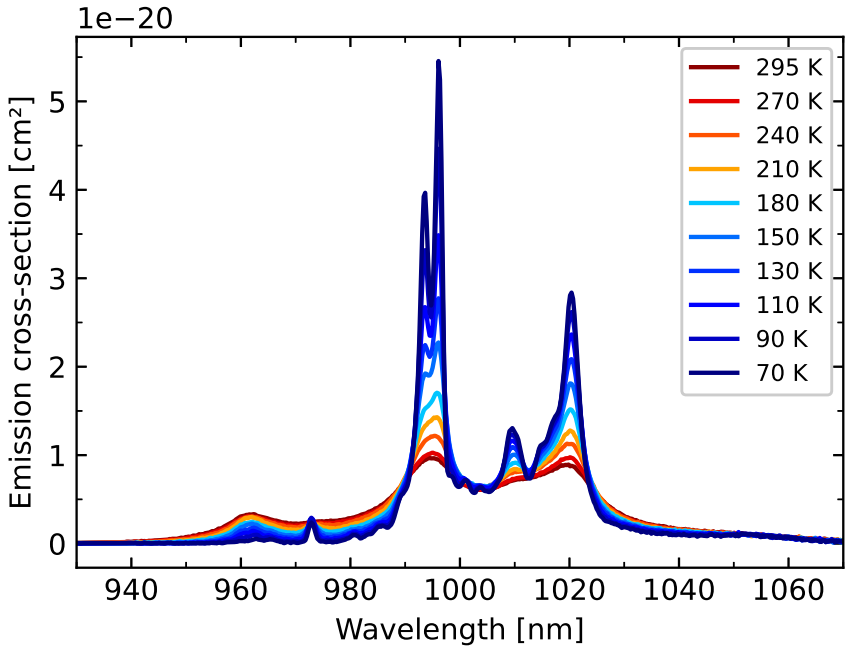

Figure 2.31: *Polarized $E \parallel c$ emission cross-section of 10%Yb:YLF as a function of temperature, calculated from intensity data measured by reference [25].*

Yb:YLF mean fluorescence wavelength: After the measurement of fluorescence intensity, intrinsic mean fluorescence wavelength as a function of temperature can be obtained if fluorescence was collected in conditions of minimal re-absorption. Mean fluorescence wavelength is defined as the first moment of fluorescence intensity normalized with the

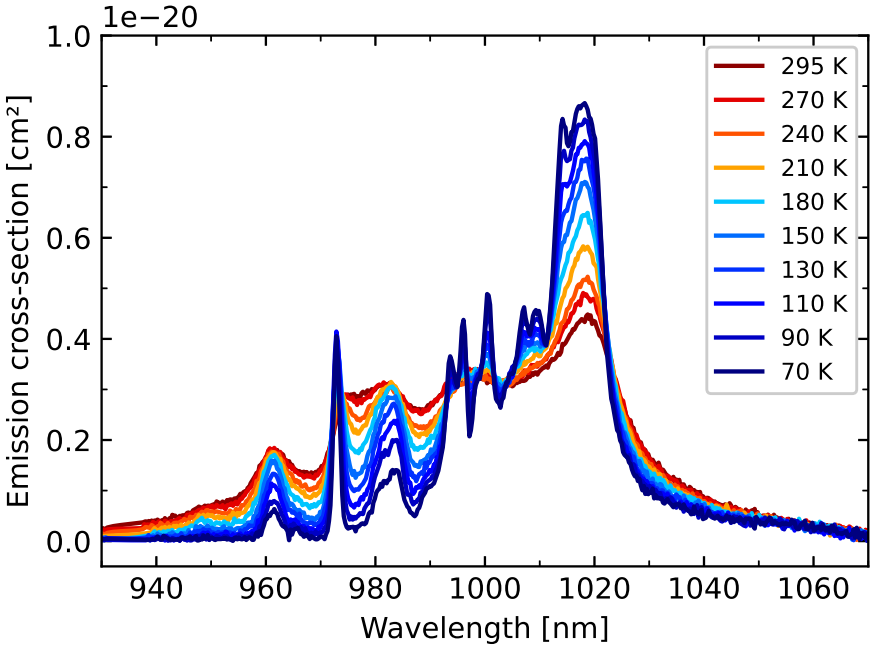

Figure 2.32: *Polarized $E \perp c$ emission cross-section for 10% Yb:YLF as a function of temperature, calculated from intensity data measured by reference [25].*

fluorescence power:

$$\bar{\lambda_f} = \frac{\int \lambda . I(\lambda) d\lambda}{\int I(\lambda) d\lambda} \tag{2.60}$$

As seen previously, absorption and emission spectra of rare-earths doped crystals depends on temperature. The implications of this phenomenon is that a non-contact thermometer can be made just by looking at the fluorescence mean wavelength. This method known as differential luminescence thermometry (abbr. DLT) is at the basis of our cryogenics temperatures measurement presented in Chapter 5.

For best measurements accuracy, some considerations should be taken into account. First, the fluorescence emitted power is isotropic but polarized fluorescence spectra is anisotropic: if observed in the direction parallel to c axis, little $E \perp c$ fluorescence should propagate in that direction and hence the overall spectra observed should be in majority the contribution of $E \parallel c$ fluorescence. Hence, the measurement of mean fluorescence wavelength depends on the observation direction with respect to c axis.

One solution is to know the ratio between $E \parallel c$ and $E \perp c$ emitted powers. As stated in reference [31], this measurement is not easy to make. The first method is to compare the absolute emission cross-sections in both polarizations, obtained with the Füchtbauer-Ladenburg formula. This method requires precise estimation of the radiative lifetime (either estimated with the pinhole method or by comparing with emission cross-sections obtained with McCumber reciprocity from absorption). A ratio of 2:1 was observed between E//c and E//a emitted powers at room temperature, which increases to 2.5:1 around 80 K [31].

A second method is to observe fluorescence in the $E \perp c$ plane, where the measured intensity is the sum of $E \parallel c$ and $E \perp c$ emissions, as performed in [34]. Measurements on 5% Yb:YLF yielded the following formula for mean intrinsic fluorescence wavelength as a function of temperature:

$$\bar{\lambda_f}(T) = 1008.9 - 0.031T \tag{2.61}$$

A higher precision method could involve putting the fluorescing crystal in an integrating sphere, thus allowing to collect the whole fluorescence at the sphere's output and measure the exact mean fluorescence wavelength.

Figure 2.33 compares the mean fluorescence wavelength obtained by direct observation in reference [34] and obtained by averaging mean fluorescence wavelengths in both polarizations intensities from reference [25] after setting the weights given in reference [31]. Both measurements are very close to each-others. The linear fit from direct observation agrees perfectly with a slightly higher value of the ratio $E \parallel c$ to $E \perp c$ emission, 2.3:1 at room temperature and 2.8:1 at 80 K.

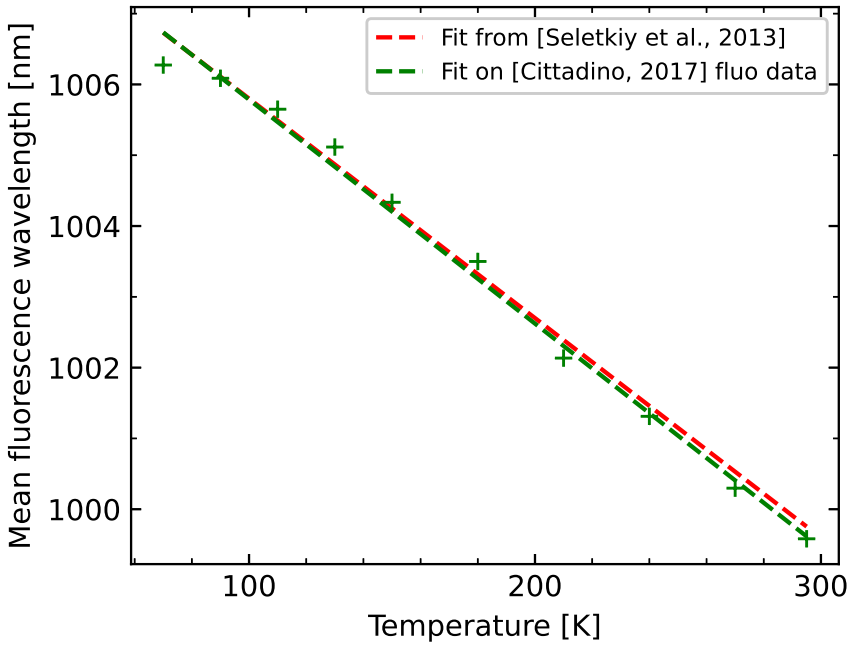

Figure 2.33: *Mean fluorescence wavelength as a function of temperature, plotted for 5%Yb:YLF [34] and calculated with 10%Yb:YLF normalized fluorescence spectra from [25] corrected with estimated $E \parallel c$ to $E \perp c$ emission ratios from [31].*

2.4.4 Cooling efficiency

Cooling efficiency in rare-earths doped solids is the result of three competing effects: light which is absorbed and re-emitted at higher energy known as the Anti-Stokes shift $\frac{\lambda}{\lambda_f}$; light which is absorbed and converted to heat due to impurities, accounted for in the absorption efficiency η_{abs} ; and light which is lost inside the material due to total internal reflections, scattering from defects or converted to phonons through non-radiative processes.

Calculation of the cooling efficency in Yb:YLF

In the four levels model, the cooling efficiency is well known and given by the formula:

$$\eta_c(\lambda, T) = 1 - \eta_{ext} \left(\frac{\alpha(\lambda, T)}{\alpha(\lambda, T) + a_b} \right) \left(\frac{\lambda}{\bar{\lambda_f}(T)} \right) \tag{2.62}$$

Following this equation, knowing the absorption $\alpha(\lambda, T)$ and the mean fluorescence wavelength $\bar{\lambda_f}(T)$ as a function of temperature, one can calculate the cooling efficiency as a function of the parameters η_{ext} and a_b.

For example, the cooling efficiency of a crystal with similar performances to those of reference [35], with $\eta_{ext} = 0.996$ and $a_b = 2e - 5$ cm^{-1} was calculated and plotted in Figure 2.34, for temperatures between 295 K and 90 K. The performance of a "good" 10%Yb:YLF cooling crystal is typically around 3% at room temperature, and around 1% at 150 K.

The wavelengths range where cooling is allowed is sometimes referred as "the cooling window". Usually, the cooling window is also represented under the form of a two-dimensional color plot, with the cooling efficiency as a function of temperature and wavelengths, as shown in Figure 2.35.

It is worth noticing that at low wavelengths, the cooling efficiency is dominated by the product of the external quantum efficiency and the Anti-Stokes shift, such that at the first zero crossing wavelength we have:

$$\eta_{ext} \left(\frac{\lambda_{cross}}{\bar{\lambda_f}} \right) = 1 \tag{2.63}$$

Equivalent to the relationship:

$$\eta_{ext} = \frac{\bar{\lambda_f}}{\lambda_{cross}} \tag{2.64}$$

In the presence of background absorption, the cooling efficiency collapses at long wavelengths. The lowest the background absorption, the higher the cooling efficiency peak will

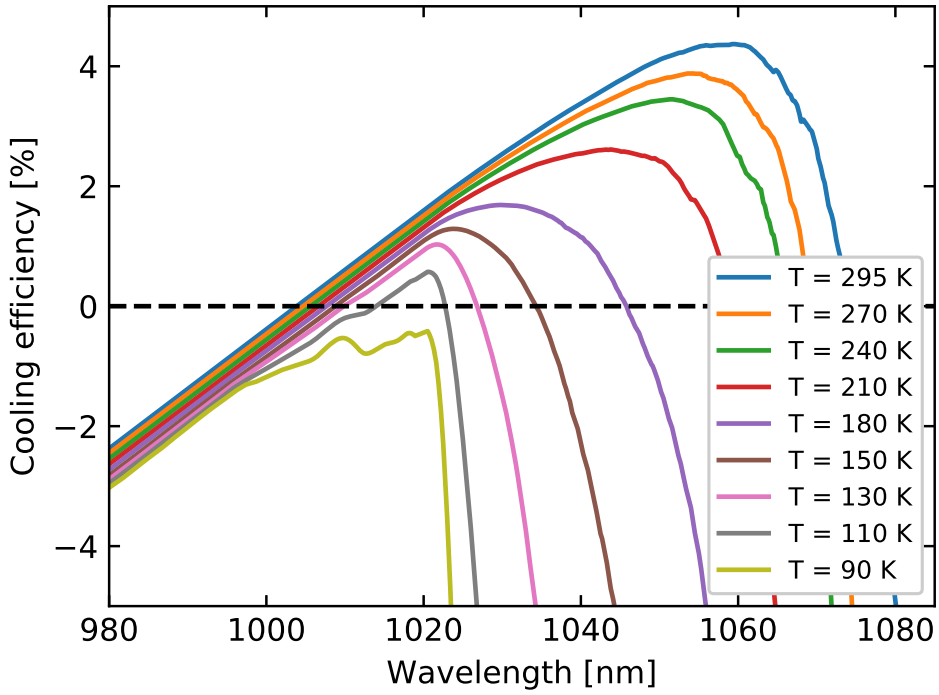

Figure 2.34: *Theoretical cooling efficiency as a function of temperature and pump wavelength for a crystal with $\eta_{ext} = 0.996$ and $a_b = 2e - 5$ cm^{-1}.*

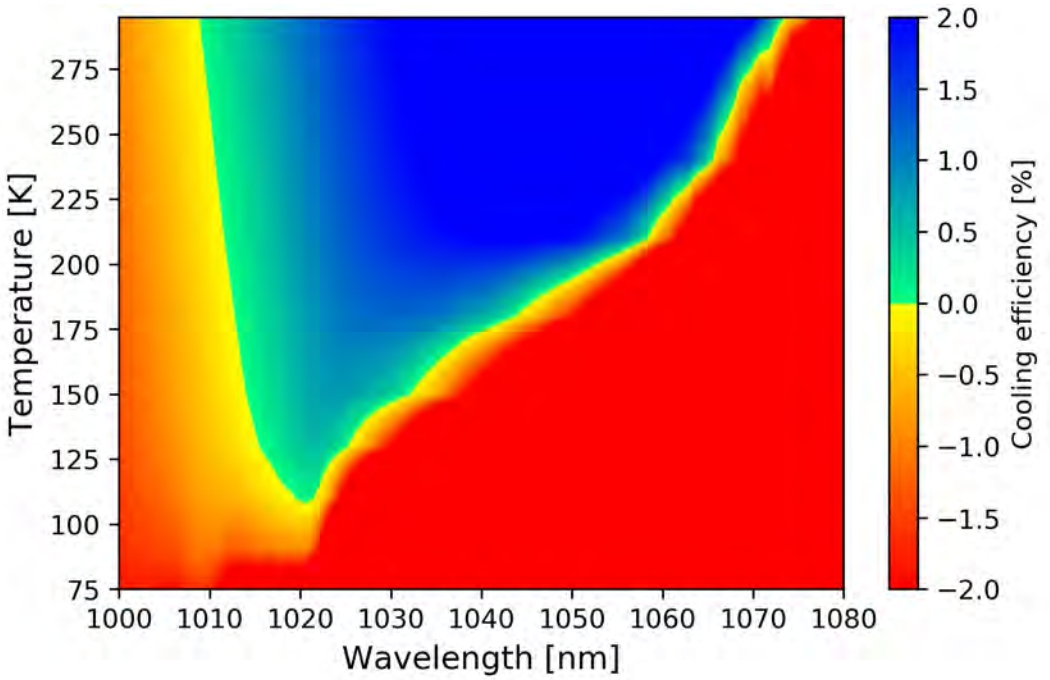

Figure 2.35: *Theoretical cooling efficiency as a function of temperature and wavelength, plotted as a 2D color plot for a crystal with $\eta_{ext} = 0.996$ and $a_b = 2e - 5$ cm^{-1}.*

be shifted towards long wavelengths.

The experimental determination of the cooling efficiency is usually done by first measuring the cooling efficiency at ambient temperature: knowing the absorbed laser power, the efficiency is proportional to the temperature difference. Performing the experiment at

several pump wavelengths allows to obtain the form of $\eta_c(\lambda, 300K)$. The parameters η_{ext} and a_b are then fitted from the measurements.

Extensions to the original cooling model

Over the last decade, with the emergence of efficient Anti-Stokes cooling materials down to cryogenics temperature, some additions were made to the standard cooling model to take into account the temperature dependency of the background absorption and external quantum efficiency.

Until now, cooling efficiency was estimated assuming constant background absorption and external quantum efficiency. That hypothesis, however was proven wrong in many crystals, where the minimal achieved temperature was smaller than predicted with the MAT. The formulation using only two parameters η_{ext} and a_b at 300 K is then inaccurate to predict the real cooling efficiency.

Precise determination of the background absorption as a function of temperature requires precise measurement of the crystal temperature (typically 0.1 K precision) at cryogenic temperatures for known pump absorption. Investigations were conducted by reference [36] in a configuration where a 5% Yb:YLF cooling crystal was maintained at known temperature inside a temperature controlled cryostat via a PID controller. The crystal temperature was monitored using a probe low power laser which provides fluorescence for the DLT method. A high power pump tunable laser was used in order to cool down or heat up the sample.

By setting the conduction between crystal and cold finger sufficiently small, for example by clamping the crystal with glass pads of known thickness, it is possible to measure the temperature change induced by the pump over a small amount of time, without the effect of the cryostat PID changing the crystal temperature. The crystal temperature is monitored on the DLT signal just before turning on the pump and just after shutting it off. The temperature difference is then proportional to the absorbed power and cooling efficiency, which can be fitted with n_{ext} and a_b as usual.

It was proven using this method that the background absorption is a temperature dependent parameter, which decreases by one order of magnitude between 300 K and 100 K with the formula:

$$a_b(T) = 7.5exp(-387.6/T)10^{-4}cm^{-1} \tag{2.65}$$

An explanation was proposed: impurities which lead to heating in rare-earths doped crystals are mainly transition metals, with the electrons populating 3d orbitals. In the same way

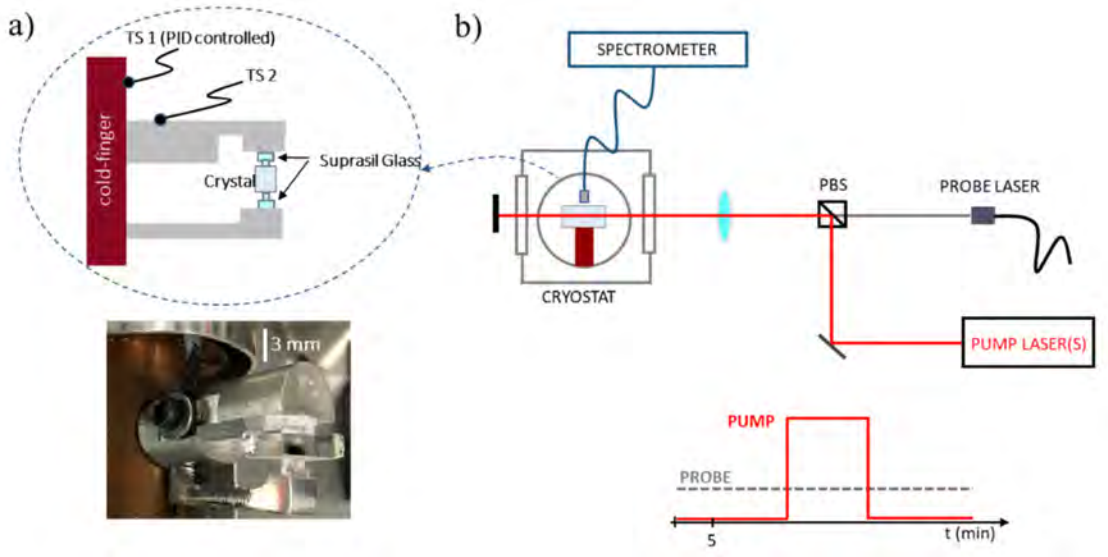

Figure 2.36: *Schematic of the pump-probe setup used for precise determination of background absorption and external quantum efficiency at cryogenics temperatures, from reference [36]. a) shows the crystal held inside the cryostat in between two glass pads with known thermal conduction, and b) shows the optical setup in the experiment.*

of 4f transitions in rare-earths doped crystals, 3d transitions can increase or decrease in absorption due to changes in the electronic levels thermal population. If 3d absorption occurs between a thermally populated ground level and an excited level, it will hence decrease in absorption if temperature is lowered. On the contrary, if absorption occurs between a ground and excited state level, it will increase with lowering temperature.

The conclusion follows that decreasing absorption as a function of temperature is the result of a given “set” of impurities, where some absorption bands can increase and some decrease with temperature. Additional investigations are needed in order to check the contribution of each transition metal impurity. Eventually, the knowledge of absorption in “on-purpose” transition metal doped YLF can enlighten this behavior. Similarly, external quantum efficiency decreased by 0.5%. It is obvious that the external quantum efficiency parameter, as defined, is correlated to the background absorption. Indeed, it describes the proportion of photons escaping out of the material. Hence, if the background absorption increases, the probability of a non-radiative decay W_{nr} should increase as well.

In the rest of this thesis, the decay of background absorption is taken into account by using Equation 2.65 normalized to the measured background absorption at 300 K for the cooling efficiency calculations. We can see that a background absorption decaying with temperature predicts much lower minimal temperatures, as shown in Figure 2.37.

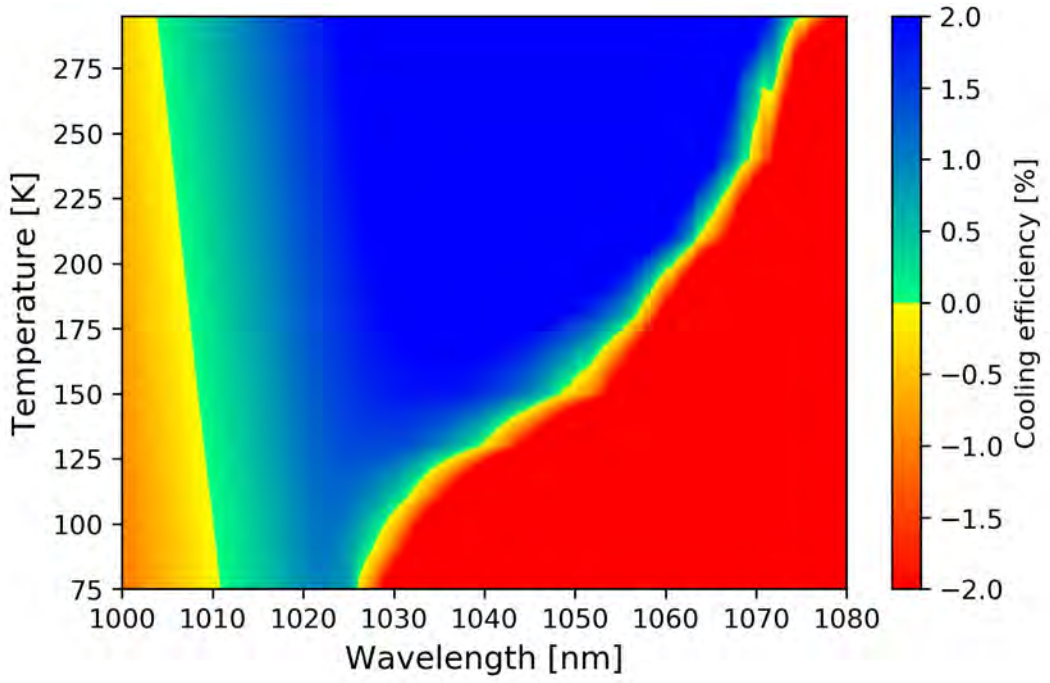

Figure 2.37: *Theoretical cooling efficiency as a function of temperature and wavelength, plotted as a 2D color plot considering the background absorption decay at low temperatures.*

References

[1] G. G. Stokes, “On the change of refrangibility of light,” *Philosophical Transactions of the Royal Society*, 1852.
DOI: 10.1098/rstl.1852.0022 (cit. on p. 45).

[2] M. Planck, “On the law of distribution of energy in the normal spectrum,” *Annalen der Physik*, 1901 (cit. on p. 45).

[3] A. Einstein, “On a heuristic viewpoint concerning the production and transformation of light,” *Annalen der Physik*, 1905 (cit. on p. 45).

[4] C. V. Raman and K. S. Krishnan, “A new type of secondary radiation,” *Nature*, 1928 (cit. on p. 45).

[5] P. Pringsheim, “Zwei Bemerkungen über den Unterschied von Lumineszenz- und Temperaturstrahlung,” *Zeitschrift für Physik*, 1929.
DOI: 10.1007/BF01340652 (cit. on p. 45).

[6] L. D. Landau, “On the thermodynamics of photoluminescence,” *USSR Journal of Physics*, 1946.
DOI: 10.1016/B978-0-08-010586-4.50067-5 (cit. on p. 46).

[7] A. Kastler, “Quelques suggestions concernant la production optique et la détection optique d’une inégalité de population des niveaux de quantifigation spatiale des atomes. application à l’expérience de stern et gerlach et à la résonance magnétique,”

Le journal de physique et le radium, 1950.
DOI: 10.1051/jphysrad:01950001106025500 (cit. on p. 46).

[8] T. Kushida and E. Geusic, "Optical refrigeration in Nd-doped Yttrium Aluminium Garnet," *Physical Review Letters*, 1968.
DOI: 10.1103/PhysRevLett.21.1172 (cit. on p. 46).

[9] R. Epstein, M. Buchwald, B. Edwards, T. Gosnell, and C. Mungan, "Observation of laser-induced fluorescent cooling of a solid," *Nature*, 1995.
DOI: 10.1038/377500a0 (cit. on p. 46).

[10] B. Edwards, M. Buchwald, R. Epstein, T. Gosnell, and C. E. Mungan, "Development of a fluorescent cryocooler," *AIAA satellite conference*, 1995. [Online]. Available: https://www.osti.gov/biblio/119975 (cit. on p. 46).

[11] B. Edwards, M. Buchwald, R. Epstein, T. Gosnell, and C. E. Mungan, "The Los Alamos Solid-State Optical Refrigerator (LASSOR) Program," *SAE 1996 Transactions - Journal of Aerospace*, 1996.
DOI: 10.4271/961476 (cit. on p. 46).

[12] Mungan and Gosnell, "Laser cooling of solids," *Advances In Atomic, Molecular, and Optical Physics*, 1999.
DOI: 10.1016/S1049-250X(08)60113-5 (cit. on p. 46).

[13] R. I. Epstein, B. C. Edwards, and M. Sheik-Bahae, "Semiconductor-based optical refrigerator," *US Patent 6378321*, 2002. [Online]. Available: https://www.osti.gov/biblio/874374 (cit. on p. 46).

[14] M. Sheik-Bahae and R. I. Epstein, "Can laser light cool semiconductors ?" *Physical Review Letters*, 2002.
DOI: 10.1103/PhysRevLett.92.247403 (cit. on p. 46).

[15] D. A. Bender, J. G. Cederberg, C. Wang, and M. Sheik-Bahae, "Development of high quantum efficiency GaAs/GaInP doubleheterostructures for laser cooling," *Applied Physics Letters*, 2013.
DOI: 10.1063/1.4811759 (cit. on p. 46).

[16] IUPAC, "The periodic table of elements," 2018. [Online]. Available: http://www.iupac.org (cit. on p. 48).

[17] A. J. Freeman and R. E. Watson, "Theoretical Investigation of Some Magnetic and Spectroscopic Properties of Rare-Earth Ions," *Physical Review*, 1962.
DOI: 10.1103/PhysRev.127.2058 (cit. on p. 49).

[18] G. H. Dieke and H. M. Crosswhite, "The Spectra of the Doubly and Triply Ionized Rare Earths," *Applied Optics*, 1963.
DOI: 10.1364/AO.2.000675 (cit. on pp. 53, 54).

[19] M. P. Hehlen, M. G. Brik, and K. W. Krämer, “50th anniversary of the Judd–Ofelt theory: An experimentalist’s view of the formalism and its application,” *Journal of Luminescence*, 2013.
DOI: 10.1016/j.jlumin.2012.10.035 (cit. on p. 55).

[20] Los Alamos National Lab, “Relic,” (cit. on p. 55).

[21] R. I. Epstein and M. Sheik-Bahae, *Optical Refrigeration, Science and Applications of Laser Cooling in Solids*. Wiley, 2009.
DOI: 10.1002/9783527628049 (cit. on p. 61).

[22] S. Bigotta, A. Di Lieto, A. Toncelli, M. Tonelli, D. Seletskiy, M. P. Hasselbeck, M. Sheik-Bahae, and R. I. Epstein, “Laser cooling of solids: New results with single fluoride crystals,” *Il Nuovo Cimento*, 2007.
DOI: 10.1393/ncb/i2007-10415-6 (cit. on p. 64).

[23] E. Garcia and R. R. Ryan, “Structure of the Laser Host Material LiYF4,” *Acta Crystallographica*, 1993.
DOI: 10.1107/S0108270193005876 (cit. on p. 64).

[24] A. Volpi, “Cooling effects on fluoride crystals,” Ph.D. dissertation, Università di Pisa, Pisa, Italy, 2015 (cit. on pp. 65–67, 71, 73–76, 78).

[25] G. Cittadino, “An increasing cooling efficiency in fluoride crystals co-doped Yb-Tm,” Ph.D. dissertation, Università di Pisa, Pisa, Italy, 2017 (cit. on pp. 66, 73, 76–82).

[26] A. K. Batra and M. D. Aggarwal, *Field Guide to Crystal Growth*. SPIE Press, 2018.
DOI: 10.1117/3.2309590 (cit. on p. 67).

[27] A. Volpi, J. Meng, A. Albrecht, M. Sheik-Bahae, D. Biner, K. W. Krämer, and M. P. Hehlen, “Bridgman growth of LiYF4 and LiLuF4 crystals for radiation-balanced lasers,” *Proc. of SPIE*, 2019.
DOI: 10.1117/12.2510691 (cit. on p. 67).

[28] S. Wildermuth, K. Bohnert, H. Brändle, and J.-M. Fourmigue, “Growth and Characterization of Single Crystalline Bi4Ge3O12 Fibers for Electrooptic High Voltage Sensors,” *Journal of Sensors*, 2013.
DOI: 10.1155/2013/650572 (cit. on p. 68).

[29] L. A. Riseberg and H. W. Moos, “Multiphonon orbit-lattice relaxation of excited states of rare-earth ions in crystals,” *Physical Review*, 1968.
DOI: 10.1103/PhysRev.174.429 (cit. on p. 70).

[30] G. Cittadino, E. Damiano, A. Di Lieto, and M. Tonelli, “First demonstration of optical refrigeration efficiency greater than 4% at room temperature,” *Optics Express*, 2020.
DOI: doi.org/10.1364/OE.390283 (cit. on p. 70).

[31] U. Demirbas, J. Thesinga, M. Kellert, F. X. Kärtner, and M. Pergament, "Detailed investigation of absorption, emission and gain in Yb:YLF in the 78–300 K range," *Optical Materials Express*, 2021.
DOI: 10.1364/OME.415253 (cit. on pp. 71, 78, 81, 82).

[32] S. Püshel, S. Kalusniak, C. Kränkel, and H. Tanaka, "Temperature-dependent radiative lifetime of Yb:YLF: refined cross sections and potential for laser cooling," *Optics Express*, 2021.
DOI: 10.1364/OE.422535 (cit. on pp. 71, 72).

[33] A. Bensalah, Y. Guyot, M. Ito, A. Brenier, H. Sato, T. Fukuda, and G. Boulon, "Growth of Yb3+-doped YLiF4 laser crystal by the Czochralski method. Attempt of Yb3+ energy level assignment and estimation of the laser potentiality," *Optical Materials*, 2004.
DOI: 10.1016/j.optmat.2003.09.015 (cit. on p. 75).

[34] D. V. Seletskiy, S. D. Melgaard, R. I. Epstein, A. Di Lieto, M. Tonelli, and M. Sheik-Bahae, "Precise determination of minimum achievable temperature for solid-state optical refrigeration," *Journal of Luminescence*, 2013.
DOI: 10.1016/j.jlumin.2011.09.045 (cit. on p. 82).

[35] S. D. Melgaard, *Cryogenic optical refrigeration: Laser cooling of solids below 123 K*. 2013. [Online]. Available: https://digitalrepository.unm.edu/ose_etds/24/ (cit. on p. 83).

[36] A. Volpi, J. Meng, A. Gragossian, A. R. Albrecht, S. Rostami, A. Di Lieto, R. Esptein, M. Tonelli, M. P. Hehlen, and M. Sheik-Bahae, "Optical refrigeration: The role of parasitic absorption at cryogenic temperatures," *Optics Express*, 2019.
DOI: 10.1364/OE.27.029710 (cit. on pp. 85, 86).

Chapter 3

Laser cooling in solids for space applications

This chapter features the size, weight and power analysis that I did during the first year of my thesis. The goal was to prove that, with the crystals existing now, a Laser Cryocooler was not only feasible, but already suitable inside an observation satellite. I presented this work at the Grenoble New-Space Week (Grenoble, France) and the 28th Space Cryogenics Workshop (Southbury, CT, USA), biennial gathering of the worldwide space cryogenics community. We published the analysis in the Cryogenics journal's special issue for the occasion: reference [1]. The work presented here is largely adapted from the initial publication with some minor additions, such as the consideration of new co-doped crystals with higher cooling efficiency and an improved calculation of the thermal link's losses. At the end, I give a short vision of the requirements for achieving a space qualified Laser Cryocooler as well as a "road-map" towards higher TRLs.

Ce chapitre expose l'analyse volume, poids, puissance que j'ai effectué au cours de ma première année de thèse. Le but était de prouver qu'avec les cristaux existant actuellement, un Cryo-refroidisseur Laser est non seulement faisable, mais également intéressant dans un satellite d'observation. J'ai présenté ce travail lors du Grenoble New-Space Week (Grenoble, France) et du 28^{me} Space Cryogenics Workshop (Southbury, CT, USA), rassemblement biannuel de la communauté mondiale de la cryogénie spatiale. Nous avons publié cette analyse dans l'édition spéciale du journal Cryogenics pour cette occasion: référence [1]. Le travail présenté ici est largement adapté de la publication initiale avec quelques ajouts mineurs, comme la prise en compte des nouveaux cristaux co-dopés avec une meilleure efficacité de refroidissement et un calcul amélioré des pertes au niveau du lien thermique. A la fin, je donne une courte vision des exigences pour réaliser un Cryo-refroidisseur Laser qualifié spatial ainsi qu'une "road-map" vers les plus hauts TRLs.

3.1 SWaP analysis at satellite level

3.1.1 Base hypotheses

Mission scenario

This study is based on a typical LEO satellite infrared observation mission such as Microcarb (CNES, 2021) [2]. The hypothesis of a high reliability 5 years mission is made, with continuous observation time (>95 % observation disponibility).

Orbit hypotheses: A quasi-circular sun synchronous orbit with 650 km altitude, 98°inclination and 10h30 mean local time of ascending node is assumed. The beta angle, defined as the angle between the satellite's orbital plane and the Earth-Sun vector is used to estimate the eclipse time. For a 10h30 orbit, the mean beta angle over 1 year is 22.5°[3]. The orbital period T is calculated using the formula [4]:

$$T = 2\pi\sqrt{\frac{(R_e + h)^3}{GM_e}} \tag{3.1}$$

With $R_e = 6371 \cdot 10^3 km$ the Earth's radius, h the altitude, $G = 6.674 \cdot 10^{-11} m^3 kg^{-1} s^{-2}$ the gravitational constant and $M_e = 5.972 \cdot 10^{24} kg$ the Earth's mass. Taking $h = 650 \cdot 10^3 km$, an orbital period of $T = 5855s = 98min$ is found. The eclipse fraction f_E is calculated using the formula [4]:

$$f_E = \frac{1}{\pi} cos^{-1}\left(\frac{\sqrt{h^2 + 2R_e h}}{(R_e + h)cos(\beta)}\right) \tag{3.2}$$

Replacing beta with its value, we find $f_E = 0.35$, leading to an eclipse time of $T_E = 0.35 \times 98 = 34min$. Mission parameters are summarized in Table 3.1.

Orbit	SSO
Altitude	650 km
Orbital period	98 min
Eclipse time	34 min
MLT (ascending node)	10:30
Mean beta angle	22.5°
Mission duration	5 years

Table 3.1: *Parameters for the considered sun-synchronous orbit observation mission.*

Focal plane thermal budget

A focal plane embedding an infrared HgCdTe detector, model Lynred NGP SWIR (1024 × 1024 pixels, 15 μm × 15 μm pitch) is considered. This detector has a thermal dissipation of typically 150 mW [5]. Other heat sources inside the cryostat are:

- The conductive losses coming from the focal plane supporting blades.
- The conductive losses coming from the electrical connections.
- The radiative flux hitting the detector and the focal plane.

The heat sources in the focal plane are schematically presented in Figure 3.1. Their estimated heat load values are summarized in Table 3.2. A total heat load of 280 mW needs to be extracted off the focal plane in order to cool the detector.

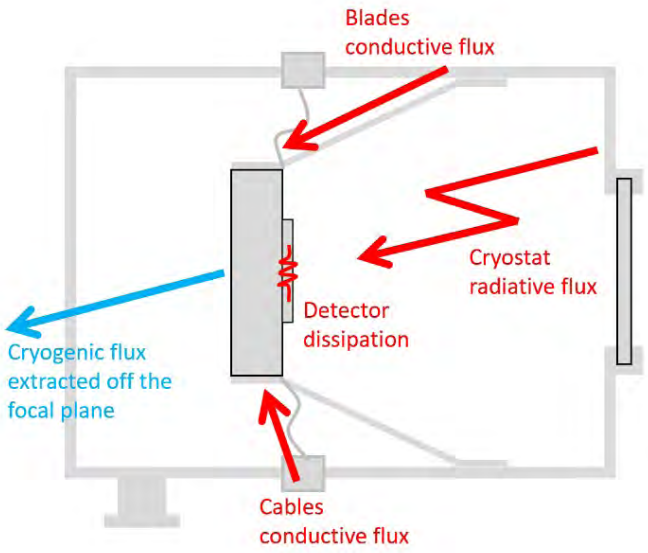

Figure 3.1: *Schematic of the considered heat sources at the focal plane level.*

Item	Heat flux (mW)
Detector	150
Focal plane support blades	65
Electrical connections	35
Radiative flux on detector	15
Radiative flux on focal plane	15
Total	280 mW

Table 3.2: *Estimated values of the different heat sources terms at the focal plane level.*

In practice, the cooling power of a cryocooler has to be higher to compensate for thermal losses coming from its architecture (internal losses and cold redundancy). Thermal losses are taken into account in section 3.1.3 for the LC architecture and section 3.1.5 for the MPTC architecture.

Electrical specifications

Power distribution specifications: As a general rule, high satellite bus power requires a large power control and distribution unit (PCDU). For a micro-satellite, the assumption is made that modern PCDUs such as the Myriade Evolution PCDU are highly efficient, modular and can withstand an extra 100 W payload equipment with marginal mass increase [6]. PCDU and satellite power regulation electronics masses are hence not considered in this study.

Solar array specifications: The solar array considered is a one-axis oriented array, able to keep the solar beta angle during the satellite revolution, assuring nearly constant solar irradiance during day time. The array is composed of triple junction Ga/As solar cells, with 30 % solar efficiency [7]. The beginning of life (BOL) surface power density of a solar array is given by:

$$\phi_{BOL} = \eta_{SA} F \tag{3.3}$$

With ϕ_{BOL} the surface power density in W/m², η_{SA} the array efficiency and $F = 1367 W.m^{-2}$ the solar constant. This yields a surface power density of:

$$\phi_{BOL} = 1367 \times 0.3 = 410 W.m^{-2} \tag{3.4}$$

The BOL surface power density is then corrected to take into account: the inherent degradation of the solar cells due to panels heating and view factors between the satellite and the solar array, the conversion efficiency from the solar array to the PCDU. Assuming an inherent degradation of 75 % due to view factors and heating of the solar cells [4] and 95 % conversion efficiency from the solar array to the PCDU, a corrected surface power density of 292 W/m² is found. The lifetime degradation L is calculated using the formula:

$$L = (1 - \delta)^N \tag{3.5}$$

with δ the array's annual degradation due to irradiation in LEO and N the number of years in orbit. Taking an annual degradation $\delta = 4\%$ and a mission life of N = 5 years, the lifetime degradation is ~82 %. The end of life (EOL) power density amounts to 220 W/m². Surface mass of a solar array is estimated to 2.5 kg/m² [8], yielding an intrinsic EOL power per mass ratio of 96 W/kg. The panel thickness was estimated to 25 mm based on recent array technologies [9]. The solar array mass and power specifications are summarized in Table 3.3.

Finally, the mass augmentation of the solar array drive mechanisms and the inertia wheel due to the over-sizing of the solar array is taken into account in the structure margin and

Solar power conversion efficiency	30 %
Surface power density (BOL)	410 W/m²
Inherent array degradation	75 %
PCDU convertion efficiency	95 %
Corrected surface power density (BOL)	292 W/m²
Degradation rate	4%/year
Lifetime degradation	82 %
Surface power density (EOL)	240 W/m²
Surface mass	2.5 kg/m²
Power to mass ratio (EOL)	96 W/kg
Thickness	25 mm

Table 3.3: *Solar array estimated efficiency and specifications, at beginning-of-life (BOL) and en-of-life (EOL).*

supporting margin presented in section 3.1.1.

Batteries specifications: A battery composed of Saft VES16 Li-Ion cells [10] is considered, as specified in Table 3.4. Indeed, this cell model is recent, space qualified and its small capacity makes it suitable for low power missions. Furthermore, its discharge performances have been assessed for LEO missions [11].

Model	Saft VES16
Type	Li-ion cell
Capacity	4.5 Ah
Voltage	3.6 V
Dimensions	60 mm x 30 mm

Table 3.4: *Saft VES16 cells specifications.*

Considering one charge/discharge cycle per satellite revolution, a 5 years mission duration with 98 minutes orbital period yields approximately 27000 cycles. From the batteries specifications , with 30 % depth of discharge (typical value for LEO missions), the battery capacity fading after 27000 cycles is estimated to 88 % [12].

Thermal control

The heat dissipated by a cooling system such as a laser cooler or a pulse tube cooler needs to be evacuated to avoid any system malfunction. Only thermal control for the cryocooling sub-systems is considered. The assumption is made that driving electronics are made in contact with the external satellite faces acting as a radiator which dissipates the heat into space. Hence it does not require additional thermal control.

Thermal control sizing depends on the cooler's thermal dissipation. LC and MPTC require the use of heat pipes with a diameter sized to the maximal extracted heat flux [13].

Each heat pipe is in contact with a radiator. On a satellite, a radiator facing outer space with an infrared emissivity $\epsilon = 0.85$ has a temperature of 280 K. It typically dissipates 300 W/m² [14]. In practice, this value is halved to account for equipment-radiator temperature gradients and illumination from the sun or the solar array, yielding an effective heat dissipation of 150 W/m². Assuming a 1.5 mm thick aluminum sheet with a density of 2700 kg/m^3, the surface mass of a radiator panel is approximately 4 kg/m².

Margins

Structure and supporting of the equipments is estimated to 20 % of the total mass in a satellite [15]. To reach that value, a +25 % margin on the final satellite mass is applied. The margin is calculated as follows: Assuming M the final mass with margins, m the final mass without margin and x the structure and supporting mass, we have the relationship $M = m + x$ and $x = M \times 0.2$. This yields $x = (m + x) \times 0.2$. Rearranging, the mass margin is found as $x = m/(1 - 0.2) = m/0.8 = m \times 1.25$

3.1.2 Laser cooler preliminary architecture

There are two main designs of laser coolers, depending if the cooling crystal is located within the laser source's cavity (intra-cavity design) or separated from the laser part (extra-cavity design). An extra-cavity design is considered here.

An extra-cavity laser cooler is divided into two sub-systems. The first one is the optical cavity containing the cooling crystal, linked with a thermal link to the load. This part is responsible for the cooling process and needs to be supplied with optical power from a laser going through the cavity. It is referred as Cryogenic Laser Optical Exchanger (CLOE).

The second sub-system is the electronic module generating the optical power and feeding it to the cavity through an optical fiber. It contains the power conversion electronics, the laser diodes, and the control/command module needed to operate the system. It is referred as Laser Electronics Assembly (LEA). The general architecture of a laser cooler is shown in Figure 3.2. The features of these two sub-systems are detailed in the next sections.

Cryogenic Laser Optical Exchanger

The Cryogenic Laser Optical Exchanger (CLOE) sub-system role is to:

- Convert the input optical power into cooling power extracted off the thermal load.
- Report the cryogenic temperature to the LEA.

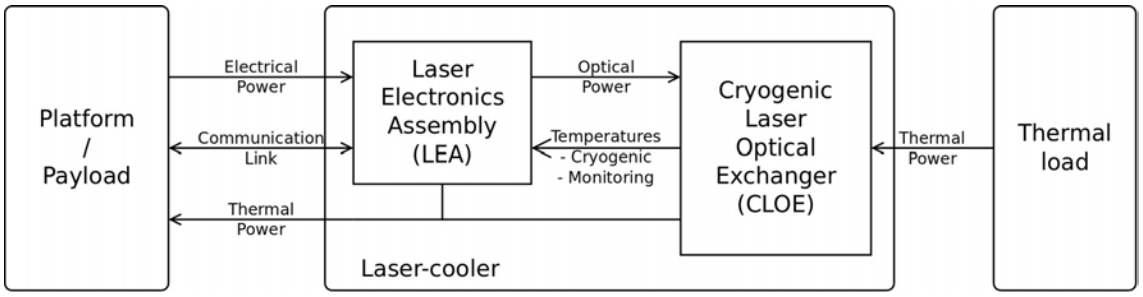

Figure 3.2: *Schematized functional architecture of a Laser Cryocooler and its subsystems, the Cryogenic Laser Optical Exchanger (CLOE) and the Laser Electronics Assembly (LEA).*

The cooling material, a rare-earth doped crystal is held at the center of a multi-pass optical cavity [16], whose purpose is to increase the interaction length between the laser beam and the material.

The cavity is made of two ultra-high reflection mirrors facing each-others. The walls of the cavity are coated with low thermal emissivity, high near-infrared absorption coating, such as TiNOX [17] or Nano Black [18]. The goal is to absorb a maximum of fluorescence radiation coming from the crystal while maintaining low thermal radiation load between the ambient temperature enclosure and the cold crystal.

A thermal link is attached between the crystal and the load to be cooled. The thermal link should ideally possess a high thermal conductivity to minimize temperature gradients or thermal lag between the crystal and the load.

When crossed by the laser beams, the crystal is re-emitting isotropically the absorbed laser power in the form of fluorescence, acting as an intense light-bulb. The link should possess a geometry minimizing the absorbed fluorescence power at the end of the link, while being the shortest possible to avoid thermal losses coming from the enclosure thermal radiation. There is an optical isolation between the thermal link and the focal plane to avoid radiation leakage.

The cooling head is attached to the cryostat containing the detector. In the case of a laser cooler, an aluminum cryostat measuring 160 mm × 180 mm and weighting 3.6 kg is considered. The CLOE along with the focal plane cryostat are shown in Figure 3.3. It fits in a volume of 0.3 L and weights 1 kg (Table 3.5).

Dimensions	100 x 50 x 60 mm^3
Volume	0.3 L
Weight	1.0 kg

Table 3.5: *CLOE size, volume and weight specifications.*

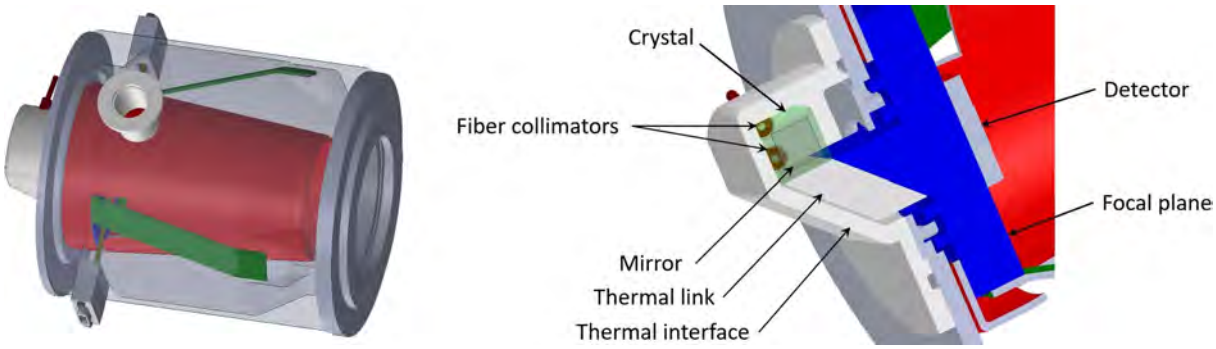

Figure 3.3: *Left: Preliminary CAD concept of a Laser Cryocooler mounted at the back of a cryostat. Right: Side cut showing the main elements contained in a Laser Cryocooler.*

Laser Electronics Assembly

The Laser Electronics Assembly (LEA) sub-system role is to:

- Convert the electrical power in optical power to feed the CLOE sub-system.
- Condition and acquire the temperature data measured in the CLOE sub-system.
- Regulate the cryogenic temperature at a reference point.
- Perform health checkups and report the results.

This subsystem is composed of a control and command module, a power generation module and an interface module. The LEA's main element is the laser diodes stage, converting the electrical power into optical power. The advantage of using laser diodes is that they can be stacked to reach the required power and they can be easily doubled.

The power stage assumes both the low power subsystem supply and the laser diodes current supply. A current amplifier allows the conversion of the command signal to power up the laser diodes. The LEA only comports DC power supplies so there is limited signal filtering.

The control and command module contains all the necessary elements to secure the laser diodes nominal operation: input current, photo-diode current, enclosure temperature monitoring. It performs a temperature regulation at the cooling point by the means of temperature acquisition and laser diode current feedback on that temperature.

The interface module assumes the outside link to the satellite platform. It gathers the modes management, protection and system surveillance information. The LEA characteristics are reported in Table 3.6.

Dimensions	255 x 138 x 85 mm^3
Volume	3.0 L
Weight	2.0 kg

Table 3.6: *LEA size, volume and weight specifications.*

3.1.3 Budget for a Laser Cooler

Redundancy

The assumption of a high reliability satellite mission was made, requiring some form of redundancy for the cryocooler. Three options are possible: redundancy of the whole system, redundancy of only the electronics, or only the cold head. Although no reliability study for a laser cooler has been made so far, the assumption was made that the Laser Electronics Assembly has the highest failure probability due to the presence of power generation electronics and laser diodes. In the opposite, the cold head was assumed less likely to fail, with no known degradation of the optical cavity or the cooling crystal over time. Hence it was assumed in this study that only the electronics are redundant for a laser cooler, as shown in Figure 3.4.

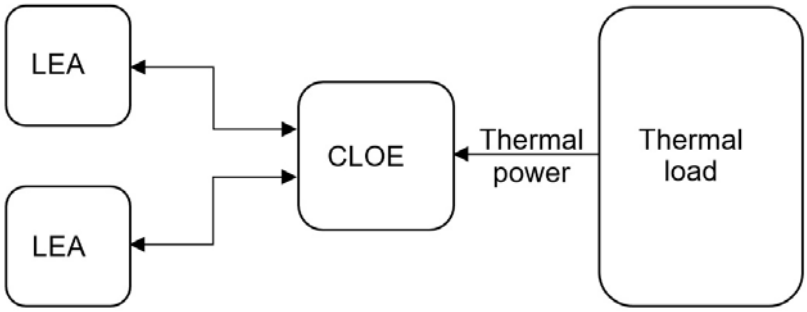

Figure 3.4: *LC sub-systems redundancy hypothesis considered in this study.*

Volume and weight

The total volume of a redundant laser cooler with cryostat is estimated approximately to 10 L. Accounting for 0.5 kg of cables, the total weight of the system and cryostat is estimated to 8.2 kg as shown in Table 3.7.

Power consumption

Optical cooling efficiency: The cooling efficiency of a laser cooler is defined as the ratio of the generated heat lift over the laser power absorbed by the crystal. For state-of-the-art

Equipment	Volume (L)	Mass (kg)
CLOE	0.3	1.0
2 x LEA	6.0	4.0
Cables	Negligible	Negligible
Cryostat	3.6	2.7
Total	9.9 L	8.2 kg

Table 3.7: *Volume and weight of a LC system.*

10% doped Yb:YLF cooling crystals, it is estimated to 0.8 % at 120 K and 1.2 % at 150 K [19].

Thermal losses: From [20], thermal link losses for a laser cooler are the sum of two contributions :

- Heating due to the absorbed fluorescence at the end of the thermal link, P_{fluo}
- Heating due to the thermal radiation of the hot enclosure surrounding the cold crystal and thermal link assembly, P_{rad}.

The first contribution depends on the thermal link's geometry and its capability to reject the light coming from the crystal. It is estimated to 22 mW at 135 K in a kinked thermal link with an inside angle of 15° [20]. Assuming nearly constant maximal absorbed laser power between 120 K and 150 K (a reasonable hypothesis for N>50 laser round-trips inside the crystal [16]), the emitted fluorescence power P_{fluo} can be approximated as the same at 120 K, 135 K and 150 K.

The second contribution depends on the surface of the crystal and thermal link which are in direct view of the enclosure's hot surface. It is estimated to 8 mW at 135 K for a 10 × 4 × 4 mm crystal attached with the kinked thermal link previously cited [20]. To give an estimation at 120 K and 150 K, Stefan-Boltzmann law is applied :

$$P_{rad} \propto k(T_1^4 - T_2^4) \tag{3.6}$$

Taking $T_1 = 300$ K and $T_2 = 135$ K, the constant $k = 1.03 \times 10^{-12}$ is calculated. Replacing T_2 by its value yields P_{rad} = 8.1 mW at 120 K, and P_{rad} = 7.8 mW at 150 K. In the next part of the study, constant thermal link losses of 30 mW are considered at both 120 and 150 K.

Power conversion: The optical power P_{Opt} that has to enter the cavity is calculated from the required cooling power P_{Cool} and the optical cooling efficiency η_c:

$$P_{Opt} = \frac{P_{Cool}}{\eta_c} \tag{3.7}$$

The laser source power has to be superior by a factor k to account for fiber coupling losses, estimated at 10 %:

$$P_{Laser} = (1 + k)P_{Opt} \tag{3.8}$$

The required electrical power P_{Elec} is calculated from the electronics conversion efficiency:

$$P_{Elec} = \frac{P_{Laser}}{(\eta_{Laser}\eta_{PC})} + P_{LP} \tag{3.9}$$

With η_{Laser} the optical conversion efficiency, η_{PC} the electrical conversion efficiency from the PCDU to the LEA and P_{LP} the electronics low power part corresponding to the systems modes and acquisition.

Laser diodes and fiber amplifiers do exist in the near infrared at wavelengths, line-width and powers that are suitable for cooling of rare-earth doped crystals. The efficiency of laser diodes in the near infrared is estimated to 50~60% [21]. For fiber lasers, the wall plug efficiency depends on both the pumping diodes efficiency and the fiber amplifier efficiency (50~80%), yielding a total efficiency of 25~50% [22]. A space qualified laser for cooling would only require adaptation and tests from an existing laser source.

In this study, a laser diode with an optical conversion efficiency η_{Laser} of about 55 % is assumed. The electrical conversion efficiency η_{PC} is estimated to 75 %. The low power part P_{LP} is based on the Cryocooler Drive Electronics of a MPTC, applying a power reduction due to a simplified control and command module. It is estimated to 4 W.

Command & control consumption	4 W
Power supply conversion efficiency	75 %
Laser diode optical conversion efficiency	55 %
Optical fiber coupling efficiency	90 %

Table 3.8: *LEA electronics estimated efficiency.*

The power optical power sizing of a Laser Cryocooler is summarized in Table 3.9. To reach 120 K, 38 W of optical power need to be supplied to the cavity, resulting in 107 W of electrical consumption for the whole system. At 150 K, an optical power of 26 W is needed, resulting in 73 W of consumption. The electrical power sizing at the sub-systems level is summarized in Table 3.10.

Solar array and batteries sizing Knowing the required power for a laser cooler, the solar array and batteries sizing for both temperatures is performed. To calculate the solar array surface it is necessary to take into account the continuous cryocooler operation plus an additional consumption due to the batteries charging during daytime. We have the following

	120 K	150 K
Cooling efficiency	0.8 %	1.2 %
Thermal link losses	30 mW	30 mW
Focal plane dissipation	280 mW	280 mW
Required cooling power	310 mW	310 mW
Required optical power	38.8 W	25.8 W

Table 3.9: *Cooling and optical requirements for a LC architecture.*

	120 K	150 K
CLOE input optical power	38 W	26 W
Optical fiber losses	4 W	3 W
LEA output optical power	42 W	29 W
Conversion efficiency losses	60 W	42 W
C/C consumption	4 W	4 W
Total electrical power	107 W	73 W

Table 3.10: *Electrical power requirements for a LC architecture.*

relationship:

$$P_{SA} = \frac{1}{T_S}\left(\frac{PT_S}{\varepsilon_{DET}} + \frac{PT_E}{\varepsilon_C}\right) \tag{3.10}$$

With P_{SA} the required solar array power, P the payload power, T_S the orbit sun-time and T_E the orbit eclipse time, ϵ_{DET} the solar array to payload direct energy transfer efficiency, ϵ_C the batteries charging efficiency, assuming ϵ_{DET} = 98 % [6] and ϵ_C = 95 %. The solar array sizing is summarized in Table 3.11.

	120 K	150 K
Power	169 W	115 W
Surface	0.7 m²	0.5 m²
Volume	17.5 L	12.5 L
Mass	1.8 kg	1.3 kg

Table 3.11: *Solar array sizing for a LC architecture.*

The batteries are sized to support the continuous cryocooler operation over a 34 minutes eclipse (0.57 h). The required capacity (in Wh) is calculated knowing the system power consumption, with 30 % DOD, a capacity fading η_B=88 % and a discharge efficiency $\epsilon_D = 95$ %. We have:

$$C_B = \frac{PT_E}{DOD\eta_B\eta_D} = \frac{P \times 0.57}{0.30 \times 0.88 \times 0.95} = P \times 2.27 \tag{3.11}$$

The cells are mounted in series to reach the required bus voltage, and then in parallel to reach the required capacity. For 3.6 V cells, 8 cells in series are needed to reach 28 V.

The number of parallel cells is calculated from the required capacity (in Ah) divided by the capacity of one cell and multiplied by two for redundancy:

$$p = \frac{C_B}{C_{Cell}} \times 2 \tag{3.12}$$

Finally, the number of required cells is found. Batteries size, volume and mass are calculated proportionally from Saft VES16 8s4p battery, measuring 308 × 180 × 90 mm³ and weighting 4.9 kg [10]. Batteries sizing for a laser cooler architecture is summarized in Table 3.12.

	120 K	150 K
Capacity	8.7 Ah	5.9 Ah
Number of cells	32 (8s4p)	24 (8s3p)
Dimensions	308 x 180 x 90 mm^3	308 x 135 x 90 mm^3
Volume	4.9 L	3.7 L
Mass	4.9 kg	3.7 kg

Table 3.12: *Batteries sizing for a LC architecture.*

Thermal control sizing

The heat dissipated by fluorescence amounts to 38 W at 120 K and 26 W at 150K. To regulate the system, 11 mm diameter aluminum-ammonia heatpipes are used, capable to extract a maximal heat of 50 W m [13]. Assuming a 1 m side satellite, a heat pipe needs to cover about 0.5 m from the center to the nearest satellite face. Heat pipes have to be tethered to a radiator and thus a higher heat pipe length is needed. Two heat pipes of 0.7 m each are assumed. With a linear mass of 0.34 kg/m for ø11 mm aluminum heatpipes [13], a mass of 0.47 kg is found. The radiators surfaces, masses and volumes are calculated using the values given in section 3.1.1. Thermal control sizing is summarized in Table 3.13.

		120 K	150 K
Heat pipes	Dimensions	1.4 m x 11 mm	1.4 m x 11 mm
	Volume	0.14 L	0.14 L
	Mass	0.47 kg	0.47 kg
Radiators	Surface	0.25 m^2	0.17 m^2
	Volume	0.38 L	0.26 L
	Mass	2.0 kg	1.4 kg
Total	Volume	0.52 L	0.40 L
	Mass	2.5 kg	1.9 kg

Table 3.13: *Thermal control sizing for a LC architecture.*

Laser Cooler at satellite level: summary

Adding the volumes and masses previously calculated the payload, platform and satellite level total volumes and masses are found for a laser cooler architecture (Table 3.14). As expected with a miniaturized cooling head, the payload impact in terms of mass and volume is modest, while at satellite level most of the volume is contained in the solar array and batteries.

		120 K			150 K	
	Volume (L)	Weight (kg)	Power (W)	Volume (L)	Weight (kg)	Power (W)
Payload						
CLOE	0.3	1.0		0.3	1.0	
2 x LEA	6	4.0		6	4.0	
Cables	Negligible	0.5		Negligible	0.5	
Cryostat	3.6	2.7		3.6	2.7	
Payload total	9.9 L	8.2 kg	107 W	9.9 L	8.2 kg	73 W
Platform						
Solar array	17.5	1.8		12.5	1.3	
Batteries	4.9	4.9		3.7	3.7	
Heat pipes	0.14	0.47		0.14	0.47	
Radiators	0.38	2.0		0.26	1.4	
Platform total	22.9 L	9.2 kg	107 W	16.6 L	6.9 kg	73 W
Total before margin	32.8	17.4 kg		26.5 L	15.1 kg	
Structure margin (+25 % mass)		4.4			3.8	
Total after margin	32.8 L	21.8 kg	107 W	26.5 L	18.9 kg	73 W

Table 3.14: *Satellite SWaP summary for a LC architecture.*

3.1.4 Miniature Pulse Tube Cooler architecture

Cryocooler Mechanical Assembly

The Cryocooler Mechanical Assembly sub-system is composed of a compressor generating an oscillating high pressure wave, going through a pulse tube. A "cold finger" is attached between the cold end of the pulse tube and the focal plane. The whole sub-system is supported by mechanical dampeners and accelerometers in order to monitor and decrease vibrations levels. The CMA role is to:

- Supply electrical power to the compressor at the pulse tube input with a waveform piloted by the CDE in order to convert mechanical power into heat lift.
- Measure the cold finger temperature and the micro-vibrations levels and report them to the CDE.

From previous miniature pulse tube coolers prototypes developed at Air Liquide Advanced Technologies for 80 K - 200 K range observation missions [23], [24], a MPTC-CMA occupies a volume of 5.5 L and weight 3.9 kg (Table 3.15).

Dimensions	250 x 150 x 140 mm^3
Volume	5.5 L
Weight	3.9 kg

Table 3.15: *CMA mechanical specifications.*

Cryocooler Drive Electronics

The Cryocooler Drive Electronics role is to:

- Acquire the temperature and forces reported by the CMA.
- Pilot with precision the cold finger temperature.
- Reduce electronically through a feedback loop the micro-vibrations in the CMA.

Just like the LEA sub-system in the laser cooler architecture, a CDE is composed of a control and command module, a power generation module and an interface module. The CDE characteristics are reported in Table 3.16.

Dimensions	255 x 138 x 55 mm^3
Volume	1.9 L
Weight	1.4 kg

Table 3.16: *CDE mechanical specifications.*

3.1.5 Budget for a Miniature Pulse Tube Cooler

To this day, Pulse Tube coolers are the standard cryocoolers used in the range 10 K to 200 K [25]. A Miniature Pulse Tube Cooler is composed of a Cryocooler Mechanical Assembly (CMA) powered by a Cryocooler Drive Electronic (CDE).

Redundancy

For the Miniature Pulse Tube Cooler architecture, a cold redundancy with two CMA and two CDE is assumed: one cooler is active while the other one is off.

Volume and weight

The cryostat has to be bigger than in the Laser Cooler setup to be able to fit two cold fingers and a thermal braid linked to the focal plane. In the case of a MPTC, the aluminum

cryostat measures 200 mm × 300 mm and weights 5.4 kg. The redundant CMA along with the focal plane cryostat are shown in Figure 3.5. The total volume is estimated to 23 L as summarized in Table 3.17. For the mass estimation, the following items were taken into account:

- The masses of two CMA and two CDE
- The expected cryostat mass
- The cables mass between the CMAs and CDEs

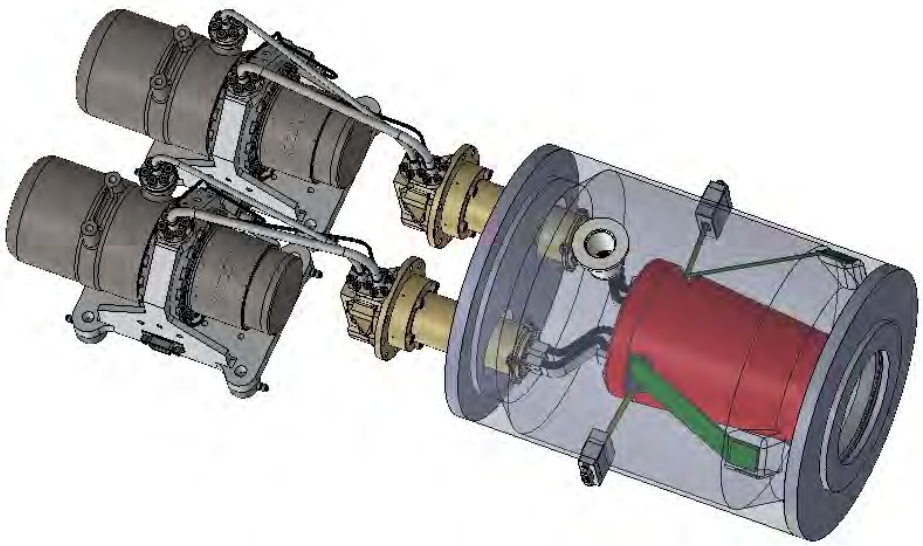

Figure 3.5: *Concept of a focal plane architecture with redundant Miniature Pulse Tube Coolers.*

The total mass is estimated to 18 kg as summarized in Table 3.17.

	Volume (L)	Weight (kg)
2 x CMA	11.0	7.8
2 x CDE	2.8	2.8
Cables	Negligible	1.0
Cryostat	9.4	5.4
Total	23.2 L	17.0 kg

Table 3.17: *Estimated volume and weight of a MPTC architecture.*

Power consumption

Cooling efficiency: The cooling efficiency of a pulse tube is defined as the ratio of the generated heat lift over the compressor electrical power. It is estimated to 9 % (11.1 W/W) at 120 K, and 12 % (8.3 W/W) at 150 K for a MPTC.

Thermal losses: Cold redundancy implies that a part of the cooling power from the working CMA is wasted in parasitic losses when cooling the second and warmer cold finger. Those cold redundancy losses are estimated to 320 mW. To extract 280 mW off the focal plane, a CMA cooling power of 600 mW is required. The CMA cooling efficiency, losses and power requirements are summarized in Table 3.18.

	120 K	150 K
CMA cooling efficiency	9 %	12 %
Cold redundancy losses	320 mW	320 mW
Focal plane dissipation	280 mW	280 mW
Required cooling power	600 mW	600 mW
Required electrical power	7 W	5 W

Table 3.18: *Estimated Pulse Tube efficiency, losses, and required cooling power.*

Power conversion: The CMA consumption is calculated from the cooling efficiency: a CMA consumption of 7 W is estimated for 120 K and 5 W for 150 K. The CDE consumption variation is assumed marginal and estimated to a constant 7 W (Table 3.19).

	120 K	150 K
CMA electrical power	7 W	5 W
CDE electrical power	7 W	7 W
Total electrical power	14 W	12 W

Table 3.19: *Power requirements for a MPTC architecture.*

Solar array and batteries sizing: Knowing the consumption of a MPTC, the required solar array power, surface, volume and mass are calculated and summarized in Table 3.20.

	120 K	150 K
Array power	22 W	19 W
Array surface	0.09 m²	0.08 m²
Array volume	2.3 L	2.0 L
Array mass	0.23 kg	0.20 kg

Table 3.20: *Solar array sizing for a MPTC architecture.*

Based on the same assumptions as before, the batteries requires a capacity of 1 Ah at both 120 and 150 K. Due to the need of a 28 V output, the minimal battery is a 8s1p with a total capacity of 4.5 Ah which is more than twice the required capacity, taking redundancy into account. 1.3 kg of batteries are found for a MPTC. That mass would be lower in a real satellite, due to the presence of other equipment and the possibility to adjust the number of parallel cells for higher capacities. However for this study the analysis is based on a standalone system. Batteries sizing for a pulse tube architecture is summarized in Table 3.21.

	120 K	150 K
Required capacity	1.1 Ah	1.0 Ah
Number of cells	8 (8s1p)	8 (8s1p)
Dimensions	308 x 45 x 90 mm^3	308 x 45 x 90 mm^3
Volume	1.3 L	1.3 L
Weight	1.3 kg	1.3 kg

Table 3.21: *Batteries sizing for a MPTC architecture.*

Thermal control sizing

To evacuate the heat off the warm side of the two CDE, 4 pipes of 11 mm diameter were chosen, with the previous hypotheses for heat pipes and radiator masses. Thermal control sizing is summarized in Table 3.22.

		120 K	150 K
Heat pipes	Size	2.8 m x 11 mm	2.8m x 11 mm
	Volume	0.27 L	0.27 L
	Weight	0.94 kg	0.94 kg
Radiators	Size	0.09 m^2	0.08 m^2
	Volume	0.14 L	0.12 L
	Weight	0.36 kg	0.32 kg
Total	Volume	0.41 L	0.39 L
	Weight	1.3 kg	1.3 kg

Table 3.22: *Thermal control sizing for a MPTC architecture.*

MPTC at satellite level: summary

Volume, mass and power requirements for a Miniature Pulse Tube Cooler architecture at satellite level are summarized in Table 3.23. For almost 300 mW cooling at 120-150 K, cold redundancy implies a required cooling power twice as high due to thermal losses. Although the power consumption stays low at those temperatures, two-thirds of the mass and 85% of the volume are contained in the satellite payload.

3.1.6 Discussion

Our main results comes from the comparison of Table 3.14 and Table 3.23, as summarized in Table 3.24. The satellite analysis shows that despite a higher total volume is needed mainly due to the increased solar array surface, the LC architecture is expected to weight less than a MPTC architecture and occupies less internal volume for both 120 K and 150 K.

		120 K			150 K	
	Volume (L)	Weight (kg)	Power (W)	Volume (L)	Weight (kg)	Power (W)
Payload						
2 x CMA	11	7.8		11	7.8	
2 x CDE	2.8	2.8		2.8	2.8	
Cables	Negligible	1.0		Negligible	1.0	
Cryostat	9.4	5.4		9.4	5.4	
Payload total	23.2 L	17.0 kg	14 W	23.2 L	17.0 kg	12 W
Platform						
Solar array	2.3	0.2		2.0	0.2	
Batteries	1.3	1.3		1.3	1.3	
Heat pipes	0.3	0.9		0.3	0.9	
Radiators	0.1	0.4		0.1	0.3	
Platform total	4.0 L	2.8 kg		3.7 L	2.8 kg	
Total before margin	27.2	19.8	14	26.9	19.7	12
Structure margin (+25 % mass)		5.0			4.9	
Total after margin	27.2 L	24.8 kg	14 W	26.9 L	24.6 kg	12 W

Table 3.23: *Satellite SWaP summary for a MPTC architecture.*

Figure 3.6 features a visual comparison between the two architectures on-board a microsatellite.

	Laser Cooler		Miniature Pulse Tube Cooler	
	120 K	150 K	120 K	150 K
Power consumption	107 W	73 W	14 W	12 W
Satellite volume	32.8 L	26.5 L	27.2 L	26.9 L
(Internal volume)	(15.3 L)	(14 L)	(24.9 L)	(24.9 L)
Satellite mass	21.8 kg	18.9 kg	24.8 kg	24.6 kg

Table 3.24: *SWaP analysis summary.*

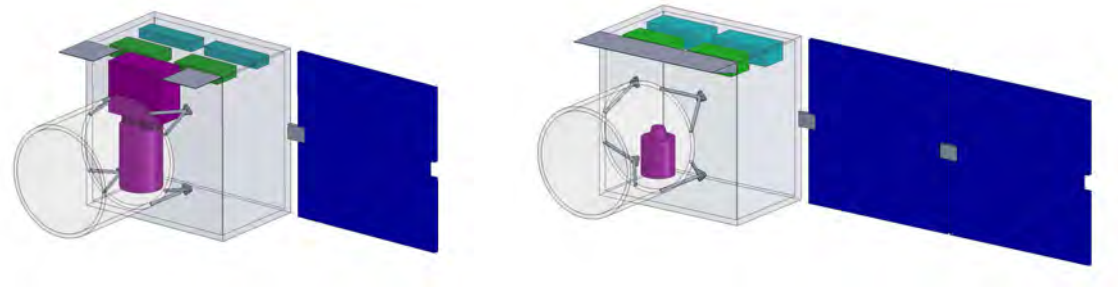

Figure 3.6: *Visual comparison between Miniature Pulse Tube Cooler (left) and Laser Cooler (right) architectures onboard an observation microsatellite at 150 K. Cryocooler and cryostat are shown in purple, electronics in green, batteries in cyan. A Laser Cryocooler requires approximately the surface of one additional small solar panel for a substantial payload volume and mass reduction.*

This study shows that laser cooling is a promising technology for the miniaturization of observation satellites. Using the same mission scenario, it is found that a laser cooler is favorable in terms of mass and internal volume savings compared to a Miniature Pulse Tube Cooler. Additionally, this solution presents other great advantages over mechanical cryocoolers:

- Zero vibrations generated due to the absence of moving parts.
- No electromagnetic perturbations near the focal plane.

- A smaller cryostat, less cables and simplified operation compared to a mechanical cryocooler.
- A simpler redundant architecture. Assuming that the cold head is less likely to fail being constituted of passive optical elements, only the electronics redundancy was considered, implying no thermal losses due to the cold head doubling.
- Increased payload flexibility with a compact cryocooler expected to fit in the volume of a glass of water.
- Increased platform flexibility with the cryocooler's power being supplied through an optical fiber, allowing the laser electronics to be located anywhere in the satellite.

All these advantages make possible the accommodation of a laser cryocooler on-board future low earth orbit small satellites as an innovative and breakthrough vibration-less alternative to mechanical cryocoolers in the 100 K - 200 K range, keeping in mind that laser cooling in solids is still a low TRL technology and has a wide potential for improvement in terms of cooling efficiency [26].

3.2 Laser cooling onboard CubeSats with co-doped crystals

In the second part, we are updating our analysis of the size, weight and power (SWaP) required at the level of a satellite to withstand the operation of a laser cryocooler. In our last study, we proved the feasibility of a laser cryocooler integrated onboard a LEO observation microsatellite [1]. This time, we are considering the new generation of co-doped Yb-Tm:YLF crystals with improved cooling efficiency. We show that the optimization of co-doped crystals would lead to a reduction of power consumption by a factor 2 at the level of the satellite, thus making it suitable for CubeSat cryogenics.

When updating our analysis, we chose this time to take into account the recent advances with co-doped cooling crystals. Indeed, it was found that adding a few ppm of Thulium inside an Ytterbium doped cooling crystal improves the cooling efficiency, by adding new energy transfers paths between Tm and Yb excited states. In co-doped samples, the background absorption appears lower due to the improved efficiency.

Recent crystal growth of 10 % Yb - 0.004 % Tm:YLF from the University of Pisa [27] exhibit a background absorption as low as $a_b = 6.10^{-5} cm^{-1}$, nearly an order of magnitude lower than standard Yb doped crystals, with an external quantum efficiency of $\eta_{ext} = 0.986$.

Under the reasonable assumptions of a co-doped sample with background absorption $a_b = 5.10^{-5} cm^{-1}$ and an external quantum efficiency as high as $\eta_{ext} = 0.995$ (often achieved in high quality YLF crystals), we are able to predict the improvement in cooling efficiency, as shown in Fig. 4. Such a sample would feature a maximum cooling efficiency of about 5% at room temperature, 2.5% and 1.6% at 150 K and 120 K respectively.

As we did in the first version, we took into account the cooling power required to cool down a total of 280 mW in the focal plane. These 280 mW account for: the detector thermal dissipation (150 mW), the conduction between the focal support and the cryostat (65 mW), the conduction between the detector wiring and the cryostat (35 mW), the radiative flux arriving on the detector from outside of the cryostat (15 mW), and the radiative flux from inside the cryostat (15 mW). The cooling power at the crystal level is proportional to the absorbed power:

$$P_{cool}^{crystal} = \eta_c(T_{crystal}) P_{abs} \tag{3.13}$$

However, one should take into account the thermal gradient between the focal plane and the crystal, such that the real cooling power at the level of the focal plane would be calculated for a colder crystal:

$$P_{cool}^{fp} = \eta_c(T_{fp} - \Delta T) P_{abs} \tag{3.14}$$

For a MgF_2 thermal link, considering a conductivity of 33.6 W/(m.K) a section 8 mm per 3 mm and 10 mm long, the estimated thermal gradient between the crystal and the end of the link is given by:

$$\Delta T = T_c - T_{fpa} = R_{link} P_{cool} \tag{3.15}$$

With R_{link} the link's thermal resistance, expressed in K/W:

$$R_{link} = \frac{l}{k \times s} \tag{3.16}$$

With l the link's length, k its thermal conductivity and s its section. Two materials are considered for the thermal link: YLF (undoped) and MgF2. MgF2 would be the most suitable material, as its thermal conductivity is almost 6 times higher than YLF (33.6 $W.m^{-1}.K^{-1}$ instead of 6 $W.m^{-1}.K^{-1}$ at room temperature), for almost matched thermal expansion coefficients. Assuming a thermal link 12 mm long with section 8mm mm yields $R_{link} = 14.88 K/W$ and $P_{cool} = 320 mW$, we find $\Delta T = 4.76 K$. In other words, it does not exceeds 5 degrees.

In addition, one has to take into account the thermal losses due to the fluorescence power

absorbed at the end of the thermal link plus radiative losses due to the hot environment. These losses total were estimated to approximately 30 mW with 47 W of laser power [6], split between 22.5 mW of mirror absorption and 7.5 mW of radiative losses for a crystal at 135 K.

With that knowledge, the losses can be estimated as a function of temperature. The thermal link absorption losses are proportional to the fluorescence power. The fluorescence power of a crystal is equal to:

$$P_{fluo} = (1 + \eta_c) P_{abs} \tag{3.17}$$

And the absorption losses can be expressed as:

$$P_{loss}^{abs} = \frac{0.045}{100} \times P_{fluo} = \frac{0.045}{100}(1 + \eta_c) P_{abs} \tag{3.18}$$

Radiative losses can be estimated relatively to the value of given in [6] at any temperature, considering a clamshell maintained at 300 K:

$$P_{loss}^{rad} = 7.5 \times 10^{-3} \frac{(T_{crystal} - T_{clam})^4}{(135 - T_{clam})^4} = 7.5 \times 10^{-3} \frac{(T_{crystal} - 300)^4}{(135 - 300)^4} \tag{3.19}$$

At the end of the thermal link, the net cooling power is expressed as:

$$P_{net} = P_{cool} - P_{loss}^{abs} - P_{loss}^{rad} = \eta_c P_{abs} - \frac{0.045}{100}(1+\eta_c) P_{abs} - 7.5 \times 10^{-3} \frac{(T_{crystal} - 300)^4}{(135 - 300)^4} \tag{3.20}$$

With $\eta_c = \eta_c(T_{fp} - \Delta T)$ the cooling efficiency calculated for a crystal colder than the required focal plane temperature. A counter-intuitive result appears: the highest the cooling efficiency, the highest the absorption losses are, due to a larger amount of fluorescence being emitted for each absorbed Watt. Fortunately, thermal link losses are modest in a Laser Cooler, such that the increase in cooling efficiency largely exceeds the increase in thermal losses due to a larger amount of fluorescence being extracted.

Figure 3.7 shows the thermal losses estimation for a constant absorbed power of 10 W, split between radiative losses and fluorescence absorption losses. Only the fluorescence absorption is proportional to the absorbed power. We can see that fluorescence absorption losses are almost constant, hence the variation of absorption losses due to the variation of cooling efficiency is negligible.

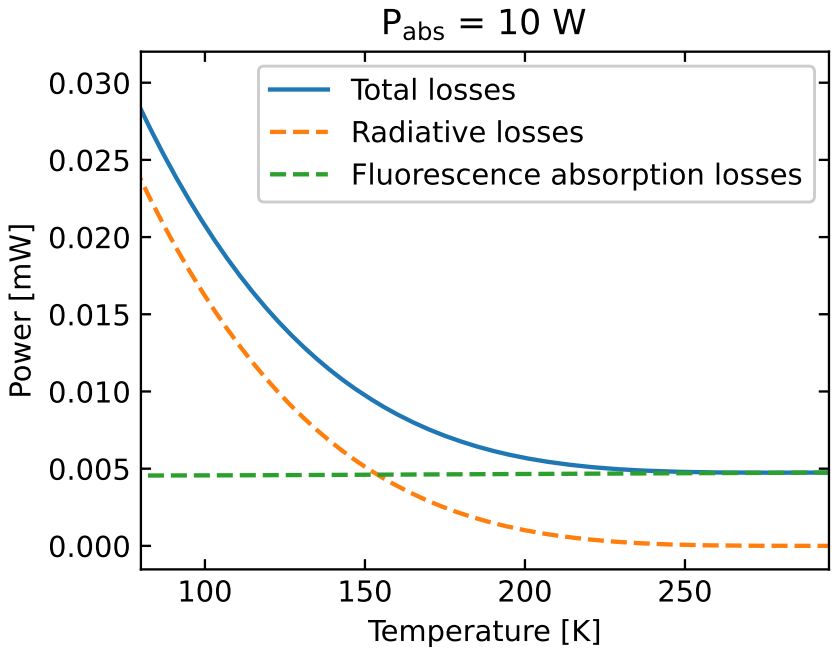

Figure 3.7: *Thermal losses estimation as a function of the crystal's temperature for 10 W absorbed power. Only the fluorescence absorption losses are proportional to the absorbed power.*

Under these new hypotheses for the thermal link and thermal losses, the SWaP calculations can be performed again for the single doped crystals ($\eta_{ext} = 0.995$ and $a_b = 5e - 4cm^{-1}$) and for the newest co-doped crystals generation ($\eta_{ext} = 0.995$ and $a_b = 5e{-}5cm^{-1}$).

For a focal plane at 150 K, a good co-doped crystal at 145 K possess a cooling efficiency of $\eta_c = 2.6\%$. For a focal plane at 120 K, a good co-doped crystal at 115 K possess a cooling efficiency of $\eta_c = 1.6\%$. Figure 3.8 and Figure 3.9 shows the estimated SWaP figures at 120 K and 150 K respectively, compared to the estimated performances using a single doping crystal from the previous generation.

We see that the foreseeable improvement in the crystal's cooling efficiency (specifically reducing the background absorption by an order of magnitude) have a huge impact on the power budget. This gain also have a repercussion on the size and weight figures, with less solar panels and batteries needed.

The main and important conclusion is that, with a power consumption of about 37 W at 150 K for the laser electronics, it is now already realistic to consider the use of a Laser Cryocooler on-board the smallest classes of satellites such as CubeSats. Depending on the mission and orbit, a Laser Cryocooler could fit into a CubeSat starting from 12U, thus enabling cryogenics applications on-board the smallest satellites such as near-infrared observation with the advantage of a vibration-free and miniaturized system.

This new paradigm could bring a small revolution in the field by creating an intermediary solution for entry-level cryogenics where before there was a gap around [100K-200K] between active mechanical cryocoolers and restrictive/bulky focal plane radiators.

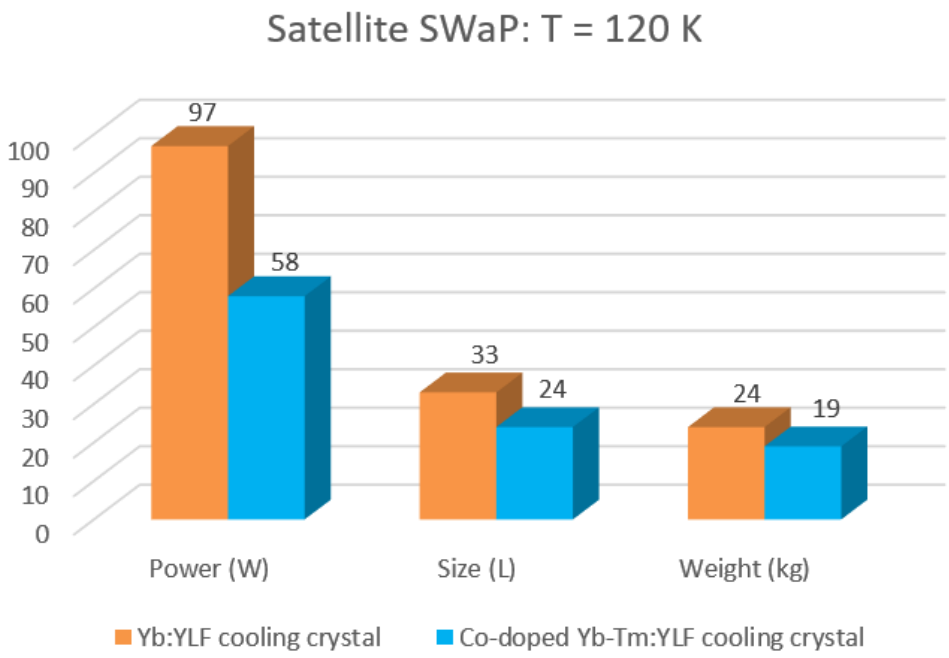

Figure 3.8: *Satellite size, weight and power analysis of a Laser Cryocooler: comparison between old and new co-doped cooling crystals generations at 120 K.*

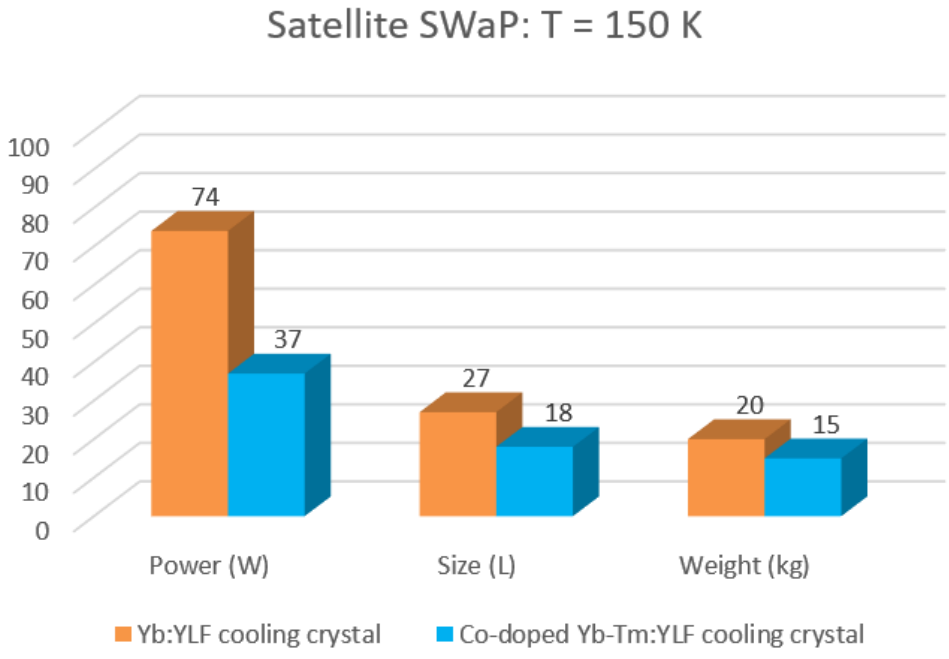

Figure 3.9: *Satellite size, weight and power analysis of a Laser Cryocooler: comparison between old and new co-doped cooling crystals generations at 150 K.*

3.3 Towards a prototype taking space constraints into account

3.3.1 Space constraints and exigences

Space products needs to be specially qualified in order to meet sufficient quality for space operation. For that purpose, in Europe, the European Cooperation for Space Standardization (ECSS) issues and maintains a number of standards, as a basis for all space actors and the improvement of the space industry in Europe. Indeed, the ECSS-S-ST-00C document defines the goals of the ECSS system as "achieving more cost effective space programs and projects in Europe", "improving the competitiveness of the European space industry", "improving the quality and safety of space projects and products", "facilitating clear and unambiguous communication between all parties involved, in a form suitable for reference or quotation in legally binding documents", and "reducing risks and guaranteeing interoperability and interface compatibility by applying proved and recognized requirements and methods".

Future qualifications for a Laser Cryocooler

We can foresee a number of tests that will have to be carried out in order to reach the space qualification of a Laser Cryocooler. The ECSS document ECSS-E-10-03A [28] defines the tests which have to be performed for the qualification of a space equipment.

Space qualification tests are generally performed in two phases: acceptance tests and qualification tests. Acceptance tests are made to check if the system functions with a moderate amount of stress. Qualification tests are made to check the functional limits and failure of the system. Within those two test phases, there are a number of tests which needs to be performed at system level.

The general tests involve the functional and performance tests, humidity compliance tests, life tests, and burn-in tests. The goal is to check if the performance are met under any conditions and the limits to these performances.

The mechanical tests and integrity tests involve vibrations tests and pressure cycling tests. The goal is to check if the system can mechanically withstand the launch into space.

The thermal tests involve thermal cycling and performance as a function of the equipment temperature. The goal is to check if the system can withstand the temperature variation expected in a space environment.

The electrical tests must assess the systems compliance when applying electromag-

netic perturbations (EMCs).

Component level radiation tests: In addition to system level tests, space components must undertake radiation tests in order to check if there is a performance degradation over time or any risk of premature failure due to the harsh radiations experienced in the space environment. For a Laser Cryocooler, the radiation tests campaign must address the lifetime of both the laser source electronics and the cold head.

Referring to the ECSS document ECSS-Q-ST-70-06C [29], *"Materials used in space applications need to be evaluated for their behavior under Particle and UV Radiation. As part of this evaluation often an exposure to a simulated space environment is performed that can raise questions regarding its accuracy and representativeness."*.

According to the scope of this standard, cooling crystals fall in this category as *"This Standard defines the procedures for electromagnetic radiation and charged particles testing of spacecraft materials. These materials include for instance thermal control materials, windows, coatings, and structural materials."* [29].

Unlike electronic components or semi-conductors, laser crystals do not suffer from sudden failure due to accumulated dose or single high energy events. Instead, they can suffer from a decrease in transmission (photo-darkening) and an increase in the number of defects, generating nanometer scale vacancies in the material which can absorb and emit at particular wavelengths, known as color centers. Radiation qualification campaigns were performed on Nd:YAG crystals for BepiColombo's qualification [30], which found a degradation of the Nd:YAG laser slope efficiency of a dozen of percent for gamma irradiation as high as 200 kRad, dependent on the pulsed laser repetition rate. The simulated radiation dose over the system lifetime was estimated to 20 kRad.

In an other publication, reference [31], the transmissions of 1%Nd:YAG, 1%Nd:YLF, undoped YAG and undoped YLF for laser applications after irradiation were evaluated. The color center transmission spectra were estimated after 200 kRad gamma ray for the doped samples. In the case of Nd:YLF, the transmission drop was minimal in the near-infrared. The decrease was about 10% in the near infrared around 1000 nm. Interestingly, the effect seems to depend on the dopant: for undoped YLF, the color centers decrease was much lower in the near infrared. Under 200 kRad gamma irradiation, the transmission dropped only by only a few percent in the near-infrared with the undoped YLF sample. The irradiation with 200 kRad protons showed similar transmissions.

Finally, the only reported radiation test specifically for laser cooling in solids was performed on Yb:YLF cooling crystals in reference [32]. The effect of radiation on cooling efficiency is still unclear. In the first reported test, in a 5%Yb:YLF sample with background absorption $a_b = 2.5e-4$ cm^{-1}, the external quantum efficiency went from $\eta_{ext} = 0.996$

to $\eta_{ext} = 0.987$ after an irradiating dose of 100 kRad. In the second reported test with 1%Yb:YLF, parameters $a_b = 6.0e-4$ cm^{-1} and $\eta_{ext} = 0.997$, no degradation at all was observed, after a much higher irradiation of 1 MRad.

In the future, the criticity of radiation effects in highly doped, high cooling efficiency samples needs to be studied, and adequate shielding margins taken into account if needed. These radiations tests should also to be put in perspective with the radiations doses experienced in LEO: on the order of 1 to 10 kRad per year, depending on the system shielding and the particular mission orbit. In other words, considering a 5 years mission, 2 to 20 times lower than the tested doses in laboratory.

3.4 Crystal growths requirements to reach nominal performances

Another important step in the scope of building engineering models is to specify how many boules should be grown and how many crystals should be cut before getting a crystal with at least the nominal cooling performances.

Indeed, obtaining a cooling crystal is not a trivial matter. It typically takes 1 month of Czochralski growth, up to 2 weeks in shaping (orienting, cutting, polishing). An estimated final cost for one growth is on the order of 5-10 k€ due to these mandatory steps, which splits mainly between the qualified manpower needed to watch over the growth and the electricity costs to power up a furnace with 10 kW power during 1 month.

We present here an analysis which can help to address and specify the future needs regarding cooling crystals for the development of Laser Cryocoolers.

A non-exhaustive list of cooling grade Yb:YLF crystals with different dopings grown at Pisa and in the USA can be found in reference [33] from 2013. These crystals were characterized with η_{ext} and a_b values. As we know, doping has little influence on the background absorption [34], hence it is relevant to compare a_b values for crystals which have different dopings, assuming they were grown in similar conditions with 5N-6N purity precursors with standard methods.

From the reported a_b values, we can fit a probability density function which describes the distribution of background absorption values for independent growths. Here, we chose to fit the data with a Generalized Extreme Values (GEV) distribution to account for the fact that the probability density of having $a_b = 0$ should be zero, and to account for rare-events where the background absorption is higher than $10^{-3}\ cm^{-1}$, as shown in Figure 3.10.

Knowing the probability density function $F(u)$, we are able to calculate the probability p of

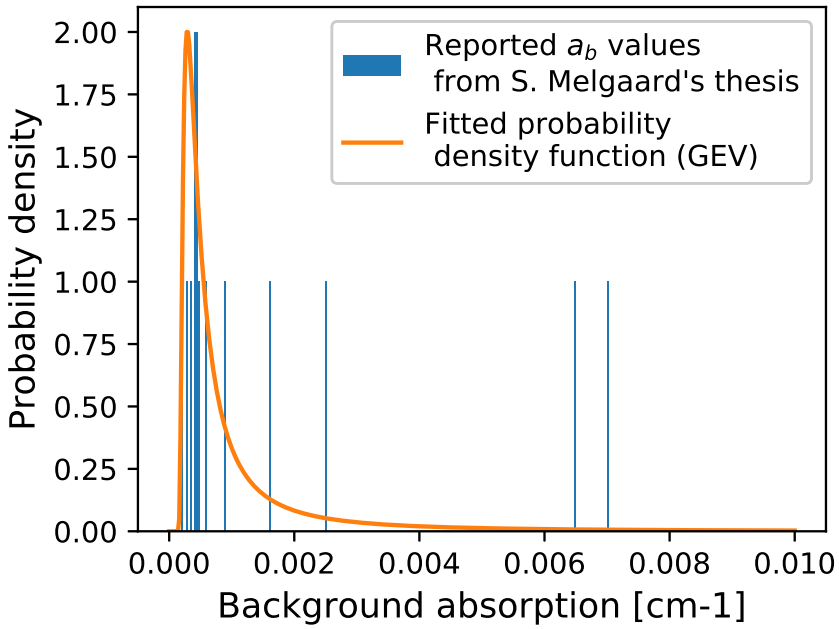

Figure 3.10: *Histogram of independent Yb:YLF Czochralski growths as a function of background absorption for the values reported in [33], fitted with a GEV probability density function.*

getting a_b inferior to a certain value x:

$$p[a_b < x] = \int_0^x F(u)du \tag{3.21}$$

The probability $p(a_b < x)$ is shown in figure Figure 3.11. We can see that the average background absorption value where $p(a_b < x) = 0.5$ is about $6.10^{-4}\ cm^{-1}$, while the probability of getting a background absorption lower than 2.10^{-4} is a one in a hundred event in the case of "standard" 4N/5N raw powders. The average number of growths required to get a crystal with a_b lower than a fixed value is equal to the inverse of p:

$$\bar{N}_{growths} = 1/p[a_b < x] \tag{3.22}$$

The average number of growths is shown in Figure 3.12. To conclude, for a reasonable number between 5 and 10 growths of Yb:YLF, one should statistically expect at least 1 boule with a_b equal or lower than $3.10^{-4}\ cm^{-1}$.

However, post-2013 results [19] showed that it is possible to improve a_b such that it reaches values below $10^{-5}\ cm^{-1}$, as shown with the record-setting 10%Yb:YLF crystal grown at AC Materials, Tarpon Springs, USA. The authors of these studies did not communicate the technical details of this particular growth, except that a lot of work on their side has been performed in order to find the correlation between the different transition metals concentration and the overall background absorption [35]. Fe^{2+} iron was found as the main contributor of background absorption around 1000 nm [36], an element which might be

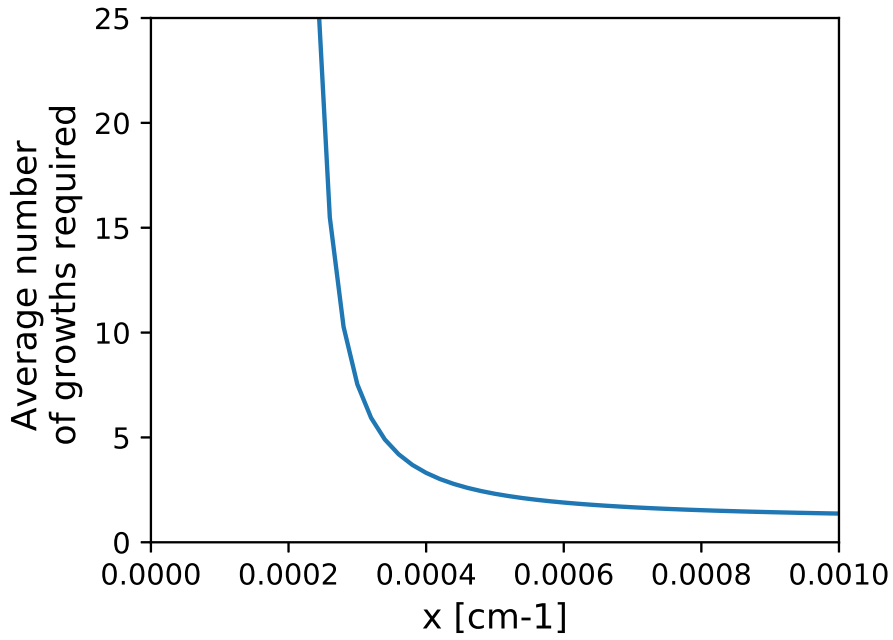

Figure 3.11: *Probability of getting a crystal with $a_b < x$, plotted for x between 0 and 10^{-3}.*

added by the YF_3 precursor before the growth [37].

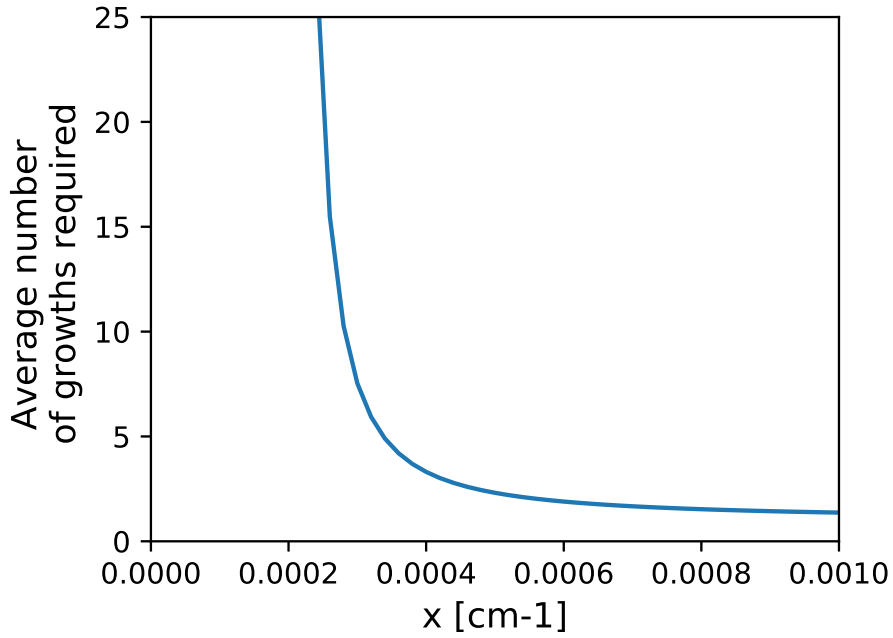

Figure 3.12: *Average number of growths required to get a crystal with $a_b < x$, plotted for x between 0 and 10^{-3}.*

This analysis highlights the fact that growing high quality crystals is the most time and money consuming task in building a laser cooler, as several crystal growth might be required before obtaining a sufficient quality crystal with standard growth procedures.

Breakthrough progress in the last decade showed that it is possible to reach background absorption lower than $10^{-5}\ cm^{-1}$, and several purification methods proved to be effective

[35][37] in reducing the impurities concentrations, although it was pointed out that these techniques might be tedious and slow to implement [38]. Ultimately, these purification techniques might prove cost-effective in comparison of growing a large number of boules with standard methods, and they should be developed further in order to improve the performances of laser cryocoolers.

Our statistical analysis should be performed again for co-doped crystals or with different dopants to get an idea on how to specify the background absorption and the number of growths. We can also think of further improvements to this analysis by developing an estimation model with more variables: for example taking into account the defects distribution inside a boule (micro bubbles) and its relationship with n_{ext}, or taking into account the different impurities concentrations.

3.5 Conclusion: towards an engineering model

In this chapter, we performed for the first time the specification and pre-study steps leading to the satellite integration of a Laser Cryocooler onboard a small class satellite.

The size, weight and power analysis of a Laser Cooler at the level of a whole satellite showed that the system is highly miniaturized, compared to an architecture with mechanical cryocoolers, leaving a lot of space in the satellite payload part, for comparable total volume (about half of the total volume being located in the solar array increase) and reduced overall mass at 150 K.

While a Laser Cryocooler is already possible with single doped crystals, an increase in cooling efficiency is foreseen, due to the increase in crystal growths purity, and the mastering of co-doped Tm,Yb:YLF crystals. This efficiency increase would allow the next generation of cooling crystals to be so efficient that they can be embarked on Cubesats, leading to exciting new possibilities for miniaturized cryogenics infrared instruments.

The next step now is to tend towards an engineering model which can then be qualified following the ECSS test requirements. Particularly, the laser source and cooling crystals radiation tests will be of importance. In the future, a road-map must be implemented which takes into account the concepts presented in this chapter as a basis for the TRL increase.

More than ever, the path to an optical cryocooler onboard an observation satellite is now a matter of time, boosted by the recent exceptional results in the last decade with YLF cooling crystals, which always keeps improving with time. We can estimate the first Laser Cryocooler engineering qualification prototype being within reach in a matter of 5 years.

References

[1] R. Vicente, G. Nogues, J.-M. Niot, T. Wiertz, P. Contini, and A. Gardelein, "Impacts of laser cooling for low earth orbit observation satellites: An analysis in terms of size, weight and power," *Cryogenics*, 2020.
DOI: 10.1016/j.cryogenics.2019.103000 (cit. on pp. 92, 111).

[2] F. Buisson, "The MicroCarb Project: recent achievements and review of the project status," *IWGGMS-15, Sapporo*, 2019 (cit. on p. 93).

[3] R. J. Boain, "AB-Cs of sun-synchronous orbit mission design," *14 AAS/AIAA Space Flight Mechanics Conference*, 2004. [Online]. Available: https://trs.jpl.nasa.gov/handle/2014/37900 (cit. on p. 93).

[4] B. Nadir, "MIT Open Courses, Satellite Engineering," 2003. [Online]. Available: https://ocw.mit.edu/courses/aeronautics-and-astronautics/16-851-satellite-engineering-fall-2003/ (cit. on pp. 93, 95).

[5] A. Delannoy, B. Fièque, P. Chorier, and C. Riuné, "NGP: a new large format infrared-detector for observation,hyperspectral and spectroscopicspace missions in VISIR, SWIR andMWIR wavebands," *Proc. of SPIE*, 2015.
DOI: 10.1117/12.2197239 (cit. on p. 94).

[6] E. Lapeña, J. L. Herranz, F. Gómez-Carpintero, and M. Rodríguez, "The LEO PCDU EVO-A Modular and Flexible Concept for Low to Medium Power LEO & Scientific Missions," *E3S Web of Conferences*, 2017.
DOI: 10.1051/e3sconf/20171618009 (cit. on pp. 95, 103).

[7] W. Guter, L. Ebel, D. Fuhrmann, W. Kostler, and M. Meusel, "Development, Qualification and Production of Space Solar Cells with 30% EOL Efficiency," *10th European Space Power Conference*, 2014. [Online]. Available: https://ui.adsabs.harvard.edu/abs/2014ESASP.719E..72G (cit. on p. 95).

[8] SpaceTech GmbH, "Solar arrays product information," 2021. [Online]. Available: https://www.spacetech-i.com/products/solar-arrays (cit. on p. 95).

[9] M. Imaizumi, T. Takamoto, N. Kaneko, Y. Nozaki, and T. Ohshima, "Qualification Test Results of IMM Triple-Junction Solar Cells, Space Solar Sheets, and Lightweight&Compact Solar Paddle," *11th European Space Power Conference*, 2017.
DOI: 10.1051/e3sconf/20171603012 (cit. on p. 95).

[10] D. Y. Borthomieu and S. Remy, "VES16 cells and batteries for LEO & small GEO," *11th European Space Power Conference Proceedings*, 2014 (cit. on pp. 96, 104).

[11] S. Remy, D. Prevot, D. Reulier, and D. F. Vigier, "VES16 Li-Ion Cell For Satellite," *9th European Space Power Conference Proceedings*, 2011 (cit. on p. 96).

[12] D. Prevot, Y. Borthomieu, E. Ligneel, R. Hague, J.-P. Peres, and C. Cenac-Morthe, "Performances of Saft Lithium-Ion Cells in LEO Cycling," *11th European Space Power Conference Proceedings*, 2017.
DOI: 10.1051/e3sconf/20171606005 (cit. on p. 96).

[13] C. Hoa, B. Demolder, and A. Alexandre, "Roadmap for developing heat pipes for ALCATEL SPACE's satellites," *Applied Thermal Engineering*, 2003.
DOI: 10.1016/S1359-4311(03)00039-5 (cit. on pp. 96, 104).

[14] J. Schilke, A. Natusch, and H. Ritter, "BepiColombo Radiator Breadboard Performance Test," *SAE Technical Paper*, 2008.
DOI: 10.4271/2008-01-2063 (cit. on p. 97).

[15] J. H. Saleh, D. E. Hastings, and D. J. Newman, "Spacecraft Design Lifetime," *Journal of Spacecrafts and Rockets*, 2003.
DOI: 10.2514/2.3806 (cit. on p. 97).

[16] A. Gragossian, J. Meng, M. Ghasemkhani, A. R. Albrecht, and M. Sheik-Bahae, "Astigmatic herriott cell for optical refrigeration," *Optical Engineering*, 2017.
DOI: 10.1117/1.OE.56.1.011110 (cit. on pp. 98, 101).

[17] Almeco, "TiNOX Solar Absorber," [Online]. Available: https://www.almecogroup.com/en/pages/479-absorbers (cit. on p. 98).

[18] Acktar, "Nano-Black," [Online]. Available: https://www.acktar.com/product/nano-black/ (cit. on p. 98).

[19] S. D. Melgaard, A. R. Albrecht, M. P. Hehlen, and M. Sheik-Bahae, "Solid-state optical refrigeration to sub-100 kelvin regime," *Nature Scientific Reports*, 2016.
DOI: 10.1038/srep20380 (cit. on pp. 101, 119).

[20] M. P. Hehlen, J. Meng, A. R. Albrecht, E. R. Lee, A. Gragossian, S. P. Love, C. E. Hamilton, R. I. Epstein, and M. Sheik-Bahae, "First demonstration of an all-solid-state optical cryocooler," *Light: Science & Applications*, 2018.
DOI: 10.1038/s41377-018-0028-7 (cit. on p. 101).

[21] Jenoptik, "Jenoptik laser diodes array DL-BAB-50-23-1020-TE-120-2.0," 2021. [Online]. Available: https://www.jenoptik.com/products/lasers/ (cit. on p. 102).

[22] Ottenhues, C. et al., "Single mode monolithic fiber laser with 200 w output power at a wavelength of 1018 nm," *Optics Letters*, 2015.
DOI: 10.1364/OL.40.004851 (cit. on p. 102).

[23] T. Trollier, J. Tanchon, J. Buquet, and A. Ravex, "Status of Air Liquide Space Pulse Tube Cryocoolers," *Cryocoolers 15*, 2009 (cit. on p. 105).

[24] C. Chassaing, J. Butterworth, G. Aigouy, C. Daniel, and M. Crespin, "50K – 200K Miniature Pulse Tube Cooler for MicroSatellites," *AIP Conference Proceedings*, 2014. DOI: 10.1063/1.4860746 (cit. on p. 105).

[25] Air Liquide Advanced Technologies, "Active cryocooling for space applications, Turnkey solutions from 10K to 200K," 2021. [Online]. Available: https://advancedtech.airliquide.com/active-cryo-cooling-space-application (cit. on p. 106).

[26] S. Rostami, A. Volpi, A. R. Albrecht, and M. Sheik-Bahae, "Progress towards optical cryocooling in Mid-IR," *Proc. of SPIE*, 2019. DOI: 10.1117/12.2509017 (cit. on p. 111).

[27] G. Cittadino, E. Damiano, A. Di Lieto, and M. Tonelli, "First demonstration of optical refrigeration efficiency greater than 4% at room temperature," *Optics Express*, 2020. DOI: 10.1364/OE.390283 (cit. on p. 111).

[28] European Cooperation for Space Standardization, "ECSS-E-ST-10-03C – Testing," 2012. [Online]. Available: https://ecss.nl/standard/ecss-e-st-10-03c-testing/ (cit. on p. 116).

[29] European Cooperation for Space Standardization, "ECSS-Q-ST-70-06C – Particle and UV radiation testing for space materials," 2008. [Online]. Available: https://ecss.nl/standard/ecss-q-st-70-06c-particle-and-uv-radiation-testing-for-space-materials/ (cit. on p. 117).

[30] Kallenbach, R. et al., "Space-qualified laser system for the BepiColombo Laser Altimeter," *Applied Optics*, 2013. DOI: 10.1364/AO.52.008732 (cit. on p. 117).

[31] T. S. Rose, M. S. Hopkins, and R. A. Fields, "Characterization and control of gamma and proton radiation effects on the performance of Nd:YAG and Nd:YLF lasers," *IEEE Journal of Quantum Electronics*, 1995. DOI: 10.1109/3.406369 (cit. on p. 117).

[32] K. W. Martin, S. D. Melgaard, V. M. Cowan, J. Hubbs, T. Fraser, and M. Sheik-Bahae, "Radiation effects on Yb:YLF crystals used in cryogenic optical refrigerators," *Proc. of SPIE*, 2015. DOI: 10.1117/12.2189843 (cit. on p. 117).

[33] S. D. Melgaard, *Cryogenic optical refrigeration: Laser cooling of solids below 123 K*. 2013. [Online]. Available: https://digitalrepository.unm.edu/ose_etds/24/ (cit. on pp. 118, 119).

[34] S. Bigotta and M. Tonelli, "Laser cooling in fluoride single crystals," *Optical Refrigeration: Science and Applications of Laser Cooling of Solids*, 2009. DOI: 10.1002/9783527628049.ch3 (cit. on p. 118).

[35] M. Hehlen, W. Boncher, M. Blair, R. Jackson, T. Littleford, and S. Love, “Preparation of high-purity lif, yf3, and ybf3 for laser refrigeration,” *Proceedings of SPIE*, 2014.
DOI: 10.1117/12.2039547 (cit. on pp. 119, 121).

[36] S. Melgaard, S. Denis, V. Polyak, Y. Asmerom, and M. Sheik-Bahae, “Identification of parasitic losses in yb:ylf and prospects for optical refrigeration down to 80k,” *Optics Express*, 2014.
DOI: 10.1364/OE.22.007756 (cit. on p. 119).

[37] W. Boncher, E. Judge, J.-M. Sansinena, M. Dirmyer, and M. Hehlen, “Purification of precursors of yb3+ doped ylf crystals by solvent extraction and electrochemical processing,” *Proceeding of SPIE*, 2015.
DOI: 10.1117/12.2077235 (cit. on pp. 120, 121).

[38] A. Volpi, J. Meng, A. Albrecht, M. Sheik-Bahae, D. Biner, K. W. Krämer, and M. P. Hehlen, “Bridgman growth of LiYF4 and LiLuF4 crystals for radiation-balanced lasers,” *Proc. of SPIE*, 2019.
DOI: 10.1117/12.2510691 (cit. on p. 121).

Chapter 4

Laser Cryocooler design and development

This chapter covers the design and development of our fibered Laser Cryocooler prototype. Based on the requirements of a laser cooler for space applications, we selected an optical architecture among existing laser cooling schemes. Our Laser Cryocooler features an astigmatic multi-pass cavity with the cooling crystal at its center. An innovation is the optical power being supplied remotely from the laser source through a fibered design for the first time in the world. Optical simulations were performed to specify the multi-pass cavity and the coupling laser bench parameters. The prototype was then fabricated and the coupling and cooling benched assembled. Finally, we present a series of tests which were performed to assess the quality of cooling crystals before starting the experiment.

Ce chapitre couvre la conception et le développement de notre prototype de Cryo-refroidisseur Laser fibré. Basé sur les spécifications d'un refroidisseur laser pour les applications spatiales, nous avons sélectionné une architecture optique permis les schémas de refroidissement existant. Notre Cryo-refroidisseur Laser présente une cavité astigmate multi-passages avec le cristal situé en son centre. Une innovation est le design fibré permettant d'acheminer la puissance laser depuis n'importe quelle distance, une première dans le monde. Des simulations optiques ont été faites pour spécifier les paramètres de la cavité multi-passages et du banc de couplage laser. Le prototype a ensuité été fabriqué et les bancs de couplage et de refroidissement assemblés. Enfin, nous présentons en fin de chapitre une série de tests réalisés afin de féterminer la qualité des cristaux refroidisseurs avant de lancer l'expérience.

4.1 Optical design

Optical design refers to the process of translating a set of requirements into an optical system which can be then manufactured and tested. In the same way as any other engineering field, optical design criteria are based on a mix between performances, complexity, raw costs, and heritage/development costs of a certain solution.

We can divide optical systems in two classes: imaging and non-imaging systems. The design of a Laser Cryocooler belongs to the latter. At the difference of imaging systems where performances often exclusively focuses on the image quality in terms of aberration and light collection, non-imaging optical systems can have widely different "merit functions" depending on the design purpose.

In a Laser Cryocooler, the main system level requirement is to achieve a maximal absorbed laser power while keeping the losses at a minimum, in other words, the sole merit function for performance is the cooling power per Watt of pump laser power. As stated before, the absorption of cooling crystals decreases with temperature by an order of magnitude between ambient and cryogenics temperatures. The main challenge that the optical design has to address here is how to ensure the largest laser path inside the crystal such that most of the power is absorbed.

The two system requirements arising from the space applications are the need to attain the performance in the most compact volume, and if possible without mechanisms which could decrease the system's reliability, i.e. we should avoid relying on actuated optical elements and prefer a fixed design.

Finally, another system requirement is to separate the laser source and the cold head in two distinct parts in order to make a device which can be easily adapted to different architectures. Within this paradigm, the Laser Cryocooler is now fibered, with a coupling between the source and the crystal.

Before starting the optical design, it was useful to study the literature and the solutions explored by our predecessors in the field of laser cooling. As detailed in the next sections, laser cooler can be designed following two different paradigms: intra-cavity and extra-cavity. Within those paradigms, different solutions exist in order to achieve a high number of passes and high absorption of the pump laser beam inside the crystal.

4.1.1 Pumping schemes

A laser cooler requires fundamentally two parts : a laser source and a cooling medium. There are two classes of laser coolers. If the cooling medium is inserted in the middle of

the laser source cavity, the setup is referred to as intra-cavity laser cooler. If the cooling medium is external to the laser source, the setup is referred to as extra-cavity.

Intra-cavity laser cooler

The idea of intra-cavity laser cooling has been tested at the University of New Mexico using a VECSEL pumped with a 808 nm laser diode [1], as shown in Figure 4.1.

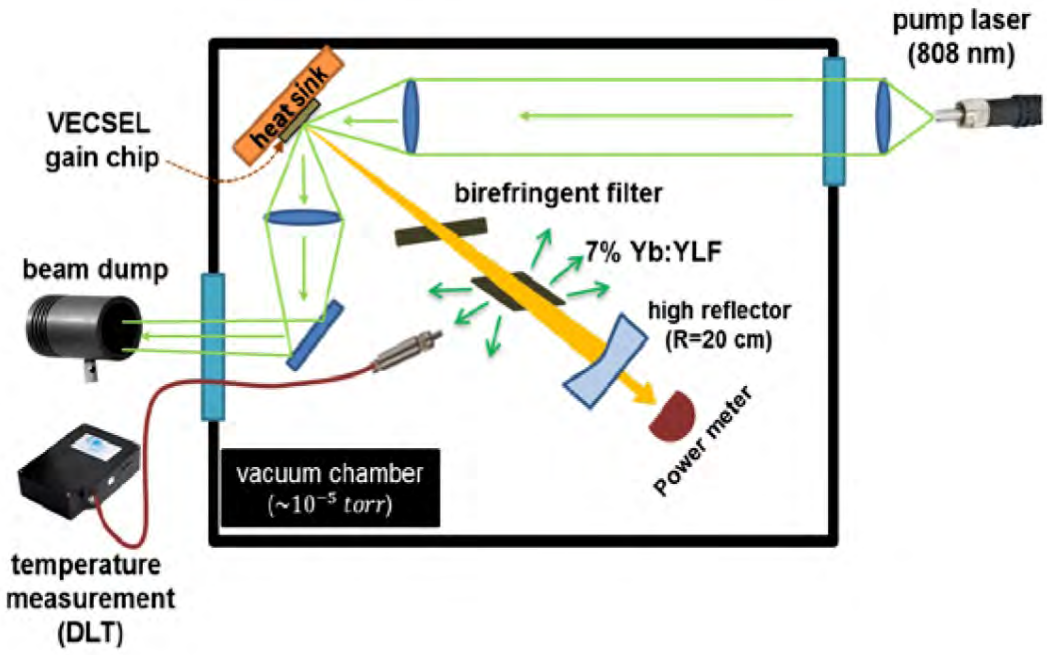

Figure 4.1: *Schematic of an intra-cavity laser cooler, from reference [1]. The cooling crystal is located inside a VECSEL's extended cavity. A birefringent filter allows to tune the VECSEL emission wavelength.*

The advantages of an intra-cavity setup is the shorter dimension of crystals which can be employed, thus limiting re-absorption losses. The drawback is that the pumping source may be less efficient than a separate dedicated laser source.

In the VECSEL case, assuming 50% conversion efficiency for the 808 nm laser diodes and the 40% VECSEL slope efficiency, the overall wall plug efficiency would be only 20%. Comparatively, laser diodes at 1020 nm typically possess efficiencies as high as 50%.

Another main drawback is the cooling medium absorption at room temperature. Indeed, in the case of the reported 7%Yb:YLF intra-cavity, room temperature absorption at 1020 nm is on the order of 1 cm^{-1}. As the authors of the study point out, this absorption is an issue because it is "*well above the* [VECSEL] *lasing threshold*". The options to kick-start the cooling process are either to increase the laser source power, or tune the VECSEL wavelength above 1020 nm where Yb:YLF absorption starts decaying. These problems needs to be addressed for a practical implementation inside a satellite, where power consumption is critical and a tunable laser source might not be easily available or require increased

complexity.

A special type of intra-cavity laser cooler is the radiation-balanced laser, or athermal laser. In that configuration, the crystal assumes both roles of lasing medium and cooling medium. The first athermal laser has also been demonstrated at the University of New Mexico in a 5%Yb:YAG disk laser [2], as shown in Figure 4.2.

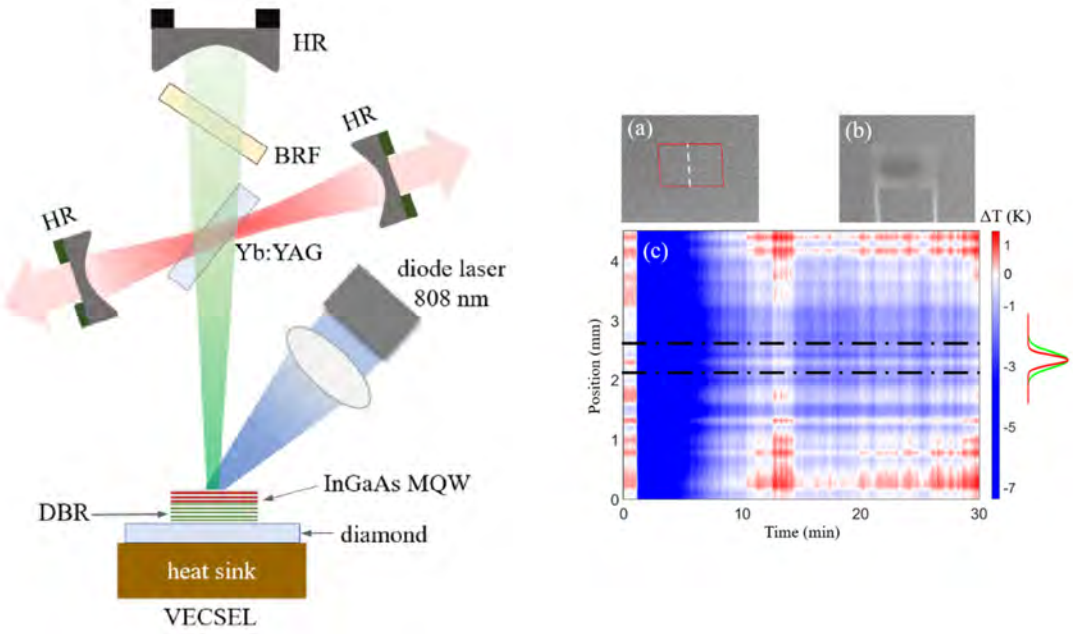

Figure 4.2: *Schematic of a radiation balanced laser, adapted from reference [2]. Left: Optical layout of the RBL experiment. The Yb:YAG cooling crystal is located in intra-cavity cooling configuration. Two HR cavity mirrors allow to use the crystal's fluorescence to make a laser in the transverse direction. Right: Temperature profile of the Yb:YAG crystal showing the colder region at its center.*

In such lasers, the expected efficiency is smaller compared to classical lasers, part of the energy being used in the cooling cycle. We can say it is neither an excellent laser, nor an excellent cooler. However, the operation of such a laser allows to limit thermal lensing effects, which are critical and limiting parameters for kiloWatt-class lasers, requiring active thermal management. In the future, athermal lasers possess the potential to ease the implementation of very high power lasers.

Extra-cavity laser cooler

The second class of laser cooler is the extra-cavity scheme. In that scheme, the laser source is separated from the cooling crystal. The energy can be supplied to the cooling crystal in free space, or through an optical fiber which is an advantage for practical implementations. While the laser source can be chosen freely and potentially more efficient, in turn, there are additional coupling losses compared to the intra-cavity scheme as detailed in the next section, due to the non-unit absorption efficiency.

Both architectures possess advantages and drawbacks. In our work the choice has been made to implement an extra-cavity laser cooler, where the design efforts can be concentrated around the cooling crystal and the cold head without the laser source problems.

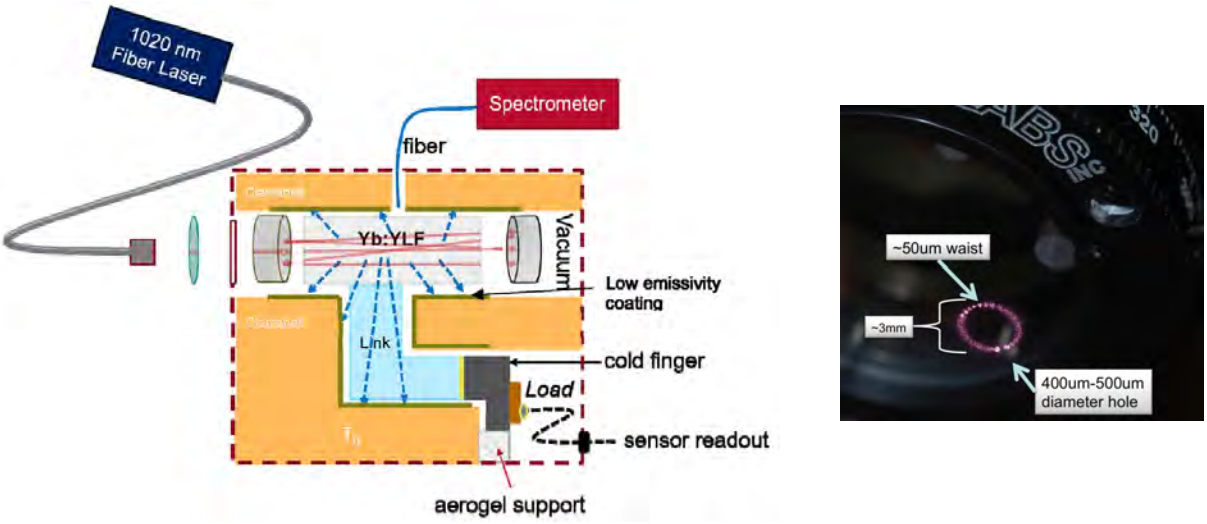

Figure 4.3: *Left: Schematic of the extra-cavity Laser Cooler at the University of New Mexico, from reference [3]. Right: View of the roundtrips on first mirror in a multipass design with two spherical mirrors, from reference [4].*

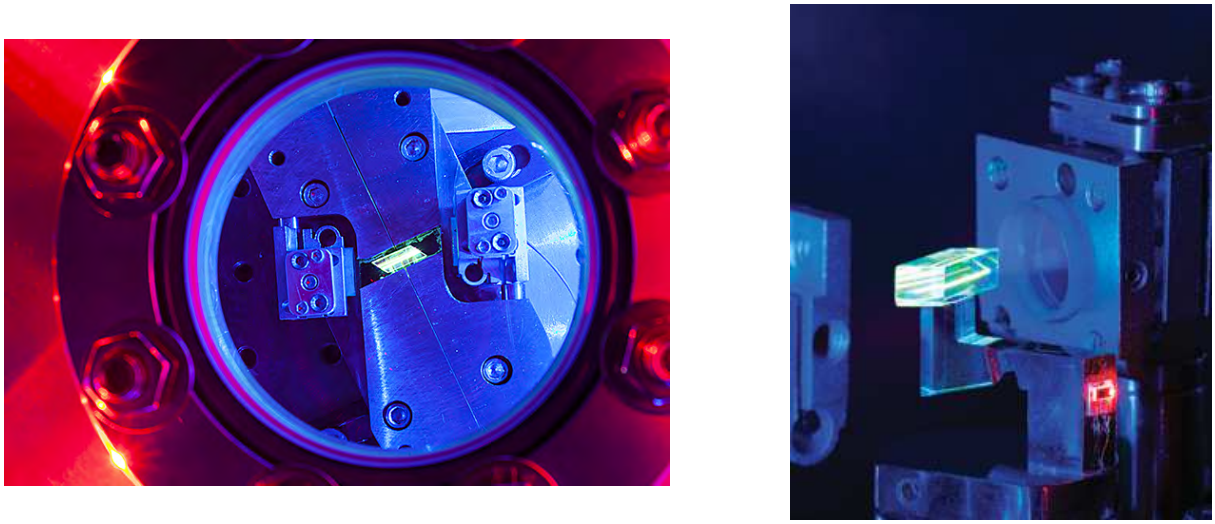

Figure 4.4: *Left: View of the cooling crystal in the American Laser Cooler, from reference [5]. Right: View of the cooling crystal without clamshell, from reference [6].*

4.1.2 Suitable crystal geometries

Rectangular shape

The rectangular shape is the most convenient shape to craft, as it is easy to cut and polish. Usually, crystals are directly carved in rectangular shapes from the boule. Rectangular

shaped crystals possess the advantage of being straightforward to align for absorption and cooling efficiency measurements, with the pumping beam entering and exiting the crystal at normal incidence.

Cylinder shape

The cylinder shape has a better external quantum efficiency compared to the rectangular shape due to the absence of angles which cause total internal reflections. However, attaching a thermal link to a cylinder crystal would require a more complex system than for a plane interface and has never been done so far.

Optical maze

The optical maze is a class of special shapes which allows the pump beam to be totally internally reflected inside the crystal, while the fluorescence can escape freely. Such examples of optical mazes can be found in references [7] and [8], as shown in Figure 4.5.

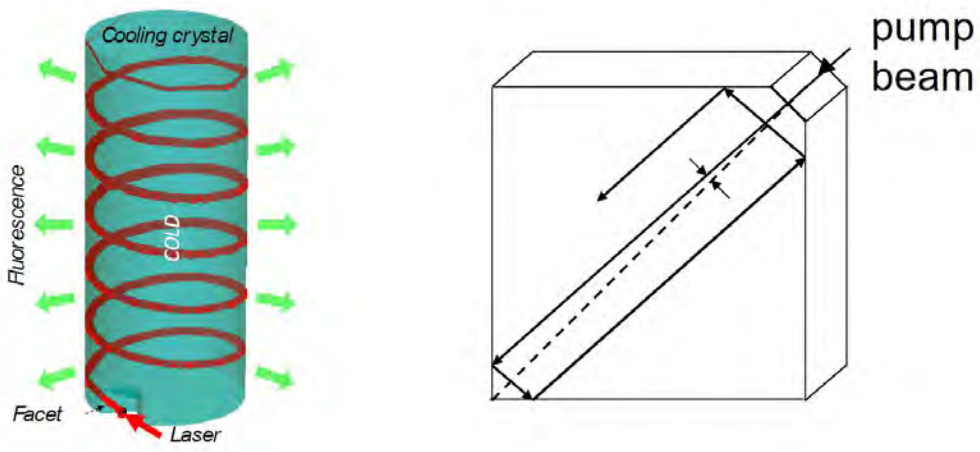

Figure 4.5: *Examples of optical maze shaped crystals. Left: Cylindrical maze with an entrance facet, as suggested by reference [8]. Right: Monolithic Optical Maze, as suggested by reference [7].*

Brewster cut

The Brewster cut is a shape of laser crystal that allows to cancel the Fresnel reflections of transverse electric (TE) modes on the entry and exit faces. Traditionally, this kind of optical design is used in Ti:Sapphire laser cavities or others cavities when there is a need to work without anti-reflection coatings. It makes sense to use Brewster cut crystals in laser cooling experiments in order to maximize the power absorbed in the crystal. The drawbacks of Brewster cut crystals are:

- A more complex optical design with an off centering of the optical axis generated by the refraction of the laser through the crystal.
- The need for longer dimensions to craft the Brewster angles.
- More efforts in the cutting and polishing steps to precisely set the Brewster angle.
- Crystals are more brittle and prone to scratches around the sharp angles.

The angles of a Brewster cut crystal are shown in Figure 4.6.

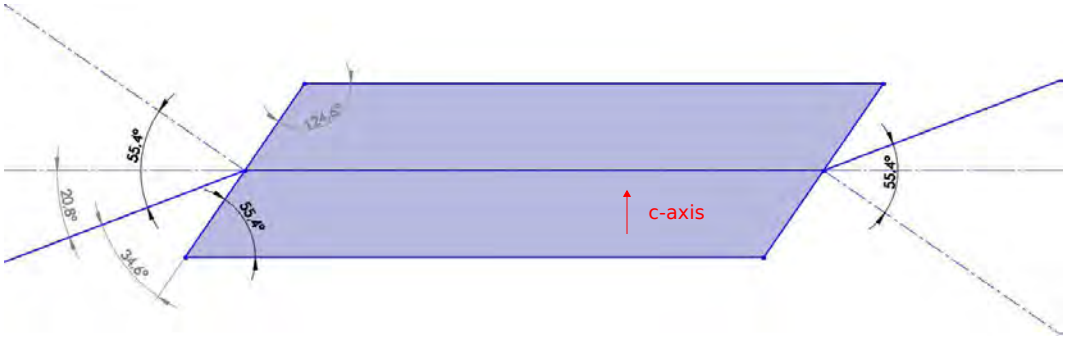

Figure 4.6: *Brewster cut geometry for a crystal with 10 mm length and 3 mm section.*

4.1.3 High power fiber coupling design

One of our goals in the laser cooling experiment is to demonstrate the feasibility a cold head powered up by a laser source located remotely at any distance with the laser beam being guided through an optical fiber. Transporting and delivering high optical powers through optical fibers is no problem, as it is commonly achieved with fiber lasers and amplifiers. The main issue here is how to send the laser beam inside the fiber and how much injection losses there would be, i.e. the part of optical power being reflected at the interface air/glass and the part of optical power being absorbed near the fiber due to cladding absorption.

For this purpose, there are two solutions. The laser source used in the cooling experiment at 1020 nm is an Yb fiber laser. Inside the laser, a small length of Yb doped optical fiber making the optical cavity is precisely coupled or spliced to a length of undoped optical fiber. There is a collimator at the fiber's end, ensuring that the output beam has a beam diameter Ø = 5 mm. The first solution would be to cut out the standard collimator from the fiber's end, attach a new collimator and bring this assembly inside the vacuum enclosure. This solution would be preferred in the case of a practical implementation inside a satellite. However, in case of problems, the laser guarantee would be void as it consists of a modification of the commercial setup.

The preferred solution in the lab is to send out the laser beam in open space and re-couple it inside a disposable optical fiber, which can be cut out or re-made in case of problem. Upon contacting the 1020 nm laser manufacturer IPG, we got the fiber's reference used in the laser: polarization maintaining fibers with large mode area from the company Nufern, which we decided to use as well.

We designed a coupling bench with the function of sending a polarized laser beam up to 50 W power into a polarization maintaining fiber with high coupling efficiency; sending a low power laser beam from the Ti:Sapphire laser for alignment purposes and coupling the setup at different wavelengths; and containing at maximum the free space laser inside a box or limited area to ensure the user's safety.

The coupling bench design is schematized in Figure 4.7. There are two laser paths: the first one with the high power laser and the other with the low power Ti:Saph.

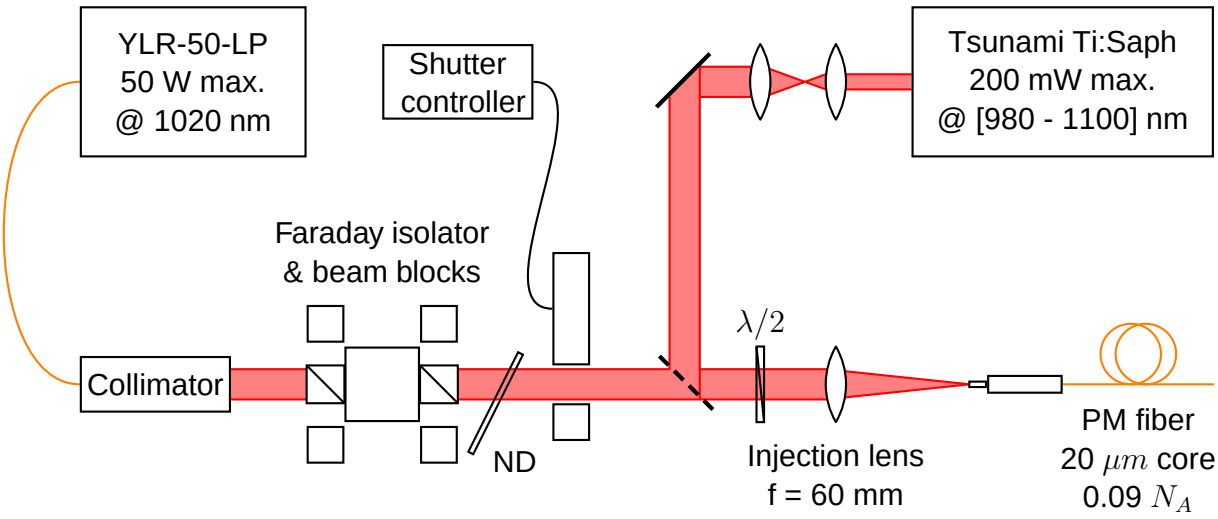

Figure 4.7: *Coupling bench schematic showing the different elements.*

First, the high power laser exits out of the collimator to free-space with 5 mm beam diameter ($1/e^2$). An optical isolator is placed directly after the collimator. These isolators based on the magneto-optical Faraday effect rotates the input beam polarization in such a way that the beam can travel in the direction laser -> experiment but it is deviated in the opposite direction. This setup allows to protect the laser source from potentially harmful reflections. Faraday isolators provide more than 30 dB optical power isolation (1/1000 ratio). Beam dumps are disposed on the isolator's sides to absorb the reflected power.

The laser crosses then a variable neutral density filter. When rotating the plate, its transmission varies continuously from 0 to 10^{-4}. With a minimal laser power of 2.5 W, this allows to operate the experiment at a power lower than 1 mW if desired. A mechanical shutter is used to block the laser beam without turning off the laser source. This is implemented as a

security measure.

A half wave plate allows to rotate the beam's polarization. Indeed, in a polarization maintaining fiber, the input polarization needs to be aligned either parallel or perpendicular to the fiber's eyes. The beam is then collimated with a focusing lens into the fiber core. The lens is mounted on a two axes XY stage, while the optical fiber is held by a chuck in a three axes XYZ stage, ensuring micrometer precision displacement using differential micrometer heads.

On the second path, the Ti:Saph laser with 2 mm initial beam diameter is first expended by a pair of lenses to attain 5 mm. It is then coupled into the fiber using a 45° removable mirror.

Coupling lens and fiber selection

In order to maximize the power injected through the fiber, the focusing lens must be chosen such that the focused beam diameter matches the fiber's mode-field diameter (MFD).

The adapted focal length can be calculated with the relationship:

$$f = \frac{\pi D \omega}{4\lambda} \tag{4.1}$$

Usually though, optical fiber suppliers do not state the mode-field diameter directly as it depends on wavelength but they specify the fiber's core radius and numerical aperture. The mode-field diameter of a fiber can be estimated using the relationship:

$$\omega = 2a\left(0.65 + \frac{1.619}{V^{3/2}}\right) + \frac{2.879}{V^6} \tag{4.2}$$

With V the fiber's "*v-value*" at the laser wavelength, defined as:

$$V = \frac{2\pi a \times N_A}{\lambda} \tag{4.3}$$

The optimal focal length for injection at 1020 nm is shown in Figure 4.8 for different polarization maintaining fibers available online. To get the best performance, one must select ideally an aspheric lens or an achromatic doublet matching one of the fibers with a core diameter of 20 μm, which translate to focal length around 60 mm. Commonly available "stock" focal lengths for aspheres and doublets are 30, 50, 60 and 100 mm. Aspheres feature typically lower aberrations than achromatic doublets but they are often more expensive do to higher manufacturing times.

At the end, we chose a couple with an achromatic doublet ACA 254-060-B with f =

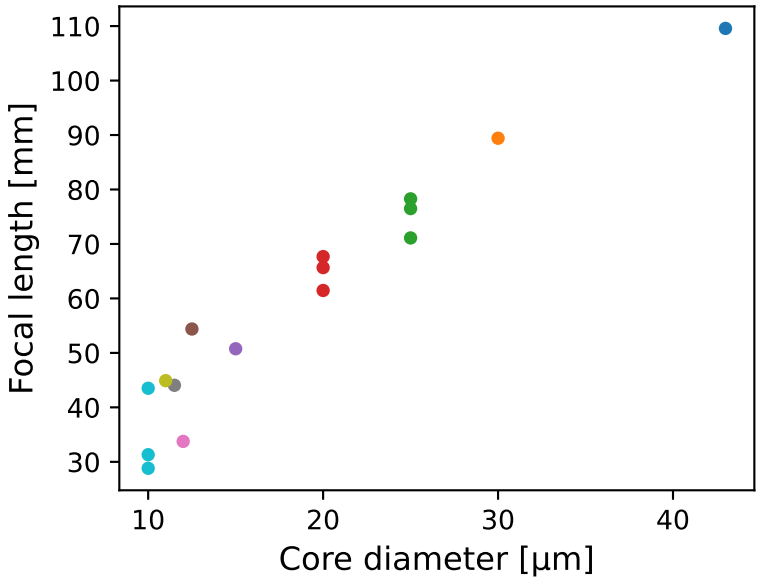

Figure 4.8: *Required coupling focal length at 1020 nm as a function of the optical fiber core diameter, plotted for several couples of fiber core/numerical aperture found on Nufern's catalog.*

60 mm from Thorlabs matching the fiber PLMA-GDF-20-250-09 PM with d = 20 μm and $N_A = 0.09$ from Nufern.

4.1.4 Optical cavity design

Independently of the laser source location (extra or intra-cavity), the two main types of optical cavities are resonant and non-resonant cavities.

Among resonant cavities, the most common is the Fabry-Pérot cavity, consisting of two flat mirrors facing each-others. The option of using a Fabry-Perot laser cooling cavity has been studied and tested by reference [4], as shown in Figure 4.9. The main drawback is that in order to get an impedance matching giving a unit absorption, the input mirror's reflectivity should be progressively increased to match the product αL decrease. Given a constant high input mirror reflectivity, the cavity will have low absorption at high temperatures.

In the resonant cavity experiment at UNM, the back cavity mirror was mounted on 3 axis piezo-controllers in order to tune a bit the variable YLF crystal absorption at low temperature with the Fabry-Pérot cavity length (Figure 4.9). They reached "*a minimum of 203 K* [...]*at 1023 nm with 9 W of pump power*". However they concluded that pump instabilities could provoke random resonance losses and subsequent rapid heating, making it unsuitable for practical implementations.

The other type of optical cavity is known as non-resonant multi-pass cavity, or multipass cell. There are several designs, with varying complexity, size, and number of roundtrips Figure 4.10.

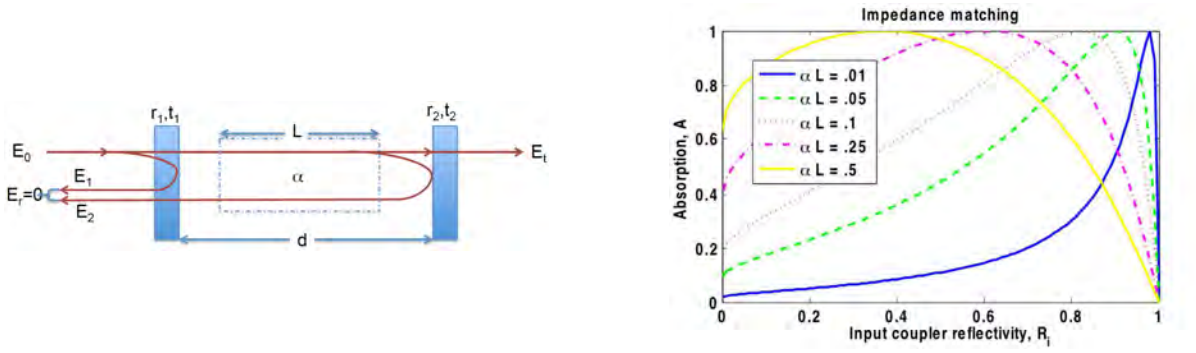

Figure 4.9: *Fabry-Perot resonant cavity and impedance matching condition, from reference [4]. Left: Schematic of the Fabry-Perot resonant cavity. Right: Absorption as a function of the input mirror reflectivity.*

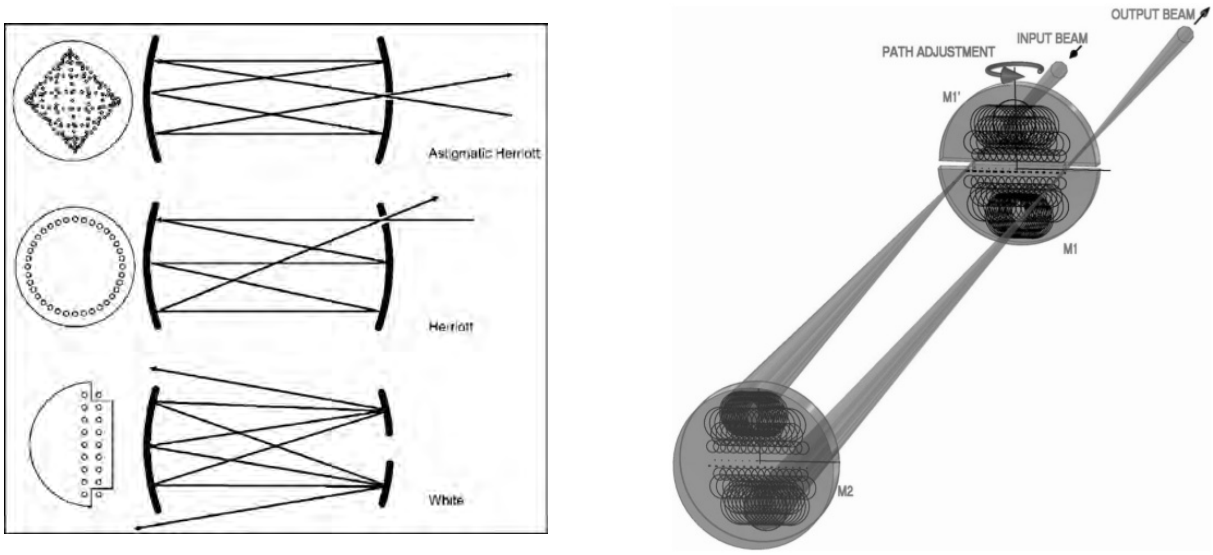

Figure 4.10: *Common types of multi-pass cells. Left: Astigmatic Herriott, Herriott and White cells. Left: Robert cell.*

The Laser Cooler designer's formula

The most important parameter for the design of an extra-cavity laser cooler is the number of round-trips. It is concretely the parameter that needs to be specified at the beginning of the design phase and that will affect the whole architecture. The absorbed power as a function of round-trips can be calculated using the formula:

$$\boxed{P_{abs} = P_{pump}(1 - e^{-2\alpha \times N_{rt} \times l_c})} \tag{4.4}$$

Figure 4.11 shows the fraction of absorbed power as a function of round-trips in 10%Yb:YLF, for several temperatures between 300 K and 100 K. Everything that is not absorbed will be lost in pure losses reflected back from the cavity. As a rule of thumb, it is a good criterion that the reflected power does not exceed 1 percent of the pump power, hence that the fraction of absorbed power is kept above 99%.

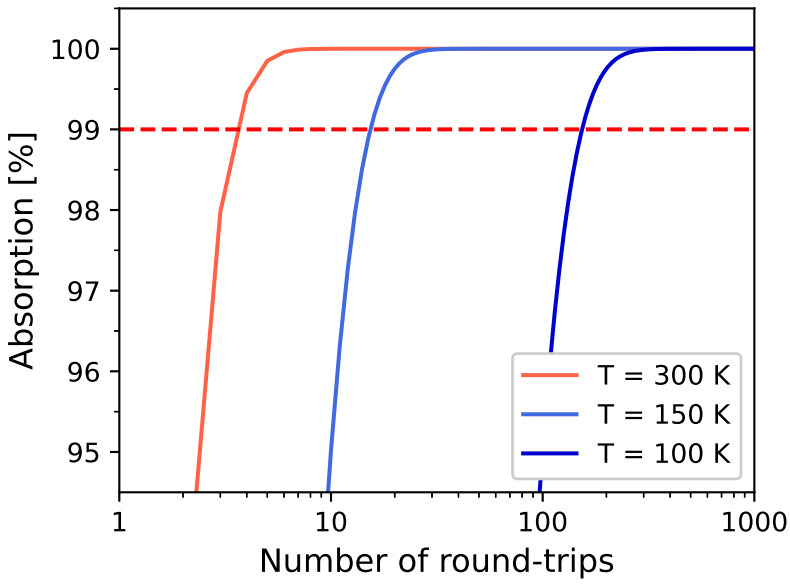

Figure 4.11: *Percent of absorbed pump power as a function of round-trips number in 10%Yb:YLF, plotted for several temperatures. Losses in the mirrors are neglected.*

Between 300 K and 150 K, Yb:YLF absorption loses approximately one order of magnitude, and another one between 150 K and 100 K. As a consequence, the optical specification becomes fundamentally different whether the target temperature is near room temperature or deep into cryogenic temperatures :

- At 300 K, $N_{99\%} = 4$. Many configurations with two mirrors facing each-others and adequate tilt setting on one of the mirrors can reach that value.
- At 150 K, $N_{99\%} = 16$. The specification is more stringent and only some optical cavities can provide that number in a compact volume.
- At 100 K, $N_{99\%} = 154$. The specification becomes hard to achieve, unless carefully designed. Tolerances become critical at this point.

Before plunging into a specific design, one can estimate the needed input hole size and tolerances in order to achieve a certain number of round-trips. Let us assume as first approximation a multi-pass cavity where there is in average N_{rt} round-trips contained in a square surface of side length s. This translates as an ideal case of multi-pass cavity making a linear distribution of N_s spots incident on a square surface around the input mirror with a hole in the middle, as shown in Figure 4.12. We have the relationship between number of spots and number of round-trips $N_{rt} = 2(N_s + 1)$ and the relationship between section and number of round-trips:

$$s = d \times (\sqrt{N_s + 1}) \tag{4.5}$$

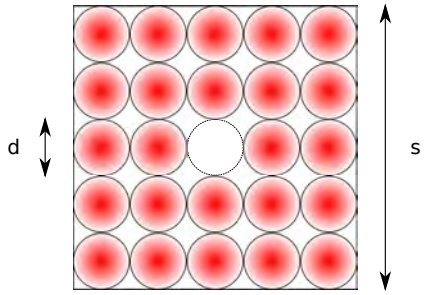

Figure 4.12: *Schematic of an ideal square round-trips pattern with N_s spots with beam diameter d in a section of side s around the input mirror. Here, N = 24.*

Let us assume no beam divergence as an approximation. The hole should possess a maximal radius equal to the beam radius in order to avoid the beams from overlapping with the center:

$$r = d/2 = \frac{s}{2\sqrt{(N_s + 1)}} \tag{4.6}$$

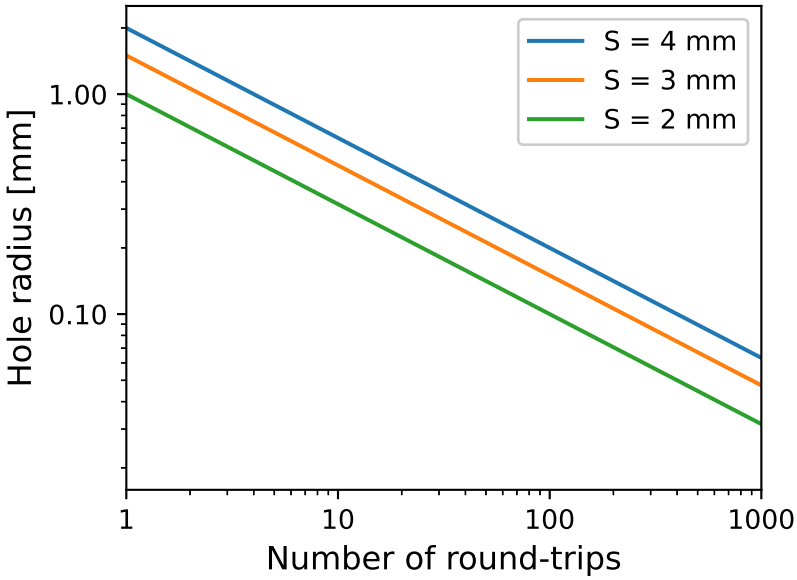

Figure 4.13: *Input hole radius as a function of the number of round-trips, plotted for crystal sections 2 mm, 3 mm and 4 mm.*

Figure 4.13 shows the hole radius as a function of the number of round-trips. We see that a radius on the order of $100 - 200\ \mu m$ depending of the crystal section is required in order to reach at least a hundred round-trips.

Assuming a beam entering the hole with a given beam radius where 99% of power of a gaussian beam is transmitted, the input hole upper and lower radial tolerance can be calculated as well.

The lower bound tolerance is given by the input transmission. The transmitted power as a function of hole radius is equal to the integral of the gaussian beam intensity transmitted

through the aperture:

$$\int_{-r}^{r} I(r)dr = \int_{-r}^{r} \frac{2P_{in}}{\pi w^2} e^{-2\frac{r^2}{w^2}} dr = P_{in}(1 - e^{-2\frac{r^2}{w^2}}) \tag{4.7}$$

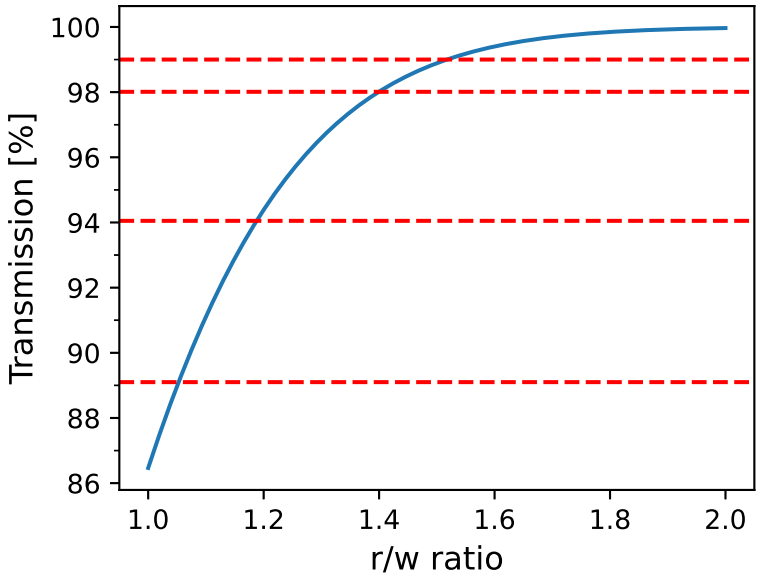

Figure 4.14: *Input transmission and lower bound tolerances.*

Assuming a nominal hole radius where 99% of power is transmitted, we have $r_{99} = 1.52 \times w$. The transmitted power along with 1%, 5% and 10% lower bound tolerances are shown in Figure 4.14. We can see that the 1% degradation is attained for $r = 1.4 \times w$, i.e. the input hole radius should not be allowed to change by more than 8% in order to keep the input transmission within 99% - 1%.

The upper bound tolerance is given by two terms which depends on the number of round-trips.

The first term is given by the overlap between the input hole and the last round-trip spot number i which escapes the cavity (how much power from inside the cavity is leaking out of the hole back to the source):

$$\int_{\Omega} I_i(\Omega)d\Omega \tag{4.8}$$

Where Ω is the overlap domain between the last spot and the input hole. This terms is equal to the power of the last beam P_i if this beam overlaps exactly with the hole (the beam is said to be re-entrant). For a high number of round-trips, we can assume that the last beam i has a minimal amount of power and we can neglect this term.

The second term is given by the variation of absorbed power as a function of varying round-trips number when varying the hole radius. In our approximation, we know the

relationship of N_{rt} as a function of the hole radius:

$$N_{rt} = 2(s/2r)^2 \tag{4.9}$$

Replacing $N_p = N_{rt}/2$ by its value in expression 4.1, we get:

$$P_{abs} = P_{pump}(1 - e^{-\alpha\left(\frac{s}{2r}\right)^2 l_c}) \tag{4.10}$$

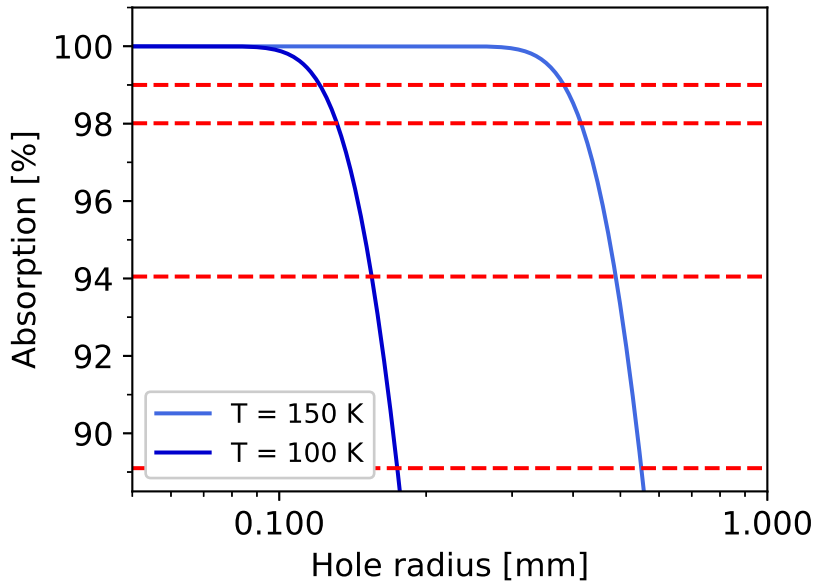

Figure 4.15: *Absorption as a function of the hole radius, plotted for cryogenic temperatures.*

Figure 4.15 shows the cavity absorption as a function of the hole radius in our simple square pattern round-trips model. We can see that at 150 K, the hole radius should be on the order of 400 μm, while at 100 K, it should be around 120 μm. We can see that the relative tolerances do not change as a function of temperature. For example, the 1% degradation tolerance is equal to approximately 10% in radius.

Mini-conclusion: The lesson of this exercise is that optical specifications of a laser cryocooler should be derived assuming the crystal absorption and efficiency parameters at the cryocooler's specified nominal temperature, i.e. at cryogenic temperature.

Until 150 K, relatively high absorption of 10%Yb:YLF makes optical design straightforward. Achieving 99% absorption requires less than 20 round-trips and the input hole can be manufactured with classical tools such as drilling or turning.

Below 150 K, absorption collapses and for exemple, achieving 99% absorption at 100 K requires more than 150 round-trips. Input hole radius should be on the order of 120 μm. Tolerances becomes more stringent and the hole should be manufactured with plus-

or-minus 10 μm at radius to keep an absorption within 99% - 1%.

Such a precision requires special process. Micro-hole drilling can be achieved through a number of specific techniques divided into three categories: mechanical, thermal and chemical. An exhaustive review of these micro-hole drilling techniques in glass substrates can be found in reference [9]. Based on this review, pulsed laser drilling [10] seems like the preferred way to manufacture 100 μm holes with several mm depth in reasonable drilling times (approximately 100 $\mu m/s$).

To relieve the pressure and costs off the optical design, we see the benefits of increasing the crystal section or the doping percentage in order to get higher round-trips number/higher absorption per round-trip. However those two parameters have adverse effects due to fluorescence re-absorption. This highlights the need in the future for an accurate fluorescence re-absorption model.

Astigmatic Herriott cell design

The astigmatic Herriott cell is a variant of the Herriott cell where one or both mirrors break the rotation symmetry. Among non-resonant cavities, the astigmatic Herriott cell is particularly suitable for square section cooling crystals: its round-trip pattern is a Lissajous figure fitting in a rectangular area and it features a high number of round-trips [11]. Furthermore, it has already been investigated for Laser Cooling applications [12]. For the first prototype, the choice was made to design such a cavity.

Theoretical cavity model

The astigmatic cavity can be modeled based on the mathematical description from reference [13]. This description uses the ray-matrices formalism in two dimensions (x and y) to propagate the rays between both mirrors. In this model, a ray is described by a 4 components vector containing its position and angle in x and y directions, where the ray propagates along z:

$$\vec{r} = \begin{bmatrix} x \\ \phi_x \\ y \\ \phi_y \end{bmatrix} \tag{4.11}$$

Free space propagation of the ray over a length L is given by the matrix multiplication:

$$\vec{r'} = \begin{bmatrix} 1 & L & 0 & 0 \\ 0 & 1 & 0 & 0 \\ 0 & 0 & 1 & L \\ 0 & 0 & 0 & 1 \end{bmatrix} .\vec{r} = T.\vec{r} \tag{4.12}$$

And reflection by a spherical or cylindrical mirror is given by:

$$\vec{r'} = \begin{bmatrix} 1 & 0 & 0 & 0 \\ -2/R_x & 1 & 0 & 0 \\ 0 & 0 & 1 & 0 \\ 0 & 0 & -2/R_y & 1 \end{bmatrix} .\vec{r} = M.\vec{r} \tag{4.13}$$

Where $R_{x,y}$ is the mirror's radius of curvature with respect to direction x or y. When entering the cavity, at the input hole position, the ray is at coordinates $x = 0$ and $y = 0$. The initial position is given by:

$$\vec{r_0} = \begin{bmatrix} 0 \\ \phi_x \\ 0 \\ \phi_y \end{bmatrix} \tag{4.14}$$

During one round-trip, the ray travels a distance L between both mirrors, gets reflected on mirror M2 which can possess a tilt, travels a distance L in the inverse direction, and gets reflected on mirror M1. Mathematically, the ray position and angle viewed on mirror M1 after one round-trip is calculated by the operations:

$$\vec{r_1} = M_1.T.(M_2.T.\vec{r_0} + \vec{t_2}) + \vec{t_1} \tag{4.15}$$

With M_1 and M_2 the ray matrices of mirrors one and two, t_1 and t_2 being the tilt angles of mirrors one and two. Calculating the position of a spot along N round-trips is done by propagating the first ray recursively along the system:

$$\vec{r_N} = M_1.T.(M_2.T.\vec{r_{N-1}} + \vec{t_2}) + \vec{t_1} \tag{4.16}$$

Theoretically, the calculation can be performed for N going to infinity: if the cavity was closed and non-lossy, a ray could be trapped forever between two mirrors. In practice, the maximum number of round-trips in a real astigmatic cavity is limited by the input hole size, when the beam eventually escapes back from the cavity.

A python script modeling the astigmatic cavity was written. In our script, the calculation

is terminated when one of the round-trips hits back in an area inferior to the input hole dimensions. Figure 4.16 shows an example of a round-trip pattern for cavity mirrors with 200 mm curvature radius, input hole radius $a = 0.1mm$ and input angles 1° in x and y, plotted for the first 50 round-trips. The pattern acheives in reality 122 round-trips before re-entering the hole.

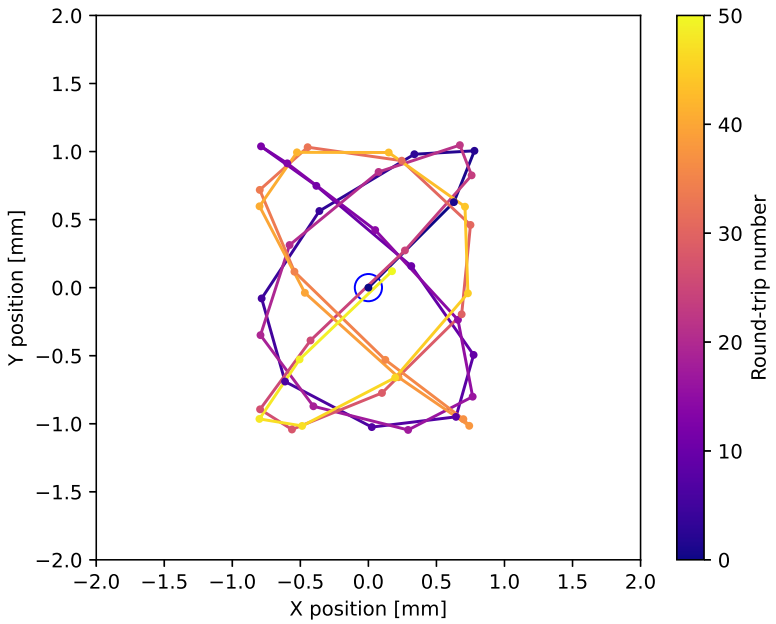

Figure 4.16: *Example of a Lissajous figure calculation plotted for N up to 50 round-trips for input angles of 1° in both x and y directions. Parameters:* $L = 200mm; a = 0.1; R_{1x} = 200mm; R_{1y} = \infty; R_{2x} = 200mm; R_{2y} = 200mm; x_0 = 0; y_0 = 0; \phi_x = \phi_y = 1°; t_{1x} = t_{1y} = t_{2x} = t_{2y} = 0.$

The maximal number of round-trips can be calculated as well as a function of any parameter. For small variations, the first Lissajous points remain around the same positions. The position of high round-trips values however can change significantly, introducing a variability of the maximal number of round-trips achievable. For example, Figure 4.17 shows the variation of round-trips when varying the effective cavity length.

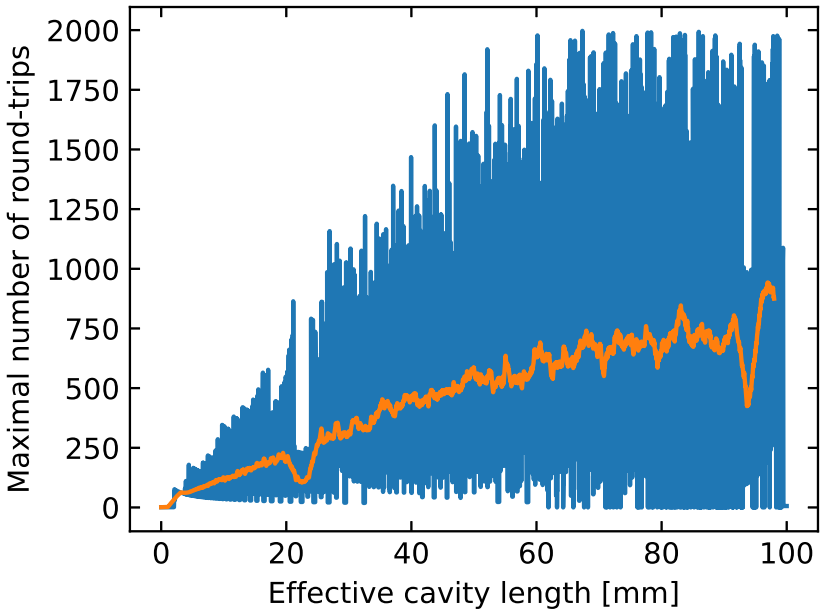

Figure 4.17: *Maximal number of round-trips as a function of effective cavity length between 0 and 100 mm. The orange curve shows the averaged values. Parameters:* $a = 0.1; R_{1x} = 200mm; R_{1y} = \infty; R_{2x} = 200mm; R_{2y} = 200mm; x_0 = 0; y_0 = 0; \phi_x = \phi_y = 1°; t_{1x} = t_{1y} = t_{2x} = t_{2y} = 0$.

We see that for single rays, increasing the cavity length can improve the average number of round-trips, while it can increase as well the variability/sensitivity and hence the probability of falling to zero.

An important point to consider is the input beam's divergence. Indeed, in standard ray-tracing, Gaussian beams are implemented as line segments which are generated from a single point with a certain random launch angle sampled for the Gaussian distribution. Since rays are simulated as line segments, they will follow a linear divergence.

In reality, due to diffraction, the propagation of light in a laser beam does not follows a linear divergence. Instead, there is a position along the beam where its divergence is zero and its diameter is at a minimum, known as the waist diameter $2w_0$. The Gaussian beam radius as a function of the position z in the propagation direction is defined as:

$$w(z) = w_0\sqrt{1 + (z/z_0)^2} \tag{4.17}$$

With z_0 the Rayleigh range defined as:

$$z_0 = \frac{\pi w_0^2}{\lambda} \tag{4.18}$$

A concern regarding the astigmatic cavity is to know whether the beam will become too large at some point such that it would escape the crystal. The linear Gaussian approximation can be used to calculate the initial angles of 4 cardinal rays around the ray center,

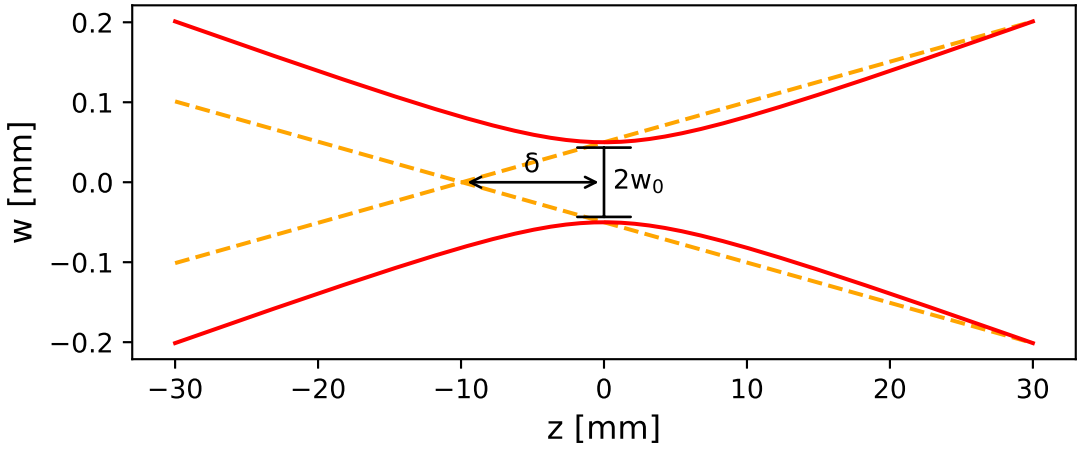

Figure 4.18: *Red: Gaussian beam 1/e² radius as a function of the z position along the beam, for a 1020 nm beam with 50 μm waist radius. Orange: Linear approximation of the Gaussian beam for a 30 mm effective cavity length.*

which are then propagated into the system, as shown in Figure 4.19.

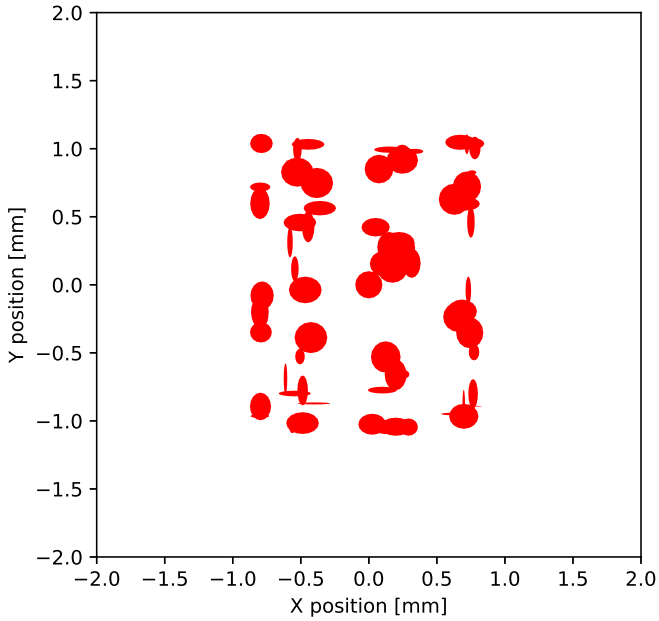

Figure 4.19: *Lissajous figure calculation taking into account the Gaussian beam divergence for input angles of 1° in both x and y directions, plotted for the first 50 round-trips. Parameters:* $L = 200mm; a = 0.1; R_{1x} = 200mm; R_{1y} = \infty; R_{2x} = 200mm; R_{2y} = 200mm; x_0 = 0; y_0 = 0; \phi_x = \phi_y = 1°; t_{1x} = t_{1y} = t_{2x} = t_{2y} = 0.$

Happily, the beams do not keep diverging after each mirror reflection. Instead, the beams are refocused each time they hit a mirror such that their maximal size when going back to the first mirror does not exceed too much the initial spot size. There are this time only 73 round-trips compared to Figure 4.16. We can check again the effect of varying cavity length on the number of round-trips, taking the Gaussian beam divergence into account, as shown in Figure 4.20.

We can see that the beam's divergence increases the probability of the ray escaping the

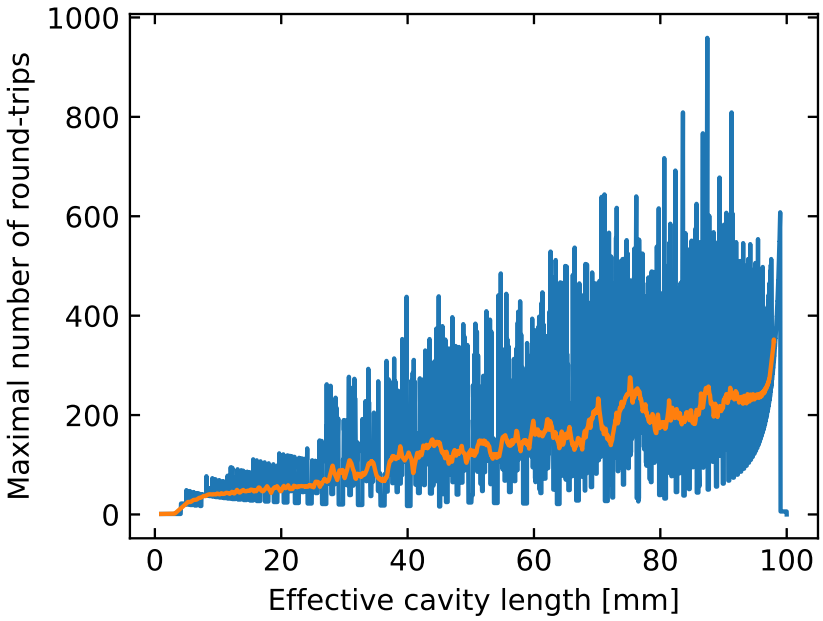

Figure 4.20: *Maximal number of round-trips as a function of effective cavity length between 0 and 100 mm, taking into account the Gaussian beam divergence. The orange curve shows the averaged values. Parameters:* $a = 0.1; R_{1x} = 200mm; R_{1y} = \infty; R_{2x} = 200mm; R_{2y} = 200mm; x_0 = 0; y_0 = 0; \phi_x = \phi_y = 1°; t_{1x} = t_{1y} = t_{2x} = t_{2y} = 0.$

cavity, thus reducing the average number of round-trips. Still, for effective cavity lengths around 20 mm it is on the order of 50 round-trips. Increasing the cavity lengths still has the effect of increasing the number of round-trips. However, that effect is less pronounced than for single rays. We can note a sharp increase in the number of round-trips when approaching a length of 100 mm before falling to less than 10 round-trips, in other words, when the mirrors are approaching a confocal configuration.

Full analysis of the astigmatic Herriott cell is not a trivial matter. Indeed, there are in total 15 free parameters to play with: 4 tilts (2 on each mirror), 4 radius of curvature (2 on each mirror), 5 input beam parameters (2 offsets, 2 angles and 1 beam waist), the input hole diameter and the effective cavity length. At the time of writing this thesis, the only other existing Laser Cryocooler, demonstrated at UNM, possess 500 mm radius mirrors and an input hole of 0.4 mm mechanically drilled in the first spherical mirror [14].

The starting point of the cavity design is to set a target dimension for the Lissajous figure, corresponding to the crystal's dimensions. The x and y dimensions sets the allowed input angles, mirrors curvature and mirrors tilt. For example, one can make a centered Lissajous figure by setting only the input angles and no tilt on the mirrors. This situation is equivalent to tilting the whole system after the input beams, by tilting both mirrors and the crystal as well from the same value. There are hence two philosophies: either setting the adequate dimensions by adjusting the cavity input angles, or by adjusting the mirrors tilts.

Untilted mirrors case (centered Lissajous figure): In the case where the ray enter the cavity with tilt angle and both mirrors are facing each-others without tilt, the Lissajous figure size is directly proportional to the launch angles, as shown in Figure 4.21.

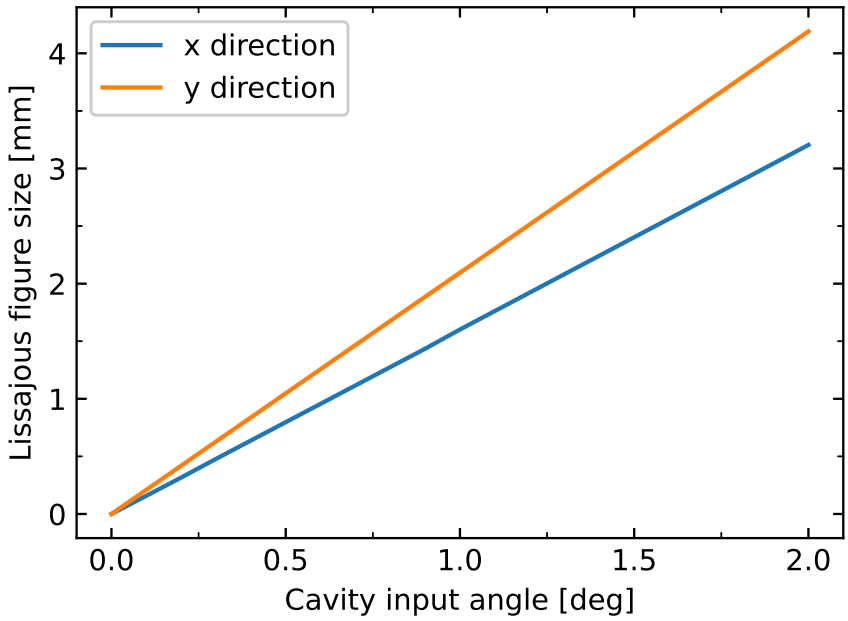

Figure 4.21: *Lissajoux figure size as a function of input tilt angles. Parameters:* $L = 200mm; a = 0.1; R_{1x} = 200mm; R_{1y} = \infty; R_{2x} = 200mm; R_{2y} = 200mm; x_0 = 0; y_0 = 0; t_{1x} = t_{1y} = t_{2x} = t_{2y} = 0.$

The average number of round-trips as a function of tilt angles is shown in Figure 4.22 for effective cavity length of 20 mm, 30 mm and 40 mm.

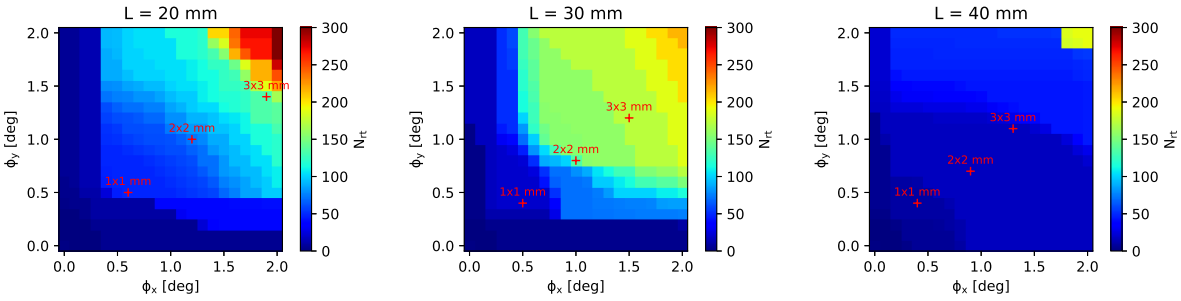

Figure 4.22: *Average number of round-trips as a function of input tilt angles, calculated for effective cavity lengths 20/30/40 mm. Tilt values corresponding to Lissajous figures of sizes 1 mm², 2 mm² and 3 mm² are marked. Parameters:* $a = 0.1; R_{1x} = 200mm; R_{1y} = \infty; R_{2x} = 200mm; R_{2y} = 200mm; x_0 = 0; y_0 = 0; t_{1x} = t_{1y} = 0.$

We see that increasing the tilts values has the effect of increasing the maximal number of round-trips: as the Lissajous figure occupies a larger surface the probability of a ray escaping the cavity decreases. The effect of increasing the cavity length for fixed tilt values shows a variability of the number of round-trips which can either increase or decrease, consistent with Figure 4.20. It is hence an parameter which needs to be tuned in a real application if a fine control of the number of round-trips is expected. Fortunately, for Laser Cooling

applications, the absorbed power varies as $e^{-2N_{rt}\alpha(T)}$ which means that for example, the absorbed power variation between 100 and 150 round-trips is much less than for the first 50 round-trips.

Tilted mirrors case (off-centered Lissajous figure): As stated previously, setting the same tilt on both mirrors is equivalent to entering the cavity with an angle and will result in a centered Lissajous figure.

Though, setting a tilt on solely one of the mirrors while entering the cavity with zero angle has the effect of entirely shifting the whole figure in the tilt direction such that the hole is at the edge of the figure, with a size proportional to the tilt and depending on the total curvature radius in that direction.

It is possible to combine tilt and input angle in order to shift the Lissajous figure in a direction such that the hole is located at any position within the figure. In that case, the Lissajous figure size cannot go below a certain value, determined by:

- the input angle with zero tilt, if an input angle was set and the tilt is varied.
- the tilt angle with zero input angle, if a tilt angle was set and the input angle is varied.

Tilting only one of the mirrors presents another advantage. Since an additional symmetry is broken (the two mirrors do not exactly face each-others anymore), the rays exiting out of the cavity do so with an angle which is different than the input angle. Hence, the rays going back to the laser source with a different path, allowing to filter them out with a diaphragm and reducing the need for an optical insulator.

Design philosophy: To make an astigmatic Heriott cell, the laser beam should enter the cavity with a certain tilt angle in x and y directions or be reflected with a tilted mirror. The tilt angles, along with the curvature radius sets the Lissajous figure size.

For our prototype, a hybrid approach was adopted. The cylindrical mirror was chosen as first mirror in order to minimize the input beam aberration after being transmitted.

We know that the Lissajous figure is approximately twice as sensitive to tilt or input angle variations in the direction where the cylindrical mirror is flat, compared to the direction where a ray with an angle will get reflected by two curvatures. We chose to put a horizontal input angle on the collimator in the "less-sensitive" direction where the ray sees two curvatures, and to finely put a vertical tilt angle in the "most-sensitive" direction with the spherical second mirror.

The choice was made to set a tilt in one direction on the input beam, and set the other tilt with the second mirror. At the beginning of the design, the goal was to find the proper input hole size and curvature radius in order to achieve the high absorption.

After determining the angles parameters for fitting a 3x3 mm section crystal, a cavity model was constructed with Zemax in order to check the absorbed power, the Fresnel reflected power and the power exiting out of the cavity.

Ray-tracing cavity model

The optical cavity was designed with Zemax in order to implement the effect of the beam divergence and make a more realistic ray-tracing out of the paraxial approximation. The cavity model takes into account the rays polarization and the crystal's birefringence. The cavity model doesn't take into account the fluorescence emission, as the goal here is to predict only the absorbed power. For this purpose, YLF optical properties had to be entered in Zemax's glass catalog. Absorption coefficients in both polarization were taken from Pisa data. Refractive index for YLF can be found along with its thermo-optic coefficients in reference [15]. Index were entered for ambient temperature in Sellmeier equations forms:

$$n_o{}^2 = 1.38757 + \frac{0.70757\lambda^2}{\lambda^2 - 0.00931} + \frac{0.18849\lambda^2}{\lambda^2 - 50.99741} \tag{4.19}$$

$$n_e{}^2 = 1.31021 + \frac{0.84903\lambda^2}{\lambda^2 - 0.00876} + \frac{0.53607\lambda^2}{\lambda^2 - 134.95660} \tag{4.20}$$

Figure 4.23 shows YLF refractive index at ambient temperature. Refractive index variations with temperature was neglected in this model, as they are on the order of 0.01 between 300 K and 100 K.

The astigmatic cavity is composed of only 3 optical elements, as shown in Figure 4.24:

- The first cavity mirror M1. This concave cylindrical mirror is defined with anti-reflective coating on its flat back surface and with high-reflection coating on its curved surface. A transmission zone is located at the mirror's center, implemented as a physical hole from which the rays can escape the cavity.
- The cooling crystal. It is defined from a rectangle volume object with the Brewster angles set on its faces and uses the Yb:YLF absorbing media previously added in the glass catalog.
- The second cavity mirror M2. This spherical mirror is defined with anti-reflective coating on its back and high-reflection coating on its curved surface.

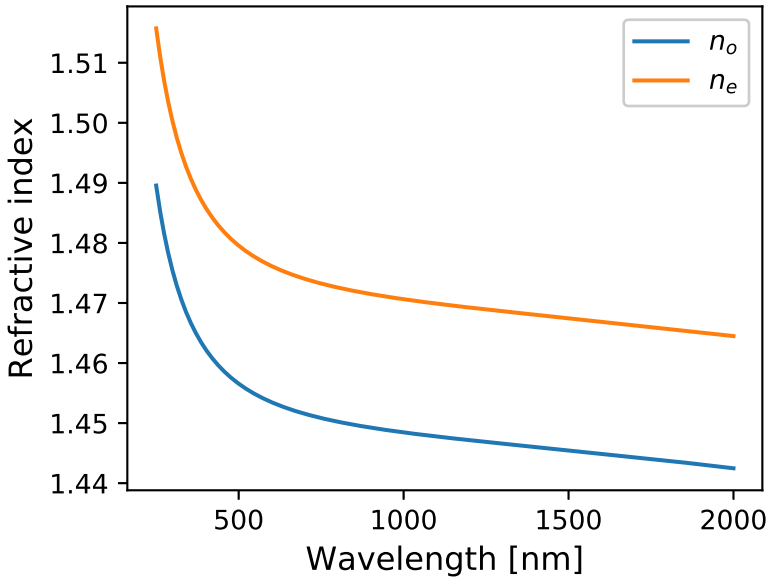

Figure 4.23: *YLF ordinary refractive index no and extraordinary refractive index ne at 300 K.*

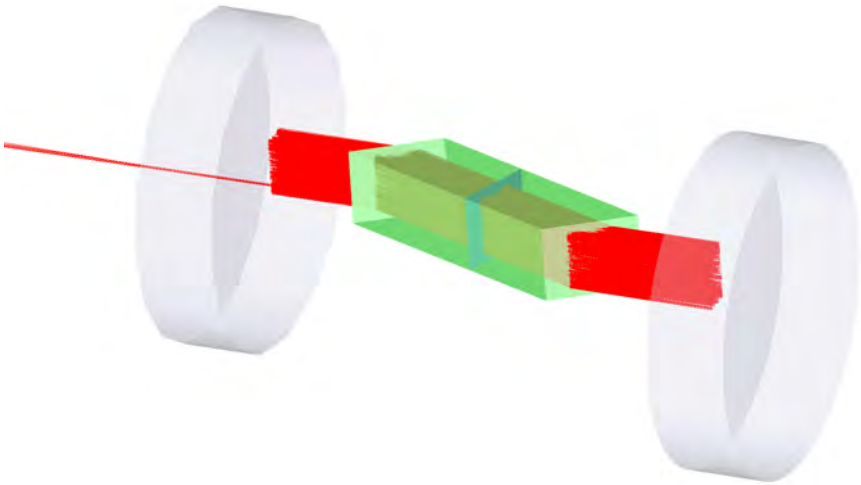

Figure 4.24: *Zemax CAD view of the optical cavity with the crystal at its center.*

The pump laser is implemented as a Gaussian source emitting at 1020 nm. The beam divergence within the cavity is still calculated as a linear approximation of the Gaussian beam divergence. Real Gaussian beams propagation can only be calculated using Zemax's sequential mode with the Physical Optics Propagation tool. In our model, a true Gaussian beam is simulated using a Gaussian source launching a cone of rays with Gaussian angular intensity distribution.

The linear Gaussian approximation is used to propagate a beam position and a divergence distance δ from which the rays are launched. At its origin, the linear beam possess a diameter equal to the real waist diameter $2w_0$. At a position z equal to the effective cavity length L_e, the linear beam possess a diameter equal to the true Gaussian beam at position

z. In between, the linear model is an overestimation of the real beam size, as shown in Figure 4.18. We have the relationship:

$$\delta = -\frac{L_e w_0}{w(L) - w_0} \tag{4.21}$$

We can compute the error committed as a function of the beam size. Figure 4.25 shows that this approximation does not exceeds 15% of error over the whole beam dimensions, which comforts our analysis.

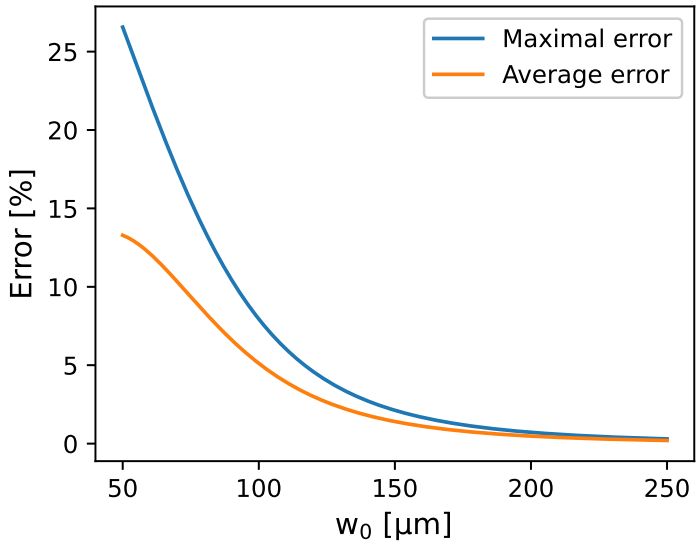

Figure 4.25: *Maximal and average errors committed by the linear approximation compared to the real Gaussian beam divergence, for waist radius between 50 μm and 250 μm.*

Figure 4.26 shows the cavity model implemented in Zemax. Several types of detectors are used in the cavity simulation. Surface detectors are placed around the cavity and behind the mirrors to compute the power exiting the cavity. A surface detector is also placed at the crystal's center to check the round-trips pattern (visible in Figure 4.24). Finally, a volume detector is placed around the crystal to compute the crystal absorption. These detectors allow to track the distribution of power inside the cavity.

The absorbed power as a function of input angles was examinated as well, as shown in Figure 4.27. We see that a maximal absorption zone appears, corresponding to the zone were the round-trips covers the crystal section.

The different detectors allows to compute the power repartition: total detected power, Fresnel losses, power reflected out of the cavity from the input hole in the input beam axis and off-axis. Figure 4.28 shows that Fresnel reflections do not vary too much in the zone where the absorbed power is maximal, i.e. when the beams match the crystal section.

For angles fitting the crystal section, the absorbed power and Fresnel losses were studied as a function of mirrors separation for different mirrors radius of curvature while keeping

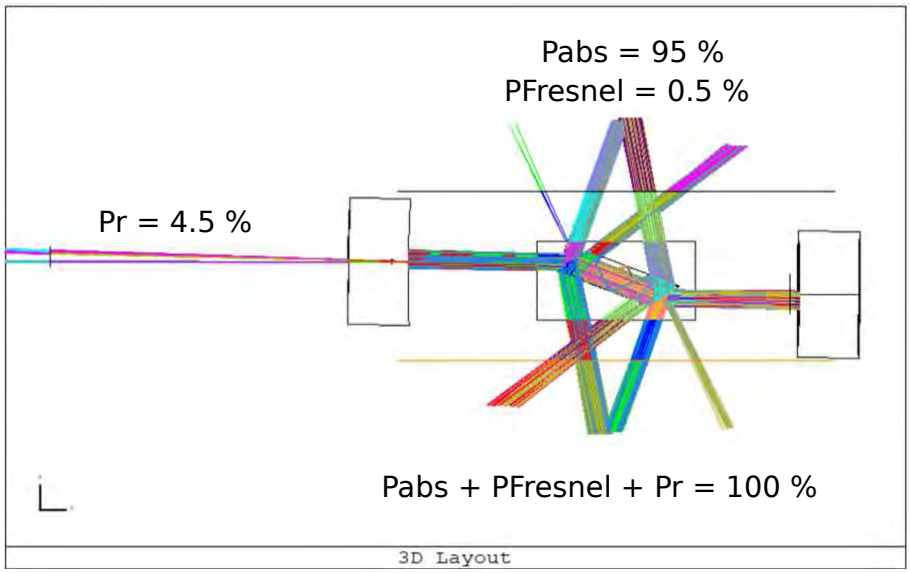

Figure 4.26: *Power repartition at the multi-pass cavity level for a crystal at a temperature of 150 K. For 100 % of power entering the cavity, 95 % are absorbed, 0.5 % are lost due to Fresnel reflection on the crystal faces and the remaining 4.5 % are lost after being reflected out of the cavity.*

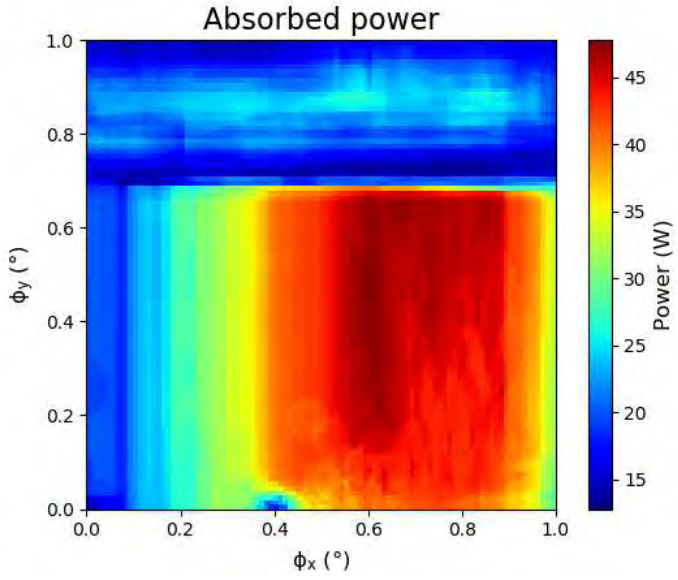

Figure 4.27: *Simulated absorbed power as a function of tilt angles of the second mirror, for an input power of 50 W.*

the crystal at the center of both mirrors, as shown in Figure 4.29.

We see that with the effect of beam divergence, there is a cavity length above which the Fresnel reflections show an increase. The flattest the mirrors, the shortest should be the cavity in order to minimize the Fresnel losses. For the absorbed power, we see the combined effect of varying round-trips numbers and Fresnel losses. Considering those results, we chose to use mirrors with 200 mm curvature radius.

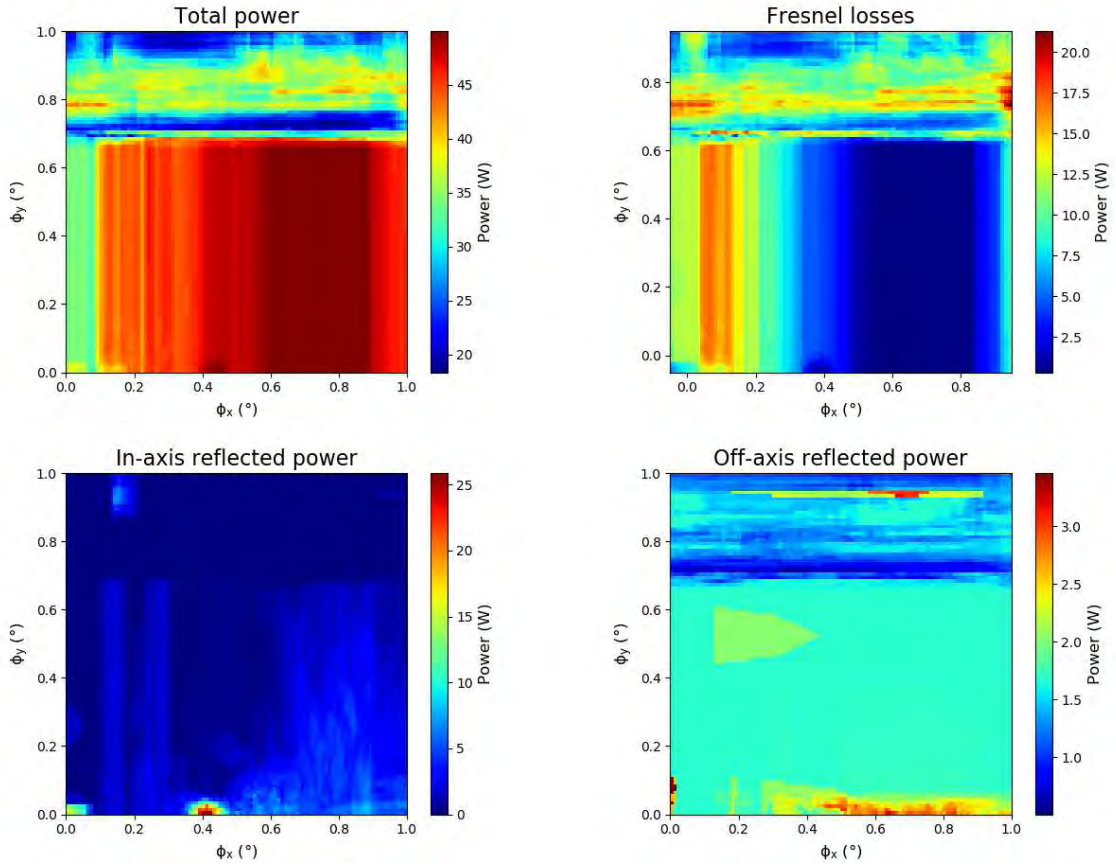

Figure 4.28: *Power repartition as a function of tilt angles of the second mirror for an input power of 50 W.*

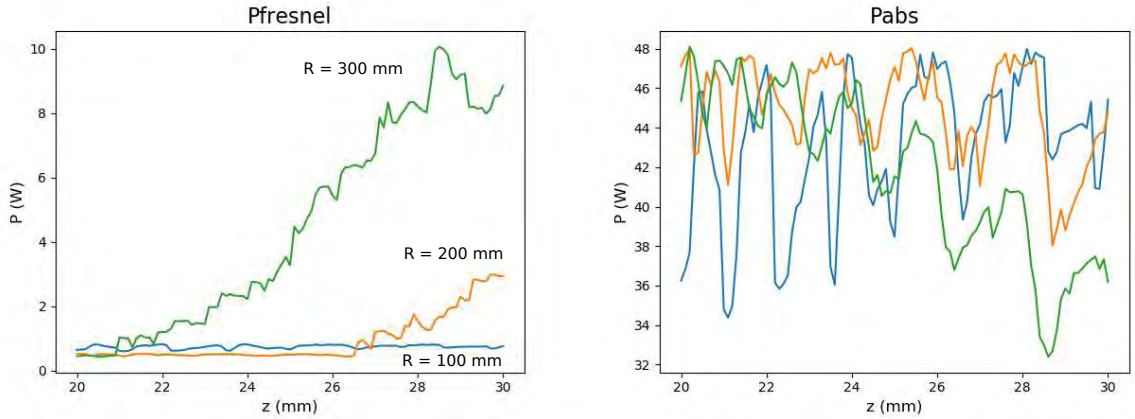

Figure 4.29: *Fresnel losses and absorbed power as a function of cavity length for different mirrors curvature radius. for an input power of 50 W.*

Fiber collimator model

The fiber collimator was simulated under Zemax as well, in sequential mode with the physical optics propagation tool which allows to propagate realistic beams accounting for the divergence between optical surfaces. The goal was to compute the fiber and aspheric lens positions for several aspheric lens available in the market, matching the PM fiber PLMA-

GDF-20-250-09 PM with d = 20 μm and $N_A = 0.09$ from Nufern. For an input hole of 150 μm diameter, the waist radius at the mirror's hole needs to be approximately 1.52 times smaller than the hole radius to ensure 99% transmission, i.e. w_0 = 49.34 μm.

The aspheric lens 354350-B from Thorlabs with parameters f = 4.50 mm and NA = 0.43 was selected because it allowed the off axis beam exiting out of the cavity to come back to the lens with about 1 mm offset (which can be blocked with an aperture), while distance between aspheric lens and first mirror was still acceptable (about 30 mm).

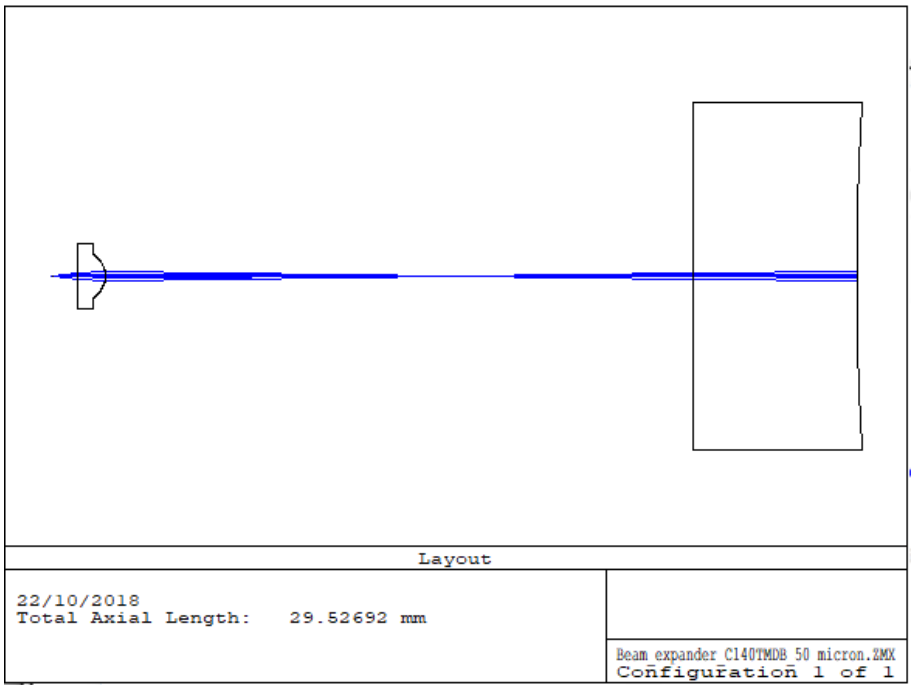

Figure 4.30: *Fiber collimator optimization during the design process in Zemax.*

Optimization was performed to compute the fiber position and lens position such that the beam waist hits exactly at the mirror's hole position. Once the optimal parameters were found, a small sensitivity analysis was performed as well in order to check the variation of the waist position and the waist size when varying the fiber to lens distance, as shown in Figure 4.31 and Figure 4.32.

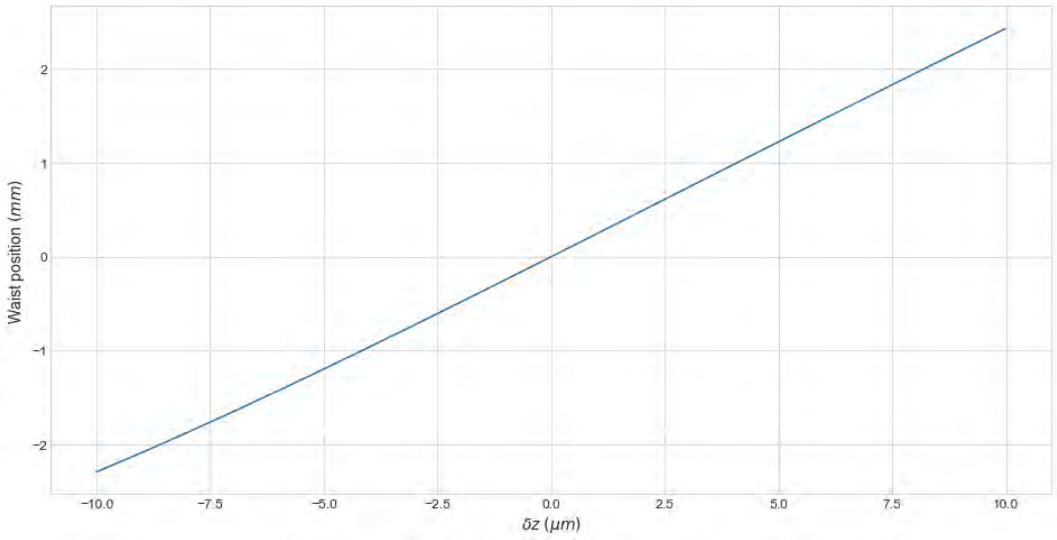

Figure 4.31: *Variation of the waist position as a function of the variation of the fiber to lens distance, relatively from the optimal fiber position* $\delta z = 0$.

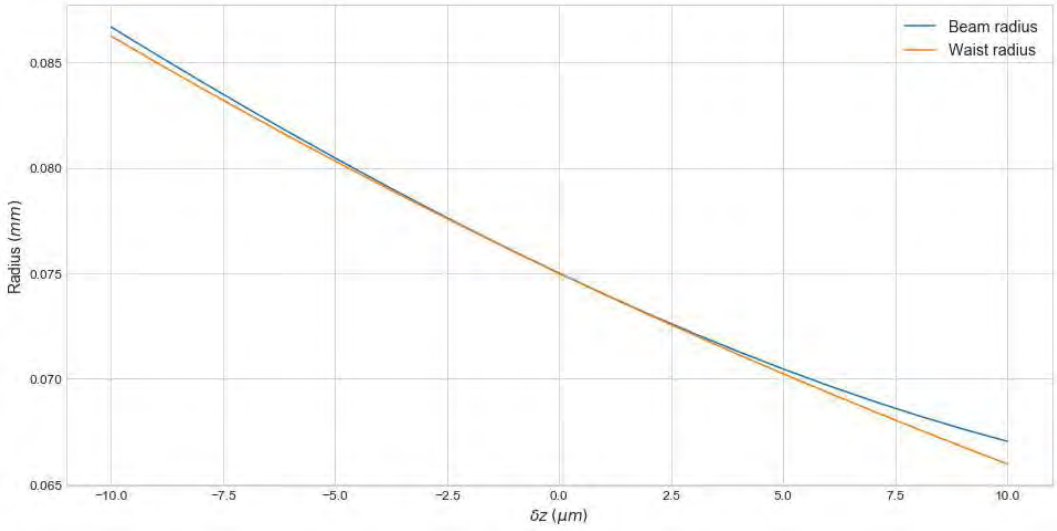

Figure 4.32: *Variation of the waist radius as a function of the variation of the fiber to lens distance, relatively from the optimal fiber position* $\delta z = 0$.

Considering these results, the fiber position is not too critical within a variation of $\pm$ 10 μm, which we are able to set precisely in our experiment by putting the fiber on a micrometer precision translation mount and gluing it after it has been positioned.

Final design

In our final design, we decided to use mirrors with 200 mm radius and a cavity length of 20 mm. In order to get a Lissajous figure as shown in Figure 4.33 filling a size of 2x2 mm inside the crystal section, an input angle of 0.8° was need ed in the horizontal plane (as schematized in Figure 4.34 ans simulated in Figure 4.35), and a tilt angle of 0.3° was needed for the second mirror in the vertical direction (as schematized in Figure 4.36 and simulated in Figure 4.37).

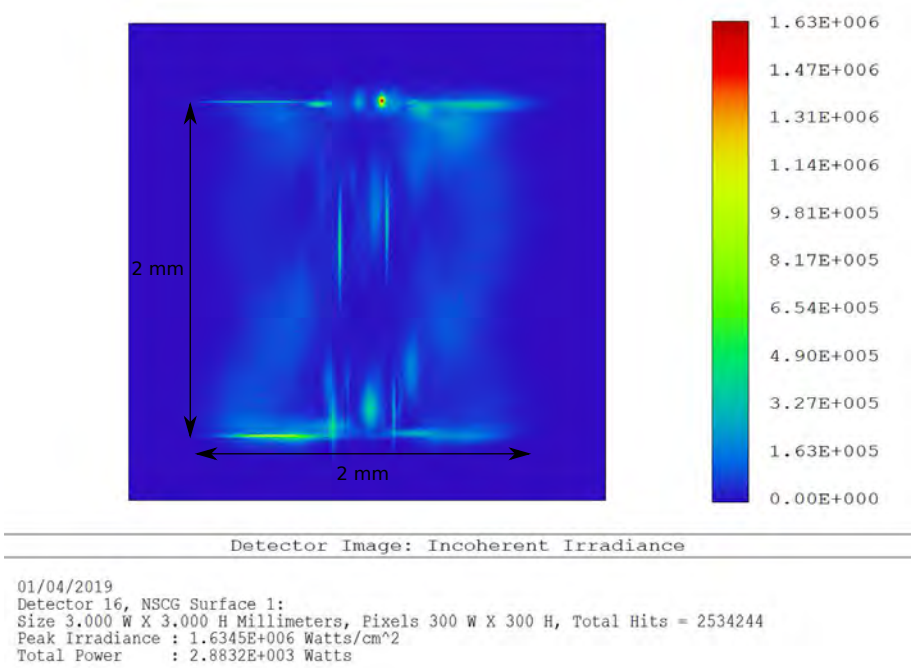

Figure 4.33: *Lissajous figure inside a section of 3x3 mm in the final design with an angle on the input beam and a tilt on the second mirror.*

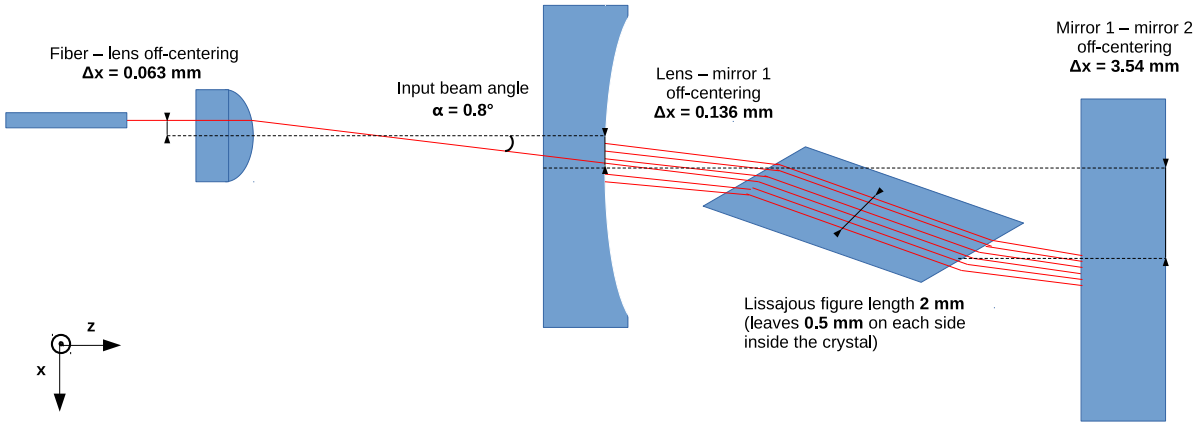

Figure 4.34: *Schematic of the cavity viewed from the top, indicating the distances in the final design.*

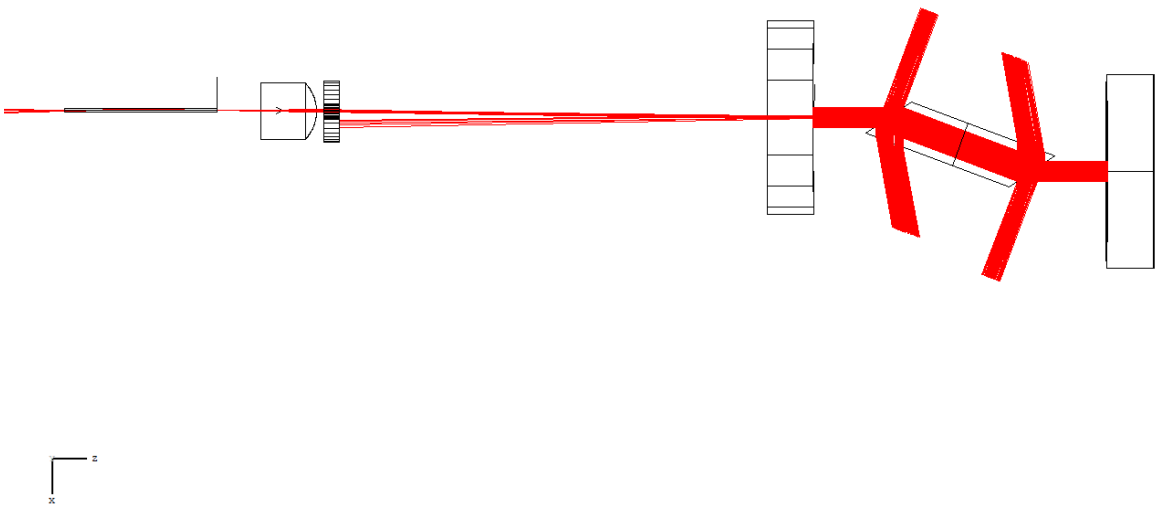

Figure 4.35: *Zemax simulation of the cavity viewed from the top.*

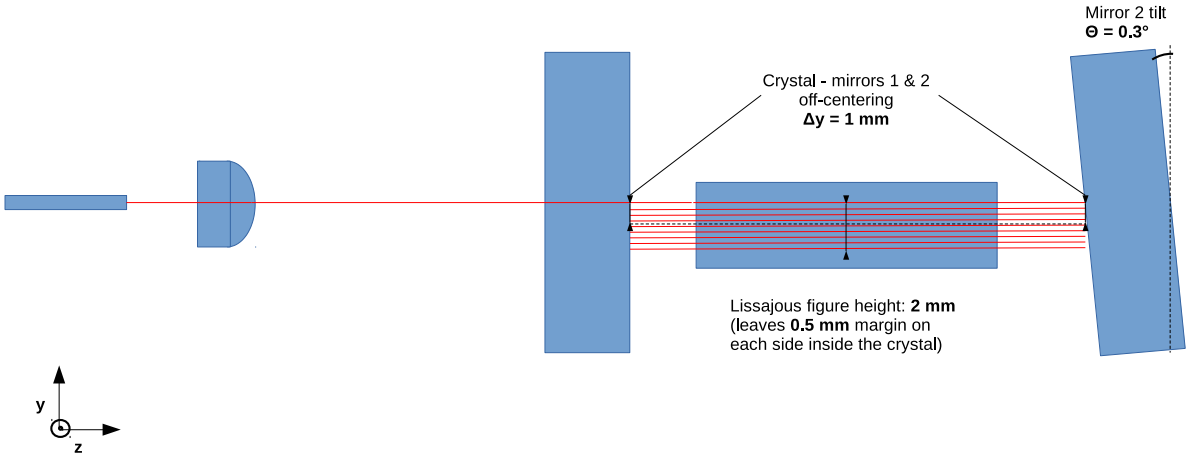

Figure 4.36: *Schematic of the cavity viewed from the side, indicating the distances in the final design.*

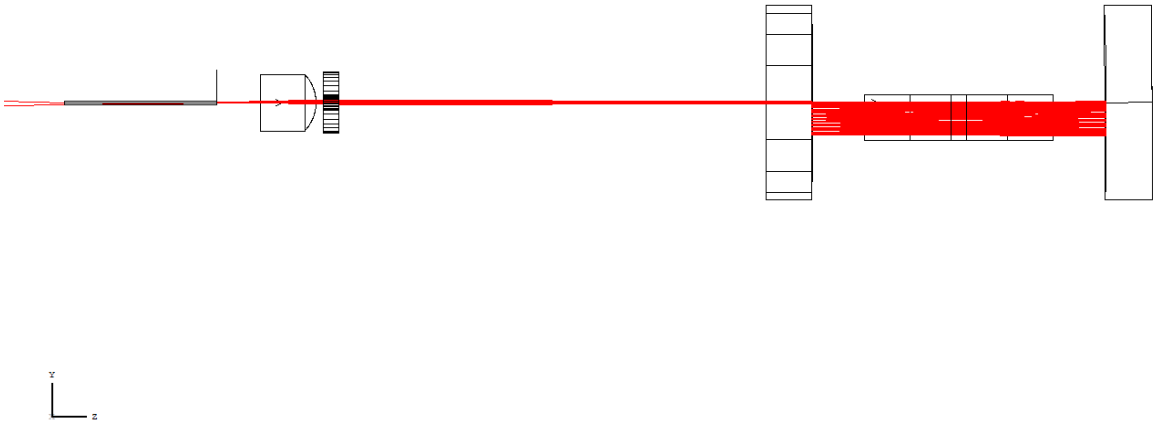

Figure 4.37: *Zemax simulation of the cavity viewed from the side.*

4.2 Prototype development

4.2.1 Coupling bench

Overview

As presented before in the design part, the coupling bench is the part which is used to send a laser beam with a maximal power of 50 W from the laser source (model IPG 1020 LP) into the polarization maintaining fiber.

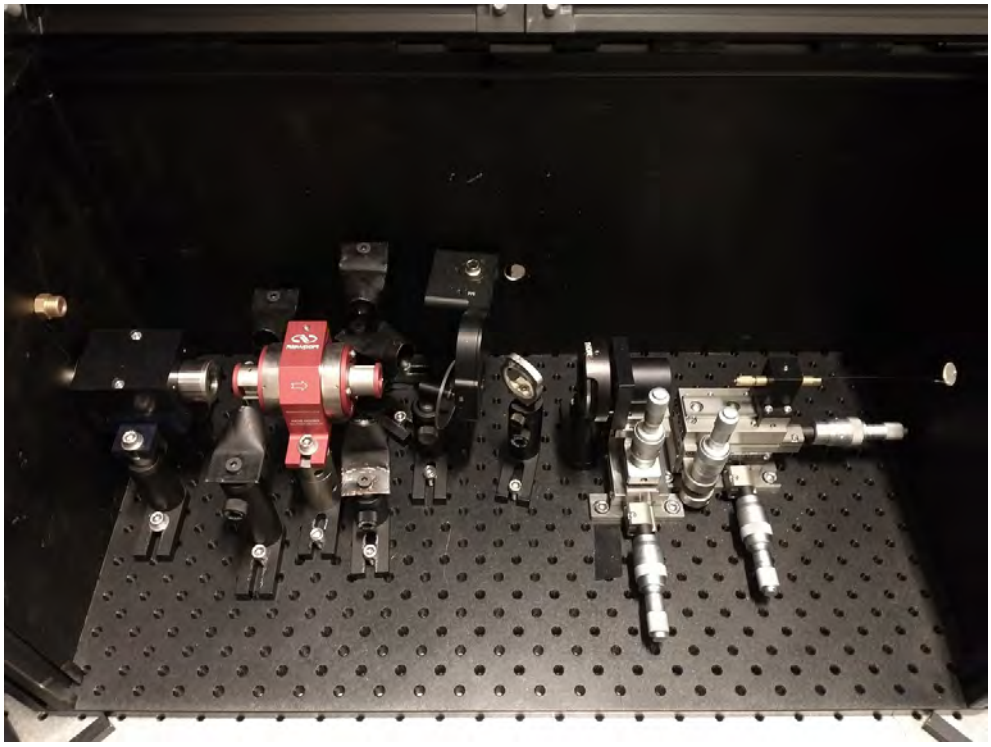

Figure 4.38: *Photograph of the coupling bench open showing all the optical elements.*

Due to this high power sent into free space, we designed and assembled an enclosure which allows to maintain the risks in a limited space when the laser is turned on, as shown in Figure 4.38 and Figure 4.39.

Coupling performances validation

The coupling bench performances were evaluated after trying to achieve the best coupling of the laser inside the fiber. To do so, after an optical fiber was prepared, a power meter was installed at the fiber's end. At low power, the fiber position was varied to reach a maximum transmission. In the best coupling observed, we reached transmissions as high as 90 % to 95 %. The linear polarization ratio was measured as well by placing a polarizer at the

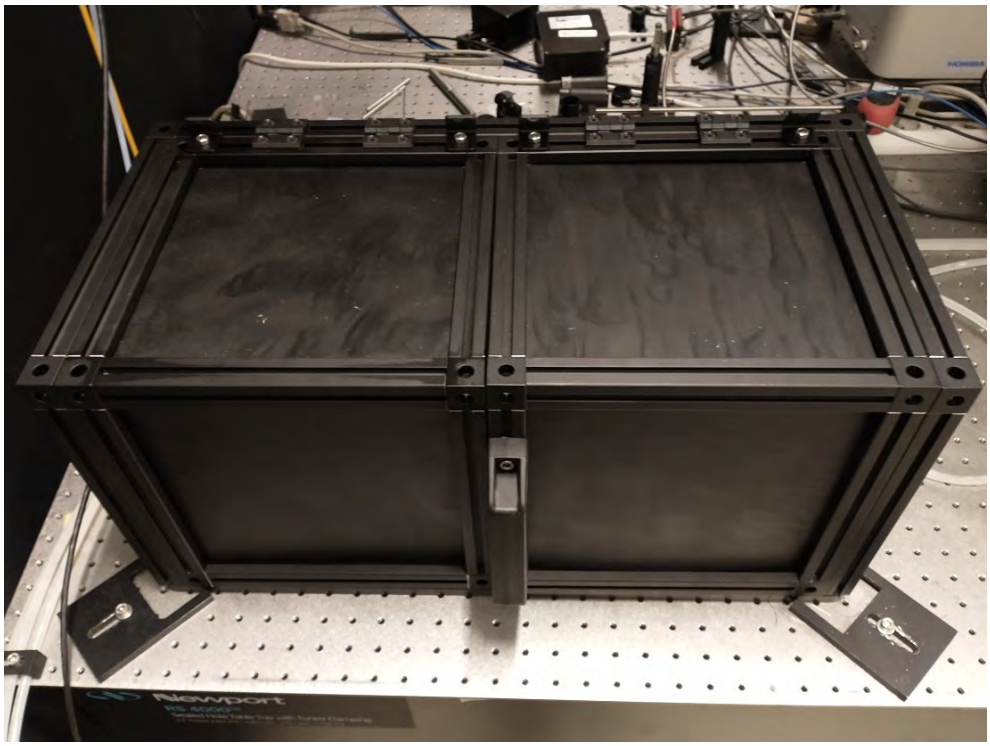

Figure 4.39: *Photograph of the coupling bench closed.*

fiber's end and measuring the power in both polarizations. We found that polarization was transmitted at 95 % in the correct horizontal direction.

Finally, we tried sending as much power as possible in the fiber. The fiber withstood the maximal power of our laser, 50 W, without any failure or burning observed, sign of the successful fiber coupling.

4.2.2 Cooling bench

Heat management

Heat management in the Laser Cryocooler design is the second driving design point after optical design. Indeed, when the cooling crystal absorbs the laser light power, the entire optical power will be re-emitted in the form of fluorescence. In practice, the crystal will act like a light-bulb with a power of several Watts to several dozen of Watts.

We cannot allows fluorescence to be left un-managed and going into free space: the systems surrounding the Laser Cryocooler may not be compliant with that light source which would cause parasitic heat and stray light. It means that a "clamshell" has to surround the crystal in order to absorb and thermalize as much fluorescence as possible. The first requirement of the clamshell surfaces viewing the crystal is to absorb light in the near infrared around 1000 nm.

A problem arising is how to avoid the clamshell surfaces surrounding the crystal from heating up too much. In vacuum, heat can only dissipate through conduction and radiation. If the clamshell is isolated from is environment or if some parts in the clamshell heat up and have low surface thermal conduction with the rest of the clamshell, they might overheat and potentially reach temperatures over 100℃.

To maintain the clamshell around the same temperature through the experiment, most of the elements in the cold head are made of copper, and two water flow were implemented in the design. The first water flow passes through the clamshell base, while the second water flow passes inside the clamshell hat To monitor the temperatures of the clamshell elements, we put blind bores at different spots: one in the clamshell base, one in the collimator mount and one in the clamshell hat. PT100 temperatures resistance detectors (RTDs) were then placed in these holes and drown in Stycast epoxy glue, as shown in Figure 4.40.

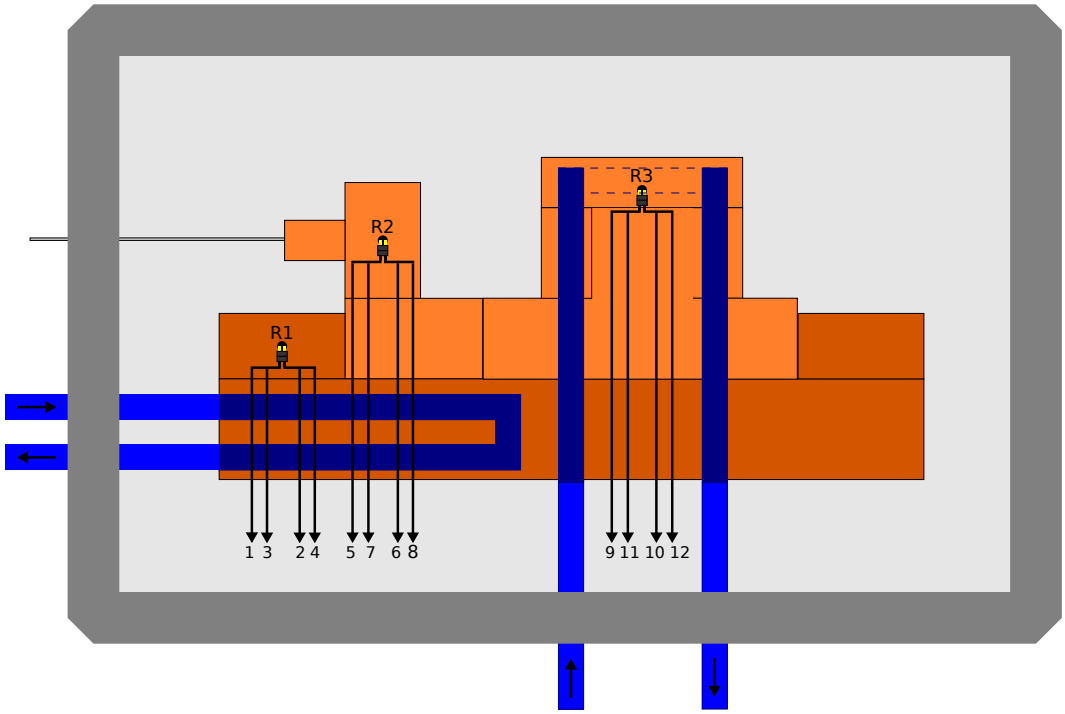

Figure 4.40: *Schematic of the fluid and electrical connections in the cooling bench.*

The second clamshell requirement is the surfaces viewing the crystaly possess low infrared emissivity, in order to avoid the warm clamshell from heating up the cold crystal by thermal radiation. Indeed, if the crystal reaches cryogenics temperatures while its environment is at room temperature, there will be two sources of losses: radiative and conductive losses. For two surfaces facing each-others, the radiative power from the hot to the cold surface is equal to:

$$P_{rad} = (\frac{\epsilon_{Hot} A_{Hot}}{\epsilon_{Cold} A_{Cold}})\sigma(T_{Hot}^4 - T_{Cold}^4) \tag{4.22}$$

With ϵ_{Hot}, A_{Cold} and A_{hot} the hot and cold surfaces, ϵ_{Cold} the hot and cold surface's emissivity, σ the Stefan-Boltzmann constant, T_{Hot} and T_{Cold} the hot and cold surfaces temperatures. To reduce the radiative losses, the solution is either to cool down the surfaces facing the crystal, or to find a surface with low emissivity. In practice, it is easier to decrease the clamshell emissivity because making an actively cooled clamshell would require a more complex design.

As stated in chapter 1, some materials such as polished metals have low infrared emissivity. However, we cannot just deposit a layer of gold on the surfaces facing the crystal because gold is an excellent reflector in the near-infrared, which would cause the fluorescence to be trapped and re-absorbed by the crystal, completely suppressing the initial cooling process. The choice material must feature high near-infrared absorption and low infrared emissivity at the same time.

Solar absorbers such as TiNOX [16] or stray-light mitigation coatings such as Nanoblack [17] possess this property of high absorption and low emissivity. Ultimately, we made the choice to work with TiNOX due to its cheap price, its excellent performances as shown in Figure 4.41, and also because it is standardly supplied on a copper foil which can be then cut and soldered at our convenience.

The clamshell should also be tightly fitting the crystal's surfaces (without touching them), because the radiative power heating the crystal is proportional to the ratio between the exposed crystal surface and the exposed clamshell surface.

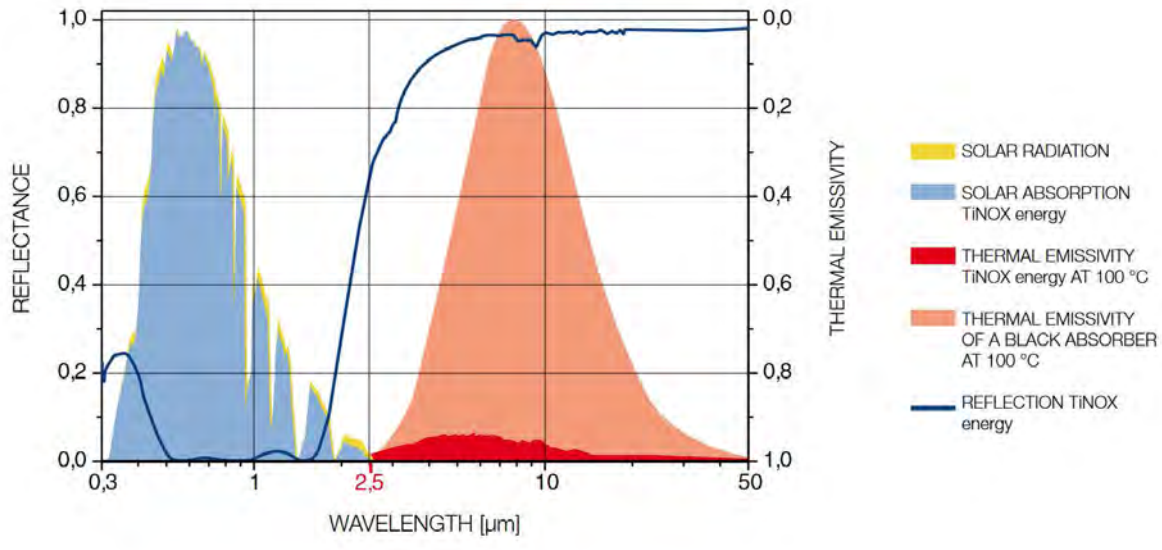

Figure 4.41: *Reflectance and thermal emissivity of Almeco's TiNOX solar absorber coating, from reference [16]. TiNOX possess about 5% infrared emissivity with near unit absorption in the near-infrared around 1000 nm.*

The last problem with thermal management is how to maintain the crystal and align it pre-

cisely in the absence of thermal link. In a first version of our design, we chose to align the crystal to Brewster angle by pushing it against two fibers, while the crystal layed on three optical fibers glued in tiny screws which were adjusted below the clamshell by screwing or unscrewing. However, it was difficult to achieve good mechanical stability of the crystal over the three bottom fibers, as the fibers were brittle and prone to moving if not perfectly glued.

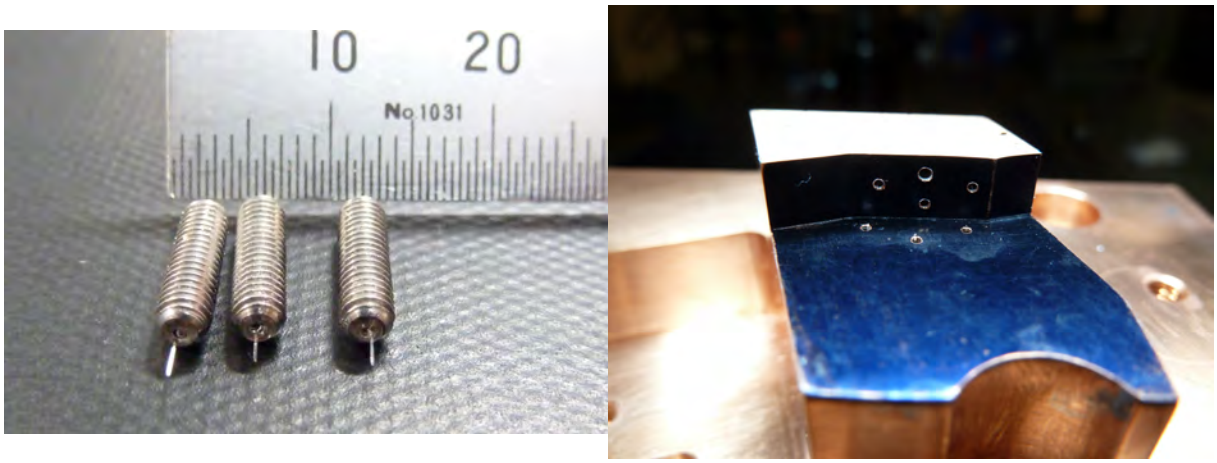

Figure 4.42: *Left: Photograph of the screws with fiber used in the first version to hold the crystal. Right: Photograph of the clamshell with the fibers mounted.*

We finally replaced the three bottom fibers with two Airloy® X56 silica aerogel pads, providing an easier alignment. Silica aerogel is the world's most insulating solid material with thermal conductivity in the order of 20 to 30 mW/m.K.

Mechanical design and mounting of the prototype

The copper parts were designed and fabricated at Institut Néel by the experimental engineering support team, upon providing the optical specifications.

The prototype features a chariot with the collimator mount being fixed to the input mirror. The collimator can be moved with a two axis XY adjustment which allows to aim for the hole at the center of the first mirror. The length of the multi-pass cavity can be varied by adjusting the chariot position before clamping it to the base. We chose to mount the second cavity mirror which needed fine tilt adjustment on a Polaris kinematic mount from Thorlabs. On the clamshell hat, an aperture was left open in order to monitor the crystal's temperature with a thermal camera from above.

After the parts were designed and fabricated, they were assembled and mounted in the vacuum enclosure, as shown in Figure 4.43. We can see the blue color of TiNOX at the center of the cavity, which was brazed on copper using soldering tin spheres on each of the surfaces around the crystal.

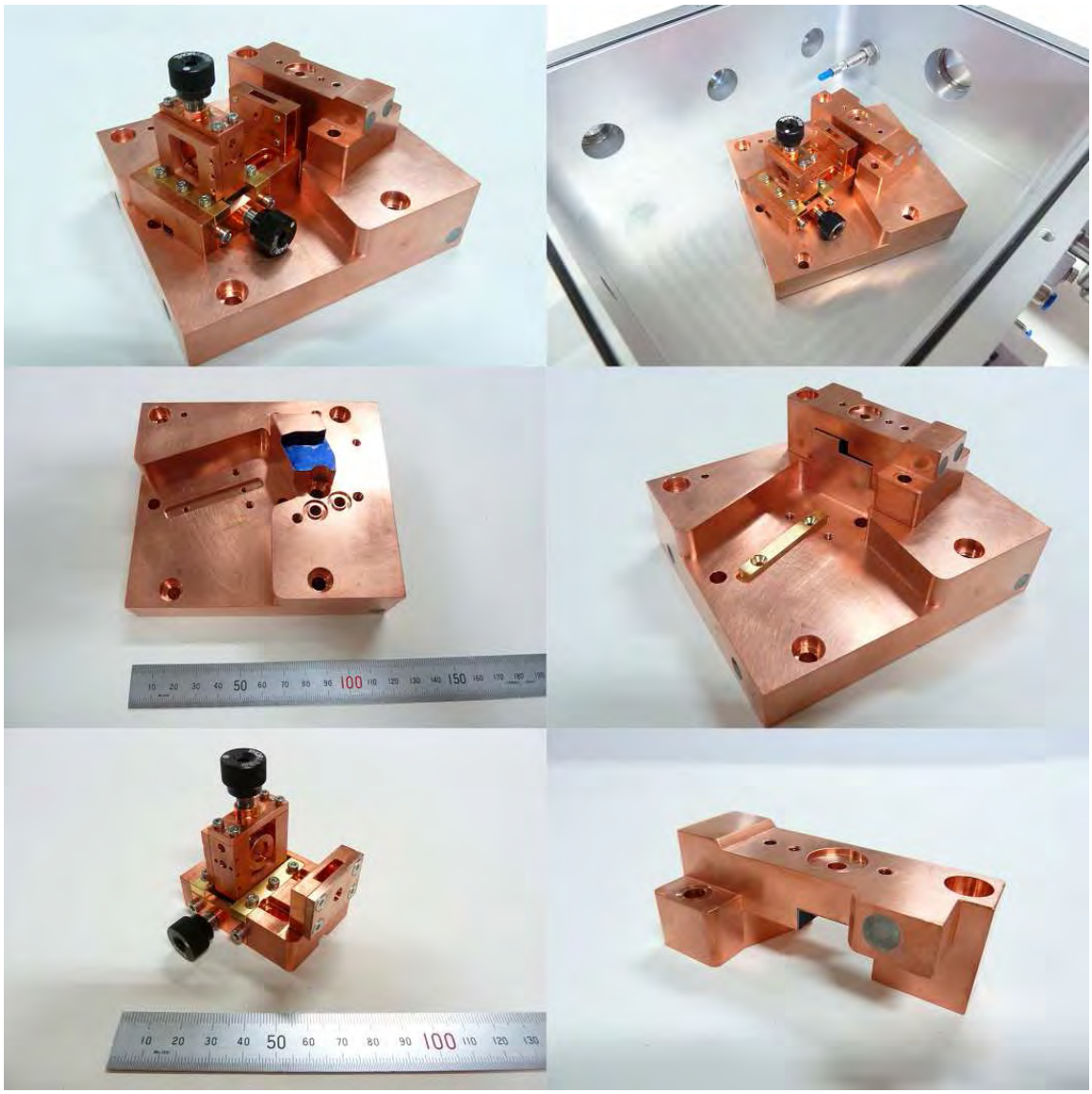

Figure 4.43: *Photographs at different steps of the clamshell base, clamshell hat and collimator mount after fabrication and during assembly.*

Vacuum enclosure

Specifications and interfaces definition: Before starting a design, it was necessary to specify our needs, the constraints and interfaces we wanted in the cooling bench. The vacuum enclosure had to accommodate:

- One fiber feed-through for the input fiber.
- One fiber feed-through for the fluorescence collection fiber.
- Electrical feed-throughs for the clamshell 4-wires RTD measurements.
- Ports for vacuum pumping and for the vacuum gauge
- One port for the observation of the Lissajous figure behind the second mirror.

- One port for the observation of the crystal temperature above the clamshell.
- Two water flows for the clamshell thermal control.

Figure 4.44 shows the final vacuum enclosure with the prototype mounted. We can see the different feed-through (fibers, electrical, fluids, optical).

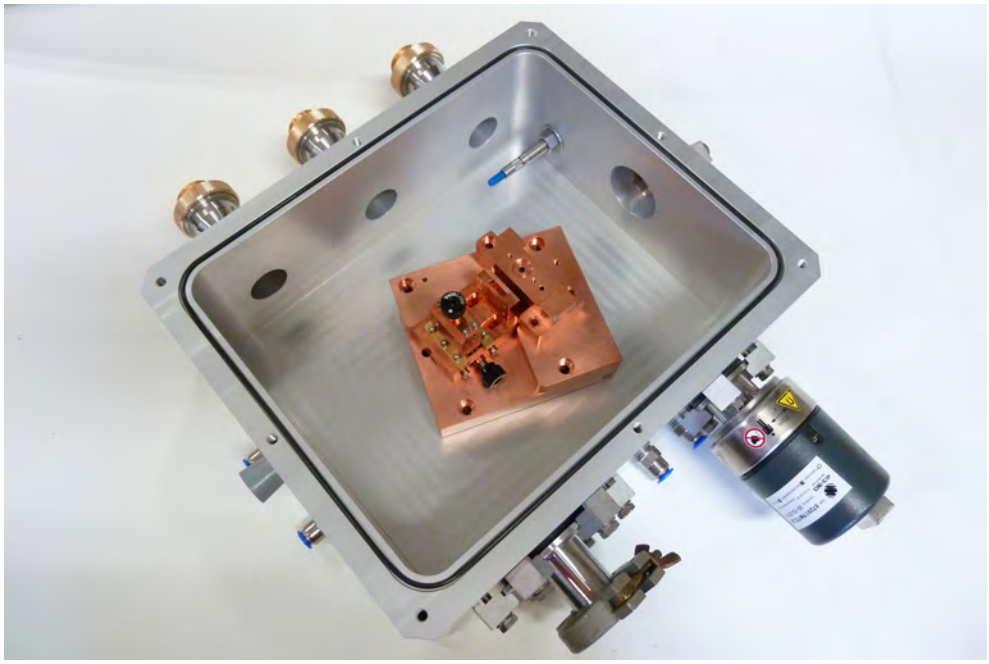

Figure 4.44: *Photography of the cooling bench mounted in the vacuum enclosure, showing all the interfaces.*

Vacuum tests: Before starting the cooling experiment, the vacuum enclosure was tested to check how low the vacuum could get. The pressure was measured with a filament pressure gauge (model Infinicon VGC501) mounted on the enclosure. The enclosure was then pumped with a pumping station featuring a primary pump automatically switching to a secondary turbo-molecular when reaching a vacuum of 1 mbar. After three days of pumping, the limit vacuum was on the order of 6.10^{-6} mbar.

Optics preparation

Coupling fiber preparation: Before using the PM fiber, they needed to be prepared and their plastic coating partially removed in order to avoid a potential unwanted heat-up. A fiber length of about 2 meters was first cut. The tips (about 5 cm) were plunged in acetone for 30 minutes in order to soften the plastic polymer. The fibers ends were then mechanically stripped from the polymer coating with the adapted fiber stripping tool. Figure 4.45 shows the transition from stripped fiber to coated fiber as observed with an electronic microscope.

We see that the transition is very clean with very little plastic residuals on the stripped region.

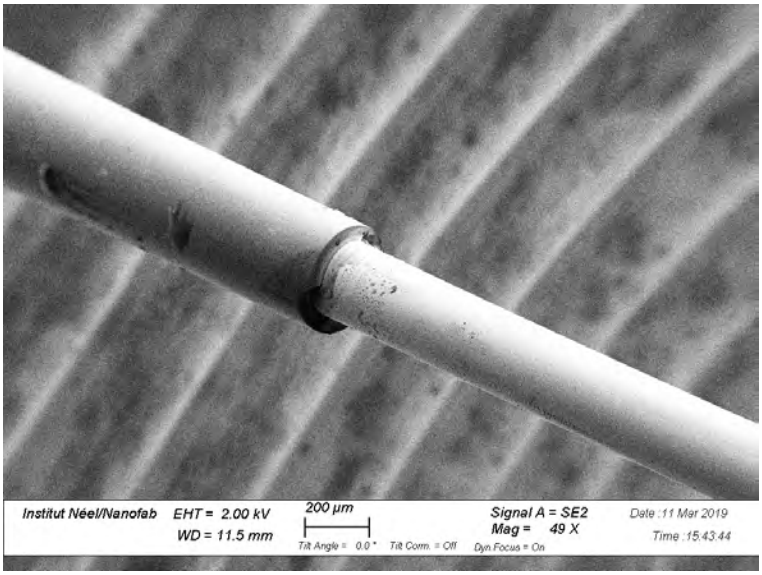

Figure 4.45: *Image of a prepared PM optical fiber at the beginning of the stripped section observed with an electronic microscope (secondary electrons image).*

After stripping, fiber chucks were put on both ends. The fibers tips were then cleaved with a sharp fiber cleaving tool in order to get nice and flat fiber ends.

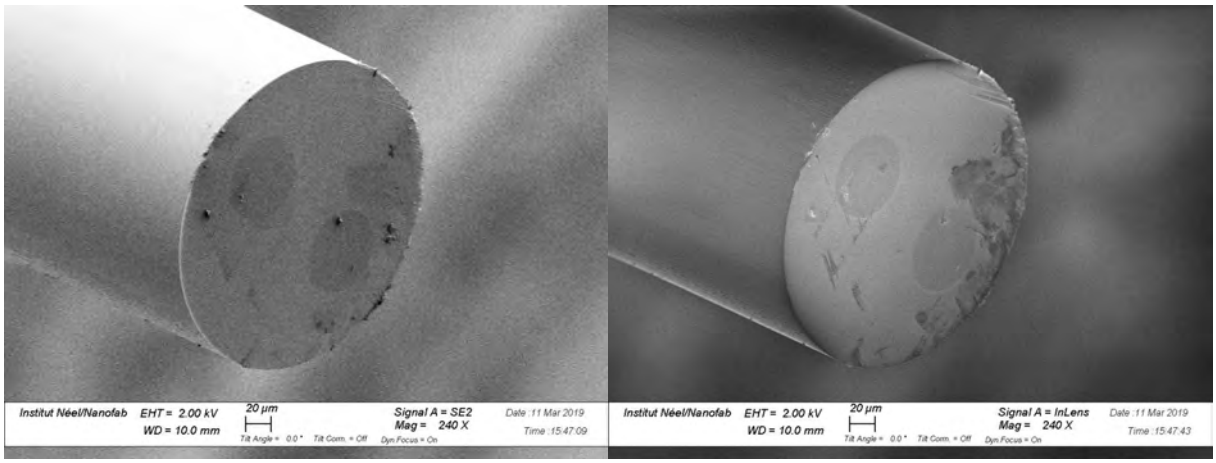

Figure 4.46: *Tip of a stripped and cleaved PM optical fiber observed with an electronic microscope.*

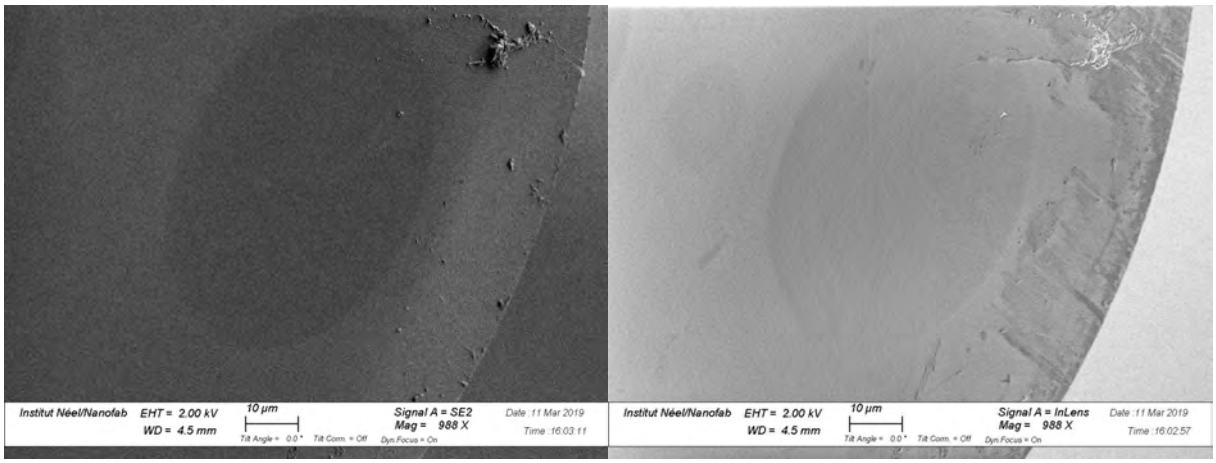

Figure 4.47: *Tip of a stripped and cleaved PM optical fiber observed with an electronic microscope, zoom on the fiber's core.*

Collimator alignment and gluing: The collimator was aligned on a separate optical bench. The alignment was performed in three steps. First, a camera with fixed focus was positioned to make an image of a fused silica plate simulating the first mirror, located in the plane at a distance of 30 mm after the collimator. A calcite polarization displacer was placed after the camera in order to check the output polarization. Then, the laser was turned on at low power, and we observed the image of the fiber's output. The output fiber to lens distance was then adjusted in order to get the smallest laser spot. In order to adjust the polarization, the fiber's eyes were rotated in the horizontal plane. Figure 4.48 shows the image of the PM fiber for different camera exposure times. We can see the secondary image of the deviated polarization falling on the side of the camera.

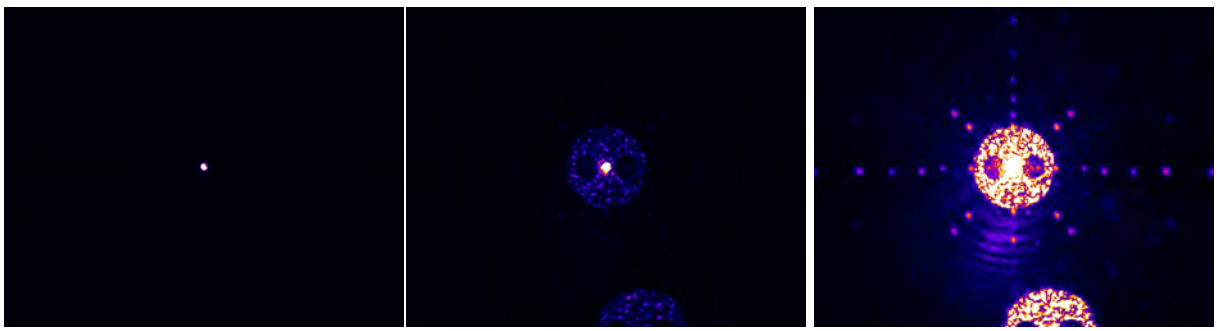

Figure 4.48: *Laser beam at the fiber collimator's output observed with a Vis-NIR camera with increasing exposure times.*

The output tilt angle was then adjusted by translating the fiber relatively to the collimator lens. The tilt and beam divergence are measured by translating the camera along the optical axis, over about 20 cm. When the angle was set, we fixed the chuck holding the fiber inside the collimator by pouring Stycast glue with a syringe inside a dedicated hole in the collimator. When the Stycast was dry (after about 1 day), the collimator was remove from the alignment bench (as shown in Figure 4.49) and placed on the cooling bench.

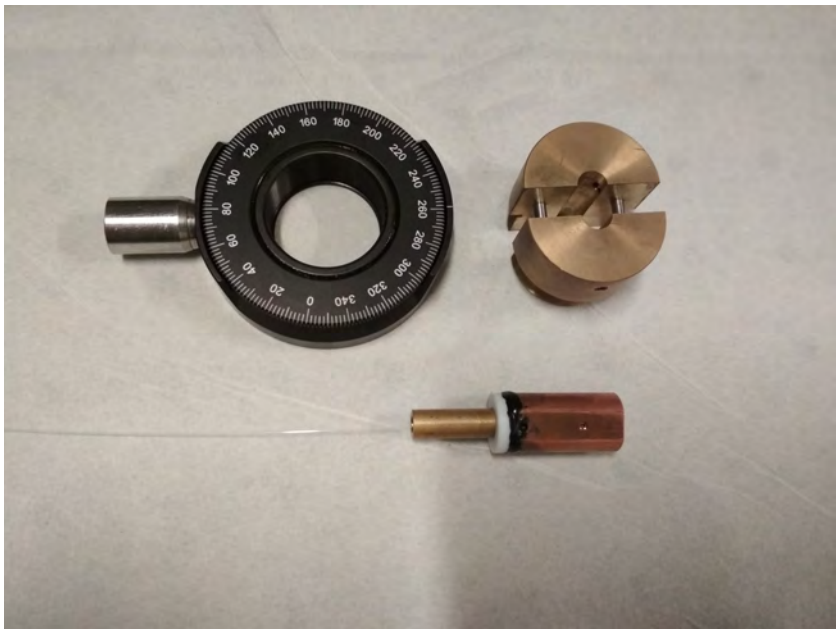

Figure 4.49: *Photograph of the glued collimator and the pieces used to hold the collimator during the alignment step.*

Mirrors characterization and mounting: After our initial optical design phase, we chose to use a cylindrical mirror with 200 mm radius of curvature, and a spherical mirror with 200 mm radius of curvature too. We contacted the German company LaserOptik, specialists in custom optical coatings, with a special request for the cylindrical mirror manufacturing. We wanted a mirror with HR coating at 1020 nm everywhere on the mirror surface except on the middle, where we asked for a tiny 150 μm zone to be AR coated.

Unfortunately, the lithography turned out to be more troublesome than expected and the supplier was not able to perform the last step, the lift-off process, leaving a resin ca, covered with HR coating on the center of our mirrors as shown in Figure 4.50.

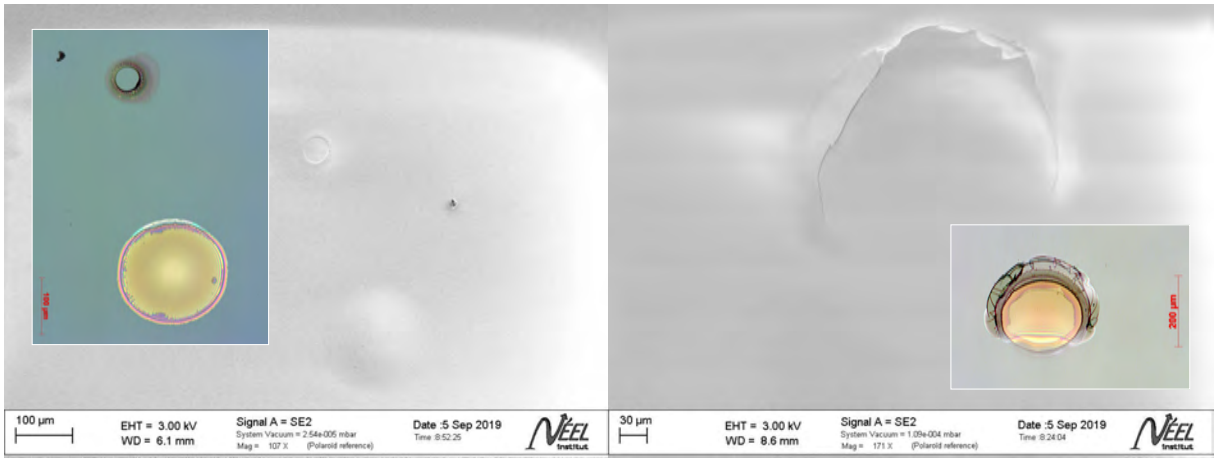

Figure 4.50: *Cylindrical mirrors center observed with an electronic microscope (full figure) and optical microscope (inset). Left: Center of the first mirror. Right: Center of the second mirror.*

Most probably, this problem was due to insufficient thickness of the middle sacrificial

layer deposition. We decided to try and fix the problem at Institut Néel using the Focused Ion Beam (FIB) available at the Nanofab clean room.

A first test was to check the Bragg mirror multi-layer structure by digging a hole on the side of a mirror, as shown in Figure 4.51. This allowed to know exactly how deep we had to dig in the mirror until reaching the anti-reflection layer underneath the high reflection coating. A thickness of 6μm was found for the Bragg HR layers.

After making this test, a circular trench was dig-up at the mirror's center in order to expose the resin, as shown in Figure 4.52. The center cap was finally successfully removed after a passage in an ultrasonic bath with acetone for 30 minutes. Figure 4.53 shows the mirror's center observed with the optical microscope in white light and in dark field.

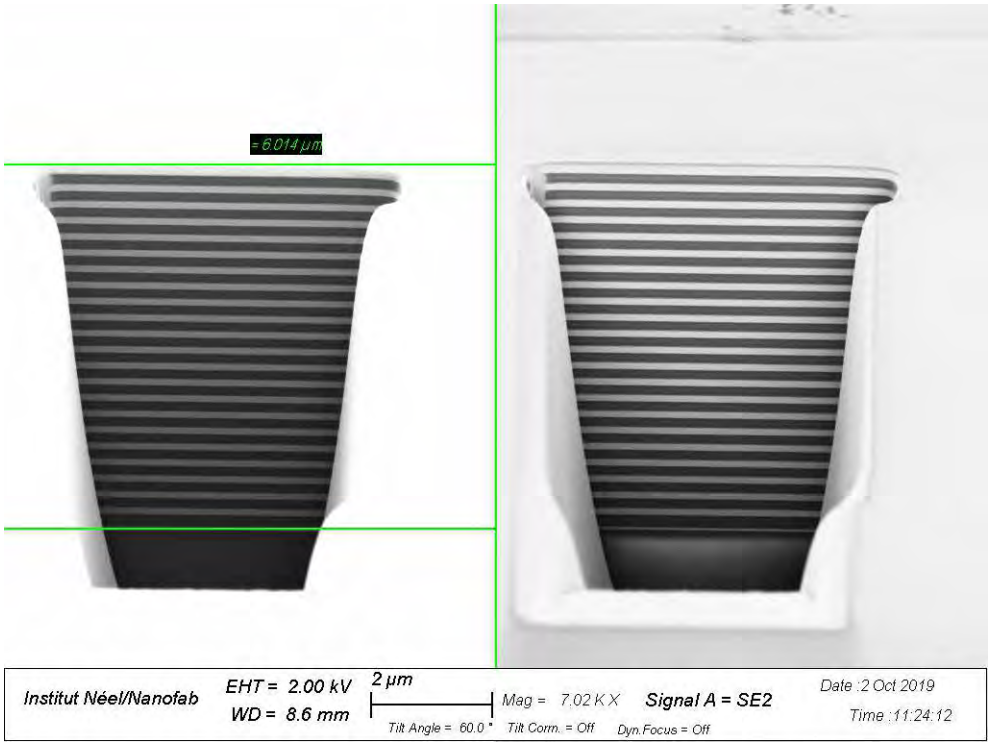

Figure 4.51: *Trench in the first supplied cylindrical mirror made with focused ion beam (FIB), observed with an electronic microscope. The Bragg mirror structure is exposed, showing two alternating layers of different composition and optical index appearing in black and white. There is a quarter wave bi-layer at the bottom (first layer 40 nm, second layer 200 nm), and 43 Bragg layers (100 nm and 150 nm) for a total thickness of approximately 6 μm.*

The mirror was then mounted on the experiment. In order to test it, we aligned the collimator such that the beam hit on the middle inside the input hole. A transmission of approximately 70 % to 75 % was measured for the first mirror, sufficient in a first iteration to perform our cooling experiment.

At first, the cavity alignment with the Yb:YLF crystals was very difficult just by looking at the back mirror with the camera. Indeed, the strong absorption of Ytterbium at room temperature makes the laser beam to be completely absorbed in two or three passes. To make the alignment easier, we decided to use a mock-up crystal made from fused silica,

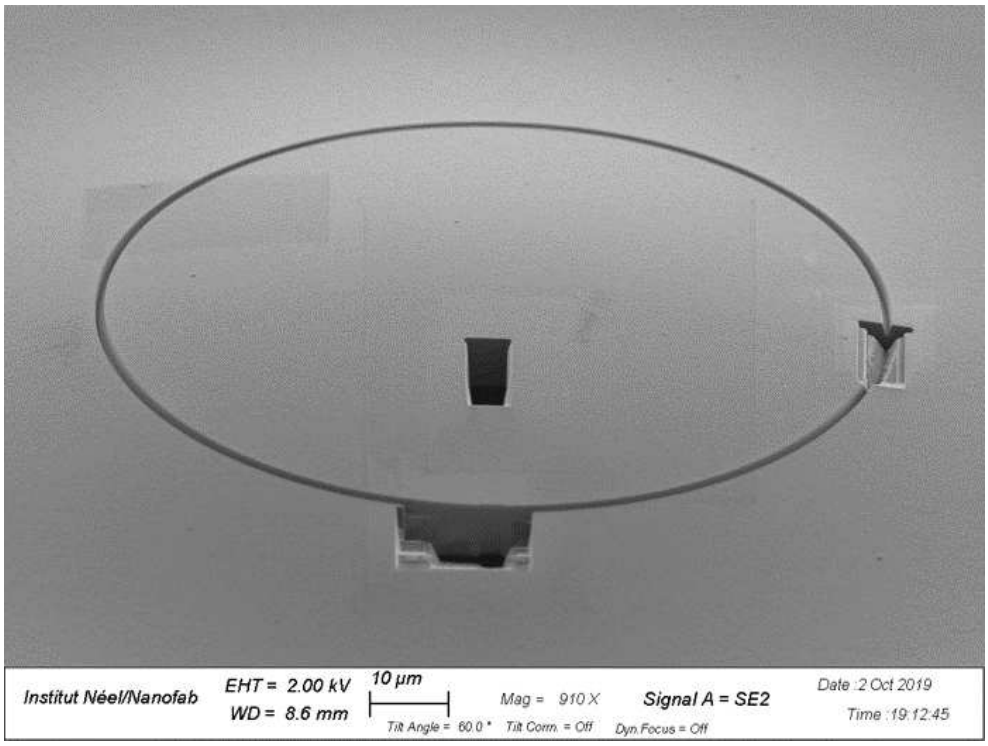

Figure 4.52: *FIB lithography of the first mirror observed with the electronic microscope.*

Figure 4.53: *Center of the first supplied cylindrical mirror after lithography and laquer cap removal, observed with an optical microscope in white light (right) and in dark field (left).*

which posses a refractive index very close to that of YLF. The "fake crystal" was cut at Brewster angle and put in the multi-pass cavity. This time, the Lissajous figure round-trips were clearly observable, as shown in Figure 4.54.

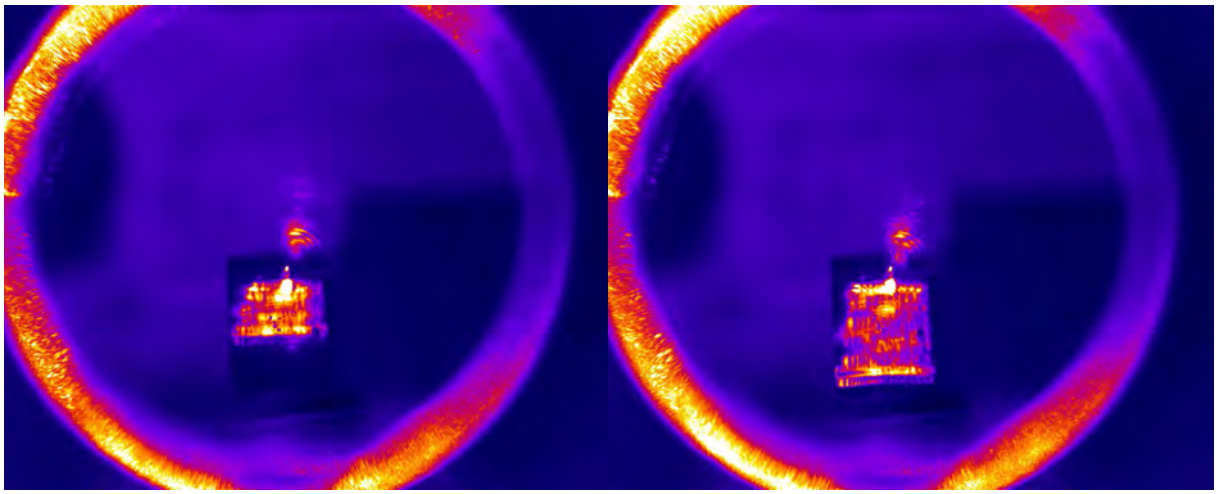

Figure 4.54: *Images of the Lissajous figure observed through the cavity second mirror with the dummy fused silica crystal. The change of Lissajous figure size is noticeable when varying the second mirror's vertical tilt of about 1/4 revolution, equal to about 2.75 μrad or 0.16°.*

4.3 Cooling crystals validation

Before starting any cooling experiment, it is crucial to characterize the cooling crystals employed for two reasons. First, gaining good knowledge on a crystal allows to predict its cooling performances. The second reason is that practical applications using cooling crystals requires high traceability in order to avoid costly mistakes. As stated in section 3.4, obtaining a cooling crystal with nominal performances is the result of several irreducible months of work. A crystal which doesn't corresponds to specifications in terms of dimensions, cooling efficiency, orientation or defects can introduce significant time delay in a project.

The validation of cooling crystals can be performed in two times. Usually, a crystal preform is first carved from the boule, c-axis oriented, rectangular shaped and undergoes initial tests to check its cooling efficiency at room temperature. It is then re-worked to get its final shape and undergoes a series of tests to assess its cooling efficiency at cryogenic temperatures. The required tests are summarized in Table 4.1.

As the cooling experiments were being set up, different crystals were progressively received. The whole testing sequence was not performed on each crystal for timing reasons. However, each one of the tests stated above were performed at least one time to confirm that we were able to implement them successfully. In the following sections, the crystal samples we received are presented and the characterizations that were performed on them are described.

Part	Specification	Description	Tests
Initial shaping			
	Dimensions	Are the crystal preform dimensions superior to the specified values ?	Caliper / Optical measurement (microscope)
Crystal preform	Orientation	Are the crystal axes correctly oriented ?	X-ray diffraction
	Cooling efficiency (300 K)	How much does the crystal cools down at ambient temperature with specified pumping wavelengths ?	Absorption spectroscopy (300 K) + Cooling down test (300 K)
	Surface & volume defects	What is the crystal preform surface state before shaping ? How many volume defects are visible inside ?	Visual inspection + Surface inspection (optical microscope, electronic microscope) + Volume defects analysis (red and blue lasers scattering)
Shaping			
	Dimensions	Are the crystal dimensions superior to the specified values ?	Caliper / Optical measurement (microscope)
Final crystal	Surface & volume defects	What is the crystal surface state after shaping ? How many volume defects are visible inside ?	Visual inspection + Surface inspection (optical microscope, electronic microscope) + Volume defects analysis (red and blue lasers scattering)
	Cooling efficiency (T_{cryo})	How much does the crystal cools down at required cryogenic temperatures with specified pumping wavelengths ?	Absorption spectroscopy & fluorescence spectroscopy (T_{cryo}) + Cooling down test (T_{cryo})

Table 4.1: *Specifications and required tests for the validation of cooling crystals.*

4.3.1 Samples

During this thesis, several cooling crystals were gracefully lent by the University of Pisa in order to set-up and perform our cooling experiments. We received in total 3 Yb doped YLF crystals, all of them grown with the Czochralski method at Pisa and identified with a collection number. Table 4.2 lists the crystals used during this work.

We first received a co-doped crystal which does not cool in order to practice the crystal handling and to use in the spectroscopy benches in order to reproduce the absorption and fluorescence spectra which were measured at Pisa on different samples.

Then, as the laser cryocooler prototype design reached its end, we received a cooling crystal to use in the experiment. However, after pumping it in single pass configuration at 1020 nm, we came to the conclusion that it did not cool. The author went to Pisa to perform extensive cooling efficiency tests, which confirmed that the cooling efficiency in that sample at the pumping wavelength was close to zero, due either to some scratches on the crystal surface or too many residual impurities. After re-polishing, the crystal's cooling efficiency was measured again. It improved a bit but remained still small in comparison to the expected typical efficiency.

Sample number	Designation	Specifications	Comments
(1)	10%Yb-0.01%Tm:YLF Collection 190	Dimensions: 5 mm ($\perp \vec{c}$) x 3 mm ($\parallel \vec{c}$) x 9.8 mm Brewster cut, 6-faces mirror polished, Cooling efficiency: $\eta_c < 0$ (heating)	Practice crystal used for spectroscopy, no cooling. Oriented, Brewster cut and polished at Institut Néel.
(2)	10%Yb:YLF Collection 148	Dimensions: 2.8 mm ($\perp \vec{c}$) x 2.8 mm ($\parallel \vec{c}$) x 9.8 mm, Brewster cut, 6-faces mirror polished, Cooling efficiency: $\eta_c(300K, 1020nm) = 0.2\%$	First crystal intended for the multi-pass cavity. Tiny cooling efficiency at 1020 nm after re-polishing and single-pass testing at Pisa.
(3)	7.5%Yb:YLF Collection 143	Dimensions: 2.24 ($\perp \vec{c}$) mm x 2.5 mm ($\parallel \vec{c}$) x 9.5 mm, Brewster cut, 6-faces mirror polished, Cooling efficiency: $\eta_c(300K, 1020nm) = 0.6\%$	Final crystal used in the experiment, fair cooling efficiency at 1020 nm tested at Pisa.

Table 4.2: *Summary of the cooling crystals samples used during this thesis.*

Finally, we received a third crystal which possess high cooling efficiency, for which we performed our multi-pass cavity experiment and were able to reach cryogenic temperatures.

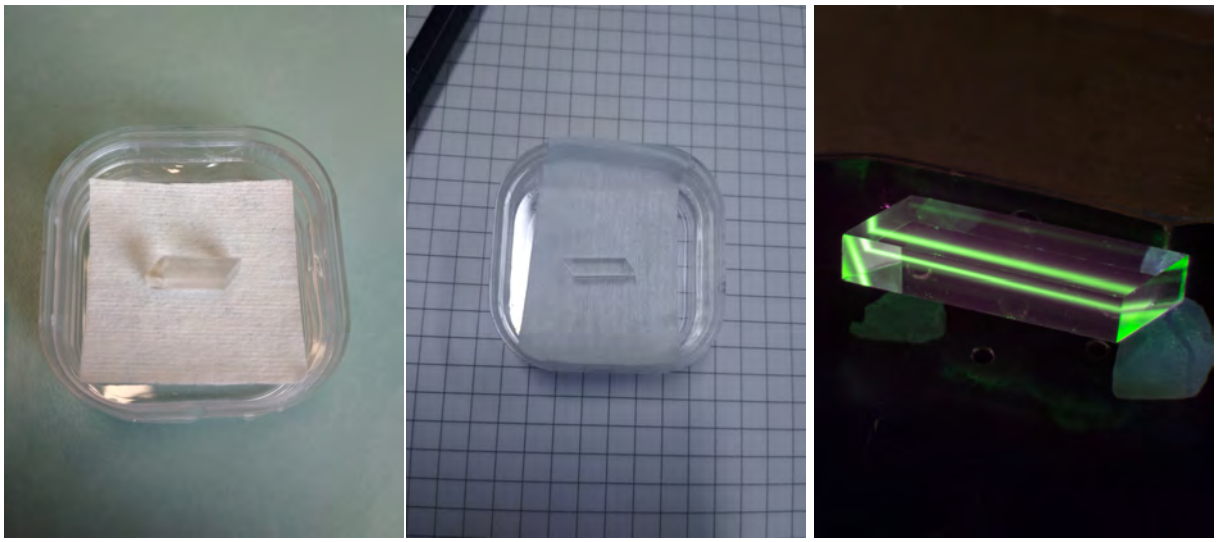

Figure 4.55: *From left to right: Photography of cooling crystals number 1, 2 and 3 used during this thesis.*

4.3.2 Orientation, cutting and polishing

After receiving sample number 1, it was first pre-cut with a diamond saw at 55° angle (Figure 4.56). Its orientation was then checked before fine setting the Brewster angle (55.4° for YLF).

The Laue X-ray back-scattering method (Figure 4.57) was used, using the Orient Express

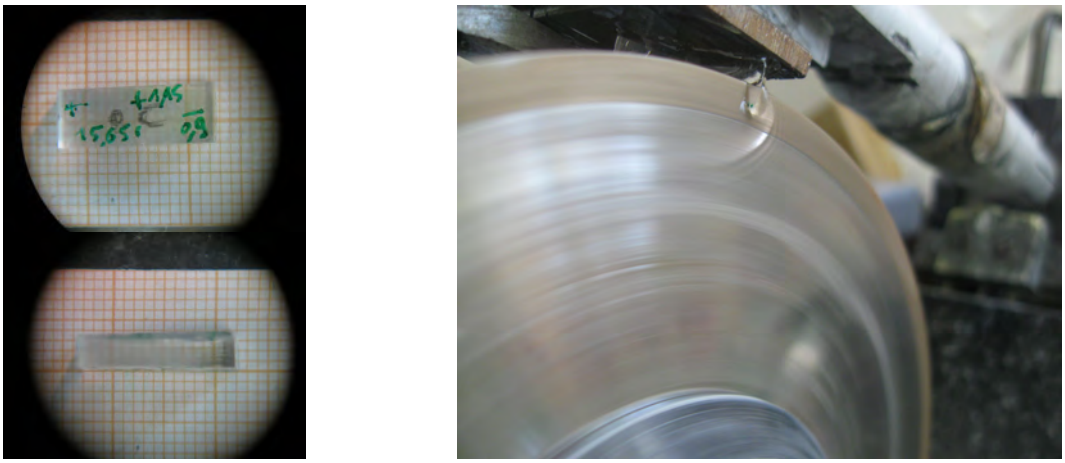

Figure 4.56: *Co-doped crystal collection 190 before and during Brewster cutting.*

software which allows to compare the measured diffraction pattern with the predicted pattern for YLF. We found that the crystal's c-axis was a little bit off by 1.5°in the small direction.

Installed on a goniometer head, the crystal's orientation was then corrected by the measured angles and installed on a polishing head. The crystal's dimensions were thinned down such that the c-axis was orthogonal with the expected propagation direction and the Brewster angles were set with an estimated error of +/- 0.25° (Figure 4.58).

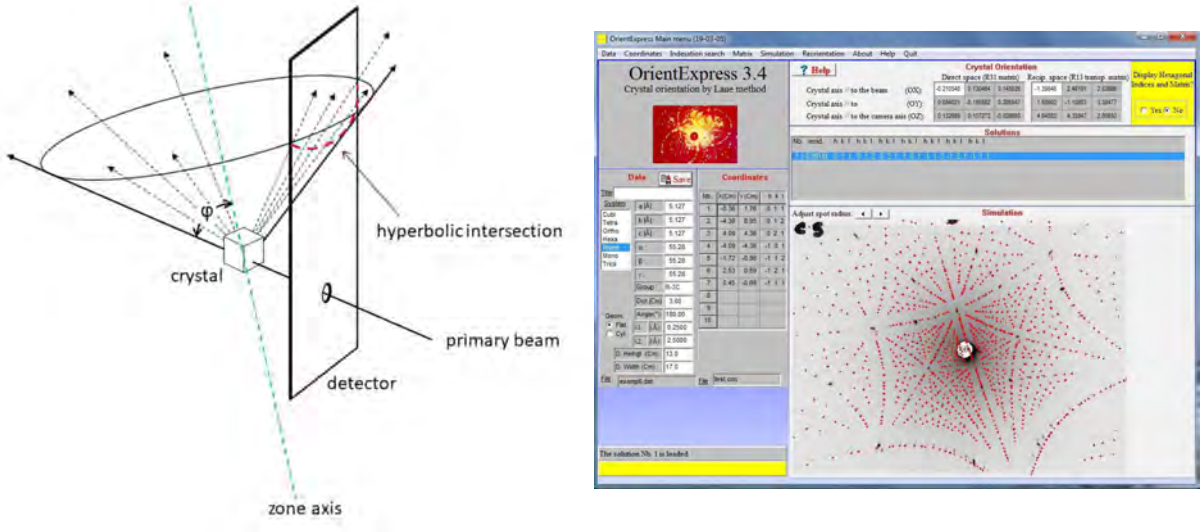

Figure 4.57: *Left: Principle of the Laue X-ray back scattering. The crystal sample is placed on the path of an X-ray beam with its dielectric axis making an angle ϕ with the beam. The scattered rays are collected by a detector or a photosensitive plate in a plane before the crystal. The hyperbolic positions of these spots correspond to intersections of scattering ellipses with the detection plane. Right: Orient Express software used to retrieve the crystal's dielectric orientation by superimposing a simulated diffraction pattern with the measured one.*

Figure 4.58: *Left: Photograph of the crystal attached at the left to a goniometer head in order to precisely orient its c-axis on the Laue diffractometer. Right: Photograph of the crystal polishing step. The polishing head is rotating on a fabric plate with diamond powder.*

4.3.3 Surface and volumes defects inspection

Surface inspection

Surface inspection is useful to keep a trace of the surfaces state, micro-scratches and polishing quality over a crystal's lifetime. Particularly, Brewster angles are very brittle and prone to cracks, even with the smallest shock. Another issue is surface contamination with glue or polishing residuals which can stay on the surface and hinder the cooling process. The surface of our cooling crystal samples were checked using two methods.

FESEM observation: After Brewster cutting and re-polishing the first crystal (collection 190) we decided to take a look at its surface with the Zeiss Ultra + Field Effect Scanning Electron Microscope (FESEM). The method provides the advantage of being able to resolve nanometer scale features, at the difference of an optical microscope which is diffraction limited.

Figure 4.59 shows some pictures of the crystal's surface. We can see that right after the polishing process, even if the crystal was cleaned up with acetone in a bath for several hours, many residuals remained. A particularity of this crystal was the use of colloidal silica in the polishing instead of diamond. We can clearly see the remaining silica grains on the surface and filling the holes in the crystal.

Upon seeing this contamination, we decided to put the crystal to cleaning again in an

ultrasound bath with acetone.Figure 4.60 show that this new cleaning reduced the amount of surface contamination, but some silica clusters and grains still remained.

These observations highlight the fact that contamination of the cooling crystal's surfaces should be controlled and quantified in order to get reproducible cooling performances. In the future, only diamond polishing solutions should be employed in order to keep the pollution of the cooling crystals surfaces at a minimum. In order to reduce the surface contamination further, a process similar to the RCA process could even be adapted, allowing to remove in a few step organic, inorganic and metallic impurities from the surface.

Optical microscope observation: During our early tests when trying to put it in a single pass configuration over two optical fibers, the second crystal (collection 148) accidentally fell from a few centimeters damaging the Brewster angles and scratching the surface. Since then, we learned from our mistake and use extra caution in handling the cooling crystals, avoiding unsafe tests. We also decided to systematically take a snapshot of the crystal's surfaces state upon receiving them, in order to get an initial point of reference. High resolution pictures over the whole third crystal surface were taken in clean-room by using the Zeiss Axio Imager optical microscope, as shown in Figure 4.61.

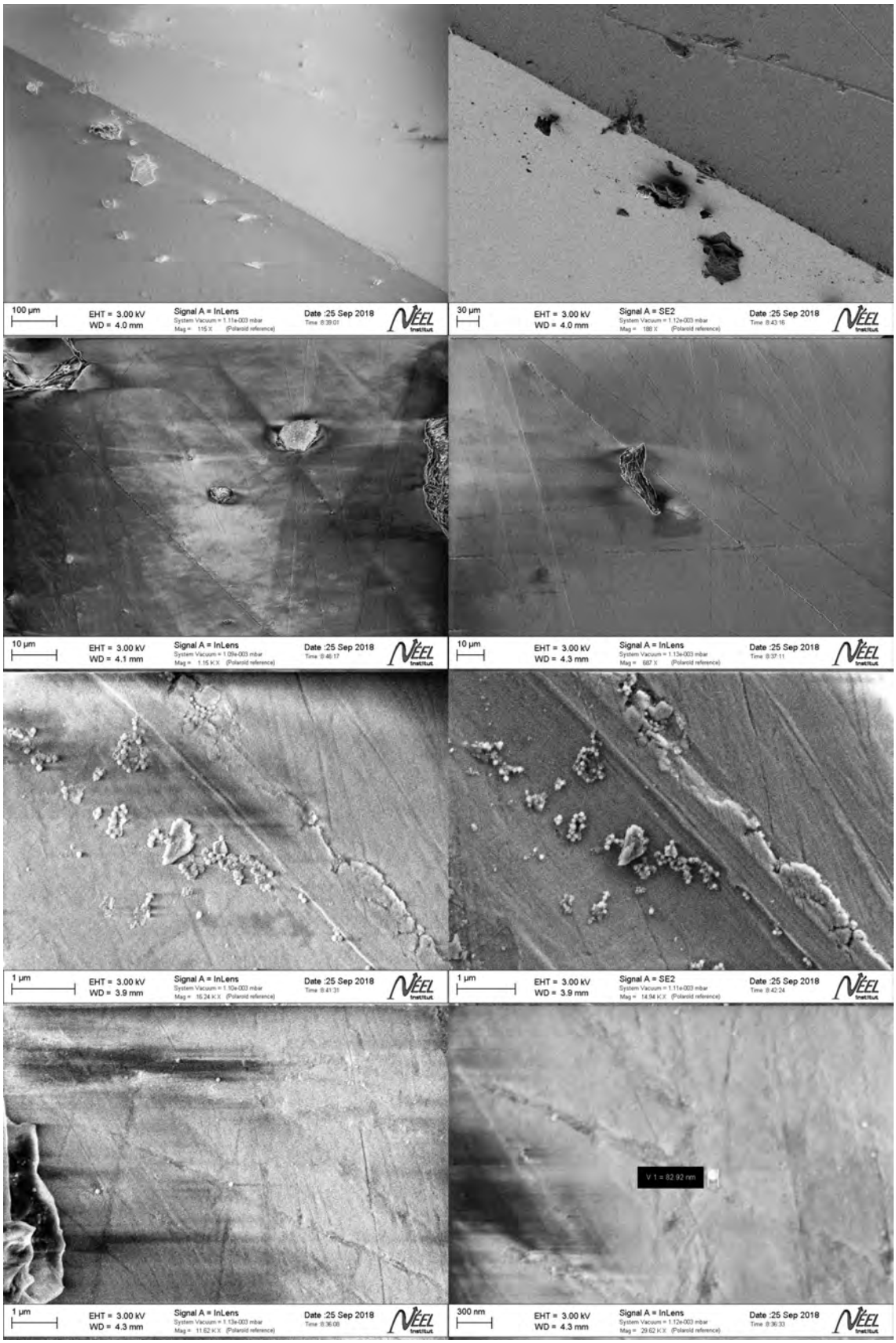

Figure 4.59: *Electronics microscope images of the crystal surface state after polishing before cleaning.*

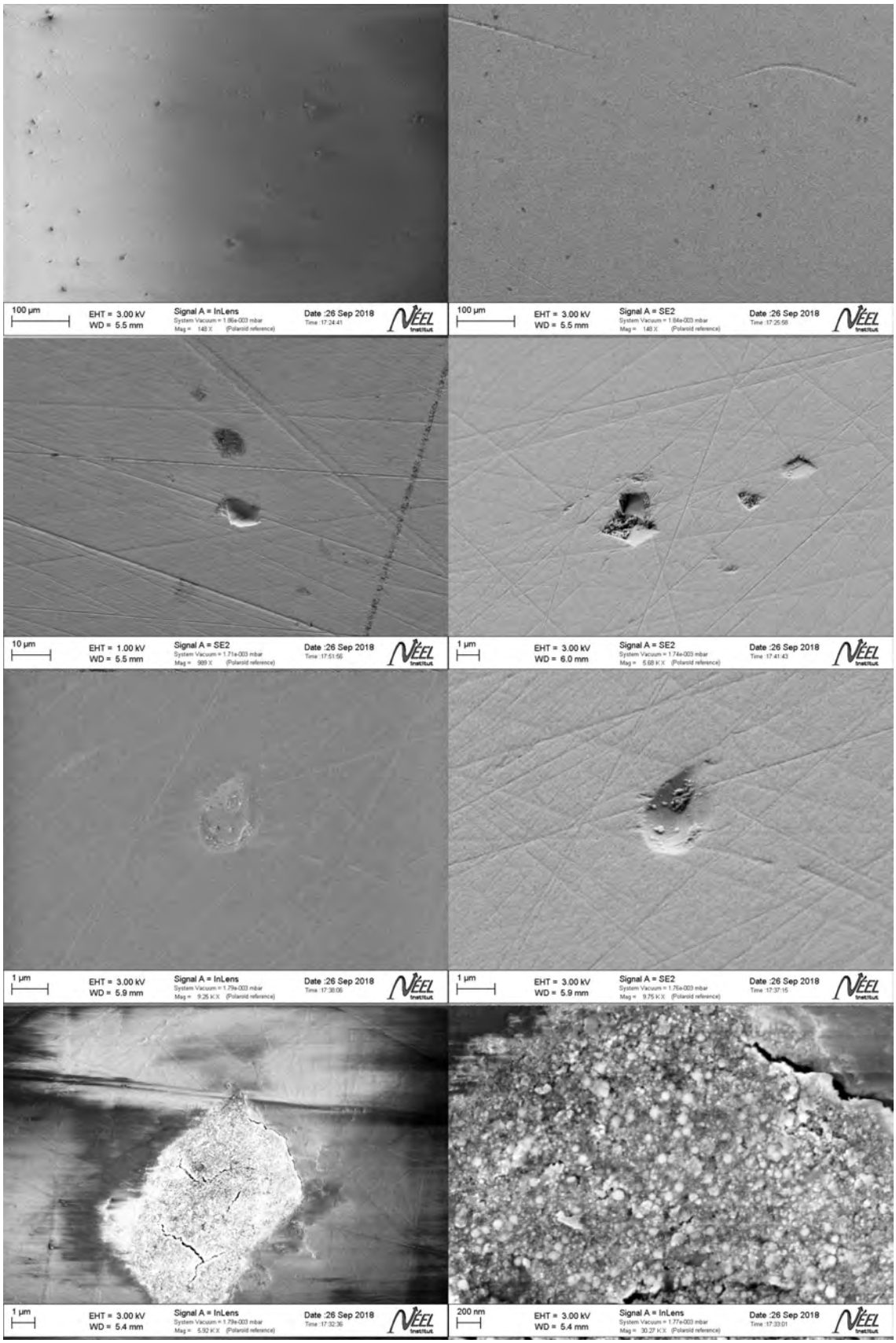

Figure 4.60: *Electronics microscope images of the crystal surface state after polishing and cleaning.*

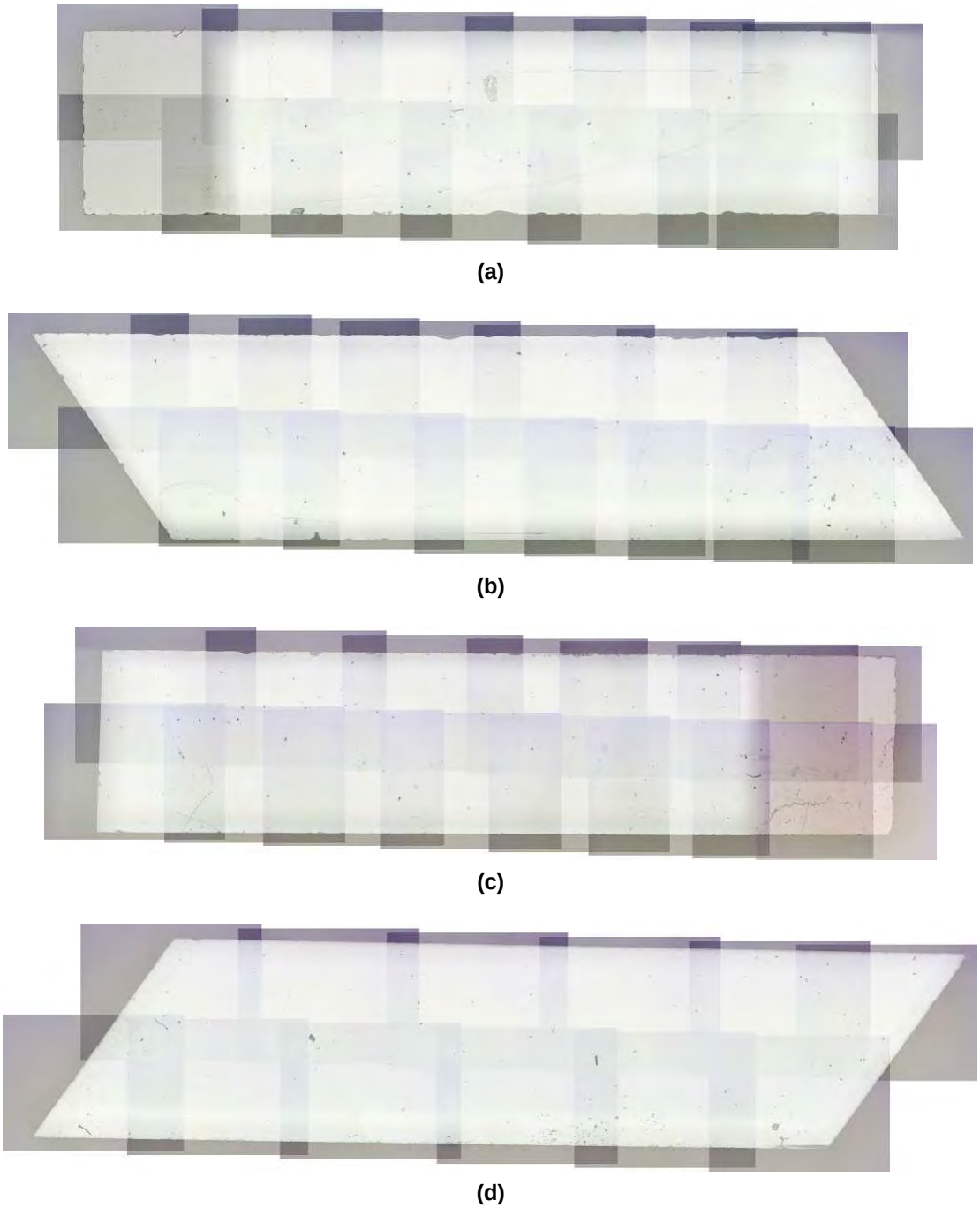

Figure 4.61: *Optical microscope observation of crystal 3, 7.5%Yb:YLF taken in clean room environment just after receiving the crystal. Images were stacked in order to get high resolution images covering the whole crystal surface.*

Volume scattering

In practice, after growing a boule the best region for carving a cooling crystal should be one with no micro-bubbles, cracks or defects of any kind. Such defects will reduce the external quantum efficiency by increasing the probability for a photon to be scattered before escaping the crystal.

During my stay at Pisa in January 2020, we checked the second crystal 10% Yb:YLF (coll. 148) with scattering analysis to make sure that it was not the cause of the smaller than expected cooling efficiency.

Scattering analysis is implemented by two methods at the University of Pisa. In the "red" scattering analysis, the crystal is put on a translating XYZ platform. A red laser beam allows to scan the sample by manually translating the platform relatively to the laser beam. Above the sample, a binocular microscope allows to take a closer look at the crystal to see if any scattering center appears while scanning. Figure 4.62 shows the image of the second crystal lit with the red laser. Very few bubbles were observed during our verification with the red laser (less than 3 tiny blinking spots on the whole volume were observed).

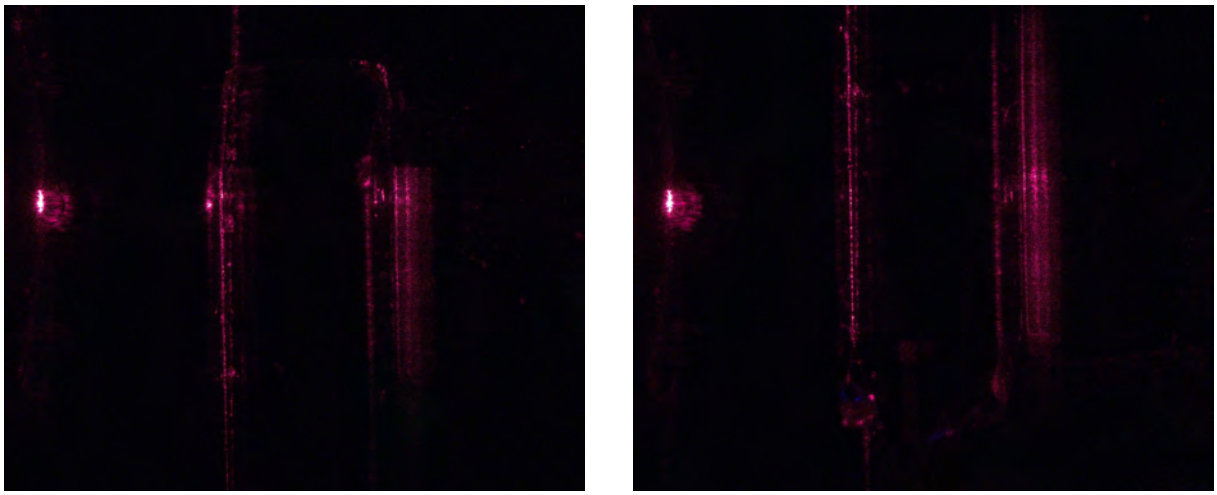

Figure 4.62: *Photographs of the red laser scattering analysis in two places along the length of the second crystal. The images do not reveal any scattering in the crystal center, proof of the absence of micro-bubble.*

A variant involves using a blue laser to see at naked eye if there is any scattering center, as shown in Figure 4.63. The analysis with the blue laser did not reveal any additional defect.

4.3.4 Absorption spectroscopy

Absorption spectra of cooling crystals is an important information, as it tells the quantity of light that is absorbed by a sample at a particular wavelength. It was meaningful for us to show that we were able to reproduce, or at least come close to the results obtained by our colleagues at the University of Pisa. First, it is a useful work for the community in the sake of cross-checking the results and scientific reproducibility. Secondly, it is also interesting to implement those methods and make sure our test equipments were operational in the case we would have to validate in second hand the performances of particular crystals or participate in measurements campaigns on new crystal types.

We performed the absorption measurements on the first crystal we received, 10%Yb-

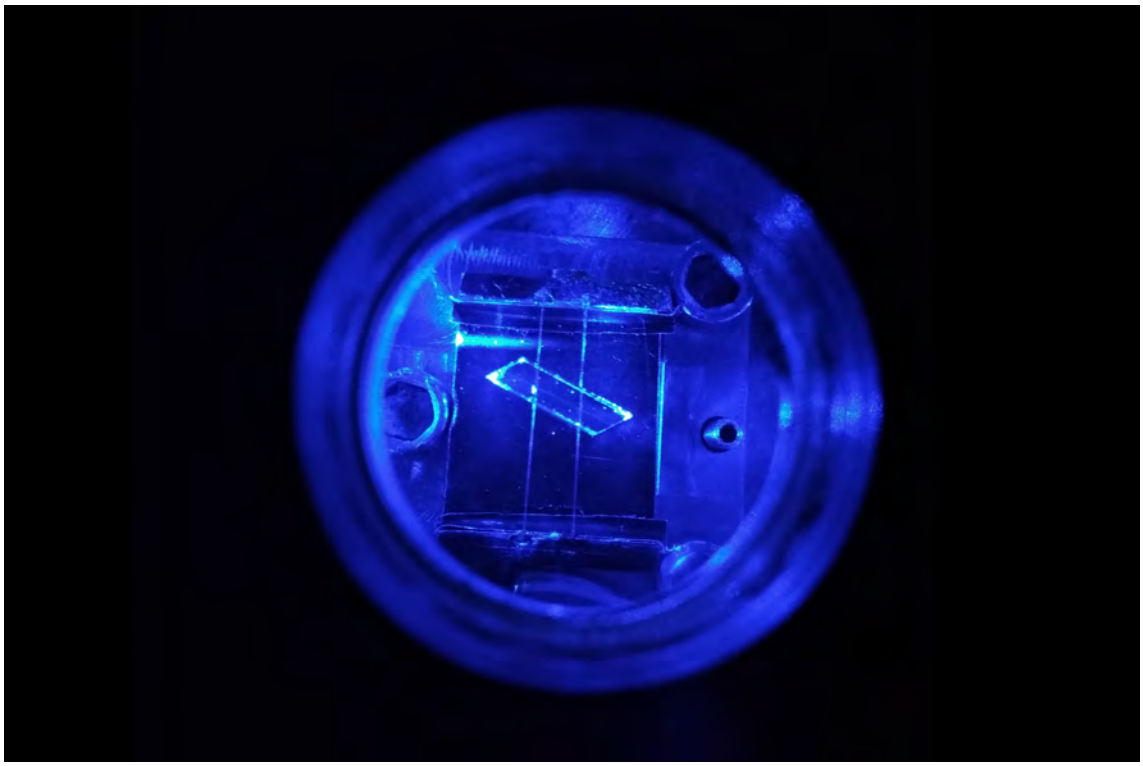

Figure 4.63: *Photograph of the crystal scattering when illuminated with a blue laser.*

0.01%Tm:YLF collection 190. In the course of my thesis, I used two different kinds of spectrometers at Institut Néel: a dispersive spectrometer and a Fourier Transform spectrometer.

Absorption spectroscopy with Perkin-Elmer Lambda 900

The first absorption test was performed using the Perkin-Elmer Lambda 900 spectro-photometer at Institut Néel, an instrument very similar to the Varian-Cary 5000 used at Pisa, at the difference that in our instrument we do not have yet the possibility to fit a cryostat and perform cold measurements.

Our instrument allows polarized light selection with an automated controlled set of Glan-Thomson polarizers on both the reference and sample paths. Unfortunately, those automatic polarizers encountered a mechanical problem and they were stuck upon starting our measurements. We decided to use a single Glan-Thomson in the sample path and change the crystal orientation to measure the transmission in both polarizations. The crystal was put on the spectro-photometer on the sample path, while the reference path was kept free. Figure 4.64 shows the transmission spectra measured with light polarized in E$\parallel$c and E$\perp$c directions.

Absorption was then calculated from transmission using Equation 2.54, knowing that the crystal was 0.3 cm long in E$\parallel$c direction and 0.5 cm long in the E$\perp$c direction. Measured

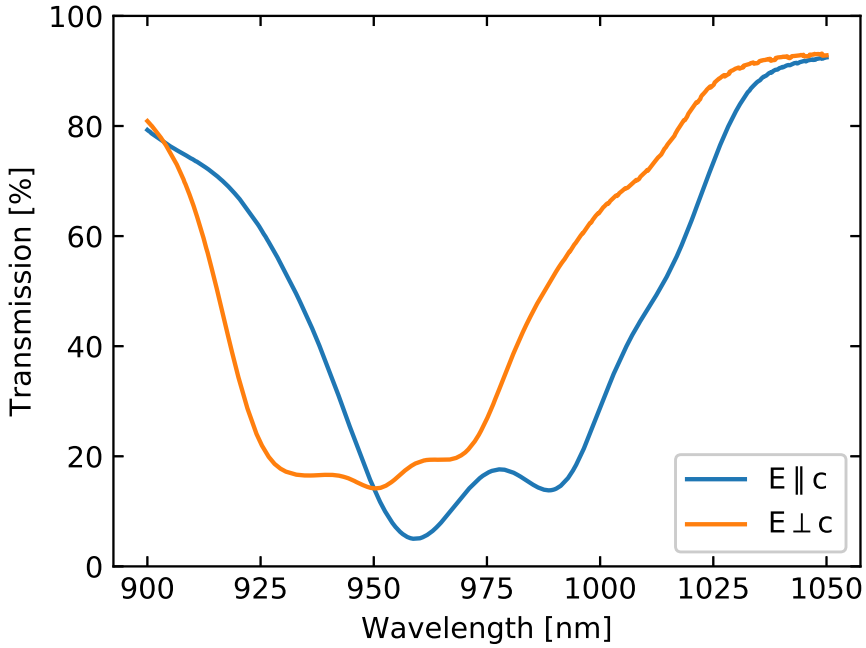

Figure 4.64: *Transmission obtained with Lambda 900 spectro-photometer on sample 1.*

absorption coefficients in both polarizations are shown in Figure 4.65.

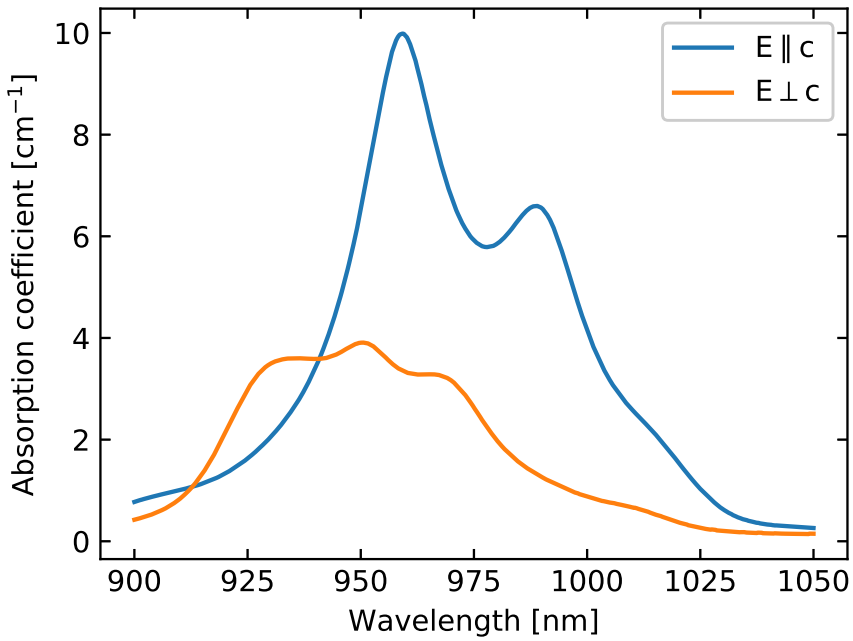

Figure 4.65: *Measured absorption for sample 1 taken obtained with the Lambda 900 spectro-photometer.*

We see that the shape of both absorption curves agrees with the reference absorption spectra measured at the University of Pisa shown in Figure 2.22. However, the peaks are much less resolved and the amplitudes are inferior to the reference room temperature absorption in 10%Yb:YLF, probably due to the instruments settings. This result is encouraging but more work is needed to find the optimal parameters for this measurement. Notably, the use of a unique Glan-Thomson polarizer in the sample path in the experiment might explain

the absorption discrepancy: in the mechanical setup provided by the instrument's manufacturer, there is polarizer on each path and they are rotated together to ensure that the same power is transmitted in the reference and sample paths. We did not perform additional measurements with the Lambda 900, as the polarizers mechanism needed to be repaired.

Absorption spectroscopy with Bruker 70v FTIR

We later had the opportunity to try absorption measurements using the Institut Néel's FTIR spectrometer Bruker 70v. The FTIR has some advantages over the Lambda 900 spectrophotometer. First, its design allows to put the sample chamber under vacuum and even to adapt a Helium cryostat in order to perform low temperature measurements. Secondly, in principle, the spectral resolution and photometric resolution of a FTIR can be higher than that of spectro-photometer for the same source power. Indeed, in a FTIR, the spectral resolution is fixed by the maximal optical path difference achieved by the scanning mirror which can be as large as wanted whereas in a spectro-photometer it is limited by the minimal slit size. The absence of slit makes also a FTIR able to collect more light than a dispersive spectrometer (this is known as Jacquinot's or throughput advantage). The fact that each pixel in the FTIR's detector receives at the same time the full information about the whole spectra allows to improve the SNR comparatively with a dispersive spectrometer (this is known as Fellgett's or multiplex advantage).

The 10%Yb-0.01%Tm:YLF (coll. 190) crystal was placed in the sample path with c axis in the vertical direction, and a KRS polarized was manually oriented along the same direction. After vacuum pumping the sample chamber, the scan was performed between 660 nm and 1250 nm with 0.02 nm spectral resolution. The measurement was repeated for the horizontal polarization. Each scan took less than 10 minutes to be performed.

Post-treatment of the signal was performed by taking a background spectra for the polarizers alone (in vacuum also) without sample and dividing the signal by the background. Measurements were then corrected for the Fresnel reflection at normal incidence, accounting that the light source gets reflected two times through the sample before reaching the detector since it is placed on the arm of a Michelson interferometer. Under these conditions, the signal was divided by a factor $T_{Fresnel}$ equal to:

$$T_{Fresnel} = (1 - R_{Fresnel})^2 \tag{4.23}$$

With $R_{Fresnel}$ the Fresnel reflection associated to a parallel face window, equal to:

$$R_{Fresnel} = 2R_i/(1 + R_i) \tag{4.24}$$

And R_i the single interface reflection coefficient for the polarization i:

$$R_i = \left(\frac{1 - n_i}{1 + n_i}\right)^2 \tag{4.25}$$

Accounting for YLF ordinary refractive index n_o in E$\|$c polarization and extraordinary refractive index n_e in E$\perp$c polarization as a function of wavelength, calculated with Sellmeier equations 4.16 and 4.17. Figure 4.66 shows the transmission spectra obtained after post-treatment.

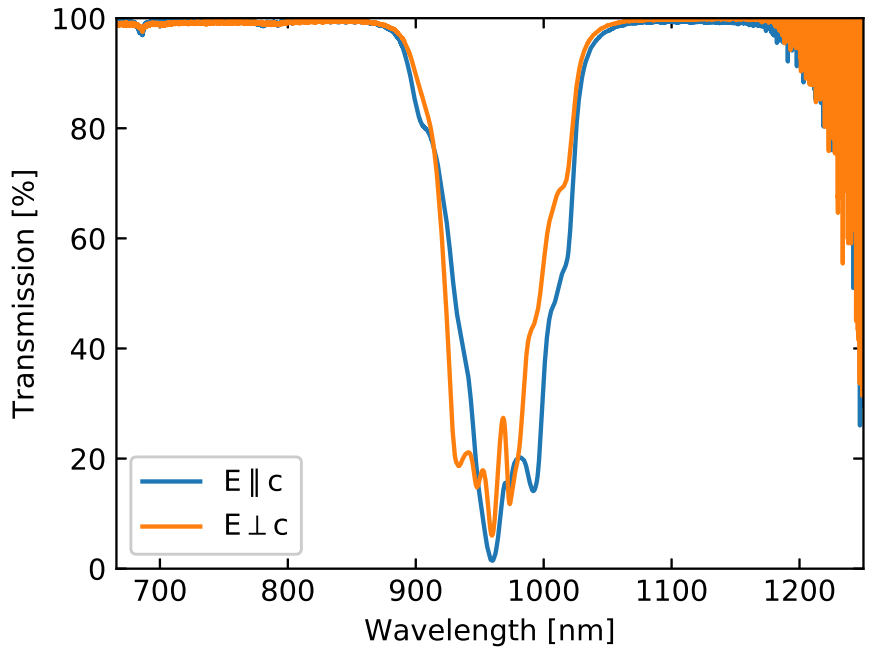

Figure 4.66: *Measured transmission for 10%Yb-0.01%Tm:YLF (coll. 190) with the Bruker 70v FTIR.*

Absorption coefficients were calculated using Equation 2.54, as shown in Figure 4.67.

This time, at the difference with the absorption spectra taken with the Lambda 900 spectro-photometer, our measurement are nearly identical to the reference data from the University of Pisa shown in Figure 2.22. There is only a slight difference on the order of a few cm^{-1} in the amplitude of the peaks. These differences can be either attributed to a temperature difference between the two measurements, small deviation from perfect alignment when rotating the KRS polarizer, or additional needed correction and setting-up in the FTIR parameters.

It is worth noticing that the FTIR does indeed provide excellent sensitivity, as we are clearly able to resolve the $^3F_3$ and $^3H_4$ absorption bands from Thulium co-doping around 685 nm and 785 nm respectively, even when they are only emerging from the noise floor with 0.1 cm^{-1} and 0.04 cm^{-1} absorption, as shown in Figure 4.68.

For comparison, absorption of Tm:YLF is shown in Figure 4.69, as measured by reference

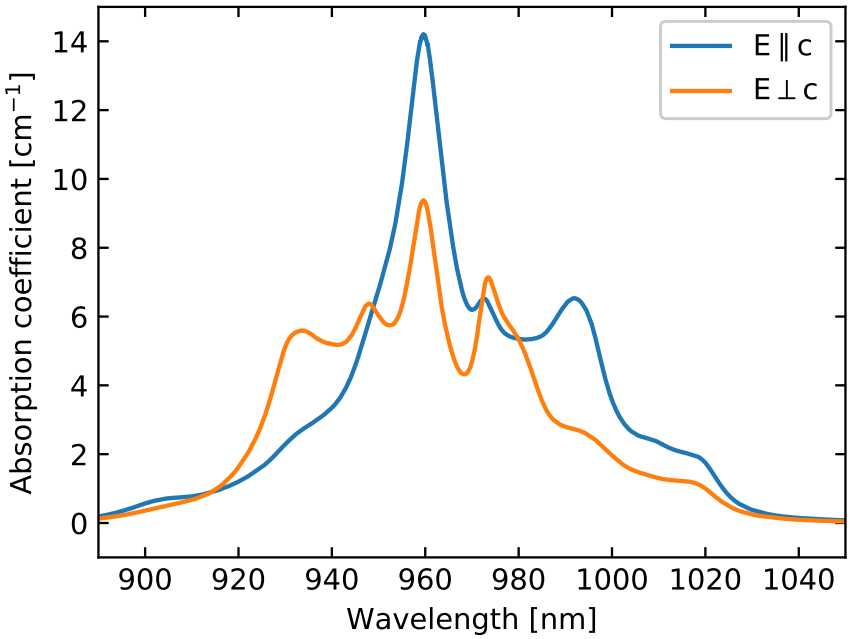

Figure 4.67: *Measured absorption coefficient for 10%Yb-0.01%Tm:YLF (coll. 190) with the Bruker 70v FTIR.*

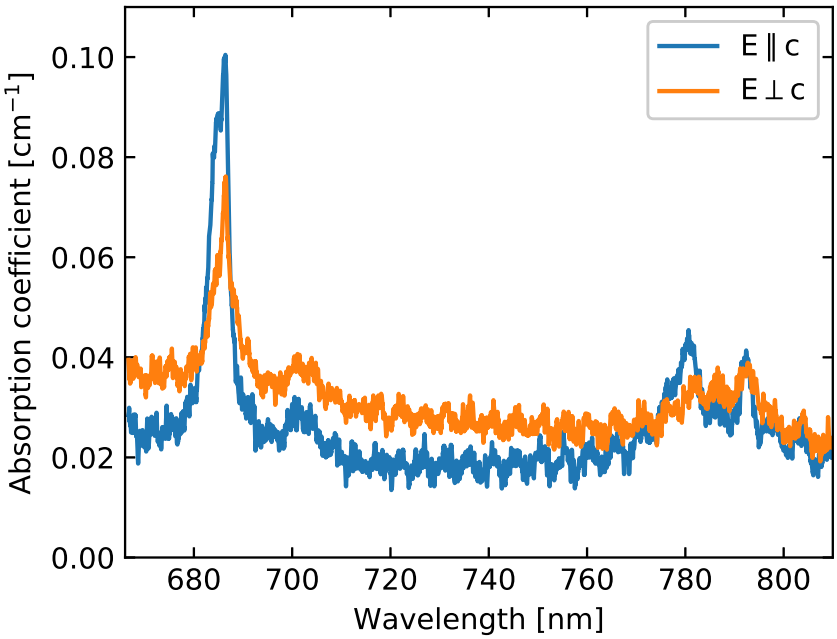

Figure 4.68: *Measured absorption coefficient for 10%Yb-0.01%Tm:YLF (coll. 190) with the Bruker 70v FTIR, zoom in the low signal features around 685 nm and 785 nm, attributable to Thulium co-doping. Data were smoothed with an 11 points window moving average in order to make the bands more visible.*

[18]. No doubt subsists regarding the nature of those peaks.

With such a sensitivity, it is reasonable to think ahead on performing measurements at cryogenics temperatures which would give the exact form of Yb:YLF absorption while maintaining good precision around 1020 nm, freeing ourselves from the problem of re-absorption when using the reciprocity method presented in chapter 2.

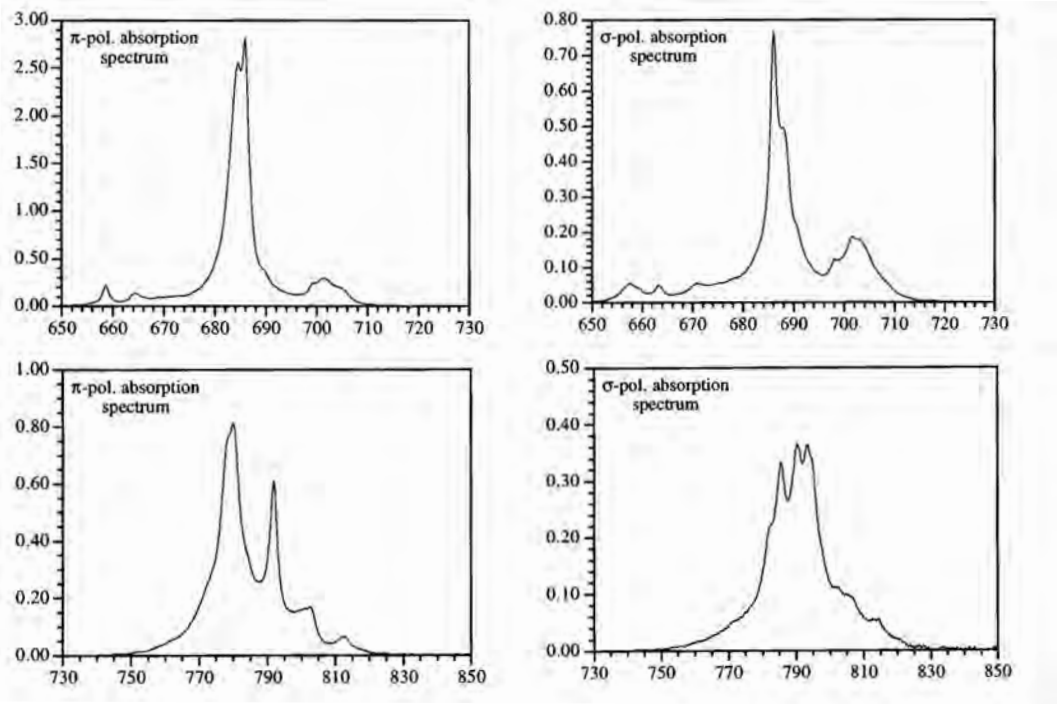

Figure 4.69: *Thulium doped YLF absorption bands in both polarizations, adapted from reference [18]. Top: $3F_3$ absorption band. Bottom: $3H_4$ absorption band.*

To conclude, FTIR spectroscopy might provide an additional value to the absorption spectroscopy measurements by being able to make a very sensitive scan over a large spectral range which includes the whole set of dopants and impurities absorption bands in a single measurement. These informations could prove useful in the perspective of more complex cooling efficiency models taking into account energy transfers between the different species. Further investigations are needed to find the limits of this method in terms of photometric precision and minimal achievable sensitivity.

4.3.5 Fluorescence spectroscopy

After checking the absorption spectra, we decided also to perform fluorescence spectroscopy of 10%Yb:YLF. As stated in chapter 2, the knowledge of emission properties as a function of temperature allows to retrieve the absorption spectra using the reciprocity method, even when the crystal's absorption loses one order of magnitude between ambient and cryogenics temperatures.

The second crystal, 10%Yb:YLF collection 148 was mounted on a Helium temperature controlled cryostat, as shown in Figure 4.70. A custom cold finger design allowed to secure the crystal and send a laser beam with a 45° silver coated mirr or. A Titanium:Sapphire laser (model Spectra-Physics Millennia) provided a tunable pump laser beam with 200 mW maximal power between 920 nm to 1030 nm. The cryostat was mounted on a translation

stage, allowing to control the beam's position on the mirror and inside the crystal.

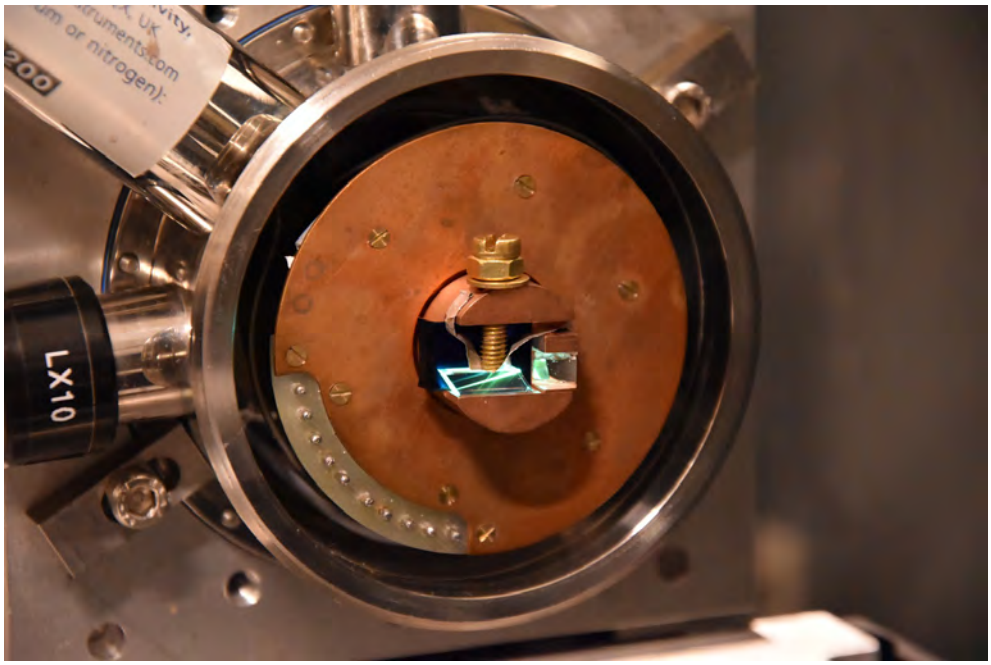

Figure 4.70: *Photographs of the crystal mounted in the He cryostat for temperature dependent fluorescence spectroscopy. We can see the 45° silver mirror and the indium foil used to ensure a good thermal contact between the securing screw and the crystal.*

The Ti:Sapphire laser was tuned at 950 nm such that the absorption was high from room temperature to cryogenics temperature, and that it did not overlap with any feature of the fluorescence spectra. On the detection side, a 2f-2f relay allowed to form the image of crystal in a plane located at a distance of approximately 50 cm from the crystal. We placed a rotating polarizer and a Vis-NIR camera in the image plane on a translation mount, which allowed to make a focus on the crystal surface and center the crystal image (Figure 4.71). When the image of the crystal was at the center of the system, the camera was unmounted and replaced with a multi-mode optical fiber which allowed to collect and send the polarized fluorescence signal to a fibered spectrometer (model Ocean Optics HR4000).

The beam position inside the crystal was adjusted such that it is very close (less than 500 μm) inside of the front crystal surface in order to minimize as much as possible the fluorescence re-absorption. A liquid Helium dewar was connected to the cryostat, the cryostat was vacuum pumped, and the crystal fluorescence was recorded as a function of temperature between 325 K and 75 K every 25 K. For each spectra, the PID temperature controller allowed a stability inferior to +/- 100 mK.

Figure 4.72 and Figure 4.73 shows the fluorescence intensity measured as a function of temperature in E parallel to c and E perpendicular to c polarizations. We found excellent agreement with the reference fluorescence data from the University of Pisa. Only some peaks are smaller than expected near the wavelengths where Yb:YLF is the highest.

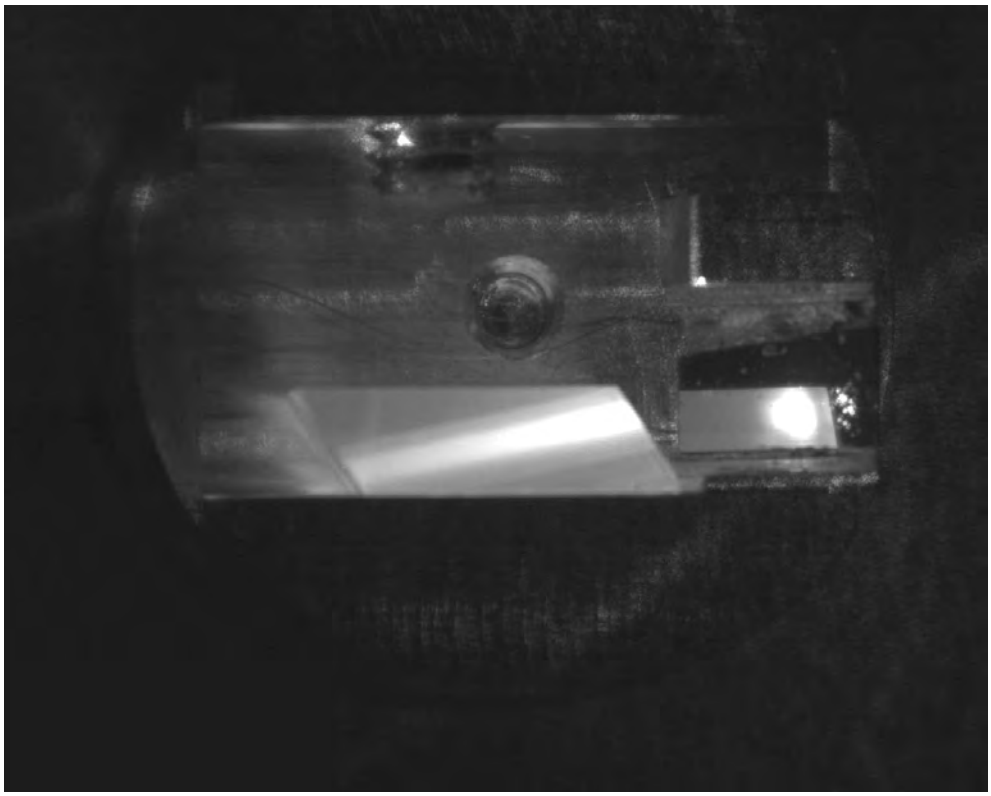

Figure 4.71: *Photograph of the crystal's image after the 2f-2f relay, as seen by the Vis-NIR camera.*

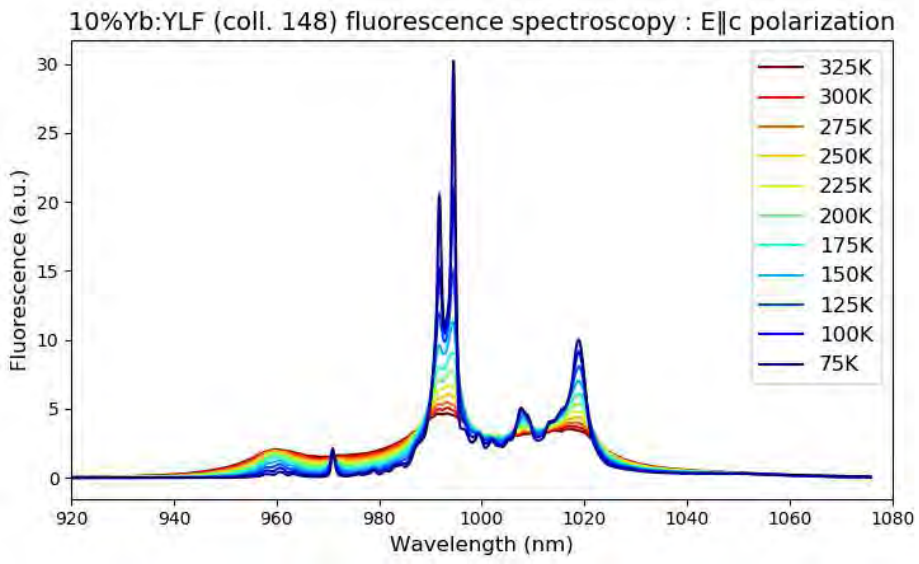

Figure 4.72: *Measured E||c fluorescence as a function of temperature.*

The ultimate fluorescence spectra quality test is to perform the reciprocity method in order to calculate the absorption spectra from fluorescence. Figure 4.74 shows the calculated absorption from the measured fluorescence intensity using reciprocity. We can see that there is an overall excellent agreement, except for the strong absorption line at 960 nm, which appears to decrease instead of increasing. It means that even with the Ti:Saph laser beam on the crystal's edge, we still have an observable amount of re-absorption. Indeed,

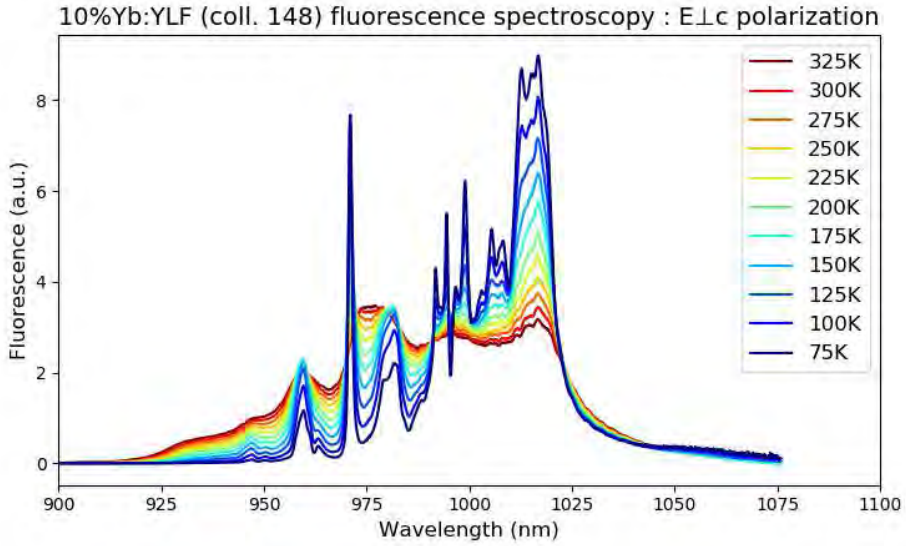

Figure 4.73: *Measured E⊥c fluorescence as a function of temperature.*

for values as large as 90 cm^1, the mean free-path of a photon defined as the inverse of the absorption coefficient is approximately equal to $1/(90cm^{-1})\ 0.01cm = 100\mu m$. In order to see the true form of absorption by using the reciprocity method, we would have to reduce the pump laser size such that the re-absorption depth is kept below that value, which was not the case.

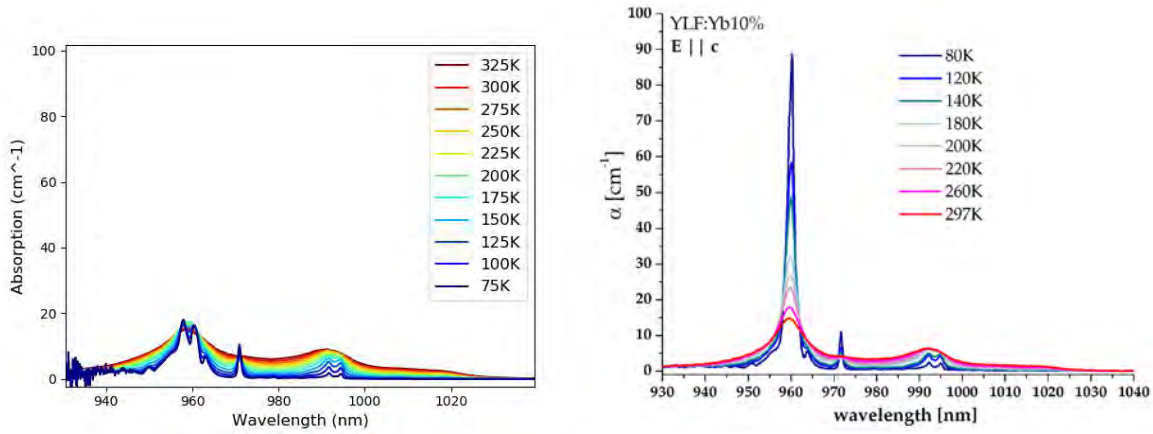

Figure 4.74: *Comparison between 10%Yb:YLF absorption obtained with reciprocity (left) and reference absorption from the University of Pisa obtained by direct measurement (right). The peak at 960 nm is completely flattened at low temperatures due to fluorescence re-absorption with the reciprocity method.*

4.3.6 Cooling efficiency measurements

Upon receiving the second cooling crystal, 10%Yb:YLF coll 148, we tried single pass cooling in air and in vacuum. The observation with the thermal camera did not show any temperature change, which was extremely puzzling at first. After checking the IPG laser

wavelength, and making sure that the thermal camera really indicated meaningful measurements, the only reason left which could explain that the crystal did not cool was that its cooling efficiency was close to zero, either due to a too high background absorption or a too low external quantum efficiency.

I went to Pisa in january 2020 in order to check the cooling efficiency of that particular crystal. The method for checking the cooling efficiency employed begins by noticing that for small temperature changes, if conductive losses are small, the temperature variation of a sample is proportional to the absorbed power and the cooling efficiency:

$$\Delta T = \frac{\eta_c P_{abs}}{\kappa} \tag{4.26}$$

With κ a factor accounting for radiative losses:

$$\kappa = \frac{4\epsilon_{YLF}\sigma A_{YLF} T_{env}^3}{1+\chi} \tag{4.27}$$

And χ a factor accounting for the view factor between the cold crystal and the hot environment:

$$\chi = (1-\epsilon_{env})\frac{\epsilon_{YLF} A_{YLF}}{\epsilon_{env} A_{env}} \tag{4.28}$$

Hence, the measurement of the crystal's temperature variation upon being pumped with a known absorbed power allows to know the cooling efficiency at the pump wavelength using the formula:

$$\eta_c = \kappa \frac{\Delta T}{P_{abs}} \tag{4.29}$$

In order to keep conductive losses at a minimum, the cooling crystal was put on two optical fiber inside a vacuum enclosure (Figure 4.75). The crystal was then excited using a laser diode at 935 nm, a tunable VECSEL at 1020 nm, 1021 nm and 1024 nm, and a Nd:YAG at 1064 nm. The crystal's temperature as a function of time was recorded with a thermal camera (model Raytheon 2500 AS). Figure 4.76 shows an example of a run for the pump laser tuned at 1020 nm.

Knowing the absorption coefficients of 10%Yb:YLF at the pumping wavelengths, the absorbed power can be calculated, and the cooling efficiency for the pumping wavelengths derived. Figure 4.77 shows the measured cooling efficiency in the collection 148 crystal, compared to the theoretical cooling efficiency of the best 10%Yb:YL1F crystal reported by reference [4] from UNM. We can see that where an efficiency on the order of 1% at 1020 nm at room temperature would be expected, the crystal efficiency from collection 148 is close to zero. Upon re-polishing the sample, it improved the cooling efficiency only marginally.

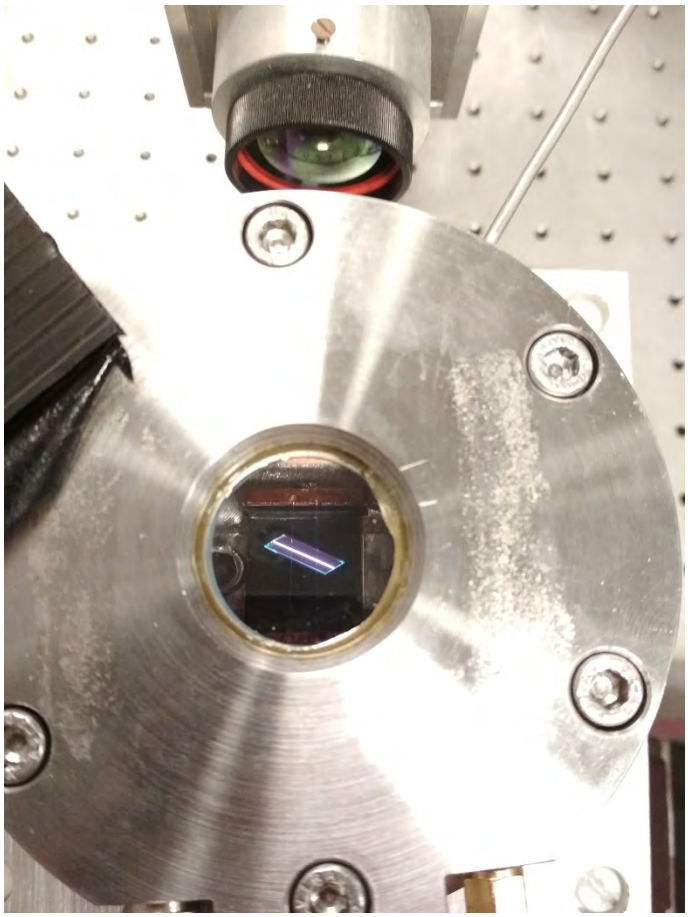

Figure 4.75: *Setup used at the University of Pisa for the measurement of cooling efficiency at room temperature. The crystal is put at the center of a vacuum enclosure on top of two optical fibers, and a thermal camera monitors its temperature when pumped with lasers at different wavelengths.*

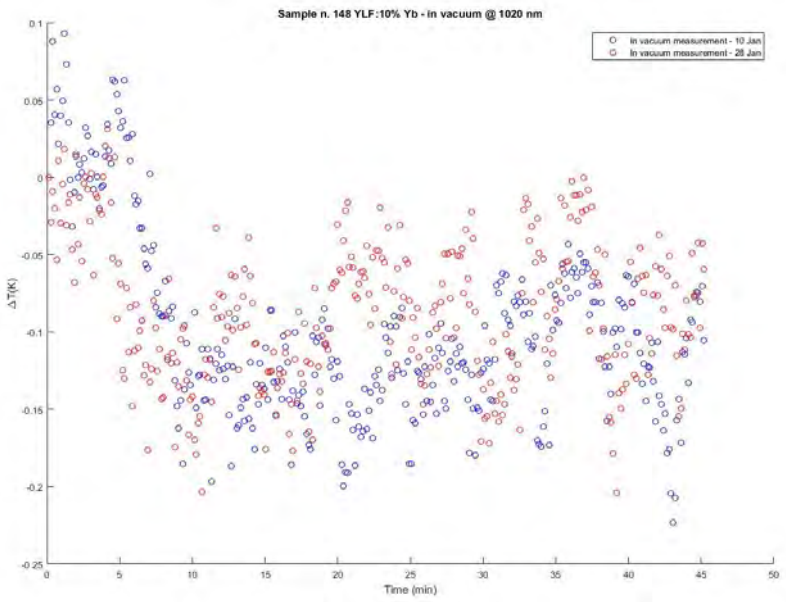

Figure 4.76: *Temperature of 10%Yb:YLF as a function of time, pumped at 1020 nm in vacuum.*

The proposed explanation is that the sample contains too many impurities.

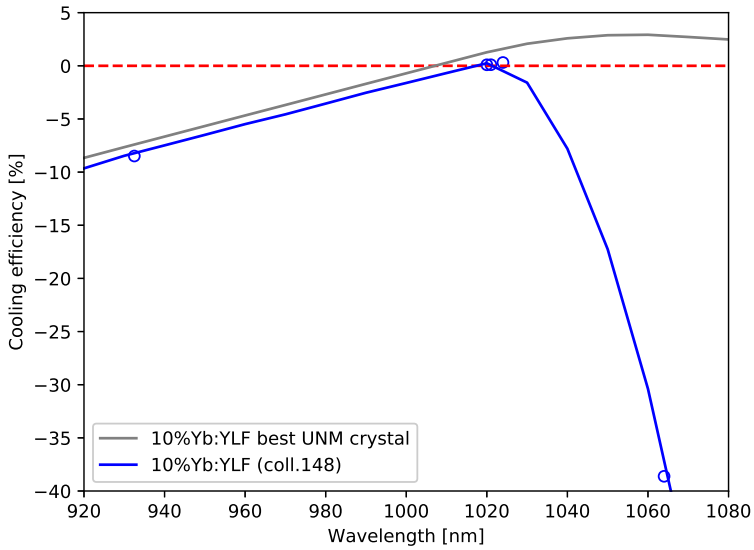

Figure 4.77: *Measured cooling efficiency for the 10% Yb:YLF crystal.*

The University of Pisa gracefully lent us another crystal, a 7.5% Yb:YLF crystal with high cooling efficiency which was actually documented in reference [19]. Back then, the measured parameters for this crystal were $\eta_{ext} = 0.985$ and $a_b = 2.65e - 4$. Newer room temperature efficiency measurements were performed as shown in Figure 4.78. The cooling efficiency fits well with slightly different parameters $\eta_{ext} = 0.986$ and $a_b = 2.8e - 4$.

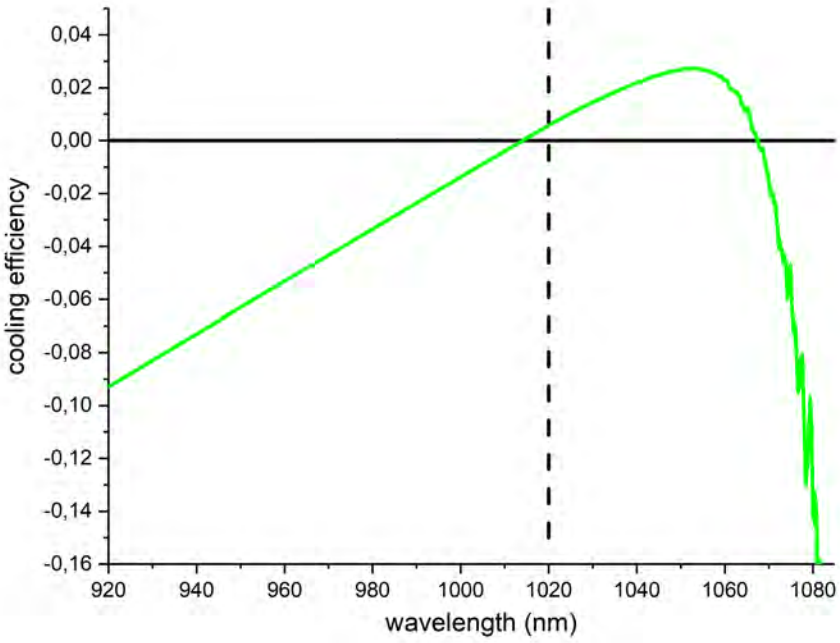

Figure 4.78: *Measured cooling efficiency for the 7.5% Yb:YLF crystal.*

From the external quantum efficiency and the background absorption, we are able to estimate the cooling efficiency as a function of temperature and wavelength, as shown in

Figure 4.79. A global minimal achievable temperature of 103 K at 1022 nm is predicted for this new crystal. At 1020 nm, the expected minimal achievable temperature is around 125 K, allowing us to perform our experiment and aim for cryogenics temperatures.

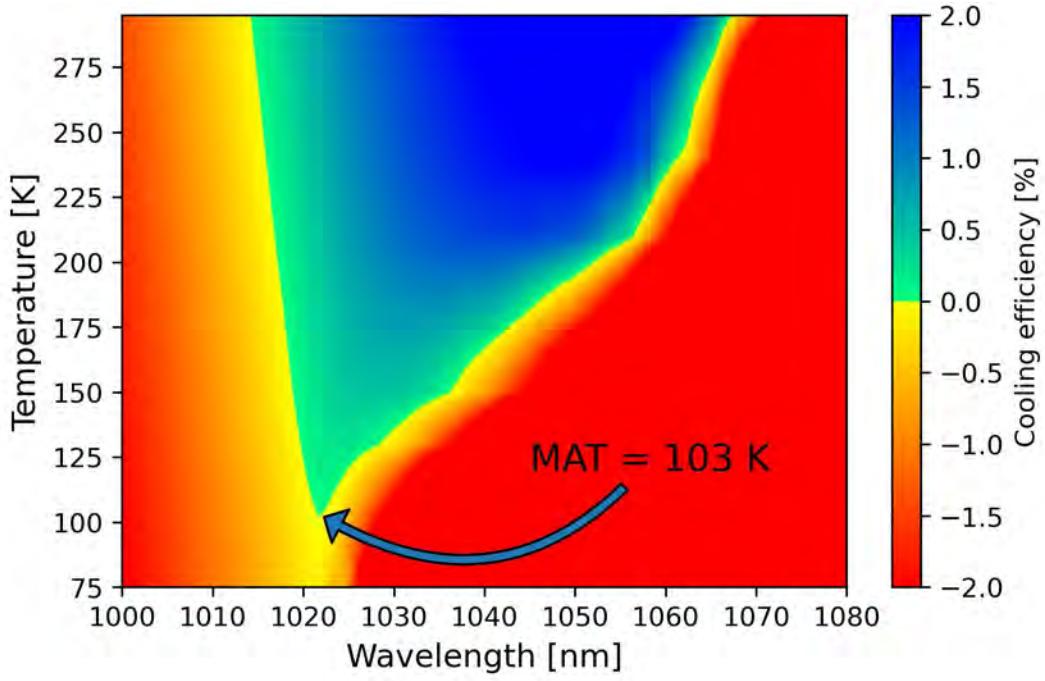

Figure 4.79: *Theoretical cooling efficiency as a function of temperature and wavelength for the 7.5% Yb:YLF crystal, calculated from it cooling efficiency at ambient temperature and the absorption and background absorption of Yb:YLF as a function of temperature and wavelength.*

References

[1] Ghasemkhani, Albrecht, Melgaard, Seletskiy, Cederberg, and Sheik-Bahae, "Intracavity cryogenic optical refrigeration using high power vertical external-cavity surface emitting lasers (VECSELs)," *Optics Express*, 2014.
DOI: 10.1364/OE.22.016232 (cit. on p. 130).

[2] Yang, Meng, Albrecht, and Sheik-Bahae, "Radiation-balanced yb:yag disk laser," *Optics Express*, 2019.
DOI: 10.1364/OE.27.001392 (cit. on p. 131).

[3] J. Meng, "Realization of an all-solid-state cryocooler using optical refrigeration," *Proc. of SPIE*, 2018.
DOI: 10.1117/12.2305195 (cit. on p. 132).

[4] S. D. Melgaard, *Cryogenic optical refrigeration: Laser cooling of solids below 123 K*. 2013. [Online]. Available: https://digitalrepository.unm.edu/ose_etds/24/ (cit. on pp. 132, 137, 138, 192).

[5] Los Alamos National Lab, “Lasers are cool—and cooling,” 2019. [Online]. Available: https://www.lanl.gov/discover/publications/1663/2019-july/lasers-are-cool.php (cit. on p. 132).

[6] J. Wallace, “Optical Cooling: All-optical cryogenic cooling of sensors eliminates vibration,” *LaserFocusWorld*, 2018. [Online]. Available: https://digital.laserfocusworld.com/laserfocusworld/201807 (cit. on p. 132).

[7] C. W. Hoyt, “Laser cooling in thulium-doped solids,” 2003 (cit. on p. 133).

[8] B. G. Farfan, A. Gragossian, G. Symonds, M. R. Ghasemkhani, A. R. Albrecht, M. Sheik-Bahae, and R. I. Epstein, “Cooling Enhancement in Optical Refrigeration by Non-resonant Optical Cavities,” *Proc. of SPIE*, 2016.
DOI: 10.1117/12.2222181 (cit. on p. 133).

[9] L. A. Hof and J. Abou-Ziki, “Micro-hole drilling on glass substrates - a review,” *Micromachines*, 2017.
DOI: 10.3390/mi8020053 (cit. on p. 143).

[10] H. Huang, L.-M. Yang, and J. Liu, “Micro-hole drilling and cutting using femtosecond fiber laser,” *Optical Engineering*, 2014.
DOI: 10.1117/1.OE.53.5.051513 (cit. on p. 143).

[11] D. R. Herriott and H. J. Schulte, “Folded Optical Delay Lines,” *Applied Optics*, 1965.
DOI: 10.1364/AO.4.000883 (cit. on p. 143).

[12] A. Gragossian, J. Meng, M. Ghasemkhani, A. R. Albrecht, and M. Sheik-Bahae, “Astigmatic herriott cell for optical refrigeration,” *Optical Engineering*, 2017.
DOI: 10.1117/1.OE.56.1.011110 (cit. on p. 143).

[13] J. B. McManus, P. L. Kebabian, and M. S. Zahniser, “Astigmatic mirror multipass absorption cells for long-path-length spectroscopy,” *Applied Optics*, 1995.
DOI: 10.1364/AO.34.003336 (cit. on p. 143).

[14] M. P. Hehlen, J. Meng, A. R. Albrecht, E. R. Lee, A. Gragossian, S. P. Love, C. E. Hamilton, R. I. Epstein, and M. Sheik-Bahae, “First demonstration of an all-solid-state optical cryocooler,” *Light: Science & Applications*, 2018.
DOI: 10.1038/s41377-018-0028-7 (cit. on p. 148).

[15] N. P. Barnes and D. J. Gettemy, “Temperature variation of the refractive indices of yttrium lithium fluoride,” *Journal of the Optical Society of America*, 1980.
DOI: 10.1364/JOSA.70.001244 (cit. on p. 151).

[16] Almeco, “TiNOX Solar Absorber,” [Online]. Available: https://www.almecogroup.com/en/pages/479-absorbers (cit. on p. 164).

[17] Acktar, “Nano-Black,” [Online]. Available: https://www.acktar.com/product/nano-black/ (cit. on p. 164).

[18] B. M. Walsh, N. P. Barnes, and B. Di Bartolo, “Branching ratios, cross sections, and radiative lifetimes of rare earth ions in solids: Application to Tm3+ and Ho3+ ions in LiYF4,” *Journal of Applied Physics*, 1998.
DOI: 10.1063/1.367037 (cit. on pp. 187, 188).

[19] A. Volpi, “Cooling effects on fluoride crystals,” Ph.D. dissertation, Università di Pisa, Pisa, Italy, 2015 (cit. on p. 194).

Chapter 5

Demonstrating Europe's first Laser Cryocooler prototype

This chapter is dedicated to the operation and cryogenics temperatures demonstration in our Laser Cryocooler prototype. After detailing the thermometers used in the experiments and their calibration, I present the results of our cooling runs obtained during the last year of my thesis. At the end of the chapter, the cooling power and heat losses are estimated using a thermal model. I show that we successfully attained cryogenic temperatures between 120 K and 130 K, thus reaching our goals and advancing the maturity of this technology to TRL 3 in Europe.

Ce chapitre est dédié au fonctionnement et à la démonstration de températures cryogéniques dans notre prototype de Cryo-refroidisseur Laser. Après avoir explicité les thermomètres utilisés dans l'expérience et leur calibration, je présente les résultats de nos descentes à froid obtenues durant ma dernière année de thèse. A la fin du chapitre, la puissance de refroidissement et les pertes sont estimées à l'aide d'un modèle thermique. Je montre que nous avons atteint avec succès des températures cryogéniques entre 120 K et 130 K, atteignant ainsi notre but et avançant la maturité de cette technologie au niveau TRL 3 en Europe.

5.1 Thermometers in the experiment

5.1.1 Crystal temperature

Measuring the temperatures in a laser cooling experiment is more complicated than it seems. Due to the crystal emitting a strong fluorescence equal to absorbed energy (Figure 5.1), it is not suitable to attach directly a calibrated thermal resistor because it would heat up the system and indicate a different temperature.

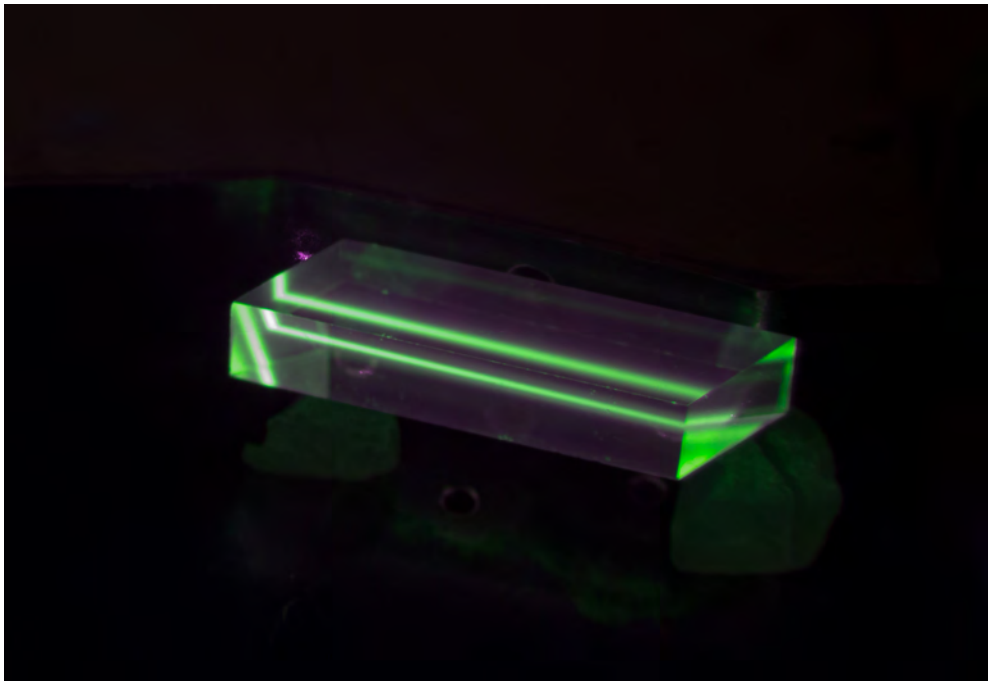

Figure 5.1: *7.5 % Yb:YLF crystal lent by the University of Pisa/MEGA Materials, pumped with 2 W of laser power at 1020 nm. The green fluorescence illuminating the laser path does not corresponds to the fluorescence of Ytterbium ions but only a tiny fraction of it, upconverted to higher energy due to Erbium residual impurities.*

The question is: how to measure the crystal's temperature without sticking a temperature sensor on the its surface ? In our setup, we implemented two non-contact complementary methods which allows to measure the sample's temperature, from ambient to cryogenics temperatures, as described in the next sections.

Thermal camera measurement

The first thermometer in the experiment is a thermal camera, model FLIR Lepton 3.5. The camera sensor is based on vanadium oxyde (VOx) micro-bolometers, a semiconductor material for which the resistivity depends on temperature. The pixels delivers a signal which is proportional to the incident thermal radiation in the range 7-15 microns, with a spectral re-

sponse function shown in Figure 5.2. The camera is factory calibrated in front of a reference black-body with a formula which internally converts the signal to temperature in radiometric mode. The manufacturer claims a radiometric accuracy of $\pm$ 5% in the calibrated range -10 ℃ to +80 ℃.

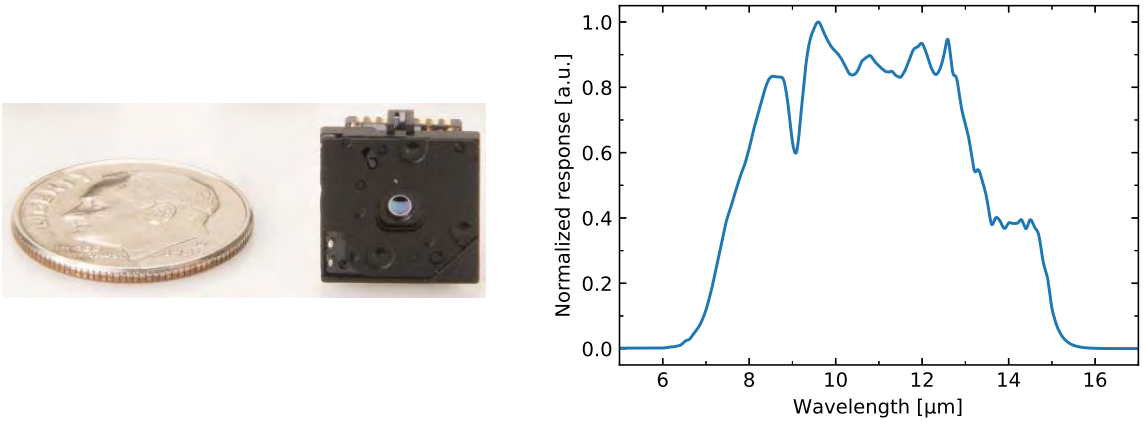

Figure 5.2: *Left: FLIR Lepton 3.5 camera package. Right: VOx micro-bolometers typical spectral response, adapted from FLIR's datasheet [1].*

In front of the detector chip, a small silicon fixed $f/1.1$ doublet with 15 cm hyperfocal distance allows to make images with approximate focus between 10 cm and infinity, with 57° horizontal field-of-view and 71°diagonal field-of-view.

The Lepton camera is provided by FLIR in a "bulk" package where there is no control electronics. The PureThermal Input/Output control board sold by GroupGets allows to interact with the camera through a micro-USB connector. FLIR has developed a C# Source Development Kit which possess a Python API to control the camera and its parameters.

Some features of the camera, primarily intended for casual use in general configurations were **disabled**:

- Spatial/Temporal Filtering, post-processing function used to smooth the image over several frames and pixels.
- Automatic Gain Control (AGC), used for lower quality 8-bits range colors display.
- Automatic Flat Field Correction (FFC), closing off the shutter every 30 seconds to re-calibrate the pixels.

To get the best thermal accuracy, some other features were **enabled**:

- High gain, for the highest radiometric accuracy with small signals occupying a larger range over the 14 bits.
- Radiometry, for a direct conversion between raw flux and temperature.

- T-Linear, for an additional correction meant to give the same scene temperature reading if the camera's temperature is changed.
- T-Linear resolution = 0.01 K.

The camera is located above the crystal, outside the vacuum enclosure. It observes the crystal through an aperture in the clamshell hat and through a ZnSe lens and a ZnSe window. In order to keep it at constant temperature during our measurements, the camera mount is connected to a industrial water flow at constant 15 ℃ temperature. Figure 5.3 shows the thermal camera mounted on the vacuum enclosure, along with a thermal image of the crystal at ambient temperature.

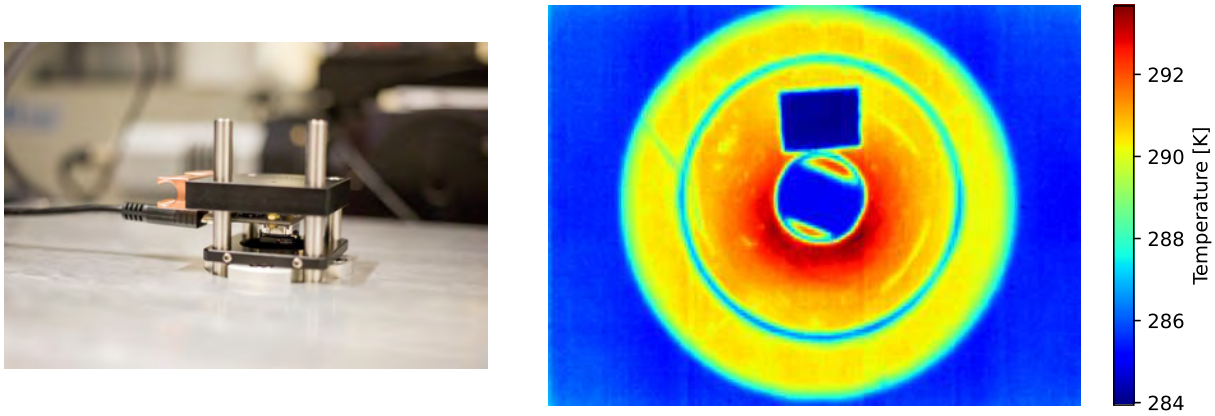

Figure 5.3: *Left: Photography of the thermal camera mounted above the crystal. Right: Thermal image of the crystal seen from above through the ZnSe lens and window. The crystal at the center appears slightly hotter (285 K) than the piece of Spectral Black (284 K) stuck on top of the clamshell hat. Copper, with lower emissivity, appears several degrees hotter (290 K) although the whole scene is actually at the same temperature.*

The thermal camera, in its vanilla measurements possess great temperature precision ($\pm$ 50 mK) and fair accuracy ($\pm$ 5 K) in the specified range from -10 ℃ to +80 ℃. However, it is not accurate enough for our purposes (an acceptable value is at least $\pm$ 1 K accuracy), it is not calibrated in our range of interest (approx. -170 to -70 ℃) and it does not take into account the thermal emissivity of objects. This last point means that a piece of YLF which possess an emissivity $\epsilon = 0.77$ will be interpreted by the camera as a black-body with $\epsilon = 1$ and converted to a false apparent temperature which is colder than the real YLF temperature.

For all these reasons, it is necessary to perform a calibration of the thermal camera, which allows to convert the apparent YLF temperature to its real temperature.

External thermal camera calibration: The calibration method involves monitoring the temperature of thermally controlled reference piece of YLF, marking the apparent values seen by the camera as a function of the true temperatures.

For that purpose, a small YLF slab (approximately 1mm thick, 3x3 mm wide) was attached to the cold finger in our Helium temperature controlled cryostat, along with a piece of Acktar Spectral Black acting as a black body. The image is of the scene is recorded through the same ZnSe window and ZnSe lens that are used in the cooling bench, as shown in Figure 5.4.

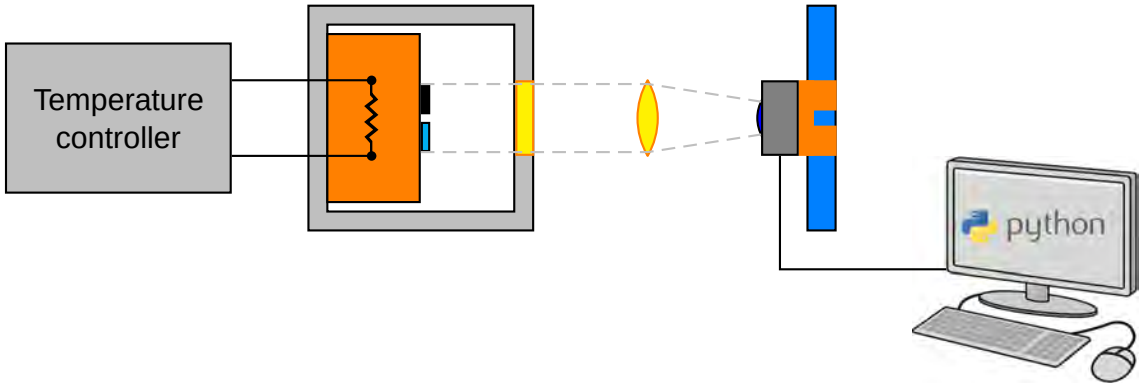

Figure 5.4: *Schematic of the external thermal camera calibration. A slab of YLF and Spectral Black are placed in a LHe temperature controlled cryostat. A water flow is connected to the camera's mount in order to keep its temperature constant around 15 degrees C through the calibration.*

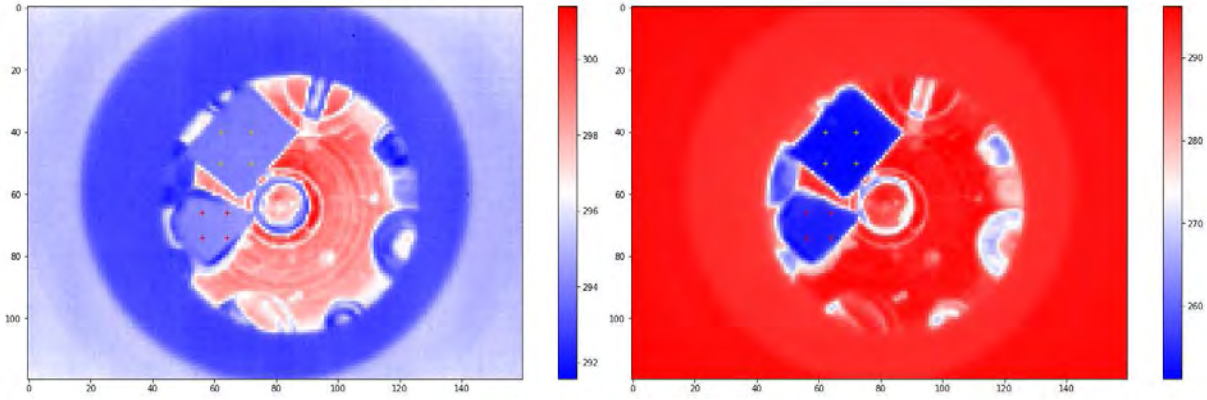

Figure 5.5: *Thermal camera images during calibration. The rectangle patch corresponds to the piece of Spectral Black while the piece of YLF is located below in the image. Left: Scene around ambient temperature; Right: Scene at lower temperature around 250 K.*

The thermal camera calibration was performed as follows. The cryostat temperature was varied from 300 K to 160 K in 10 degrees intervals, with the addition of a measure at 140 K and at 120 K. Each time, we waited for the cryostat temperature to stabilize within $\pm$ 0.1 K from the goal temperature. When the temperature was stable, a FFC was performed on the camera prior to a measurement, and we waited at least 10 seconds before taking a thermal image of the scene. For each cryostat temperature, the process was repeated in order to get 3 measurements each time. The temperature of the YLF and Spectral Black were extracted from the image by averaging the pixels temperatures in the corresponding regions-of-interests (at least over a centered region of 5x5 pixels).

The calibration process was performed two times: in high gain and low gain configurations to check if there was a large difference in the measurements accuracy. Figure 5.6 shows the measurements results. Both modes show almost the same temperature readings within $\pm$ 1 K. Errors bars were attributed based on the standard deviation for the three consecutive measurements of each data point. Standard deviation is on the order of 0.1 K for each point.

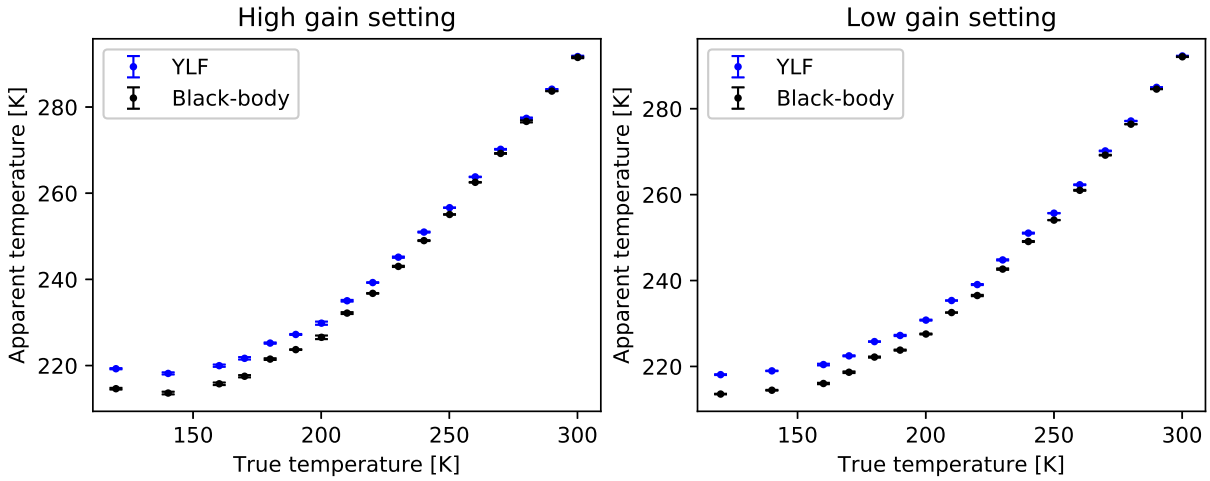

Figure 5.6: *Apparent temperature as a function of the real temperature for a slab of YLF and a piece of Acktar Spectral Black. Left: High gain mode. Left: Low gain mode.*

We can see that the camera has a limit value for objects temperatures at around 160 K, below which it stops indicating the temperature of an object. The reason is simple. The camera measures thermal radiation coming from the scene, through optical elements with non-unit absorptivity, some transmissivity and some reflectivity if the materials are transparent. At each wavelengths, energy conservation ensures the relationship between those quantities:

$$\alpha(\lambda) + \tau(\lambda) + \rho(\lambda) = 1 \tag{5.1}$$

With α the absorptivity, τ the transmissivity and ρ the reflectivity of the considered object. At thermal equilibrium, an object re-emits as much thermal radiation as it absorbs and we have:

$$\alpha(\lambda) = \epsilon(\lambda) \tag{5.2}$$

The thermal radiation received by the camera, as first approximation is the sum of thermal radiation from the actual objects plus thermal of the background temperature from all transparent objects in between. Particularly, when the camera observes at normal incidence, it sees its own thermal image (narcissus). We have:

$$\phi_{tot} = \tau\phi_{scene} + \phi_{back} = \tau\epsilon(T^4_{scene} - T^4_{back}) + \rho T_{back} \tag{5.3}$$

When T_{scene} tends to cryogenics temperatures, the thermal emission of the scene becomes negligible in front of the background thermal emission, such that only the variation of the background is seen. Hence, measuring the temperature of objects at cryogenics temperatures would require first that observations are carried out in special conditions where the sources of background reflections are kept at a minima. Secondly, it would require a camera with an ADC stage adapted to the sampling of signals with smaller dynamics and high enough detectivity/SNR.

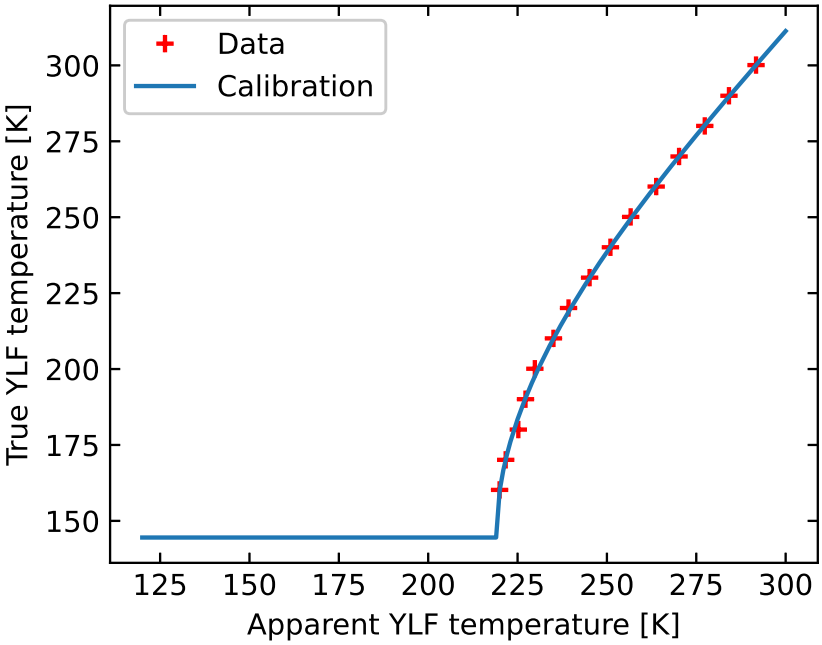

Figure 5.7: *Thermal camera calibration for the conversion between apparent and true YLF temperature.*

For the rest of the measurements, a third-order polynomial is fitted to the high gain data between 300 K and 160 K, as shown in Figure 5.7. Finding the root of the polynomial for a given apparent YLF temperature allows to convert to true YLF temperature. The calibration predicts a minimal temperature which can be seen by the camera at around 144 K. While the calibration can in theory be used at any apparent temperature to find a true temperature, we chose to use the calibration strictly in the range 300 K - 160 K where we still have confidence about the camera readings, and not below this range.

Differential Luminescence Thermometry

The second thermometer in the experiment is the cooling crystal itself. Indeed, just by looking at the spectral shape of the crystal's fluorescence when the laser in on, one is able to know its temperature. Several methods exists, such as measuring the mean fluorescence wavelength or the amplitude of a fluorescence peak or a set of peaks as a function of temperature.

The method known as Differential Luminescence Thermometry (abbreviated DLT) consists in measuring the fluorescence spectra deviation from a reference spectra at known temperature. The advantage compared to measuring directly the mean fluorescence spectra is that we subtract a base spectra which removes the spectrometer dark current and non-linear effects which can offset the spectrometer pixels values. We can define the differential spectrum as:

$$\Delta S(\lambda, T, T_0) = \frac{S(\lambda, T)}{\int S(\lambda, T)} - \frac{S(\lambda, T_0)}{\int S(\lambda, T_0)} \tag{5.4}$$

Where the fluorescence signals can be normalized by their integrals (the fluorescence power) or the amplitude of a peak in order to remove the fluorescence power fluctuations from the analysis. In general, $S(\lambda, T_0)$ is taken as the first fluorescence spectra observed at 300 K right after the laser is switched-on.

The DLT signal can be calculated as the :

$$S_{DLT}(T, T_0) = \int_{\lambda 1}^{\lambda 2} |\Delta S(\lambda, T, T_0)| d\lambda \tag{5.5}$$

Where the integral is performed in an arbitrary band where the fluorescence signal shows a variation. The absolute value is important in the expression, because the differential spectrum can have positive and negative parts in the same spectrum (some peaks decrease while some increase when temperature changes), such that its integral measures the highest variation of signal only when we take its absolute value. Depending on the signal-to-noise ratio of the DLT signal, its precision was found to attain in the order of a few hundreds of mK [2] to a few mK [3].

5.1.2 Clamshell temperature

Thermal camera measurement

The clamshell temperature is also monitored using the thermal camera with a patch of Spectral Black attached on top of the clamshell hat, which can be seen on Figure 5.3. The thermal camera calibration can be corrected in the same fashion as described for the cooling crystal to convert between apparent and true temperature. However, due to the high infrared emissivity of Spectral Black $\epsilon = 0.97$, the thermal camera already indicates the true clamshell temperature accurately within $\pm$ 1℃.

Resistance Temperature Detectors

The RTDs are electrical resistances whose resistance vary with temperature in a known way. PT100 RTDs are made of a calibrated platinum wire which has a resitance of 100 Ω at 0℃ and follows the linear temperature relationship:

$$R_{PT100} = 100 \times (1 + 0.00385) \tag{5.6}$$

The PT100 model used in the experiment is shown in Figure 5.8 along with the resistance of PT100 as a function of temperature.

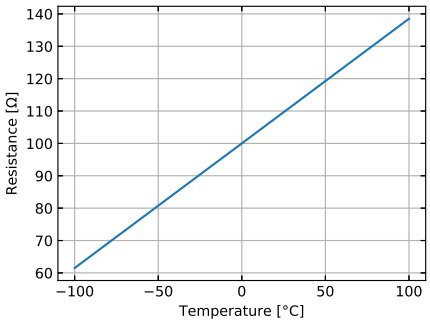

Figure 5.8: *Left: Thorlabs PT100 RTD used in the experiment. Left: PT100 resistance as a function of temperature.*

For a maximal precision, they are measured in 4-wires configuration. In 4-wires, we send a current with known value across the resistance through a first couple of wire, using a current source. We measure the voltage across the resistance through a second couple of wires using a voltmeter which has a very high resistance, as shown in Figure 5.10. This way, we are able to measure exactly the RTDs resistance, without measuring the associated wires resistances.

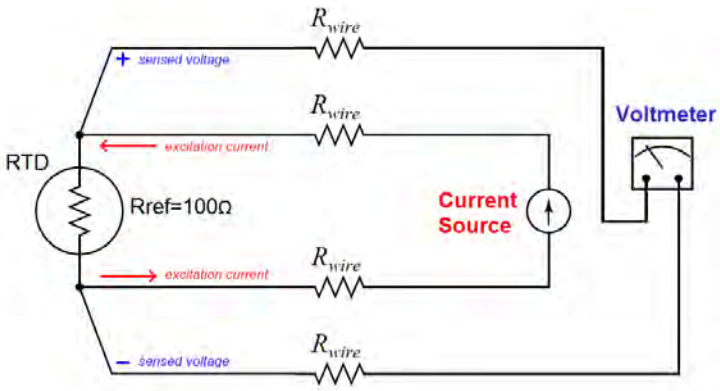

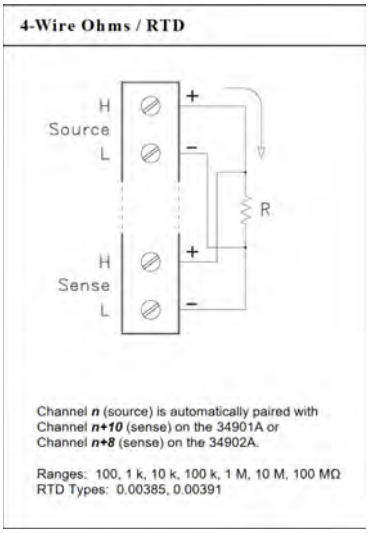

Figure 5.9: *4-wires RTD measurement principles. Left: Schematic of the 4-wires RTD measurement, from reference [4]. Right: Wiring diagram for 4-wires RTD measurements on Agilent 34970A, from reference [5].*

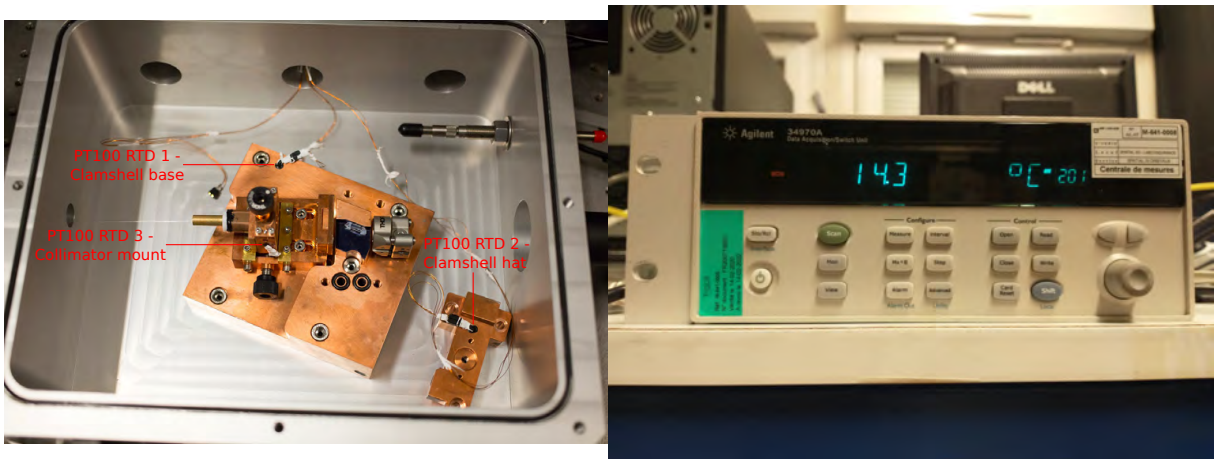

Figure 5.10: *Clamshell RTD temperature measurement in the experiment. Left: PT100 positions in the experiment. Right: temperature acquisition unit Agilent 34970A.*

The clamshell temperature was monitored as a function of time when turning on the water circulation in vacuum, as shown in Figure 5.11. In this measurement, the collimator was not clamped to the clamshell base which explains why the collimator mount took a longer time to reach thermalization.

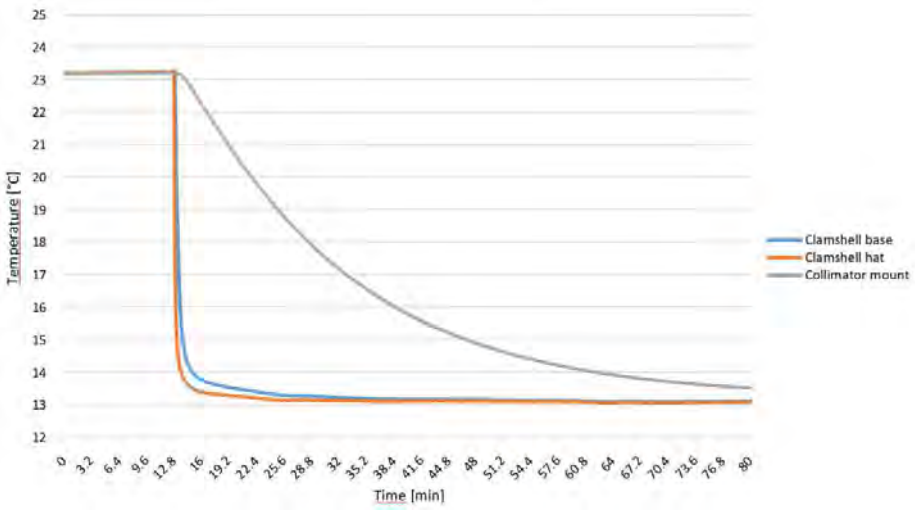

Figure 5.11: *PT100 RTDs temperatures as a function of time after opening the water flow.*

After waiting for the thermalization, the three RTDs showed good agreement with temperature values within 0.5 K with each-others. During the experiment, when turning-on the pump laser power, the collimator showed and increase of a couple of degrees with 10 W of laser power, while the clamshell base and hat did report an increase of less than one degree, proof of the water thermal regulation effectiveness.

5.2 Prototype overview and operation

Once all the design and fabrication was accomplished and the collimator aligned, we were able to use the coupling bench together with the cooling bench. The whole optical schematic of the experiment is shown in Figure 5.12.

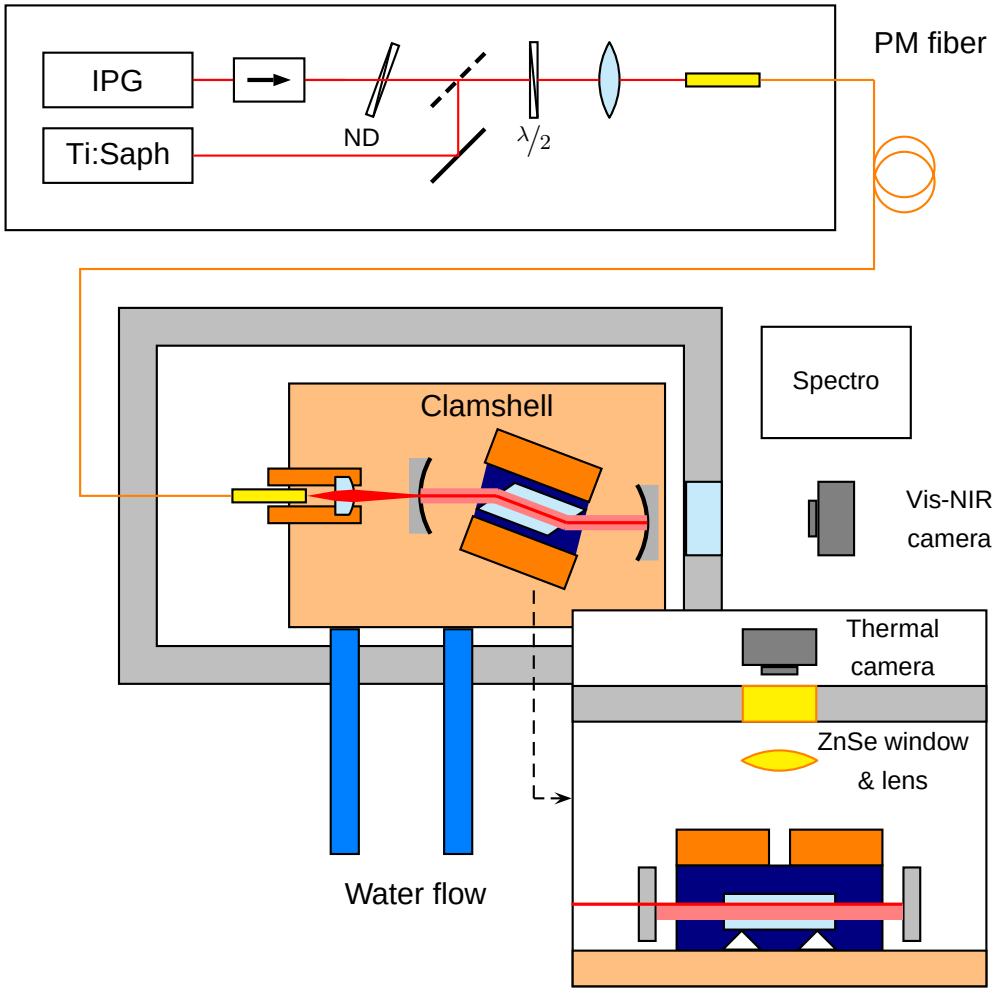

Figure 5.12: *Schematic of the optical setup in the cooling experiment.*

The cold head features the collimator on its mount, the crystal in between the two mirrors, the clamshell base and the clamshell hat with the wires connected to the RTDs, which can be seen in Figure 5.13.

An operation protocol was applied before turning on the laser and measuring the crystal's temperature to ensure the best coupling and cavity. The vacuum enclosure was opened, the clamshell hat removed and the fused silica dummy was put at the center of the cavity.

The coupling bench was then aligned such that we had a maximal transmission at the lowest power on the laser output (2.2 W) and maximal attenuation. The fiber alignment was

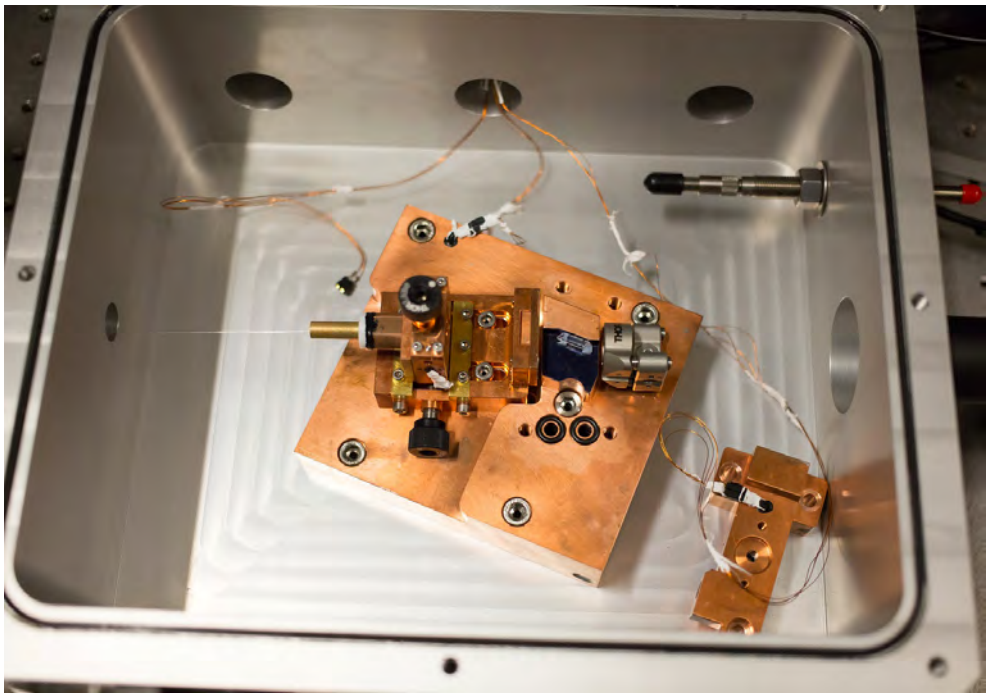

Figure 5.13: *Photography of the Laser Cryocooler prototype showing the cold head in the vacuum enclosure.*

tuned by measuring the power after of the collimator until reaching at least 90% transmission.

The position of the collimator was adjusted in order to hit at the center of the first mirror by looking at the hole image seen through the dummy and second mirror, until the laser beam appears. The second mirror was tilted until the Lissajous figure matched the dummy's section. The laser was shut off and the dummy replaced by the real cooling crystal, as shown in Figure 5.14 Alignment of the crystal was ensured by making sure that the refracted laser path inside the crystal was parallel to the crystal's faces, as shown in Figure 5.15.

Optimization of the round-trips number was hardly achievable by looking at the back camera image with the real crystal. Indeed, due to the high absorption of Ytterbium at room temperature, almost the full laser power is already absorbed after the third laser pass. However, a small tuning could be achieved by coupling the cavity at low power and measuring the far-field fluorescence intensity with a power meter placed 5 cm above the crystal. The tilt on the second mirror was then adjusted until reaching a maximum fluorescence signal. Tuning was on the order of a couple mW over a dozen of mW.

After aligning the cavity, the clamshell hat was put on, the vacuum enclosure was closed and set to pumping. Figure 5.16 shows the experiment with the vacuum enclosure closed, with the thermal camera on top and the Vis/NIR camera on the left. We waited 12 to 24 hours such that the pressure was under 10^{-4} mbar. 3 to 4 hours before starting the experiment, the water flow was open in order to cool down the clamshell and thermal camera. The experiment was then ready to start.

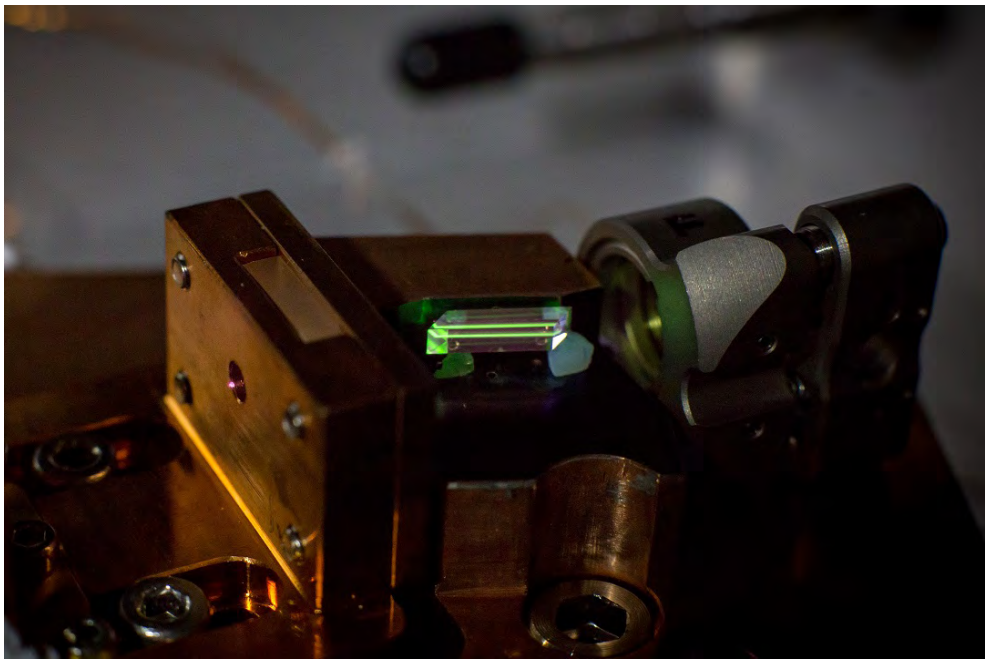

Figure 5.14: *Photography of the cooling crystal at the center of the astigmatic multi-pass cavity.*

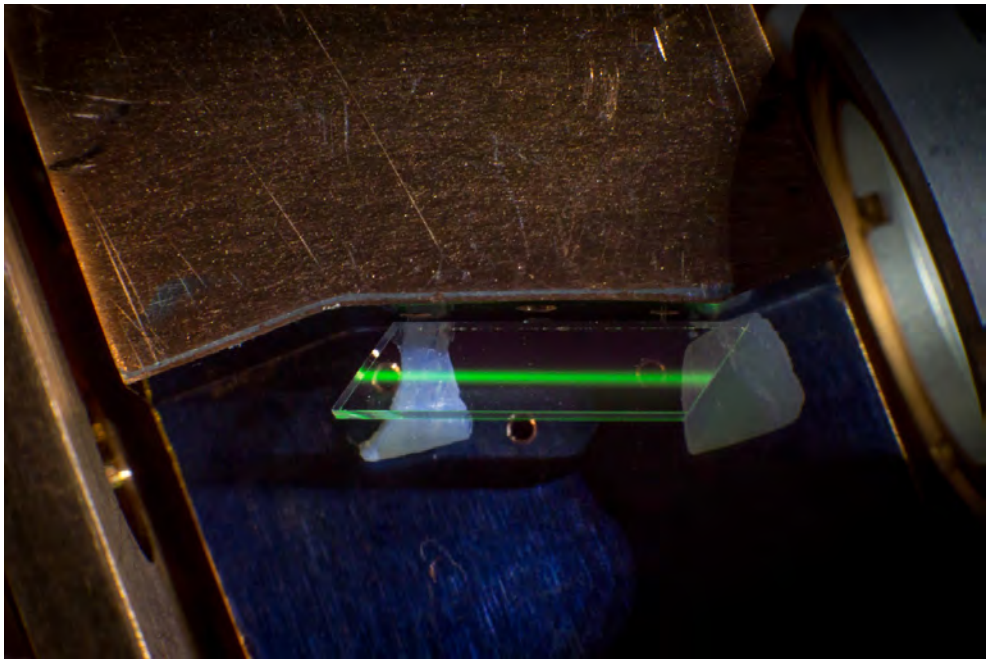

Figure 5.15: *Close-up photograph of the cooling crystal at the center of the multi-pass cavity laying on the silica aerogel pads. The laser beam enters the crystal at Brewster angle and is refracted in the direction parallel to the crystal's faces.*

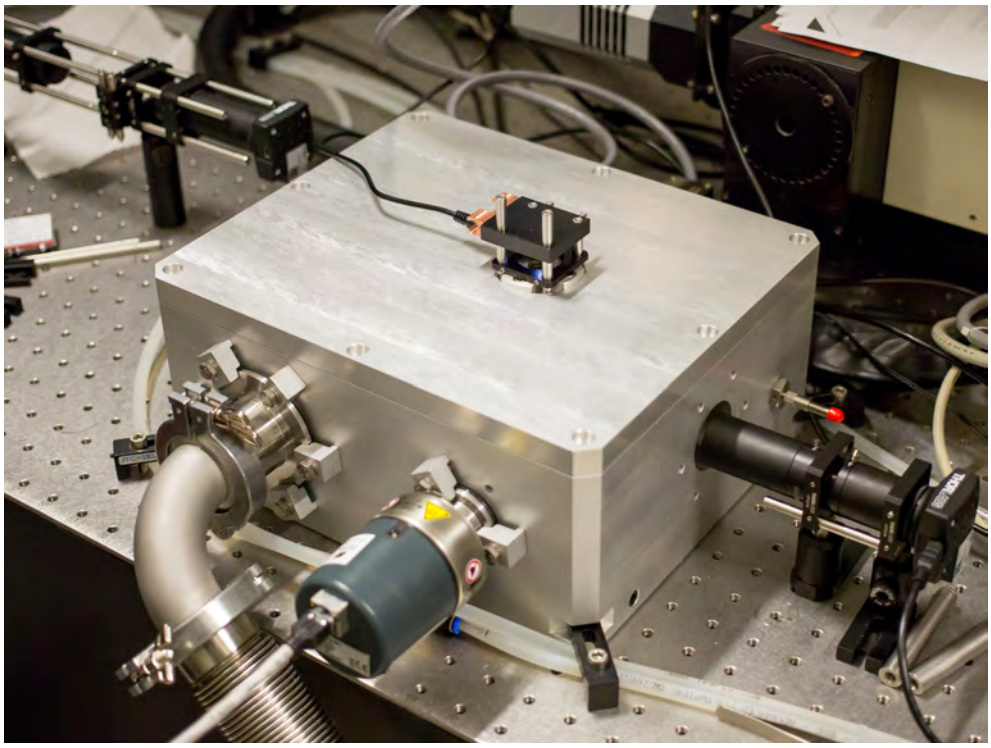

Figure 5.16: *Photography of the experiment with the vacuum enclosure closed.*

A python script was written which allows to interact with the thermal camera and make continuous images during the acquisition, as shown in Figure 5.17. Before switching on the laser, the thermal camera script, the spectrometer acquisition and the RTDs measurements were launched.

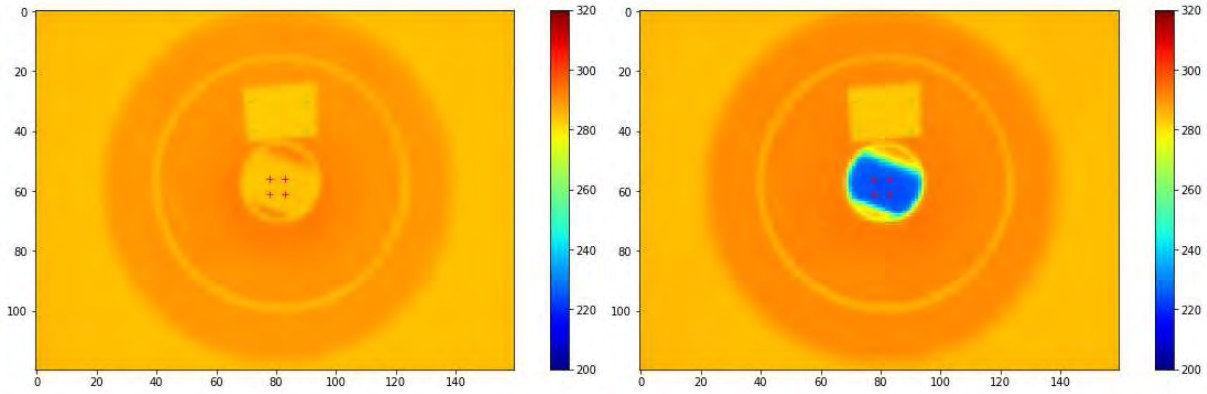

Figure 5.17: *Crystal cooling down viewed by the thermal camera. Left: scene before switching-on the laser. Right: same scene a dozen of minutes after switching on the laser and reaching low temperatures.*

5.3 Cooling demonstration at cryogenics temperatures

5.3.1 First series of results: cooling down to 160 K

A first series of tests were performed during summer 2020. During these tests, the cooling crystal was laying on two flat pieces of silica aerogel. After calibrating the thermal camera, the crystal's temperature was monitored and the fluorescence spectra recorded at the same time, as shown in Figure 5.18. An initial input laser power of 2.4 W was sent. After 50 minutes, the power was increased to 8.8 W, and to 15.5 W at minute 60. The power was then reduced to 2.4 W at minute 90, and turned-off at minute 125.

Fitting the DLT signal on the thermal camera's signal at high temperature allowed to recover the real crystal's temperature at cryogenics temperatures, where the camera can no longer measure the thermal radiation of the cold crystal. We can see that the crystal reached a minimal temperature of 160 K for a laser power of 8.8 W. Increasing the power did seem to heat up the crystal, a hint of the presence of parasitic heating, maybe due to the silica aerogel pads.

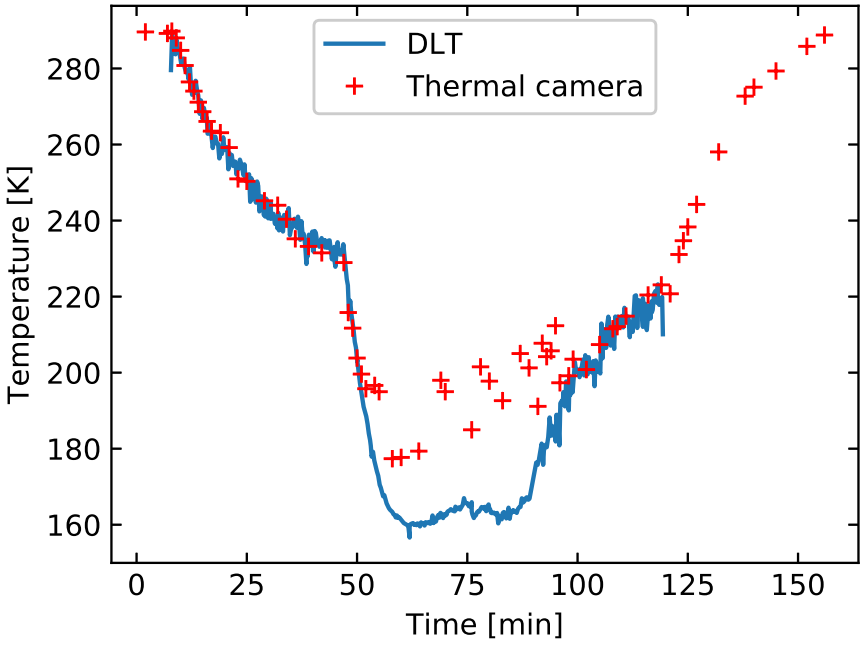

Figure 5.18: *7.5% Yb:YLF crystal temperature as a function of time monitored with the calibrated thermal camera and with the DLT method at cryogenics temperatures.*

The Lissajous figure was also checked after turning on the experiment in order to see if there was any variation of the number of round-trips. Figure 5.19 shows the image of the second mirror observed with the near-infrared camera located outside the vacuum enclosure. We can note how difficult it is to tell precisely how many round-trips are achieved just by looking

at the back camera. No change in the Lissajous figura was noticeable when observed 30 minutes later..

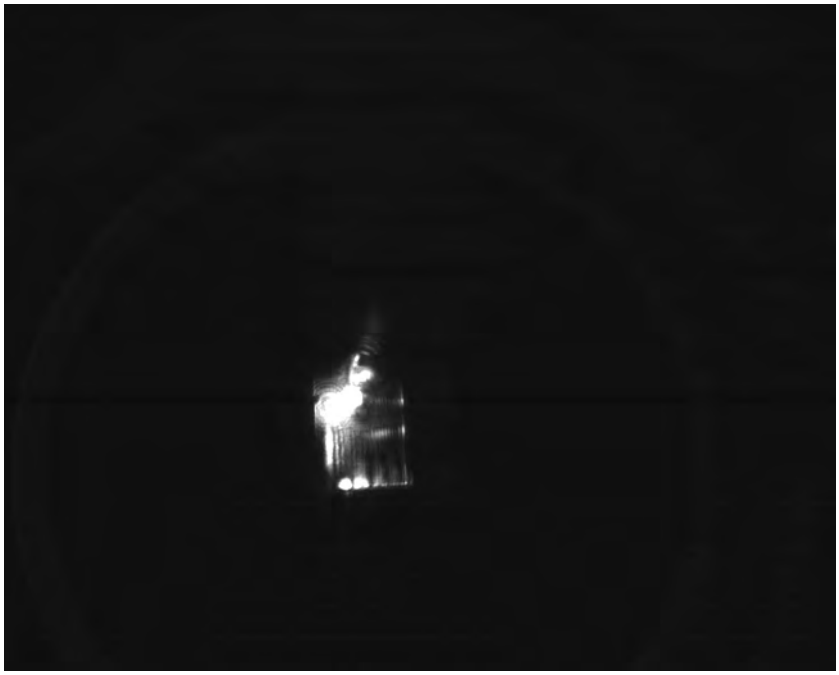

Figure 5.19: *Lissajous figure observed after 1 hour of cooling.*

After those encouraging first results, some improvements were implemented nearly immediately, allowing to reach even colder temperatures as detailed in the next sections.

5.3.2 Improved support and measurements: cooling down below 130 K

In a second iteration of cooling down tests, we tried to reduce the contact surface between the silica aerogel pads and the crystal. Instead of having two square pads, the crystal now lies on two triangular shaped pads. The crystal is now in contact with the aerogel pads on solely two ridges, thus reducing the conductive heat transfer from the cold crystal to the clamshell.

Another difference to the initial measurements is that we put a 1010 nm short-pass filter just in front of the spectrometer, in order to cut off the laser power at 1020 nm. Indeed, upon performing previous cooling runs we found that the strong laser scattering picked up by the spectrometer added a stray-light signal on the other pixels. The laser line intensity variation was enough to introduce a power dependency on the DLT calibration, which was no longer observed in the short pass filter configuration.

After re-coupling the cavity and re-aligning the crystal to make sure there was a maximal fluorescence power, we started again the measurements. Figure 5.20 shows the apparent

YLF and clamshell temperatures, as well as the camera's temperature.

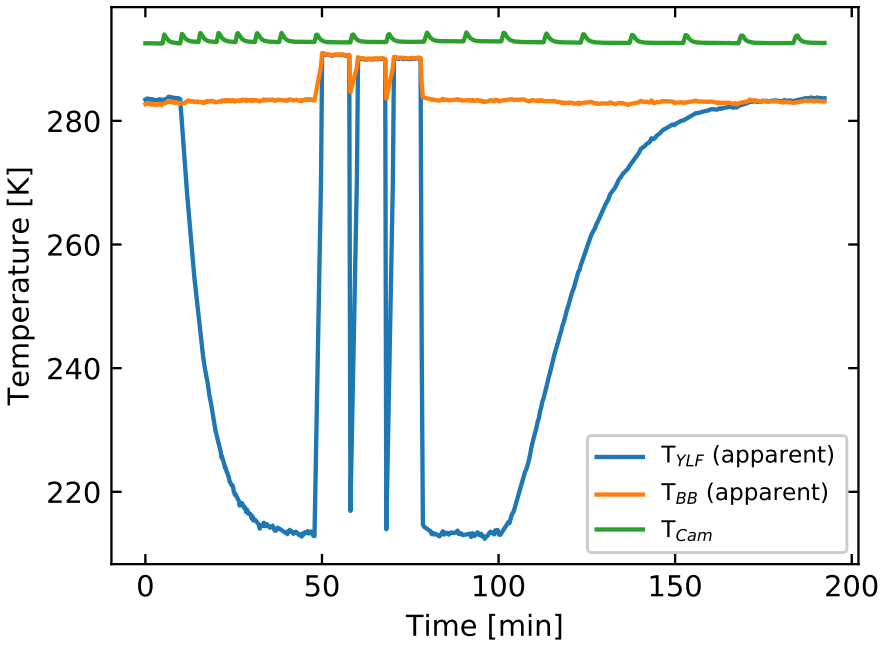

Figure 5.20: *YLF crystal, black-body and camera temperature monitored as a function of time by the thermal camera before correction.*

The thermal camera was then corrected using the external calibration in order to get the true YLF temperature, as shown in Figure 5.21. The fitting of the DLT signal over the calibrated thermal camera readings allows to find the quadratic calibration function transferring the DLT signal into temperature scale, as shown in Figure 5.22.

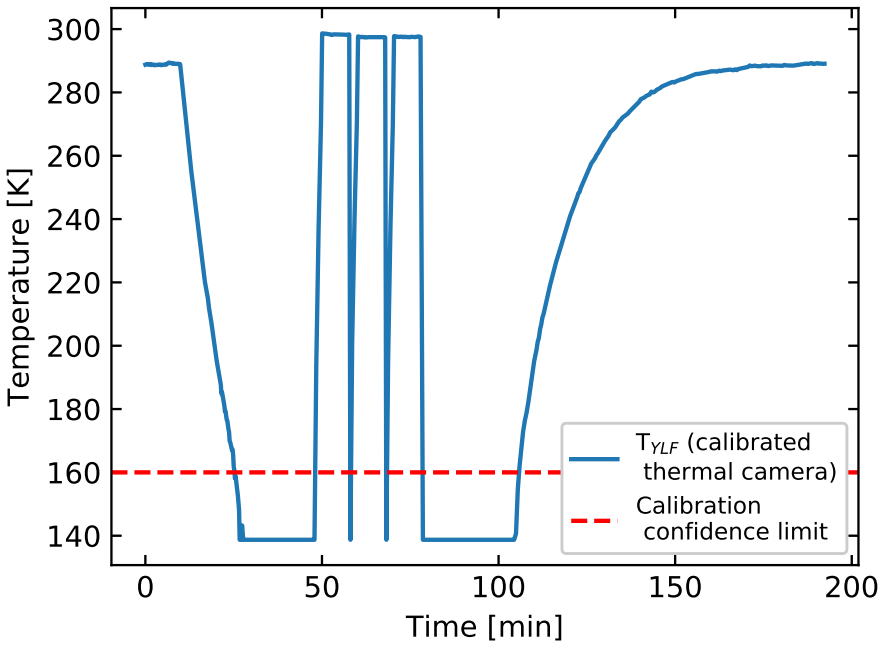

Figure 5.21: *7.5% Yb:YLF crystal temperature as a function of time, as seen by the thermal camera after calibration. The dashed red line indicates the temperature of 160 K below which the camera is uncalibrated.*

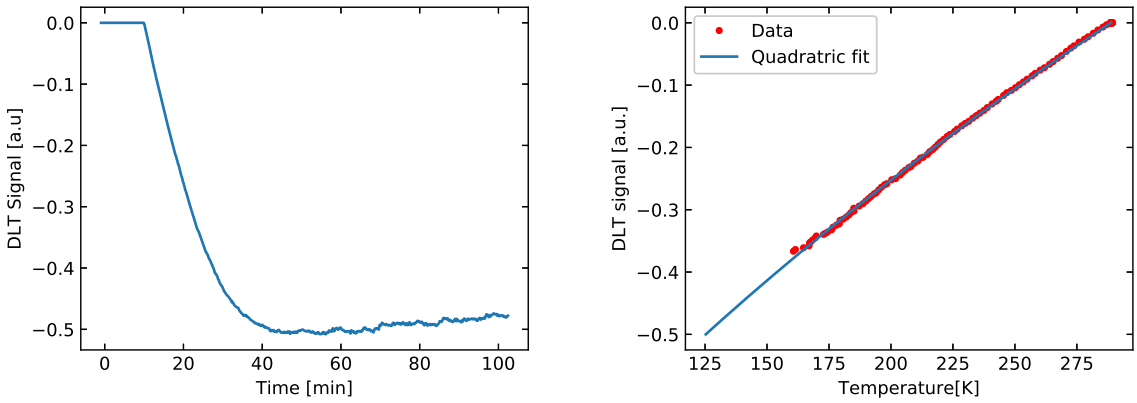

Figure 5.22: *Differential Luminescence Thermometry for the best cooling run. Left: Signal observed with DLT as a function of time. Right: DLT calibration curve obtained by fitting the DLT signal to the thermal camera data in the calibration range [300 K - 160 K].*

The temperature of YLF as seen by the thermal camera and DLT at cryogenics temperatures are shown in Figure 5.23. This time, the 7.5%Yb:YLF cooling crystal reached a temperature of about 125 K, our record so far. Slightly varying the number of thermal camera points used for the DLT fitting showed a maximal uncertainty of $\pm$ 5 K in the minimal temperature readings. Thus, we are able to say that our Laser Cryocooler prototype reached cryogenics temperatures below 130 K, for the first time in Europe.

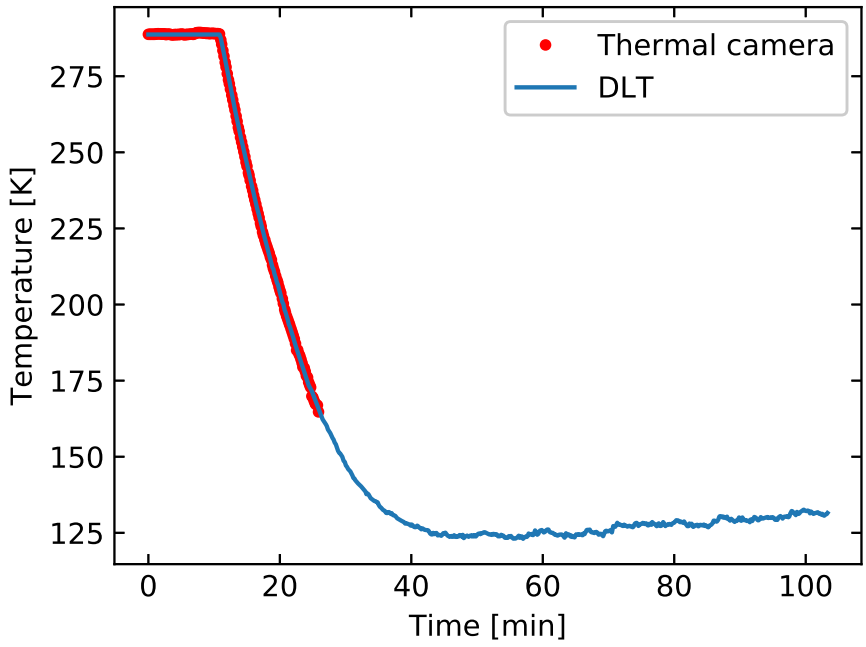

Figure 5.23: *7.5%Yb:YLF crystal temperature as a function of time with 10.7 W of laser power inside the multi-pass cavity. Temperatures are measured by the calibrated thermal camera above 160 K and with Differential Luminescence Thermometry from ambient down to cryogenics temperatures.*

We can notice the fast cooling down time, about 30 minutes from ambient to 130 K, and the overall good thermal stability, as the temperatures didn't vary by more than a few degrees over the course of one hour.

5.3.3 Thermal model and cooling power

The last step in our analysis it to estimate the crystal's cooling power. At every instant, the crystal's temperature follows the heat equation:

$$mC_v \frac{dT}{dt} = Q_{cool} + Q_{heat} \tag{5.7}$$

With m the crystal's mass and C_v the specific heat capacity of YLF calculated using Debye's model (Appendix A). The cooling power is defined as:

$$Q_{cool} = \eta_c P_{abs} \tag{5.8}$$

And the heating term defined as the sum of conductive and radiative losses:

$$Q_{heat} = Q_{cond} + Q_{rad} = k_{cond} \left(T_c - T_h\right) + k_{rad}\sigma \left(T_c^4 - T_h^4\right) \tag{5.9}$$

With k_{cond} and k_{rad} the constants for conduction and radiation heat transfer, T_c the cold crystal temperature and T_h the hot clamshell temperature. Heating terms can be estimated by analyzing the crystal's temperature variation after the laser is cut off. In that case, the crystal's temperature variation is directly equal to the sum of thermal losses. We have:

$$mC_v \frac{dT_c}{dt} = Q_{heat} \tag{5.10}$$

Knowing T_c (measured by the thermal camera), we are able to find the k_{cond} and k_{rad} parameters which gives the best fitting heat-up curve calculated with the equation, as shown in Figure 5.24. Assuming a constant clamshell temperature equal to 298 K, we find excellent agreement with parameters $k_{rad} = 2.187e-05$ and $k_{cond} = 7.976e-05$.

The losses power can now be estimated during the warm-up phase, as shown in Figure 5.25. At the coldest temperature picked up by the thermal camera, 162 K, the sum of losses were equal to about 16 mW.

By applying the same model for radiative and conductive losses to the cooling-down part of the cooling run, we are able to estimate the cooling power. But before that, in order to reduce the DLT noise from the thermal analysis, the cooling down curve was smoothed with a 11 points window Savitzky-Golay filter, as shown in Figure 5.26.

Knowing the crystal's temperature as a function of time, we are able to calculate the losses from the estimated thermal parameters, as shown in Figure 5.27.

Finally, solving the differential equation allows to find the cooling power, shown in Fig-

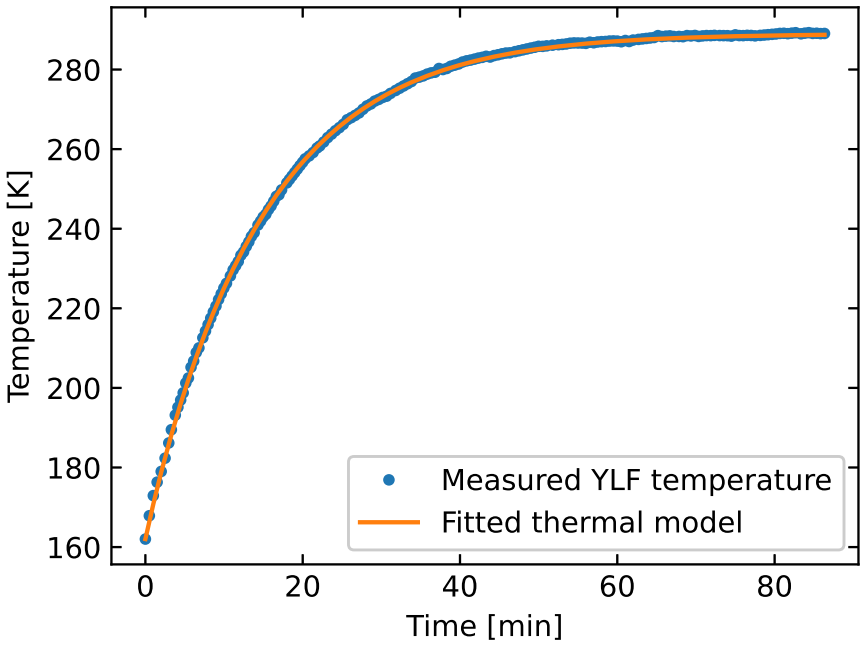

Figure 5.24: *Crystal temperature monitored by the thermal camera during its warm-up, fitted with a thermal model by solving the heat equation.*

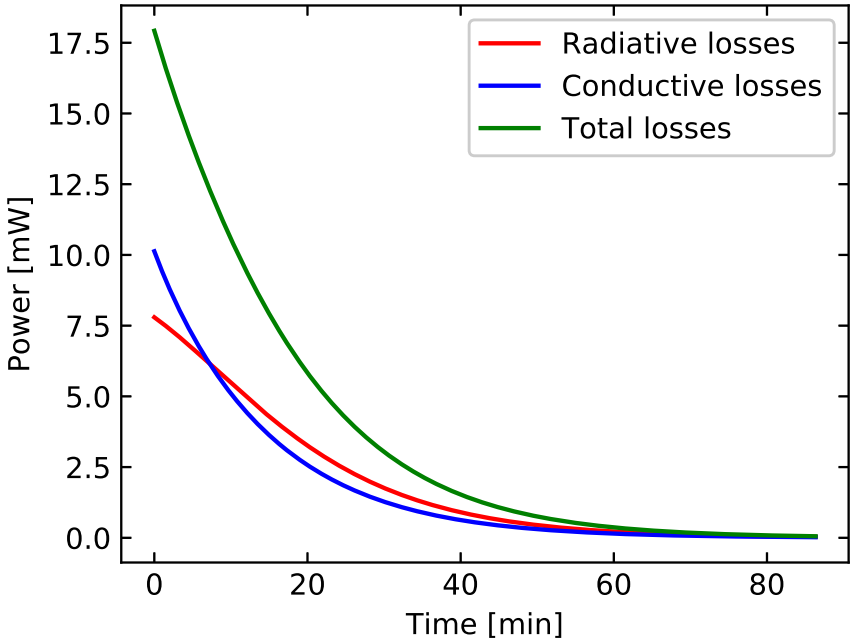

Figure 5.25: *Total of radiative and conductive losses during the warm-up phase, estimated from the fitted model.*

ure 5.28. Initially, we estimate that the cooling power was about 32 mW. As the crystal's temperature decreased, it progressively became less efficient and the final cooling power was attained around 20 mW.

These results are very encouraging, but the form of the cooling power as a function of time is a bit surprising, knowing that the predicted initial cooling efficiency should be around 60 mW, and the cooling efficiency at 125 K should be close to zero. This decay is not observed

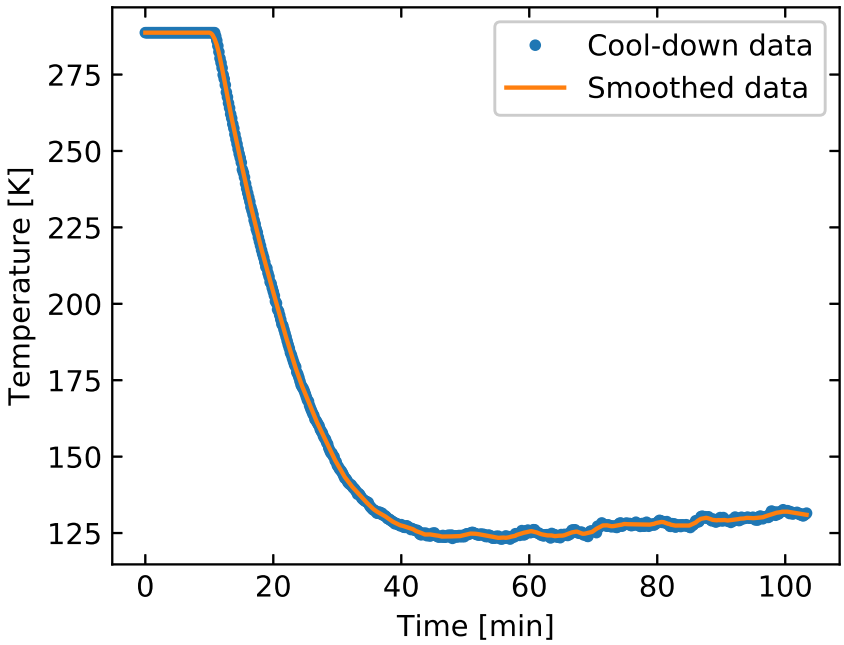

Figure 5.26: *Raw YLF temperature obtained with DLT and smoothed data used for the thermal model during cool-down.*

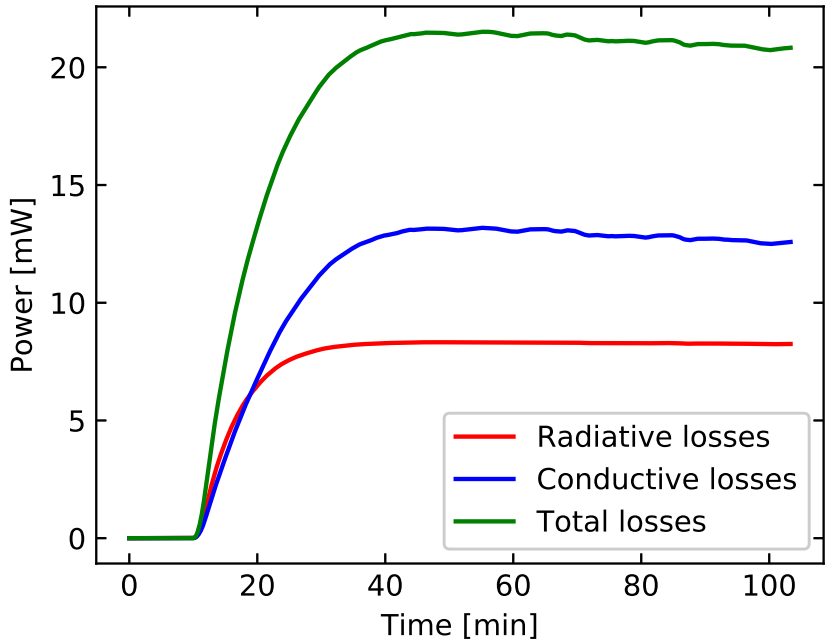

Figure 5.27: *Estimated thermal losses during cool-down.*

in our measurement.

We can plot the minimal achieved temperature for this cooling run on the 7.5% Yb:YLF theoretical cooling efficiency graph, as shown in Figure 5.29, the x mark at 125 K and 1020 nm. In comparison, for a cooling power of 20 mW and 10 W of pump laser absorbed, the predicted cooling efficiency should be close to 0.2 %, as traced by the dash-dotted contour line. In those conditions, the crystal should have attained a temperature around 180 K when

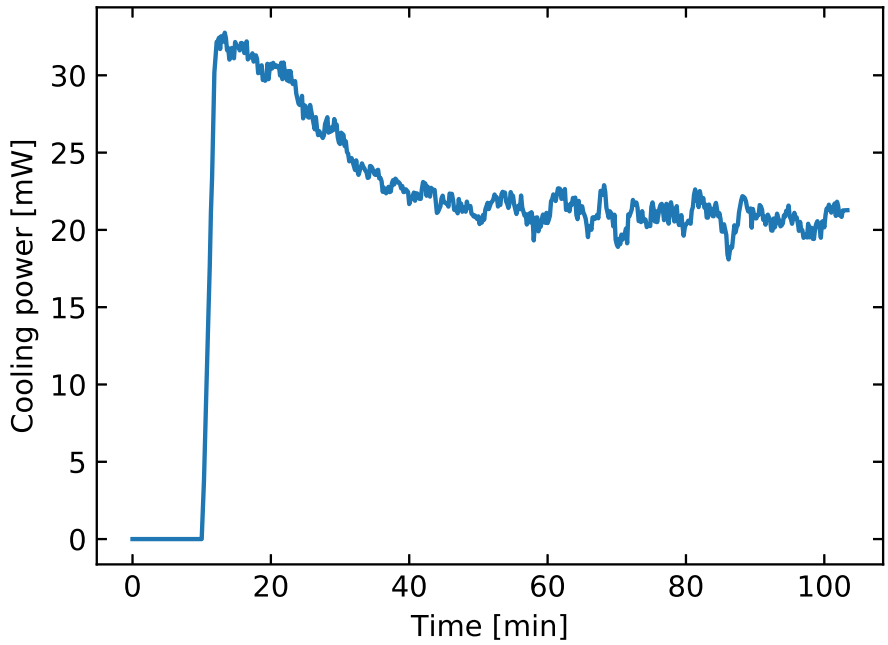

Figure 5.28: *Estimated cooling power as a function of time.*

pumped at 1020 nm.

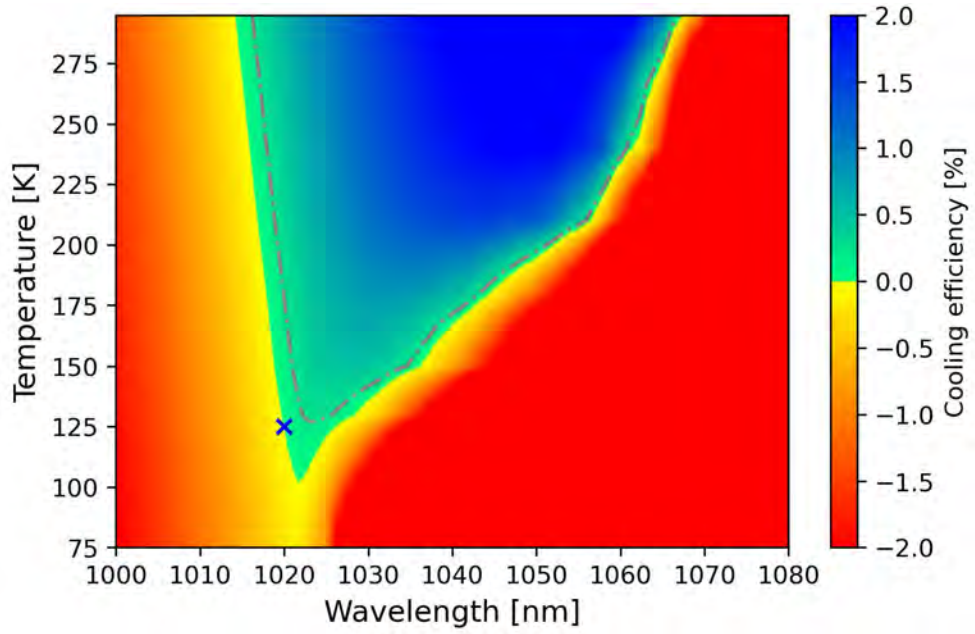

Figure 5.29: *Comparison between achieved cooling efficiency (x mark) and theoretical estimated cooling efficiency (dash-dotted line) on the cooling efficiency vs temperature and wavelength graph.*

Hence, either the final cooling power was much smaller, the initial cooling power was much higher, the crystal was more efficient than expected at low temperature, or a mix of these three effects. Provided that we are confident in the thermometers calibration and that a temperature around 125 K was really attained, we can exclude the final cooling power being smaller than measured, as it would contradict the losses model.

A discrepancy on the initial cooling power could be explained by missing heating terms in our model. For example, if part of the laser power was initially heating the silica aerogel or the clamshell, it could explain the smaller estimated cooling power.

The third explanation which is likely is that the crystal performed better at low temperatures than what was assumed theoretically. Indeed, considering cooling powers as low as a dozen of mW at cryogenics temperatures, a small difference on the external cooling efficiency can shift the minimal achievable temperature by dozens of degrees. To illustrate this point, Figure 5.29 shows the predicted cooling efficiency this time by adjusting η_{ext} such that the achieved cooling efficiency fits our measurement. We estimate the new external quantum efficiency value as $\eta_{ext} = 0.98795$ (instead of $\eta_{ext} = 0.986$), a relative error of only + 0.2 % from the measured value.

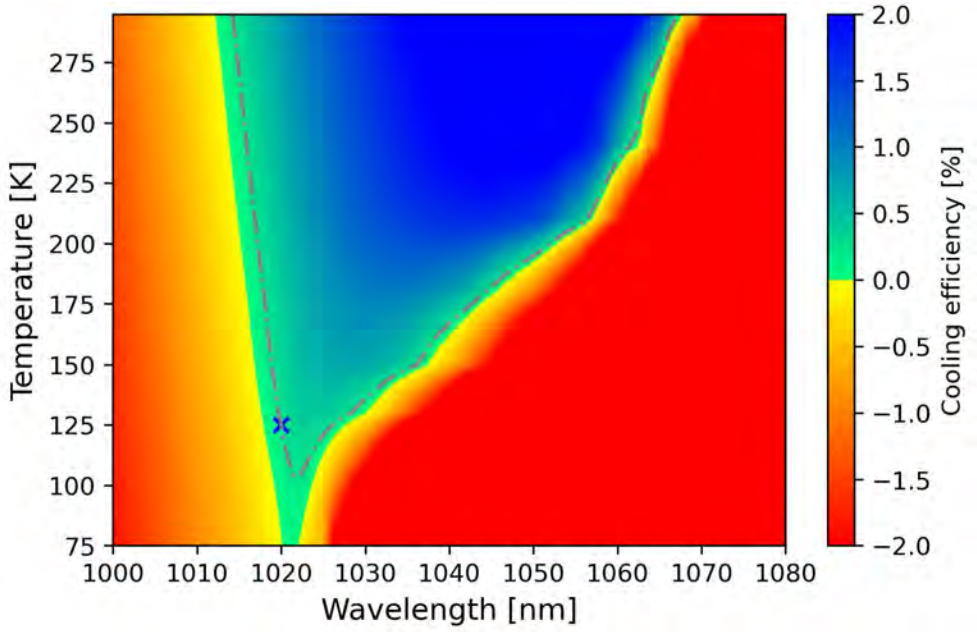

Figure 5.30: *Revised cooling efficiency as a function of temperature and pump wavelength fitting the measured cooling efficiency with* $\eta_{ext} = 0.98795$.

In other words, the theoretical cooling model which fitted a_b and η_{ext} from the cooling efficiency at room temperature requires an accuracy on the estimation of η_{ext} below 0.1 % relative error to be useful at estimating the achievable cryogenics temperatures without being off by a dozen of degrees.

This analysis stresses the need for as accurate as possible cooling efficiency measurements. It also means that in the future, we have to perform "real" cooling efficiency, background absorption and external quantum efficiency measurements directly at cryogenics temperature, as opposed to extrapolating the cooling performances at cryogenics temperatures from a set of measurements made at ambient temperature.

Additionally, measurements should be performed at different pump powers in order to check if there is a dependency of the cool-down dynamics as a function of power, which

would be the sign of an unaccounted heat source from the laser pump.

5.3.4 Analysis of a run with decreasing pump power

We present here one of our last cooling down test where the pump power was progressively decreased. The goal was to check if the pump power had any influence on the spectrometer calibration and on the temperature seen by the thermal camera. Our initial concern was that the fluorescence could heat up a bit the thermal camera and put a bias in our measurements. We show that this effect is not observable.

The crystal was cooled down by with 10.7 W initial power inside the multi-pass cavity. After it reached cryogenics temperatures, the pump power was reduced to 6.3 W, 4.0 W and 1.9 W in the cavity. Apparent temperatures measured by the thermal camera are shown in Figure 5.31.

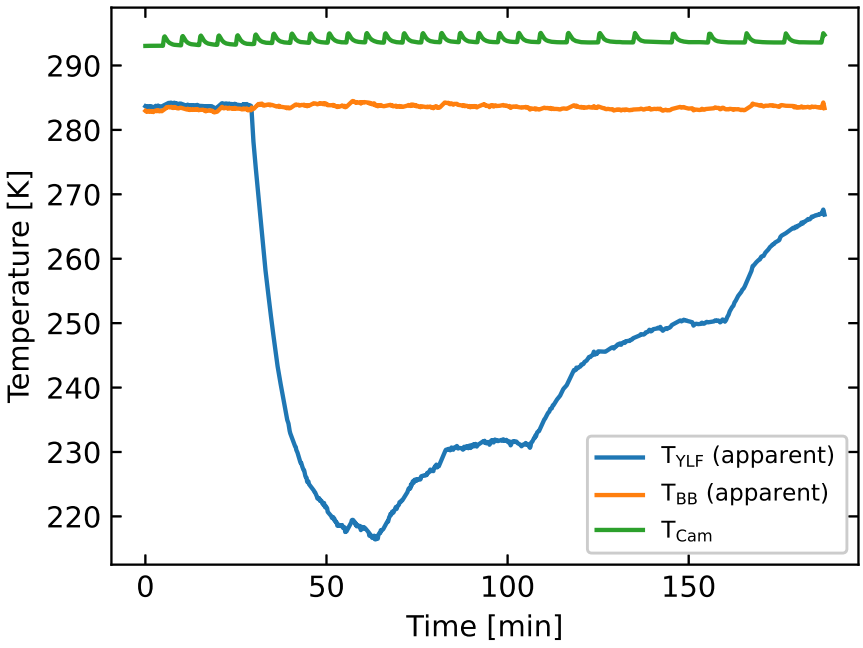

Figure 5.31: *YLF crystal, black-body and camera temperature monitored as a function of time by the thermal camera before correction for the run with decreasing pump power steps.*

The thermal camera calibration was then applied to the data in order to get the emissivity corrected YLF temperature, as shown in Figure 5.32.

Monitoring the fluorescence spectra at the same time allows to perform the Differential Luminescence Thermometry method, as shown in Figure 5.33. The DLT calibration curve is very similar to the previous run. However, it is not exactly the same, as it predicts a temperature of approximately 137 K for a DLT signal of -0.5, where it was around 125 K for -0.5 previously. This difference is probably due to the larger thermal camera error seen in this run for temperatures below 200 K, where in the other run there was less variations at

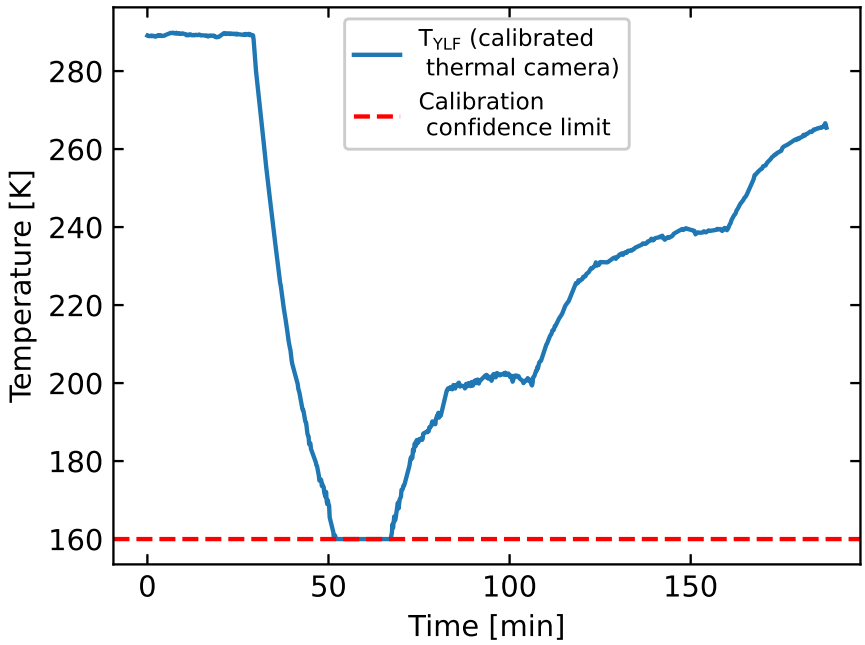

Figure 5.32: *7.5%Yb:YLF crystal temperature as a function of time, as seen by the thermal camera after calibration for the run with decreasing pump power steps. The dashed red line indicates the temperature of 160 K below which the camera is uncalibrated.*

low temperatures. Hence, we can roughly estimate the error committed at low temperature on the order of $\pm$ 5 K to $\pm$ 10 K depending on the DLT fit quality.

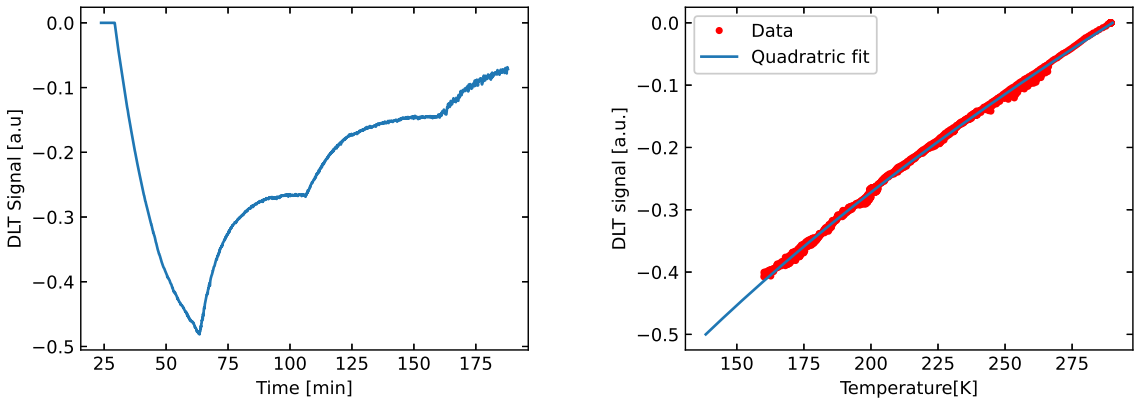

Figure 5.33: *Differential Luminescence Thermometry in the run with decreasing pump power steps. Left: Signal observed with DLT as a function of time. Right: DLT calibration curve obtained by fitting the DLT signal to the thermal camera data in the calibration range [300 K - 160 K].*

Figure 5.34 shows the crystal's temperature as a function of time. We can already notice that the initial absorbed power was reduced compared to the previous run, or the initial losses were higher. Indeed, in that run, the crystal took about 20 minutes to reach 160 K versus about 15 minutes in the previous measurement. We find excellent agreement between the thermal camera and DLT method. When the power is varied, we cannot observe any sudden bump or abrupt variation, reassuring us with the consistency of the measurements at any pump power.

Still, we see a small discrepancy on the order of a few degrees between the thermal camera and DLT towards the end, at low pump power. This discrepancy is attributable to the lower signal-to-noise ratio with lower fluorescence power, leading to a larger error relative error when performing the spectrometer baseline correction. In the future, accurate knowledge of the spectrometer CCD noise non-linearity as a function of its temperature and received intensity can account for these drift effects.

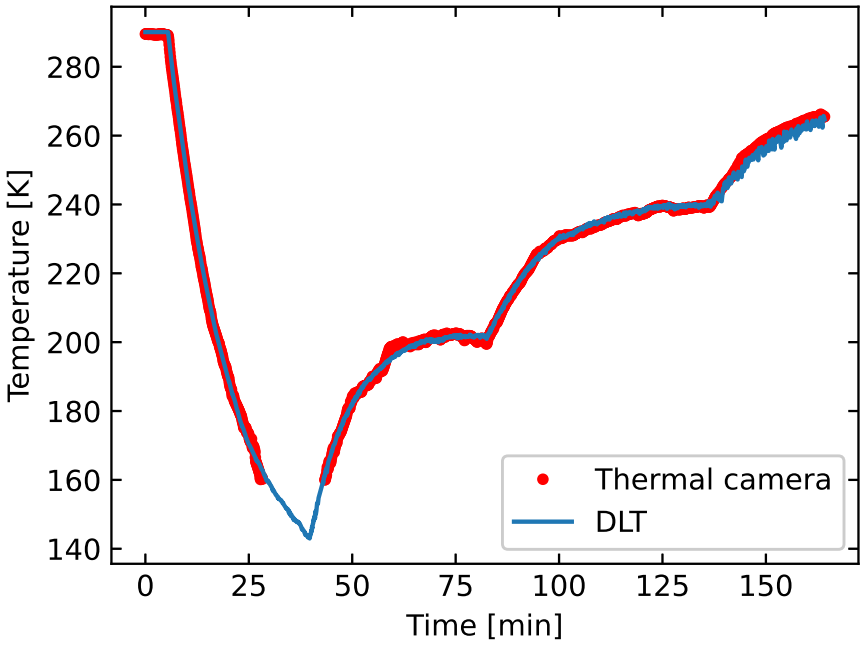

Figure 5.34: *7.5%Yb:YLF crystal temperature as a function of time with 10.7 W of laser power inside the multi-pass cavity for the run with decreasing pump power steps. Temperatures are measured by the calibrated thermal camera above 160 K and with Differential Luminescence Thermometry from ambient down to cryogenics temperatures.*

Just like in the previous run, the thermal analysis of the cool-down curve provides useful informations about the losses and the cooling power. Radiative and conductive losses were included with the same coefficients as the previous run, since the crystal was left untouched between both measurements. Before performing the thermal analysis, the data were smoothed using a Savitzky-Golay filter with an 11 point windows in order to reduce DLT noise in the thermal analysis, as shown in Figure 5.35.

The thermal losses are shown in Figure 5.36, calculated from the YLF temperature.

At last, the knowledge of thermal losses allows us to retrieve the approximated cooling power as a function of time, as shown in Figure 5.36. As expected, the slower cooling rate in this run corresponds to an initial cooling power a bit smaller, on the order of 27 mW. The first cool down at 10.7 W power inside the cavity seems to tend at a cooling power around 20 mW at low temperature, just like in the previous run.

We can observe that when switching between 10.7 W of pump power to 6.3 W, the cooling power decreased from 22 mW to 10 mW. This is a hint that some unaccounted parasitic

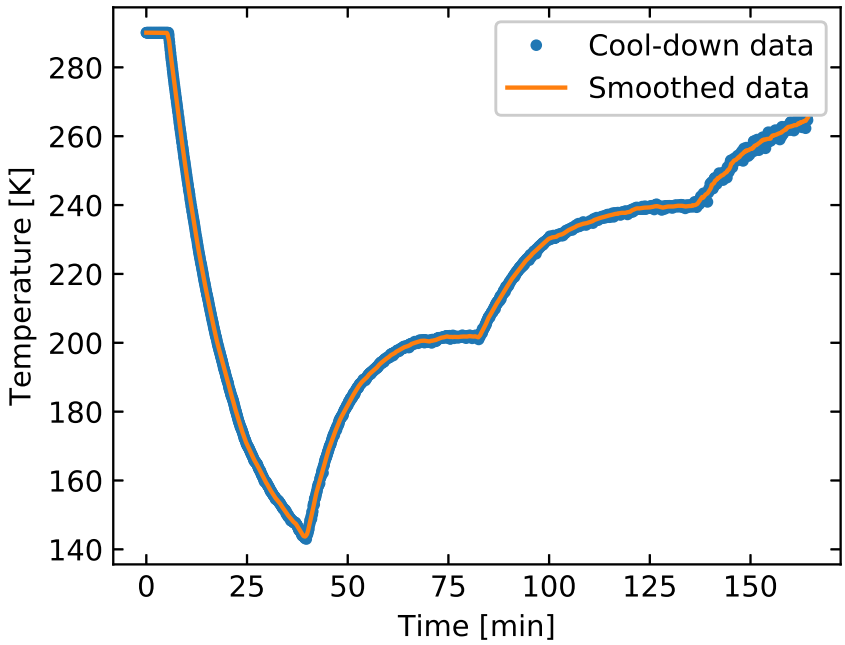

Figure 5.35: *Raw YLF temperature obtained with DLT and smoothed data used for the thermal model during cool-down for the run with decreasing pump power steps.*

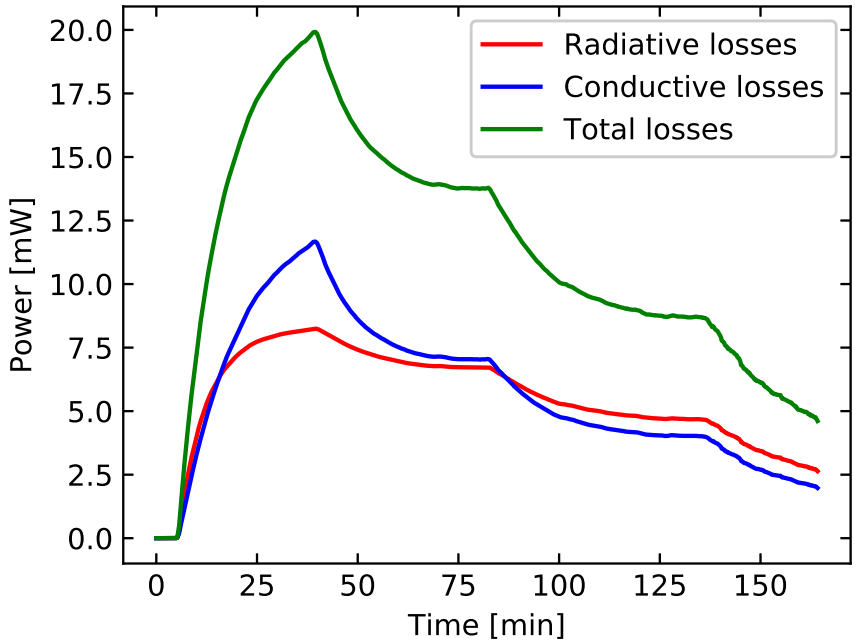

Figure 5.36: *Estimated thermal losses during cool-down for the run with decreasing pump powers.*

heating happens during cool-down, as the cooling power should have decreased from 22 mW to 13 mW instead. If a discrepancy of 3 mW is observed when reducing the pump power by 4.4 W (from 10.7 W to 6.3 W), then we can directly estimate those losses to 0.7 mW/W$_{pump}$.

Again, the discrepancy with the estimated cooling efficiency remains. For about 20 mW of cooling power at 140 K, the cooling power at ambient temperature should have been at

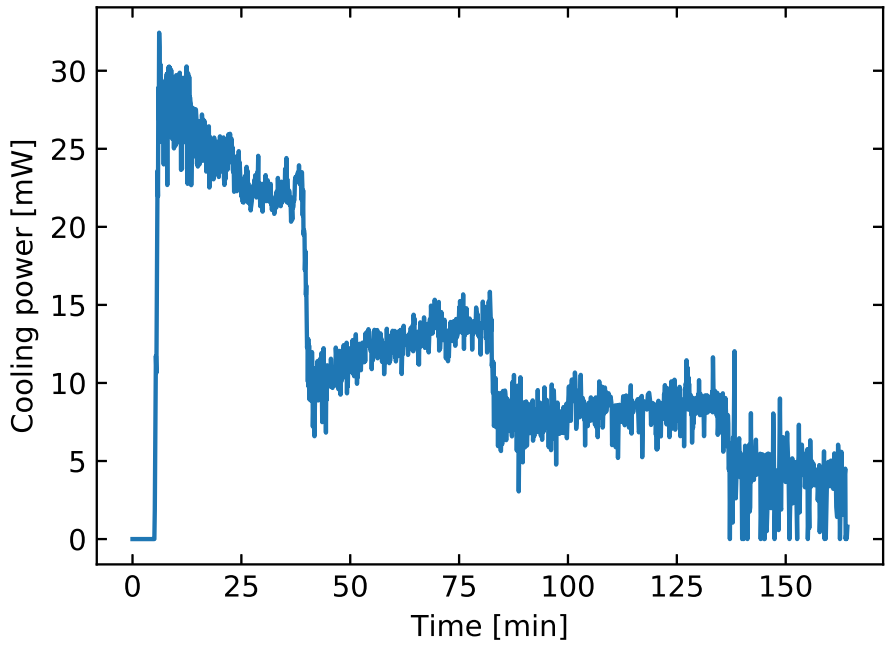

Figure 5.37: *Estimated cooling power as a function of time for the run with decreasing pump powers.*

least on the order of 4 times higher. An hypothesis could be that the crystal did in reality cool down by 80 mW, but 50 mW were lost initially due to a bit of parasitic laser absorption. Another hypothesis could be that the multi-pass cavity coupling got better after turning on the power, maybe due to thermal contraction/dilatation of the parts composing the cavity, even if less than a few degree variation was measured when turning on the power with several Watts. Further extensive analysis of the cavity minimal achieved temperature as a function of pump power are needed to fully understand the observed temperature dynamics.

5.4 Conclusion: operation of a Laser Cryocooler

With the results exposed here, we have successfully demonstrated TRL 3 (proof of concept) cooling with a Laser Cryocooler at a temperature of 125 K. To conclude on the general system operation, we can say that the strengths of a Laser Cryocooler relies in several points which we can highlight after working with the prototype.

First, we have to stress on the extreme simplicity of this cooling method, as it did not require to manufacture mechanical assemblies with exceptional precision, nor any moving parts, fluids or mechanism to test, as opposed to mechanical cryocoolers. The "magic" of laser cooling in solids is that it does only fundamentally requires a laser source, a cooling crystal, and a couple of simple optical elements in order to reach cryogenics temperatures.

Furthermore, in an un-optimized first version, the cold head already fits in a small volume, proof that this technology can pave the way towards miniaturized cryogenics. The op-

tical and conduction-losses free nature of laser cooling allowed very small thermal losses, on the order of 20 mW at cryogenics temperatures. This point is an additional argument in favor of Laser Cryocoolers in the scope of miniaturized cryogenics. The system size can be reduced in a very compact way without fundamentally deteriorating its performances, as opposed to mechanical coolers where fluids must travel in sections which cannot be reduced indefinitely, and where the distance reduction between hot and cold side eventually hinders the performances of coolers due to thermal conduction losses.

The modular design with a separation between laser source and cold head allowed a flexible development where we could focus only in the coupling part and the cold head demonstration. This fibered design is highly desirable and necessary for future applications, as we cannot afford lasers to be sent into free space for practical reasons. In real applications, this separation will allows the laser source to be located anywhere where it is the most convenient, remotely from the cold head. The fiber coupling proved to be feasible with high efficiency even with several Watts of laser power.

Finally, even if more tests are needed to fully understand the cooling power in the experiment, this work allowed us to gain significant experience in the sub-systems development and requirements in an optical cryocooler. These very encouraging results opens the way to new prototypes and exciting applications in the future.

References

[1] *FLIR Lepton® Engineering Datasheet, rev. 200*, FLIR Commercial Systems, 2014 (cit. on p. 202).

[2] W. Patterson, E. Soto, M. Fleharty, and M. Sheik-Bahae, “Differential luminescencethermometry in laser cooling of solids,” *Proc. of SPIE*, 2007.
DOI: 10.1117/12.710004 (cit. on p. 207).

[3] D. Seletskiy, M. Hasselbeck, M. Sheik-Bahae, and R. Epstein, “Fast differential luminescencethermometry,” *Proc. of SPIE*, 2009.
DOI: 10.1117/12.810856 (cit. on p. 207).

[4] T. R. Kuphaldt, “What is a Four-wire RTD ?,” 2020. [Online]. Available: https://instrumentationtools.com/what-is-a-four-wire-rtd/ (cit. on p. 208).

[5] Agilent, “Agilent 34970A User’s Guide,” 2012. [Online]. Available: https://www.keysight.com/fr/en/assets/9018-02644/user-manuals/9018-02644.pdf (cit. on p. 208).

Conclusion

This thesis addresses the practical aspects of the design, manufacturing and operation of a Laser Cryocooler for the first time in Europe. Our prototype reached a temperature of 125 K with about 20 mW of cooling power at low temperature, with an innovative fiber coupled design anticipating the constraints of future space implementations. These encouraging result allows us to claim TRL 3 for this technology.

A Laser Cryocooler is a miniature system, completely vibration-free and features a contact-less or parasitic conduction free cooling method, as opposed to mechanical cryocoolers. Moreover, there are no EMC, no fluids/gases and no moving parts in optical cryocoolers, which will be huge advantages in the frame of its future space qualifications phases.

Among existing space qualified cryocoolers, Laser Cryocoolers are the only true solid state coolers capable of reaching cryogenics temperatures, filling the gap between mechanical cryocoolers and Peltier coolers around 100 K - 200 K where passive cooling is traditionally implemented in satellites at the costs of increased mass/volume and orbit constraints.

In a comparative size, weight and power analysis at the level of a satellite, we showed the interests of using Laser Cryocoolers onboard small observation satellites for payload mass and volume reductions. Furthermore, with the constant improvement of cooling crystals and new co-doped generations, the development of the Laser Cooling technology has the potential to become efficient enough such that it can be used onboard the smallest classes of satellites such as CubeSats. This open the door to a change of paradigm in the domain of miniature earth-observation cryogenics instruments and could lead to exciting new applications and opportunities.

Importantly, we set everything up for the development of optical cryocoolers with the goal of transferring the technology from the lab to the space industry. First, we applied a panel of techniques availaible at Institut Néel for the characterization of cooling crystals, from surface contamination analysis to spectroscopy.

After an initial optical design and fabrication phase, we developed our first Laser Cryocooler prototype. This prototype, based on the extra-cavity type, implements a multi-pass

optical cavity which allows to attain a high number of laser round-trips within the crystal in order to maximize the absorbed power. Notably, the separation between laser source and cold head from the extra-cavity paradigm allowed us to focus on the parts surrounding the cooling crystal.

After setting up the experiment, we operated the prototype. The crystal's temperature was monitored using two complementary methods: using a thermal camera from ambient temperature to 160 K, and using fluorescence non contact thermometry with a spectrometer from ambient down to cryogenics temperatures.

Our results show that the cooling crystal attained a minimal temperature around 125 K with 10 W of input power, and a cooling power of about 20 mW. Cryogenics temperatures were reached from ambient in about 30 minutes and were stable for over 1 hour of operation. The extreme simplicity and the ease of use of a Laser Cryocooler is a huge asset which adds to its other advantages.

More than a local achievement, this work marks also an important and historical milestone: that of cryogenics temperatures being readily accessible with solid state optical refrigeration. Where ten years ago it would have been still unthinkable to reach cryogenics temperatures with optical cooling, in a couple of years we managed to attain them with appropriate optical design and cooling grade crystals.

The next step for us is now to improve the technology in order to meet the performances and system quality expected of a space qualified equipment. On that road, we can express three axes for the improvement of optical cryocoolers.

On the first axis, the characterization and improvement of cooling crystals is of utmost importance in order to attain even better cooling performances. Part of the work we performed on the characterization of crystals after their growth will help evaluate the performances of cooling crystals in the future. The development of purification methods before the crystal's growth is also an action which would need to be investigated and scaled up if possible, in order to reduce the variability in cooling crystals performances.

On the second axis, the improvement of optical design is an important work which needs to be continued. The optical design has now to address the thermal link part of a Laser Cryocooler, the piece which contacts the cooling crystal with the thermal load. Due to the strong crystal fluorescence, this part has a number of constraints: it has to be from a transparent material and cannot be glued upon the crystal's surface. The next step is to develop the method of optical contact bonding in order to attach a thermal link with matched thermal expansion coefficients (such as YLF or MgF2) to the cooling crystal.

Finally, on the third axis, we find the development at system level, and the space qualification of the system. There is still some work in order to develop a suitable space compatible laser source around 1020 nm. The question of the laser source architecture is still

open. Another question which needs to be investigated is the effect of radiations on cooling crystals.

To conclude, this work opens the way to a new generation of cryocoolers for future space applications: Laser Cryocoolers, which are miniaturized, vibration-less and features reduced thermal losses due to the optical and contact-free nature of the technology.

Publications

Journal publications:

- R. Vicente et al., **"Operation of a fiber-coupled lasercooler down to cryogenic temperatures"**, To be published soon.
- R. Vicente, G. Nogues, J.-M. Niot, T. Wiertz, P. Contini, A. Gardelein, **"Impacts of laser cooling for low earth orbit observation satellites: An analysis in terms of size, weight and power"**, Cryogenics, 2020.

Proceedings:

- R. Vicente, G. Nogues, L. Del-Rey, J. Debray, D. Jegouso, J.-F. Motte, G. Cittadino, A. Di Lieto, M. Tonelli, J.-M. Niot, A. Gardelein, **"Demonstration of a fiber-coupled optical cryocooler: a step towards future space applications"**, Proc. of SPIE, 2021.
- R. Vicente, G. Nogues, J.-M. Niot, Y. Juanico, A. Gardelein, **"Presenting the first European laser cryocooler prototype: A game changing technology for miniaturized cryogenics on-board small satellites"**, Proceedings of the International Astronautical Congress, IAC, 2020.

Presentations

Conferences where I was the speaker:

- **SPIE Photonics West OPTO 2021:** Invited video talk during the session "Photonics heat engines III" and live questions session. Annual worldwide gathering of the laser cooling in solids community.
- **28th Space Cryogenics Workshop 2019:** NASA conference, biennial worldwide gathering of the space cryogenics community.
- **Grenoble NewSpace Week 2019:** Grenoble Space Center (CSUG) conference with many invited actors of the space field centered about the "New-Space" concepts and Nanosatellites.

Internal presentations where I was the speaker:

- **Laser Cooling progress meetings:** Once/twice per month frequency reports where I make a summary with our latest progress.
- **Presentation at the University of Pisa, 2018:** A quick presentation about our plans and the foreseen multi-pass cavity architecture for Prof. Tonelli's group.
- **NPSC days, 2018:** The Nanophysics and Semiconductor team's annual meeting.
- **PLUM days, 2018:** The lab's department "Physique Lumière Matière" annual meeting.
- **Air Liquide internal presentations, january-february 2019:** Report on Laser Cooling activities for the colleagues at Air Liquide Advanced Technologies, space department.
- **Pousse-café, 2020:** Short format talk/live event where I presented our topic in front of the lab's attendees.

Appendix A

Yb:YLF properties

A.1 General properties

Yb:YLF properties	
Crystal structure	Tetragonal, scheelite
Point group	$I4_{1/a}$
Lattice parameters	a = 5.26 Å, c = 10.94 Å
Thermal expansion	// a : 13 x 10^{-6} K^{-1} // c : 8 x 10^{-6} K^{-1}
Thermal conductivity	0.06 W/cm.K
Density	3.95 g/cm3
Mohs hardness	4 - 5
Melting temperature	825 ℃
Refractive indices @ λ = 1000 nm	no = 1.448 ne = 1.470

Table A.1: *Yb:YLF general physical, thermal and optical properties.*

A.2 Specific heat capacity

Specific heat capacity of a substance is defined as the amount of heat required to increase a certain mass of that substance by one degree. For gases, there is a difference between the specific heat capacity at constant pressure c_p and the specific heat capacity at constant volume c_v due to the ideal gases law. In solids, there is very little variation between those values. Debye's model allows to compute the specific heat capacity of Yb:YLF as a function of temperature, using the formula:

$$c_v = \frac{9nN_Ak_B}{M}\left(\frac{T^3}{\theta_D}\right)\int_0^{x_m}\frac{x^4e^x}{(e^x-1)^2}dx \tag{A.1}$$

And knowing that doped YLF has a specific heat $c_v = 0.769J/g/K$ at 298 K, from reference R. L. Aggarwal et al., J. Appl. Phys. 98, 103514 (2005). The calculated specific heat capacity of Yb:YLF as a function of temperature is shown in Figure A.1.

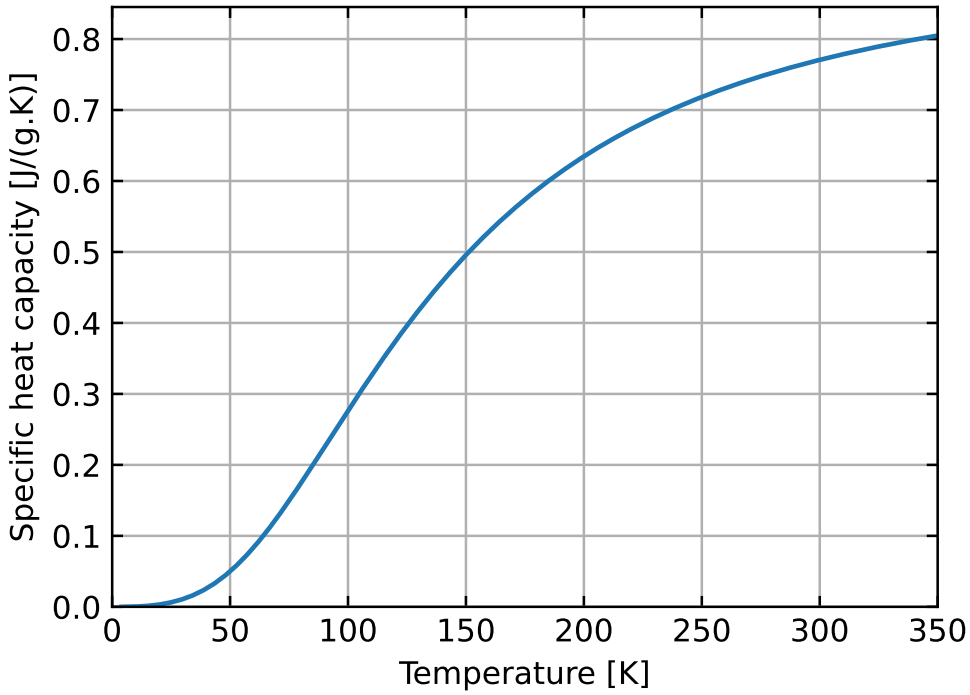

Figure A.1: *Doped Yb:YLF specific heat capacity as calculated with the Debye model.*

Appendix B

HR 4000 spectrometer calibration

B.1 Spectral response calibration

The HR4000 spectrometer uses a silicon CCD detector model Toshiba TCD1304AP. Silicon makes excellent detectors in the UV/Visible range, but the band gap of silicon is around 1100 nm (1.1 eV), which means that the quantum efficiency of silicon collapses in the infrared. In order to take that effect into account in our fluorescence spectra measurements, the spectrometer response was calibrated. A tungsten calibration lamp (model Ocean Optics DH-2000-CAL) provided a reference with known spectra, which was measured with the spectrometer. The lamp "cosine corrector" diffuser was used, and the lamp's output focused on the spectrometer fiber through a Thorlabs lens with B type anti-reflective coating and a Thorlabs 600 nm high pass filter (FEL600). Figure B.1 shows the measured lamp signal after dark background subtraction, corrected for the coating and filter transmission.

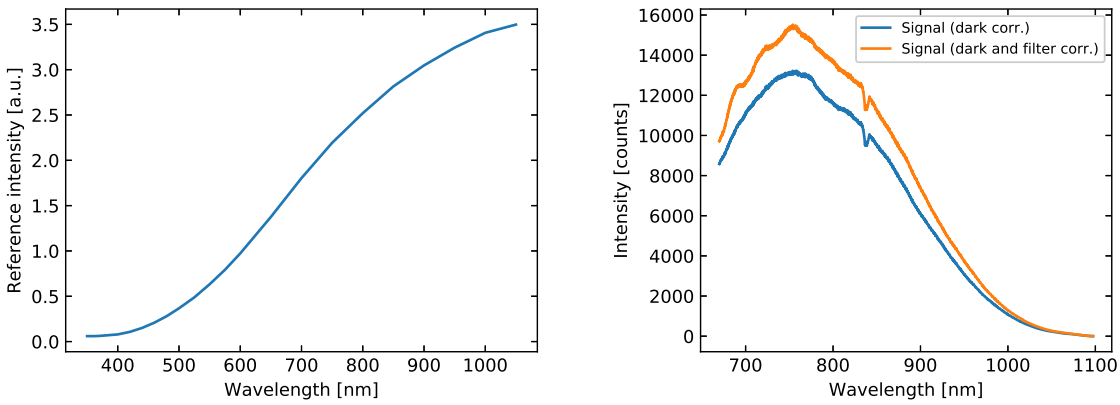

Figure B.1: *DH-2000-CAL calibration lamp reference spectra and measured signal with the HR4000 spectrometer.*

Dividing the measured intensity by the reference intensity allows to find the spectrometer response, as shown in Figure B.2.

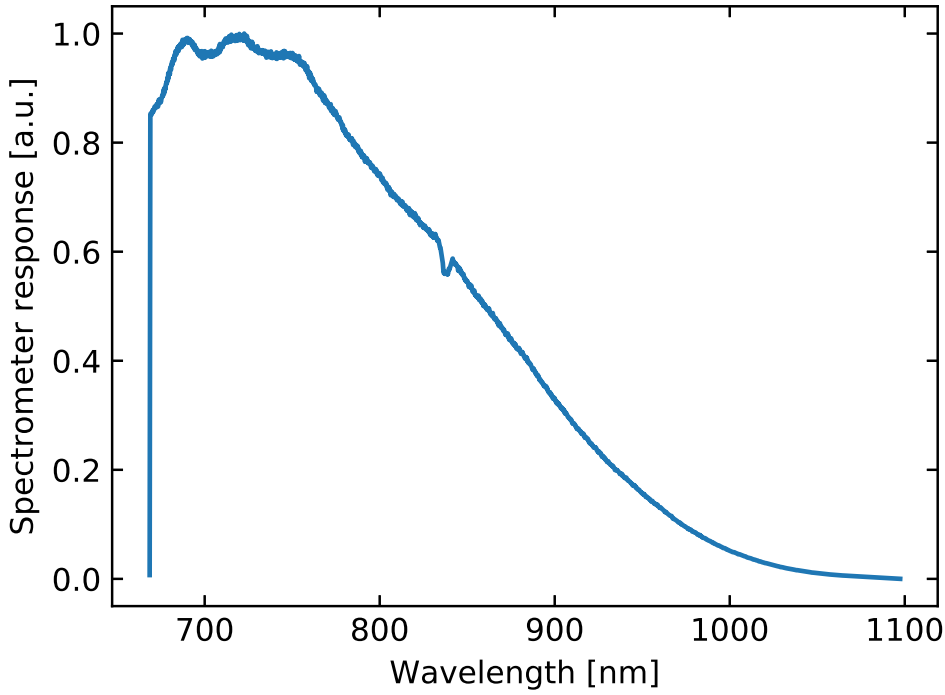

Figure B.2: *HR4000 spectrometer response.*

B.2 Wavelength calibration

In the process of measuring fluorescence spectra, we noticed some of the strong peaks in Yb:YLF were off by a few nm from the measurements from the University of Pisa. We decided to check the wavelength accuracy of our HR4000 spectrometer.

To calibrate the wavelength of our spectrometer, we used three "pencil style" calibration lamps from Newport/Oriel. These rare gases lamps provide narrow spectral lines at known positions and known relative intensities which can be then used to check the spectrometer deviation and correct it. For our calibration, we used the Neon (6032), Krypton (6031) and Xenon (6033) lamps, as shown in Figure B.3.

Each time, two spectra were taken for each calibration lamp: a measurement with high acquisition time allowed to resolve the weakest lines, and a measurement with high acquisition time allowed to see the strongest lines, as shown in Figure B.4, Figure B.5 and Figure B.6.

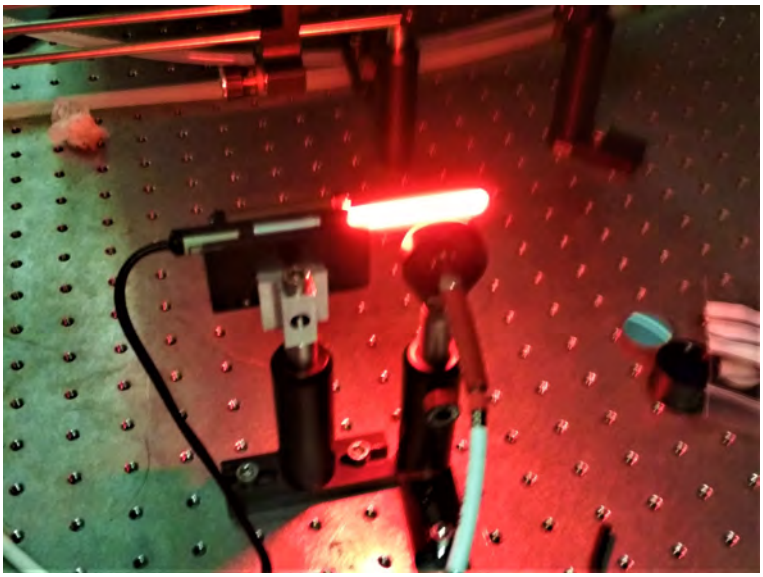

Figure B.3: *Photograph of the spectrometer's multi-mode fiber positioned in front of the Neon pencil lamp.*

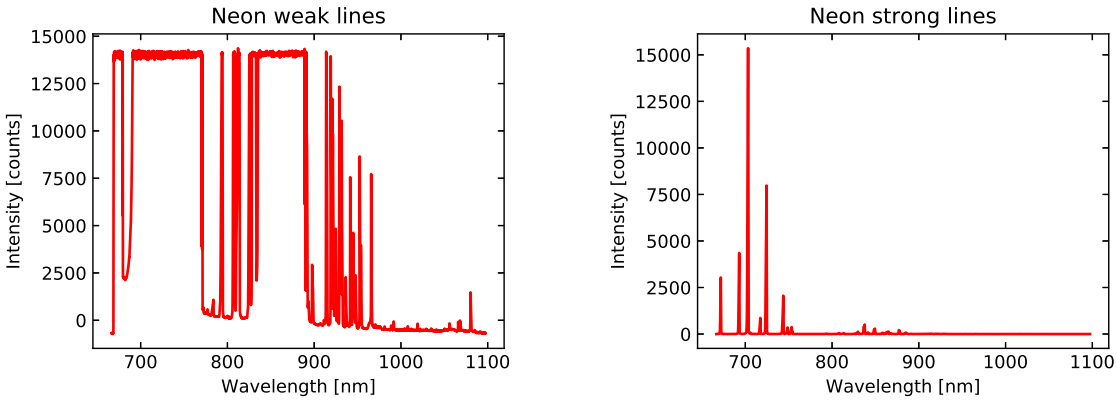

Figure B.4: *Neon lamp emission spectrum.*

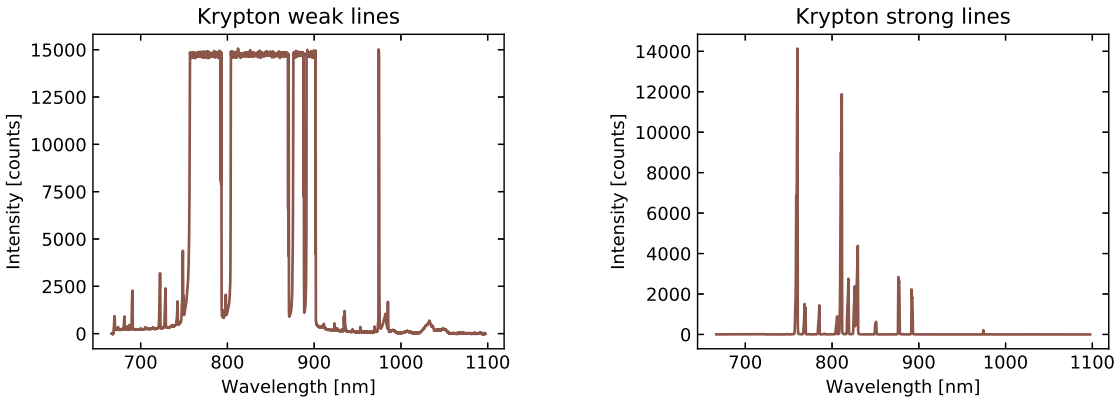

Figure B.5: *Krypton lamp emission spectrum.*

The lines which were the most easily assignable were fitted with the software Fityk with Lorentzian lineshapes in order to accurately measure their center and compared with the values reported by NIST catalogs. Xenon weak lines were not used due to the high spectral

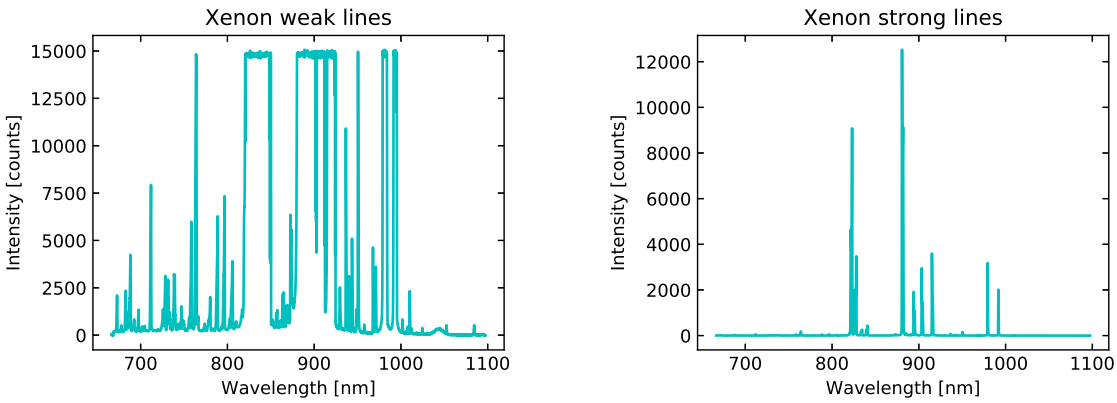

Figure B.6: *Xenon lamp emission spectrum.*

confusion between 700 and 800 nm. The spectrometer deviation (error) in measuring the calibration lines is reported in Figure B.7

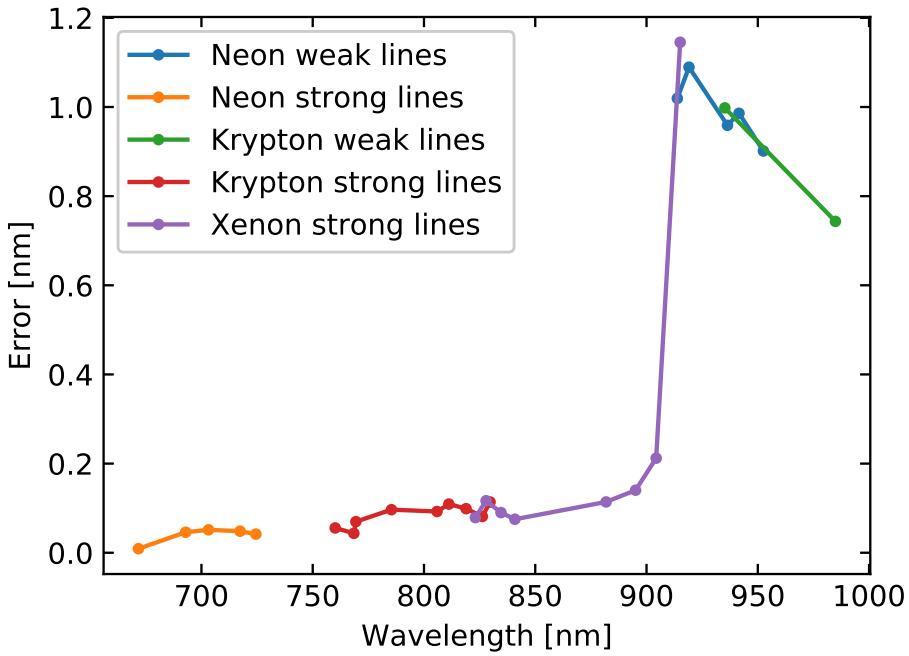

Figure B.7: *Spectrometer wavelength error for a set of well identified rare gases peaks with known wavelength.*

We can observe a bump in the error above 920 nm, probably an effect which has to do with the grating used in the spectrometer. After measuring this effect, we decided to left it untouched, as it is on the order of only 1.2 nm at maximum, and because there was no satisfying way to use the built-in HR4000 EEPROM wavelength calibration in order to account for such a "bump".

Abstract: Optical refrigeration in solids or laser cooling in solids is a breakthrough technology, reaching cryogenic temperatures (below 120 K –150 K) by the illumination of rare-earths ions doped crystals with an infrared laser at the adapted wavelength. The excitation of such a crystal near the gap wavelengths between fundamental and excited ionic states allows to predominantly stimulate the Anti-Stokes emission process, phenomenon by which the crystal re-emits more light than it has absorbed, hence cooling it down. Cryocoolers based on this revolutionary principle have the potential to ease or render possible a number of instrumental applications where vibrations and the bulkiness of traditional mechanical cryocoolers (ex. : Stirling/Pulse-Tube, Joule-Thomson, Turbo-Brayton) are stumbling blocks. The historical major targeted application is the cooling of detectors onboard Earth observation satellites, especially in the most sensitive instruments where vibrations are detrimental for performances, or onboard small satellites such as Microsatellites or even Nanosatellites, disposing of limited payloads and strong associated constraints. This thesis inserts in the frame of a French collaboration between Air Liquide Advanced Technologies (Sassenage), European leader of space cryogenics and Institut Néel, CNRS (Grenoble). The first goal of my thesis was to demonstrate the operation of a Laser Cryocooler prototype aimed at space applications for the first time in Europe. In three years, we successfully designed, developed and operated a Laser Cooler laboratory prototype capable of reaching cryogenics temperatures, thus advancing this technology to TRL 3 maturity. The 7.5% Ytterbium doped $YLiF_4$ cooling crystal lent by the University of Pisa for our experiment is capable of cooling down to temperatures close to 130 K (-153 ℃) with 10 W of absorbed laser power in about 30 minutes. In our system, the laser is supplied to the cooling crystal through an optical fiber in order to already take into account some of the constraints in a satellite application, making it a world premiere. The second goal of my thesis was to study the feasibility and suitability of Laser Cryocoolers for future Earth observation satellites. Based on the power architecture of small low earth orbit infrared observation satellites, we compared the balance of a solution with a Laser Cryocooler versus a Pulse-Tube based solution in terms of size, weight and power at the level of the whole satellite. We show that a Laser Cryocooler is a compact system which allows for internal volume and mass savings in the payload part, on top of its other advantages. This work opens the way to a new generation of cryocoolers for future space applications: Laser Cryocoolers are miniaturized, vibration-less and features reduced thermal losses due to the optical and contact-free nature of the technology.

Résumé : Le refroidissement optique dans les solides ou refroidissement laser dans les solides est une technologie de rupture, atteignant des températures cryogéniques (inférieures à 120 K –150 K) par l'éclairement de cristaux dopés aux ions de terre-rares avec un laser infrarouge à la longueur d'onde adaptée. L'excitation d'un tel cristal aux longueurs d'ondes proches du gap entre états fondamentaux et états excités ioniques permet de stimuler préférentiellement le processus d'émission Anti-Stokes, phénomène par lequel le cristal ré-émet plus de puissance lumineuse que ce qu'il a absorbé, provoquant ainsi son refroidissement. Les cryo-refroidisseurs basés sur ce principe révolutionnaire ont le potentiel de faciliter ou rendre possible nombre d'applications ou les vibrations et l'encombrement des cryo-refroidisseurs mécaniques traditionnels (ex. : Stirling/Pulse-Tube, Joule-Thomson, Turbo-Brayton) sont des points bloquants. L'application majeure historiquement visée est le refroidissement des détecteurs à bord des satellites d'observation de la terre, particulièrement dans les instruments les plus sensibles pour lesquels les vibrations sont préjudiciables aux performances, ou encore à bord de petits satellites du type Microsatellite ou même Nanosatellite, disposant d'une partie charge utile réduite et de fortes contraintes associées. Cette thèse s'inscrit dans le cadre d'une collaboration française entre Air Liquide Advanced Technologies (Sassenage), leader Européen de la cryogénie spatiale et l'Institut Néel, CNRS (Grenoble). Le premier but de ma thèse a été de démontrer le fonctionnement d'un prototype de Cryo-refroidisseur Laser en vue d'applications spatiales pour la première fois en Europe. En trois ans, nous avons conçu, développé et fait marcher un prototype de refroidisseur Laser capable d'atteindre des températures cryogéniques, avançant ainsi la maturité de cette technologie au niveau TRL 3. Le cristal refroidisseur de $YLiF_4$ dopé à 7.5% d'Ytterbium prêté par l'Université de Pise pour notre expérience est capable de refroidir à des températures proches de 130 K (-153 ℃) avec 10 W de puissance laser absorbée en environ 30 minutes. Dans notre système, le laser est acheminé vers le crystal refroidisseur à travers une fibre optique dans le but de déjà prendre en compte certaines contraintes d'une application satellite, pour la première fois au monde. Le second but de ma thèse a été d'étudier la faisabilité et la pertinence d'un Cryo-refroidisseur Laser pour les futurs satellites d'observation de la Terre. Basés sur l'architecture électrique des petits satellites d'observation infrarouge, nous avons comparé le bilan d'une solution Cryo-refroidisseur Laser versus solution Pulse-Tube en termes de volume, poids et puissance au niveau du satellite complet. Nous montrons que le Cryo-refoidisseur Laser est un système compact qui permet des économies de volume interne et de masse dans la partie charge utile, en plus de ses autres avantages. Ce travail ouvre la voie vers une nouvelle génération de cryo-refroidisseurs pour les futures applications spatiales: les Cryo-refroidisseurs Laser sont miniaturisés, sans vibrations et présentent des pertes thermiques réduites de part la nature optique et sans contact de la technologie.